Università del Salento

Facoltà di Scienze Matematiche, Fisiche e Naturali

Dipartimento di Matematica e Fisica "Ennio De Giorgi"

Dottorato di Ricerca in Fisica e Nanoscienze - XXXII ciclo

Settore Scientifico Disciplinare: FIS/04

Ph.D. Thesis

Search for electroweak production of chargino and slepton pairs decaying into final states with two leptons and missing transverse momentum in the ATLAS experiment at the LHC Run II

CERN-THESIS-2020-154
17/04/2020

Supervisors:
Prof. Edoardo Gorini
Dr. Margherita Primavera

Candidate:
Francesco Giuseppe Gravili

Contents

Introduction

The Standard Model (SM) of fundamental interactions is the underlying theory describing all elementary particles, as well as the electromagnetic, strong and weak interactions they can establish. Over the years, many experimental results have precisely confirmed the predictions of this theory, the last one being the discovery of the Higgs boson in 2012 at the Large Hadron Collider (LHC) by the joint efforts of the ATLAS and CMS Collaborations.
However, there are still some open questions whose answers cannot be presently found within the SM framework: the hierarchy problem, the existence of dark matter, the asymmetry between matter and antimatter observed in our universe. All these issues suggest a new theory, or at least an extension of the existing SM, must be considered to reach an exhaustive view of particle physics.
SUperSYmmetry (SUSY) is a theoretical extension of the SM supposing the existence in nature of fermionic (bosonic) supersymmetric partners for the bosons (fermions) predicted in the SM, whose spin differs by 1/2 unit from their SM partners. SUSY provides an elegant solution to the hierarchy problem through loop cancellations. In SUSY models that conserve R-parity, SUSY particles (sparticles) must be produced in pairs and the lightest supersymmetric particle (LSP) in the SUSY decay chains is stable and weakly interacting, thus potentially providing a viable candidate for dark matter. Finally, this theory would allow the unification of the strong, electromagnetic and weak interactions.
Sparticle production cross-sections at LHC are highly dependent on the sparticle masses, as well as on the production mechanisms. The coloured sparticles (squarks and gluinos) are strongly produced and have significantly larger production cross-sections than non-coloured sparticles of equal masses, such as the sleptons (superpartners of the SM leptons) and the electroweakinos (superpartners of the SM Higgs and the electroweak gauge bosons). If gluinos and squarks were much heavier than low-mass electroweakinos, then SUSY production at the LHC would be dominated by direct electroweak production. Since the latest ATLAS and CMS limits on squark and gluino production extend well beyond the TeV scale, this allows for electroweak production of sparticles to be a promising and important probe in searches for SUSY at the LHC.

This PhD thesis describes my contribution to the search of electroweak production of charginos $\tilde{\chi}_1^{\pm}$ (the lightest combination of the charged superpartners of the SM Higgs and electroweak bosons) and sleptons decaying into final states with two charged leptons (electrons and/or muons) using proton-proton collision data recorded by the ATLAS detector during the entire LHC Run II (from 2015 to 2018), resulting in a total integrated and validated luminosity of 139 fb^{-1} . The analysis is optimized to target the direct production of $\tilde{\chi}_1^{+}\tilde{\chi}_1^{-}$, where each chargino decays into the lightest neutralino $\tilde{\chi}_1^{0}$ (LSP, the lightest combination of the neutral superpartners of the SM

Higgs and electroweak bosons) and an on-shell W boson. Due to the similarity of SM diboson processes and decays (particularly WW), this signature is very challenging to be studied and discriminated.
The same analysis strategy is also applied to two other searches. The former is the search for the direct production of $\tilde{\chi}_1^+\tilde{\chi}_1^-$, where each chargino decays into a slepton (charged slepton $\tilde{\ell}$ or sneutrino $\tilde{\nu}$) via the emission of a lepton (neutrino ν or charged lepton ℓ) and the slepton itself decays into a lepton and the LSP. The latter is the search for direct pair production of sleptons, where each slepton decays into a lepton and the LSP. All of these three scenarios are based on simplified models, i.e. assuming a branching ratio of 100% for the considered decay.
Chapter 1 is dedicated to review the Standard Model briefly and to introduce the Minimal Supersymmetric Standard Model (MSSM). Chapter 2 provides a description of the LHC and the ATLAS experiment, alongside a presentation of the new MicroMegas detectors which will be installed in ATLAS during the LHC Long Shutdown II, in whose validation with cosmic rays I have been involved in. Chapter 3 presents the physics objects used in the analysis with their features, as reconstructed by the ATLAS experiment. Chapter 4 reports the full analysis strategy, results and interpretations. Finally, Chapter 5 describes future perspectives of this analysis, now targeting the compressed phase space still not excluded: for this purpose a new signal grid has been requested and a MultiVariate approach is being considered. The work described in this Thesis has been submitted by the ATLAS Collaboration and published on European Physics Journal C on February 2020 with the following title: *Search for electroweak production of charginos and sleptons decaying into final states with two leptons and missing transverse momentum in* $\sqrt{s} = 13$ TeV *pp collisions using the ATLAS detector* [1].

Chapter 1

The Standard Model of fundamental interactions and Supersymmetry

Our current knowledge of particle physics is enclosed in the Standard Model (SM) theory [2–7]. Starting from the second half of XX century, when it reached its complete definition and structure, many experiments were put in place in order to confirm the predictions coming from this theory.
Although several experimental results have shown an impressing agreement with the theory, there are still some open questions: the most notable ones are the so-called *hierarchy problem* [8] and the nature of *dark matter* [9]. In order to provide answers to them, it is necessary to extend the Standard Model with other theories, known as *Beyond Standard Model* (BSM) theories. *Supersymmetry* [10–15] is one of the most promising BSM theories, since a solution to the hierarchy problem is found in it, because of the natural cancellation of loop diagrams and a natural dark matter candidate is provided by it, thanks to the LSP particle within the model.
This chapter is dedicated to a brief introduction to the Standard Model and its supersymmetric extension, i.e. *Minimal Supersymmetric Standard Model* (MSSM) [16], in order to provide a general overview of the two theories, as well as of the process on which the analysis described in this thesis is focused on.

1.1 The Standard Model of particle physics

In the Standard Model leptons (e, μ, τ and their neutrinos $\nu_{\ell=e,\mu,\tau}$) and quarks (u, d, c, s, t, b) are the basic components of the matter: they are spin 1/2 fermions and they are arranged in three different families, or generations, characterized by spin s, weak-isospin T, weak-hypercharge Y and electric charge Q[1]. Moreover, according to the properties of $SU(2)$ group of weak-isospin, a further organization into singlets or

[1] The electric charge is expressed in terms of the third component of the weak isospin T_3 and the weak-hypercharge Y through the relation $Q = T_3 + Y/2$.

doublets can be achieved:

$$\begin{array}{llll} \text{First Generation} \longrightarrow & \begin{pmatrix} \nu_e \\ e \end{pmatrix}_{\mathrm{L}} e_{\mathrm{R}} & \begin{pmatrix} u \\ d' \end{pmatrix}_{\mathrm{L}} u_{\mathrm{R}} & d'_{\mathrm{R}} \\ \text{Second Generation} \longrightarrow & \begin{pmatrix} \nu_\mu \\ \mu \end{pmatrix}_{\mathrm{L}} \mu_{\mathrm{R}} & \begin{pmatrix} c \\ s' \end{pmatrix}_{\mathrm{L}} c_{\mathrm{R}} & s'_{\mathrm{R}} \\ \text{Third Generation} \longrightarrow & \begin{pmatrix} \nu_\tau \\ \tau \end{pmatrix}_{\mathrm{L}} \tau_{\mathrm{R}} & \begin{pmatrix} t \\ b' \end{pmatrix}_{\mathrm{L}} t_{\mathrm{R}} & b'_{\mathrm{R}} \end{array}$$

where d', s' and b' are the weak eigenstates obtained through linear combinations of the mass eigenstates d, s and b by applying the Cabibbo-Kobayashi-Maskawa (CKM) matrix [17, 18]. The L and R pedices stand for *left*/*right*-handed spinors, eigenstates of γ^5 matrix obtained by applying the following projection operators to a generic spinor

$$P_{\mathrm{R}} = \frac{1}{2}(1+\gamma^5) \qquad P_{\mathrm{L}} = \frac{1}{2}(1-\gamma^5).$$

In the SM neutrinos are assumed to be purely left-handed and massless[2].
For each fermion in the model there is an associate particle, called *antiparticle*, resulting from the application of the charge conjugation operator which inverts all internal quantum numbers (charge, baryon and lepton numbers, strangeness).
Opposed to fermions, gauge bosons are integer-spin particles and they are responsible of the interactions among fermions, acting as force carriers. The electromagnetic interaction, experienced by fermions with electric charge, is mediated by the *photon* γ; the strong interaction, experienced by fermions with color charge, is carried by the *gluon* g; the weak interaction, experienced by fermions with weak charge, is mediated by the $W^\pm$ and Z^0 heavy bosons; the gravitational interaction is not considered in the model, since the relative intensity, if compared to the strong one, is smaller by several orders of magnitude. Table 1.1 summarizes the properties of the Standard Model particles[3].
From a theoretical point of view, the Standard Model is a non-abelian gauge theory invariant under the symmetry group

$$SU(3)_C \otimes SU(2)_L \otimes U(1)_Y,$$

where $SU(3)_C$ is related to the strong interactions, with C being the color charge, and $SU(2)_L \otimes U(1)_Y$ is the symmetry group of the electroweak interactions. While the 8 massless gluons can be identified as the gauge bosons of $SU(3)_C$, for the electroweak sector a spontaneous symmetry breaking introduces the three massive $W^\pm$ and Z^0 bosons; this process lies within the Glashow-Weinberg-Salam model [20] and it is known as *Higgs Mechanism* [21, 22].

1.1.1 Spontaneous symmetry breaking: the Higgs mechanism

In the '60s Glashow postulated a model for the weak and electromagnetic interactions based on the $SU(2) \otimes U(1)$ gauge invariance. However, he did not get the mass for the $W^\pm$ and Z^0 bosons directly from the model, introducing them "by hand"; the

[2] Due to the absence of direct mass measurements, the quantity measured is the mass splitting, with the mass eigenstates $\nu_{i=1,2,3}$ being related to weak eigenstates $\nu_{\ell=e,\mu,\tau}$ via the neutrino mixing matrix, $|\nu_\ell\rangle = \sum_i U_{\ell i} |\nu_i\rangle$.

[3] The Natural Units system is adopted to express kinematical quantities, implying $\hbar = c = 1$.

	Generation	Particle	Q	s	B	L	Mass [GeV]
Leptons	I	e	-1	$1/2$	0	1	$\sim 511 \times 10^{-6}$
		ν_e	0	$1/2$	0	1	~ 0
	II	μ	-1	$1/2$	0	1	$\sim 106 \times 10^{-3}$
		ν_μ	0	$1/2$	0	1	~ 0
	III	τ	-1	$1/2$	0	1	1776.86 ± 0.12
		ν_τ	0	$1/2$	0	1	~ 0
Quarks	I	u	$2/3$	$1/2$	$1/3$	0	$2.16^{+0.49}_{-0.26} \times 10^{-3}$
		d	$-1/3$	$1/2$	$1/3$	0	$4.67^{+0.48}_{-0.17}$
	II	c	$2/3$	$1/2$	$1/3$	0	1.27 ± 0.02
		s	$-1/3$	$1/2$	$1/3$	0	$93^{+11}_{-5} \times 10^{-3}$
	III	t	$2/3$	$1/2$	$1/3$	0	172.9 ± 0.4
		b	$-1/3$	$1/2$	$1/3$	0	$4.18^{+0.03}_{-0.02}$
Bosons		γ	0	1	0	0	$< 1 \times 10^{-27}$
		$W^\pm$	± 1	1	0	0	80.379 ± 0.012
		Z^0	0	1	0	0	91.1876 ± 0.0021
		$g_{i=1,\ldots,8}$	0	1	0	0	0

Table 1.1: Summary of the properties of the SM particles; the electric charge Q, expressed in units of the electron charge, the spin s, the baryon B and lepton L quantum numbers are reported [19].

result was a non-renormalizable[4] model. Some years later, Weinberg and Salam succeeded in overcoming this issue by introducing a potential that causes the spontaneous breaking of the symmetry, i.e. a theory in which the Lagrangian describing the physical system exhibit a symmetry, while the lowest-energy state of the system does not exhibit the same symmetry. The general idea is that weak interaction is mediated by gauge bosons, massless at the beginning; the lagrangian also contains terms for massless leptons and it is invariant under an internal gauge symmetry; a scalar field (the Higgs field) is then introduced with a non-vanishing expectation vacuum expectation value and the resulting interaction produces a spontaneous symmetry breaking which gives mass to fermions and gauge vector bosons.
Focusing on the description of the leptonic part of the model, the corresponding La-

[4]Quantum field theories can be classified as *super-renormalizable*, in case of a finite numbers of divergent Feynman diagrams, *renormalizable*, if they have a finite number of divergent amplitudes, whose divergencies occur at all orders of perturbation theory, *non-renormalizable*, for theory with divergent amplitudes at a sufficiently high order in the perturbation theory. The advantage of renormalizable theories is the presence of dimensionless coupling costants, while for the other two categories such constants have positive or negative mass dimensions.

grangian can be expressed as follows:

$$\begin{aligned}\mathcal{L}_{SU(2)\otimes U(1)} &= \mathcal{L}_{fermions} + \mathcal{L}_{gauge} = \\ &+ i\left(\bar{\nu}_f \quad \bar{f}\right)_{\mathrm{L}} \gamma^\mu \left[\partial_\mu + ig\frac{\tau_i}{2}\cdot W^i_\mu + ig'\frac{Y}{2}B_\mu\right]\begin{pmatrix}\nu_f \\ f\end{pmatrix}_{\mathrm{L}} \\ &+ i\bar{f}_{\mathrm{R}}\gamma^\mu\left(\partial_\mu + ig'\frac{Y}{2}B_\mu\right)f_{\mathrm{R}} - \frac{1}{4}B_{\mu\nu}B^{\mu\nu} - \frac{1}{4}W^i_{\mu\nu}W^{i\mu\nu},\end{aligned} \tag{1.1}$$

where f is a generic lepton, g and g' are the coupling costants, respectively, of weak isospin and hypercharge group, τ_i are the Pauli's matrices and, finally, $W_\mu^{i=1,2,3}$ and B_μ are the gauge fields of $SU(2)$ and $U(1)$, such as

$$B_{\mu\nu} = \partial_\mu B_\nu - \partial_\nu B_\mu \tag{1.2}$$

$$W^i_{\mu\nu} = \partial_\mu W^i_\nu - \partial_\nu W^i_\mu - g\epsilon_{ijk}W^j_\mu W^k_\mu. \tag{1.3}$$

Since there are four vector gauge bosons, $W^\pm$, Z^0 and γ, three of them being massive and the last one massless, the same number of real scalar fields ϕ_i are introduced; the resulted Lagrangian contains an extra term, $\mathcal{L}_{Higgs}$, which must always ensure the total Lagrangian being $SU(2)_L \otimes U(1)_Y$ gauge invariant, therefore this new four scalar fields are arranged in a weak isospin doublet of complex scalar fields with hypercharge $Y = 1$:

$$\Phi = \begin{pmatrix}\phi^+ \\ \phi^0\end{pmatrix} \quad \text{where} \quad \begin{aligned}\phi^+ &\equiv (\phi_1 + i\phi_2)/\sqrt{2} \\ \phi^0 &\equiv (\phi_3 + i\phi_4)/\sqrt{2}\end{aligned} \tag{1.4}$$

$$\begin{aligned}\mathcal{L}_{Higgs} &= \left|\left(\partial_\mu + ig\frac{\tau_i}{2}\cdot W^i_\mu + ig'\frac{Y}{2}B_\mu\right)\Phi\right|^2 - V(\Phi) \\ &= \left|\left(\partial_\mu + ig\frac{\tau_i}{2}\cdot W^i_\mu + ig'\frac{Y}{2}B_\mu\right)\Phi\right|^2 - \mu^2\Phi^\dagger\Phi - \lambda(\Phi^\dagger\Phi)^2.\end{aligned} \tag{1.5}$$

Assuming $\mu^2 < 0$ and $\lambda > 0$, the minimum of the potential $V(\Phi)$ occurs when

$$\Phi^\dagger\Phi = \frac{1}{2}\left(\phi_1^2 + \phi_2^2 + \phi_3^2 + \phi_4^2\right) = -\frac{\mu^2}{2\lambda}; \tag{1.6}$$

this minimum identifies a set of degenerate points invariant under $SU(2)$ transformations; by making a specific choice, the symmetry $SU(2) \otimes U(1)$ is spontaneously broken. A convenient choice of the vacuum expectation value is

$$\phi_1 = \phi_2 = \phi_4 = 0, \quad \phi_3^2 = -\frac{\mu^2}{\lambda} \equiv v^2 \quad \Longrightarrow \quad \Phi_0 = \frac{1}{\sqrt{2}}\begin{pmatrix}0 \\ v\end{pmatrix} \tag{1.7}$$

with quantum numbers $T = 1/2$, $T_3 = -1/2$ and $Y = 1$. Although this procedure allows to break $SU(2)_L$ and $U(1)_Y$ symmetries simultaneously, the charge group $U(1)_Q$ symmetry is unaffected, therefore the corresponding gauge boson (photon) is left massless.

Introducing the fields θ_i, i.e. the *Goldstone bosons* [23], it is possible to expand the Φ field around this chosen minimun in terms of these new quantities, obtaining

$$\Phi(x) = \frac{1}{\sqrt{2}}\begin{pmatrix}\theta_1(x) + i\theta_2(x) \\ v + h(x) + i\theta_3(x)\end{pmatrix} \rightarrow \cdots \rightarrow \frac{1}{\sqrt{2}}\begin{pmatrix}0 \\ v + h(x)\end{pmatrix}. \tag{1.8}$$

Once a suitable gauge transformation is performed, θ_i fields vanish and the Higgs doublet can be reduced to the only real field $h(x)$, better known as the *Higgs field*, with mass of

$$m_h = \sqrt{-2\mu^2} = \sqrt{2\lambda v^2}. \tag{1.9}$$

In addition to the Higgs boson mass, the insertion of the expansion 1.8 in the Lagrangian 1.5 produces the eletroweak gauge boson mass terms to appear, thus enabling the possibility to define the corresponding mass eigenstates $W^\pm$, Z^0 and γ as:

$$W^\pm = \frac{1}{2}\left(W^1 \mp W^2\right) \qquad \begin{pmatrix} Z^0 \\ \gamma \end{pmatrix} = \begin{pmatrix} \cos\theta_W & -\sin\theta_W \\ \sin\theta_W & \cos\theta_W \end{pmatrix} \begin{pmatrix} W^3 \\ B \end{pmatrix}, \tag{1.10}$$

with θ_W being the *Weinberg angle*, defined by the relation

$$\tan\theta_W = \frac{g'}{g}. \tag{1.11}$$

Starting from relations 1.10, it is possible to derive the vector gauge boson masses[5]:

$$m_{W^\pm} = \frac{1}{2}vg \qquad m_Z = \frac{1}{2}v\sqrt{g^2 + g'^2} \qquad m_\gamma = 0 \tag{1.12}$$

Figures 1.1 and 1.2 show present experimental results of the gauge boson $W^\pm$ and Z masses, respectively.

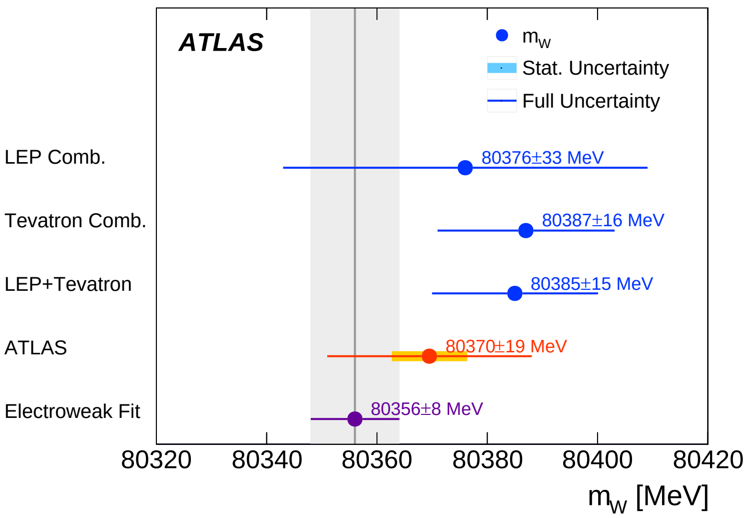

Figure 1.1: Most recent measurements [24] of the W mass, m_W, performed by the ATLAS experiment [25] and compared to the Standard Model model predictions from the global electroweak fit [26], updated using recent measurements of the top-quark mass [27], $m_t = (172.84 \pm 0.70)$ GeV, and Higgs boson mass [28], $m_H = (125.09 \pm 0.24)$ GeV. The result is compared to the combined values of m_W measured at *LEP* [29, 30] and at *Tevatron* [31] colliders.

Using the same mechanism, it is possible to generate the fermion masses introducing a *Yukawa* interaction between the fermionic fields (only the $T_3 = -1/2$ member of the

[5]For the sake of simplicity, from now on the superscript 0-index of the Z^0 boson will be dropped, i.e. $Z^0 \equiv Z$.

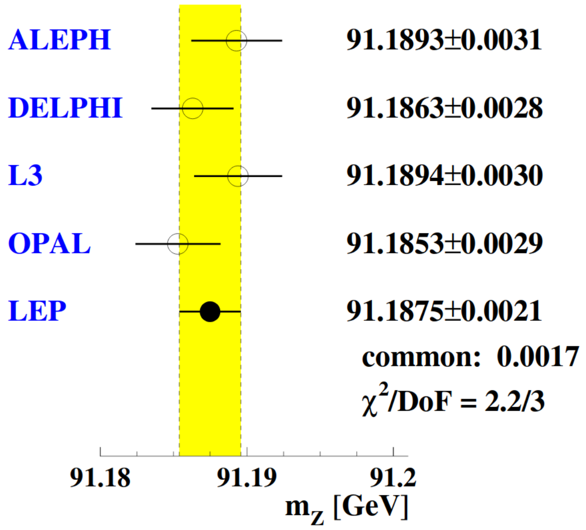

Figure 1.2: Average of the Z mass measurements [32] performed at *LEP* by the *ALEPH* [33, 34], *DELPHI* [35, 36], *L3* [37–40] and *OPAL* [41–44] experiments.

weak isospin doublet is coupled) and the previously defined Higgs doublet.
In case of leptons, this additional term becomes

$$\mathcal{L}_{Yukawa} = -G_f \left[\begin{pmatrix} \bar{\nu}_f & \bar{f} \end{pmatrix}_{\rm L} \begin{pmatrix} \phi^+ \\ \phi^0 \end{pmatrix} f_{\rm R} + h.c. \right], \tag{1.13}$$

with G_f coupling costant. The fermion mass is determined by the relation

$$m_f = \frac{G_f}{\sqrt{2}} v. \tag{1.14}$$

In case of quarks, a more complex Yukawa term is needed: it has to satisfy the additional coupling with the $T_3 = 1/2$ member of the weak isospin doublet and to take into account the CKM matrix in order to rotate flavor eigenstates into mass eigenstates. Such a term can be expressed as

$$\mathcal{L}_{Yukawa} = -G_d^{ij} \begin{pmatrix} \bar{u}_i & \bar{d'}_i \end{pmatrix}_{\rm L} \Phi d_{j\rm R} - G_u^{ij} \begin{pmatrix} \bar{u}_i & \bar{d'}_i \end{pmatrix}_{\rm L} (-i\tau_2) \Phi^* u_{j\rm R} + h.c., \tag{1.15}$$

where u_i is a generic $T_3 = 1/2$ quark (u, c, t), d' a generic $T_3 = -1/2$ quark (d', s', b') and $G_{u,d}^{ij}$ are the coupling costants between the Higgs field and the quarks. Figure 1.3 reports the agreement between the measured masses of the top-quark and W boson with the values provided by the electroweak global fit of the Standard Model.

1.1.2 Quantum ChromoDynamics

The quark model, originally developed by Gell-Mann [45] and Zweig [46], evolved over the years into a renormalizable quantum field theory, based on $SU(3)$ symmetry, known as *Quantum ChromoDynamics* (QCD) [6, 7]. This theory is dedicated to the description of the interactions of quarks and gluons.
An additional quantum number, called *color*, is assigned to each quark and, conventionally, there are *Red* (R), *Glue* (B) or *Green* (G) quarks. Gluons, mediators of the

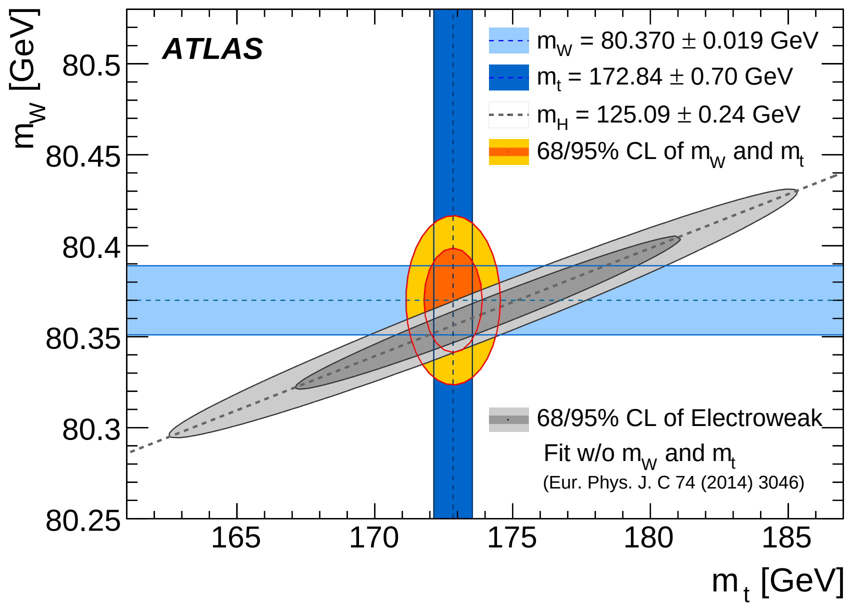

Figure 1.3: The 68% and 95% Confidence Level contours of the m_W and m_t indirect determination from the global electroweak fit [26], compared to the analogous Confidence Level contours of the ATLAS measurements of the top-quark and W boson masses. The Higgs boson mass measured at the Large Hadron Collider [28], $m_H = (125.09 \pm 0.24)$ GeV, is used as input for the determination of the global electroweak fit.

strong interactions, come in eight different color-anticolor combinations:

$$R\bar{G}, \quad R\bar{B}, \quad G\bar{R}, \quad G\bar{B}, \quad B\bar{R}, \quad B\bar{G}, \quad \frac{1}{\sqrt{2}}(R\bar{R} - G\bar{G}), \quad \frac{1}{\sqrt{6}}(R\bar{R} + G\bar{G} - 2B\bar{B}).$$

All observable particles must be in a neutral colorless state (*white*). The strong interaction can be thought as an exchange of colors through colored mediators, the gluons, which can interact each others and with quarks.
The coupling costant of the strong interaction α_s is a free parameter in QCD and it is inversely proportional to the momentum exchanged in the interaction. Strictly related to this feature, one particular property is predicted in this theory, the so-called *asymptotic freedom*: at high momentum, colored particles (or *partons*) almost behave as free independent particles, because of the small magnitude of the coupling constant; on the other hand, at low momentum or, equivalently, at large distances, the interaction is strong and it bounds partons in non-colored states known as “hadrons”.
As a consequence, there is no possibility to observe colored particles in nature, as (anti-)quarks are confined in the hadrons: *baryons* (combinations of three quarks) or *mesons* (combination of quark/anti-quark). In particle physics experiments where collisions can occur at parton level, the produced quarks and gluons “hadronize”, i.e. colored particles emerges from the vacuum in proximity of them and produce final coloreless states. The result of this process, called *hadronization* is a “jet” of particles moving in the initial direction of the produced parton.

1.1.3 Limits of the theory

The Standard Model is considered an extremely successful theory since its predictions agreed with the experimental results in several experiments. Nevertheless, some questions are still unanswered in its framework, e.g. the nature of the dark matter, the matter-antimatter asymmetry observed in the universe and the neutrino oscillations, a phenomenon not predicted by the Standard Model. All of these aspects, just to cite a few, do not make it a complete physics theory [47, 48].
However, the unification of the electromagnetic and weak interactions in the $SU(2)_L \otimes U(1)_Y$ group was a major outcome for the Standard Model, providing a desiderable feature in unifying two apparently different forces in one interaction; the Standard Model can be considered an *effective field theory* (EFT), i.e. a low energy approximation of a more fundamental and general theory also including, for instance, the strong interaction.
Theories of unified gauge groups are called *Grand Unified Theory* (GUT); they are based on the idea that all known interactions are low-energy approximation of a unique theory associated with a more general gauge group. The Standard Model makes very precise prediction concerning the running of the different coupling strengths, and their values do not coincide, even at very high energies. Therefore it becomes necessary a determination of the energy scale Λ, beyond which evidences of new physics could appear. A possible option could be to assume Λ at the Planck scale (2.4×10^{18} GeV), the fundamental mass scale where gravity is expected to become as strong as other interactions, or at the GUT scale ($\sim 10^{16}$ GeV); comparing both to the electroweak scale (~ 100 GeV), there is a difference of several orders of magnitude, issue better known as *hierarchy problem*.
Such a discrepancy is not a real issue within the Standard Model itself [8], but, as a consequence of it, the value of the Higgs mass, m_h^2, receives large quantum corrections from the loop diagrams of each particle coupling, directly or indirectly, to the Higgs field.

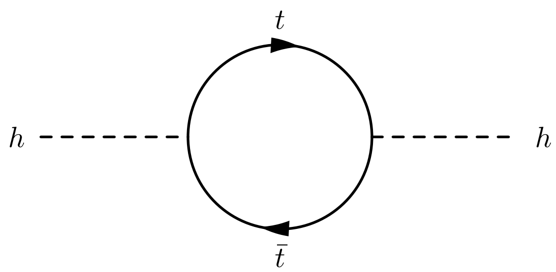

Figure 1.4: One-loop diagram coupling the top-quark to the Higgs particle. Being the Standard Model particle with higher mass, the top-quark provides a dominant contribution to the radiative corrections to the Higgs mass.

Each of the one-loop diagram, as the one reported in Figure 1.4, is quadratically divergent, hence the contribution to the mass of the Higgs particle is

$$\delta m_h^2 = \mathcal{O}\left(\frac{g^2}{16\pi^2}\right) \int^{\Lambda} d^4k \frac{1}{k^2} = \mathcal{O}\left(\frac{\alpha}{\pi}\right) \Lambda^2. \tag{1.16}$$

Assuming Λ to be the Planck or GUT scale, this quantum correction is much larger than the physical value of the Higgs mass, $m_h \sim 125$ GeV. Since the theory is renormalizable, there could be an opposite-sign large contribution to cancel it out, but this would require to adjust each correction in order to be consistent with the physical

mass value of the Higgs boson. This procedure seems to be very unnatural, therefore this issue is known as *naturalness* (or *fine-tuning*) problem.
Another phenomenon whose explanation cannot be found within the Standard Model framework is the evidence for the existence of *dark matter* [9]: many independent observations in large astrophysical systems, with sizes ranging from galactic to cosmological scales, provided evidences of "anomalies" which can only be explained either by assuming the existence of a large amount of unseen, *dark*, matter or by assuming a deviation from the known laws of gravitation and the theory of general relativity.
All previous problems can be addressed in an elegant and natural way by extending the Standard Model with the *Supersymmetry* theory. In the simplest formulation of this extension, called *Minimal Supersymmetric Standard Model* (MSSM), the running of the gauge couplings, whose calculation is done in the model in a similar way as in the Standard Model, converges to a specific value corresponding to an energy scale where couplings are unified, as shown in Figure 1.5 [49].

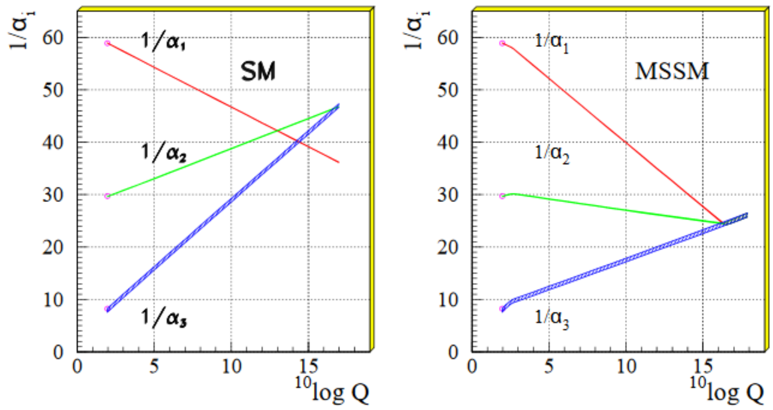

Figure 1.5: Evolution of the inverse of the three coupling constants in the SM (left) and in the MSSM (right). Only in the latter case unification is obtained [49].

Then, the one-loop corrections to a generic, fundamental fermion mass m_f are proportional to the mass itself, becoming only logarithmically divergent:

$$\delta m_f = \mathcal{O}\left(\frac{g^2}{16\pi^2}\right) m_f \int^{\Lambda} d^4k \frac{1}{k^4} = \mathcal{O}\left(\frac{\alpha}{\pi}\right) m_f \ln \frac{\Lambda}{m_f}. \tag{1.17}$$

The magnitude of this correction is no more larger than the physical value, for any $\Lambda < \Lambda_{\mathrm{GUT}}$. This holds also for the divergent term 1.16, exploiting the fact that boson and fermion loop diagrams have opposite signs. Assuming an equal number of fermions and bosons and equal couplings withing the supersymmetric theory, the quadratic divergence cancels out

$$\delta m_h^2 = -\left(\frac{g_F^2}{16\pi^2}\right)(\Lambda^2 + M_F^2) + \left(\frac{g_B^2}{16\pi^2}\right)(\Lambda^2 + M_B^2) = \mathcal{O}\left(\frac{\alpha}{4\pi}\right)|M_B^2 - M_F^2|, \tag{1.18}$$

which is a small contibution if

$$|M_B^2 - M_F^2| \lesssim \text{ TeV}. \tag{1.19}$$

This naturalness argument is one of the theoretical motivation behind the assumption that evidences of Supersymmetry may manifest at an accessible energy scale.

Finally, the *R-parity*-conserving Supersymmetry, discussed in Section 1.2, could provide naturally a good dark matter candidate through the *Lightest Supersymmetric Particle* (LSP), a stable particle predicted by this theory.

1.2 SUperSYmmetry

As already mentioned, Supersymmetry is one of the most promising among the so-called *Beyond the Standard Model* theories, which postulates the existence of a fundamental symmetry between bosons and fermions. In the MSSM, the particles are called *superpartners* (or *superparticles* o *sparticles*), with spin differing by 1/2 unit with respect to the Standard Model counterparts. Apart from the spin, masses and all other quantum numbers are the same.
Concerning the nomenclature, the name of these superpartners are derived from the names of their Standard Model counterparts. The bosonic partners of the fermions have the prefix "s" to their names, leading to names such as *squarks* and *sleptons* (standing for "scalar quark" and "scalar lepton", respectively); the symbols for squarks and sleptons are the same as for the corresponding fermion, but with a tilde on them, generically $\tilde{q}$ or $\tilde{\ell}$. On the other hand, the names of fermionic partners of bosons have the suffix "ino" to their names, such as *gluinos* for gluons, *winos* for $SU(2)_L$ gauge bosons and *bino* for $U(1)_Y$ gauge boson. Moreover, in the MSSM two chiral supermultiplets as Higgs fields are introduced, instead of the single one present in the Standard Model; their corresponding sparticles are called *higgsinos*. Tables 1.2 and 1.3 summarize the supermultiplet structures within the MSSM.

Names		spin-0	spin-1/2	$(SU(3)_C,\, SU(2)_L,\, U(1)_Y)$
squarks, quarks	Q	$(\tilde{u}_\mathrm{L} \quad \tilde{d}_\mathrm{L})$	$(u_\mathrm{L} \quad d_\mathrm{L})$	$(\mathbf{3},\, \mathbf{2},\, 1/6)$
3 families	$\bar{u}$	$\tilde{u}^*_\mathrm{R}$	$\tilde{u}^\dagger_\mathrm{R}$	$(\bar{\mathbf{3}},\, \mathbf{1},\, -2/3)$
	$\bar{d}$	$\tilde{d}^*_\mathrm{R}$	$\tilde{d}^\dagger_\mathrm{R}$	$(\bar{\mathbf{3}},\, \mathbf{1},\, 1/3)$
sleptons, leptons	L	$(\tilde{\nu} \quad \tilde{e}_\mathrm{L})$	$(\nu \quad e_\mathrm{L})$	$(\mathbf{1},\, \mathbf{2},\, -1/2)$
3 families	$\bar{e}$	$\tilde{e}^*_\mathrm{R}$	$\tilde{e}^\dagger_\mathrm{R}$	$(\mathbf{1},\, \mathbf{1},\, 1)$
Higgs, higgsinos	H_u	$(H_u^+ \quad H_u^0)$	$(\tilde{H}_u^+ \quad \tilde{H}_u^0)$	$(\mathbf{1},\, \mathbf{2},\, 1/2)$
	H_d	$(H_d^0 \quad H_d^-)$	$(\tilde{H}_d^0 \quad \tilde{H}_d^-)$	$(\mathbf{1},\, \mathbf{2},\, -1/2)$

Table 1.2: Chiral supermultiplets in the MSSM: the spin-0 fields are complex scalars, while the spin-1/2 are left-handed two-component Weyl fermions. Only the first family is reported as example [16].

Names	spin-1/2	spin-1	$(SU(3)_C,\, SU(2)_L,\, U(1)_Y)$
gluino, gluon	$\tilde{g}$	g	$(\mathbf{8},\, \mathbf{1},\, 0)$
winos, W bosons	$\tilde{W}^\pm \quad \tilde{W}^0$	$W^\pm \quad W^0$	$(\mathbf{1},\, \mathbf{3},\, 0)$
binos, B bosons	$\tilde{B}^0$	B^0	$(\mathbf{1},\, \mathbf{1},\, 0)$

Table 1.3: Gauge supermultiplets in the MSSM [16].

1.2.1 R-parity

Due to the renormalizability and gauge invariance, the Lagrangian of the Standard Model conserves the barion B and lepton L quantum numbers, without assuming it explicitly. However, when including the most general gauge-invariant and renormalizable superpotential, some terms may violate barion and/or lepton number conservation and, as a consequence, new decay channels never observed before are allowed. Proton decay $p \to e^+\pi^0$ can be considered an example.
In order to avoid the presence of such violating terms, a new symmetry needs to be added; it is called *R-parity* and the associate quantum number is defined as follows:

$$P_R = (-1)^{3(B-L)+2s} = \begin{cases} +1 & \text{for SM particles} \\ -1 & \text{for MSSM sparticles} \end{cases}, \tag{1.20}$$

with s being the spin of the particle. If R-parity is exactly conserved, no kind of mixing is allowed between particles of the Standard Model and their supersymmetric counterparts. Moreover, every interaction vertex in the theory contains an even number of sparticles having $P_R = -1$ and three main consequences are derived from this statement:

1. The lightest particle with odd R-parity, the so-called *lightest supersymmetric particle*, must be stable. If the LSP has no electric charge, then it interacts only weakly with ordinary matter, making it a potential candidate for the non-baryonic dark matter.

2. Each other supersymmetric particle different from the LSP must decay into a state containing an odd number of LSPs.

3. In collider experiments, sparticles are produced in even number, typically in pairs.

The MSSM is assumed to preserve R-parity but, apart from phenomenological reasons, there is no intrinsic motivation to support this assumption. There are other SUSY models not requiring R-parity conservation and the phenomenologically forbidden terms present in the lagrangian allow the violation of baryon or lepton quantum numbers, but not both of them [50].
Only R-parity-conserving scenarios will be considered in this thesis.

1.2.2 Soft SUSY breaking

The fundamental statement adduced when SUSY and MSSM have been introduced is that sparticles differ only by one-half spin unit from the corresponding Standard Model counterparts, then assuming particles and their superpartners to be mass degenerate. However, if Supersymmetry was an exact symmetry, sparticles would have already been observed; since this is not the case so far, *soft breaking* [8] additional terms need to be added in the MSSM Lagrangian, leading to Supersymmetry breaking but preserving, at the same time, the gauge invariance and the cancellation of the divergent terms in the radiative corrections. Only mass terms and coupling parameters with positive mass dimension can be included in the Lagrangian; applying it to the MSSM, such terms are:

- Mass terms for gluinos, winos and bino:

$$\mathcal{L}_{gaugino} = -\frac{1}{2}\left(M_1\tilde{B}\tilde{B} + M_2\sum_{i=1}^{3}\tilde{W}^i\tilde{W}_i + M_3\sum_{i=1}^{8}\tilde{G}^i\tilde{G}_i + h.c.\right) \tag{1.21}$$

- Mass terms for the scalar fermions:

$$\mathcal{L}_{s.f.} = -\sum_{i=1}^{3}\left(m^2_{\tilde{Q}_i}\tilde{Q}^\dagger_i\tilde{Q}_i + m^2_{\tilde{L}_i}\tilde{L}^\dagger_i\tilde{L}_i + m^2_{\tilde{u}_i}|\tilde{u}_{R_i}|^2 + m^2_{\tilde{d}_i}|\tilde{d}_{R_i}|^2 + m^2_{\tilde{l}_i}|\tilde{l}_{R_i}|^2\right) \tag{1.22}$$

- Mass and bilinear terms for the Higgs bosons:

$$\mathcal{L}_{Higgs} = -[m^2_{H_u}H^\dagger_uH_u + m^2_{H_d}H^\dagger_dH_d + B_\mu(H_u\cdot H_d + h.c.)] \tag{1.23}$$

- Trilinear coupling between sfermions and Higgs bosons:

$$\mathcal{L}_{tril.} = -\sum_{i,j=1}^{3}\left(A^u_{ij}Y^u_{ij}\tilde{u}^*_{R_i}H_u\cdot\tilde{Q}_j + A^d_{ij}Y^d_{ij}\tilde{d}^*_{R_i}H_d\cdot\tilde{Q}_j + A^l_{ij}Y^l_{ij}\tilde{l}^*_{R_i}H_d\cdot\tilde{L}_j + h.c.\right) \tag{1.24}$$

The MSSM just described is usually defined *uncostrained* MSSM, because of the absence of extra constraint applied to the Lagrangian. In the general case, where mixing among generations and complex phases are allowed, the soft SUSY breaking will introduce a huge number of unknown parameters, to be summed to the 19 currently in the Standard Model, reaching a total of 120 free parameters.

1.2.3 Constrained MSSM

The large number of free parameters in the unconstrained MSSM makes any analysis a hard task to be performed. A phenomenologically more viable MSSM can be built by making the following assumptions:

- all the soft SUSY-breaking parameters are real, thus no new source of CP-violation is introduced, in addition to the one coming from the CKM matrix;
- the matrices for sfermion masses and trilinear couplings are all diagonal, implying the absence of *Flavor Changing Neutral Currents* (FCNC) at tree-level;
- the soft SUSY-breaking masses and trilinear couplings of the first and second sfermion generations are the same at low energy.

As a consequence of these three assumptions, the 120 free parameters of the model are reduced to 22 parameters:

- $\tan\beta$, ratio of the vacuum expectation values of two Higgs doublet fields;
- $m^2_{H_u}$ and $m^2_{H_d}$: mass parameters for the two Higgs doublets;
- M_1, M_2, M_3: mass parameters for bino, wino and gluino;

- mass parameters for the first, second and third generation of sfermions;
- A_u, A_d, A_e: trilinear couplings of the first and second generation;
- A_t, A_b, A_τ: trilinear couplings of the first and second generation.

Having a moderate number of free parameter, this model is more predictive and suitable for any phenomenological investigation, if compared to the unconstrained MSSM; it is usually referred to as *phenomenological* MSSM or *pMSSM*. In this model the description of the electroweak symmetry breaking is tougher due to the two complex Higgs doublets being present. And, finally, the masses and the CKM mixing angles of quarks and leptons are also function of the $\tan\beta$ parameter, in addition to the Yukawa couplings of the superpotential.

1.2.4 The MSSM mass spectrum

The effects of the previously described electroweak symmetry breaking are the reason why higgsinos and electroweak gauginos do not match exactly their mass eigenstates, generating the following two mixing combinations:

- Charginos $\tilde{\chi}_i^{\pm}(i = 1, 2$ in order of increasing masses), two mass eigenstates from the mixing of the charged higgsinos ($\tilde{H}_u^+$ and $\tilde{H}_d^+$) and winos ($\tilde{W}^+$ and $\tilde{W}^-$).
- Neutralinos $\tilde{\chi}_j^0(j = 1, ..., 4$ in order of increasing masses), four mass eigenstates from the mixing of the neutral higgsinos ($\tilde{H}_u^0$ and $\tilde{H}_d^0$) and the neutral gauginos.

In the gauge-eigenstate basis $\psi^0 = (\tilde{B}, \tilde{W}^0, \tilde{H}_u^0, \tilde{H}_d^0)$ the neutralino mass term in the lagrangian is:

$$\mathcal{L}_{\tilde{\chi}^0} = -\frac{1}{2}(\psi^0)^T \mathbf{M}_{\tilde{\chi}^0}\psi^0 + h.c., \tag{1.25}$$

with

$$\mathbf{M}_{\tilde{\chi}^0} = \begin{pmatrix} M_1 & 0 & -\cos\beta\sin\theta_W m_Z & \sin\beta\sin\theta_W m_Z \\ 0 & M_2 & \cos\beta\cos\theta_W m_Z & -\sin\beta\cos\theta_W m_Z \\ -\cos\beta\sin\theta_W m_Z & \cos\beta\cos\theta_W m_Z & 0 & -\mu \\ \sin\beta\sin\theta_W m_Z & -\sin\beta\cos\theta_W m_Z & -\mu & 0 \end{pmatrix}.$$

This matrix can be diagonalized and the four mass eigenstates are labelled as $\tilde{\chi}_j^0$, $j = 1, ..., 4$.
Analogously, in the gauge-eigenstate basis $\psi^{\pm} = (\tilde{W}^+, \tilde{H}_u^+, \tilde{W}^-, \tilde{H}_d^-)$ the chargino mass term in the lagrangian is:

$$\mathcal{L}_{\tilde{\chi}^{\pm}} = -\frac{1}{2}(\psi^{\pm})^T \mathbf{M}_{\tilde{\chi}^{\pm}}\psi^{\pm} + h.c., \tag{1.26}$$

where the matrix is (in a 2×2 notation)

$$\mathbf{M}_{\tilde{\chi}^{\pm}} = \begin{pmatrix} 0 & \mathbf{X}^T \\ \mathbf{X} & 0 \end{pmatrix} \qquad \begin{pmatrix} M_2 & \sqrt{2}\sin\beta m_W \\ \sqrt{2}\cos\beta m_W & 0 \end{pmatrix}.$$

The resulting four mass eigenstates, two of them being degerate, are labelled as $\tilde{\chi}_i^{\pm}$, $i = 1, 2$.

It can be verified that there is a limit for which the electroweak symmetry breaking effects can be seen as a small perturbation on the neutralino mass matrix. In particular, the following two assumptions

$$m_Z \ll |\mu \pm M_1|, |\mu \pm M_2| \qquad \text{and} \qquad M_1 < M_2 \ll |\mu| \tag{1.27}$$

have an impact on chargino and neutralino eigenstates, becoming

- *bino-like* ($\tilde{\chi}_1^0 \simeq \tilde{B}$),
- *wino-like* ($\tilde{\chi}_2^0 \simeq \tilde{W}^0$ and $\tilde{\chi}_1^\pm \simeq \tilde{W}^\pm$),
- *higgsino-like* ($\tilde{\chi}_{3,4}^0 \simeq (\tilde{H}_u^0 \pm \tilde{H}_d^0)/\sqrt{2}$ and $\tilde{\chi}_2^\pm \simeq \tilde{H}_{u,d}^\pm$),

with, respectively, M_1, M_2 and μ as mass eigenvalues. In many SUSY models the lightest neutralino, $\tilde{\chi}_1^0$, is interpreted as the LSP.

The same mixing procedure should be also applied to scalars with same electric charge, R-parity and color quantum numbers: this implies that the MSSM mass eigenstates of the squarks and sleptons should be obtained by diagonalizing three 6×6 matrices for *up*-type quarks ($\tilde{u}_{\mathrm{L}}, \tilde{c}_{\mathrm{L}}, \tilde{t}_{\mathrm{L}}, \tilde{u}_{\mathrm{R}}, \tilde{c}_{\mathrm{R}}, \tilde{t}_{\mathrm{R}}$), *down*-type quarks ($\tilde{d}_{\mathrm{L}}, \tilde{s}_{\mathrm{L}}, \tilde{b}_{\mathrm{L}}, \tilde{d}_{\mathrm{R}}, \tilde{s}_{\mathrm{R}}, \tilde{b}_{\mathrm{R}}$) and charged sleptons ($\tilde{e}_{\mathrm{L}}, \tilde{\mu}_{\mathrm{L}}, \tilde{\tau}_{\mathrm{L}}, \tilde{e}_{\mathrm{R}}, \tilde{\mu}_{\mathrm{R}}, \tilde{\tau}_{\mathrm{R}}$), including one 3×3 matrix for sneutrinos ($\tilde{\nu}_{\mathrm{e}}$, $\tilde{\nu}_\mu$, $\tilde{\nu}_\tau$). However, it can be demonstrated that most of these mixing angles are very small and the relevant ones are in the third generation of squarks and charged sleptons. In particular, the mixing is very strong in the stop sector, generating a high mass splitting between the two mass eigenstates which makes the state $\tilde{t}_1$ much lighter than the other squarks.

1.3 SUSY searches at the LHC: Electroweak sector

A hadron collider, such as the *Large Hadron Collider* (LHC) [51], is one of the best places to look for Supersymmetry. If it exists, SUSY coloured (squarks and gluinos) particles are expected to be produced with a relatively high rate; they are strongly produced and have significantly larger cross-sections (Figure 1.6) with respect of non-coloured SUSY particles of equal masses, such as sleptons and electroweak gauginos.
If SUSY coloured particles were much heavier than the SUSY electroweak ones, then the sparticle pair production at the energies achievable by the LHC would be dominated by the electroweak sector. Recent results from ATLAS [25] and CMS [53] experiments extended exclusion limits on squark and gluino masses [54–70] well beyond the TeV scale, making the SUSY electroweak sector an important probe for future SUSY analyses at the LHC.
The search for the electroweak production of charginos and sleptons is the main subject of this thesis. At leading order, the Feynman diagrams relevant for these productions are reported in Figure 1.7, together with other diagrams entering in the electroweak production of charginos and sleptons at hadron colliders.
The results of SUSY searches at the LHC need to be presented and characterized in a precise way, considering the dimension of the parameter space probed. A small one can be efficiently and accurately studied, but the obtained results are less likely to be extrapolated on a larger parameter space, in order to derive more general considerations. However, the number of free parameters in the MSSM is so high that scanning

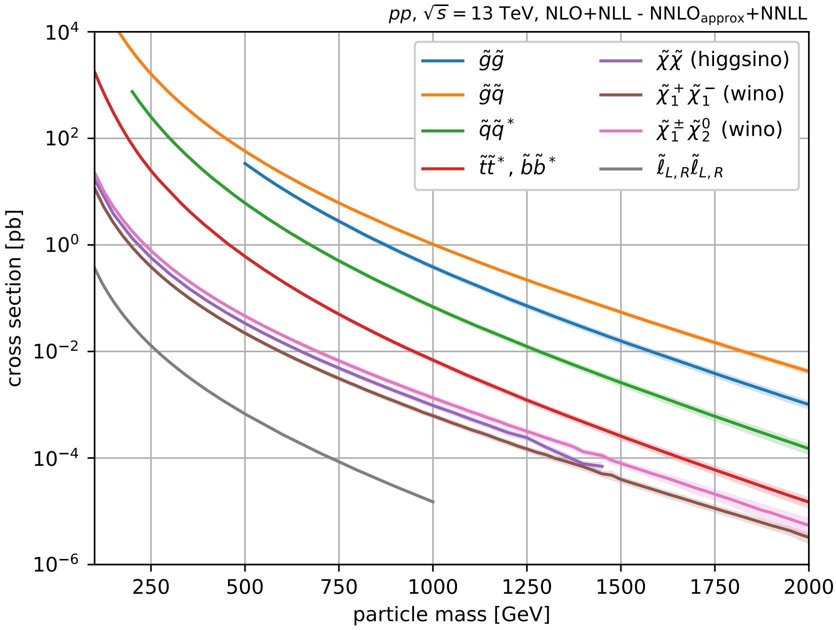

Figure 1.6: Production cross-section of several SUSY particles as a function of their mass in proton–proton collisions at a centre-of-mass energy of $\sqrt{s} = 13$ TeV [52].

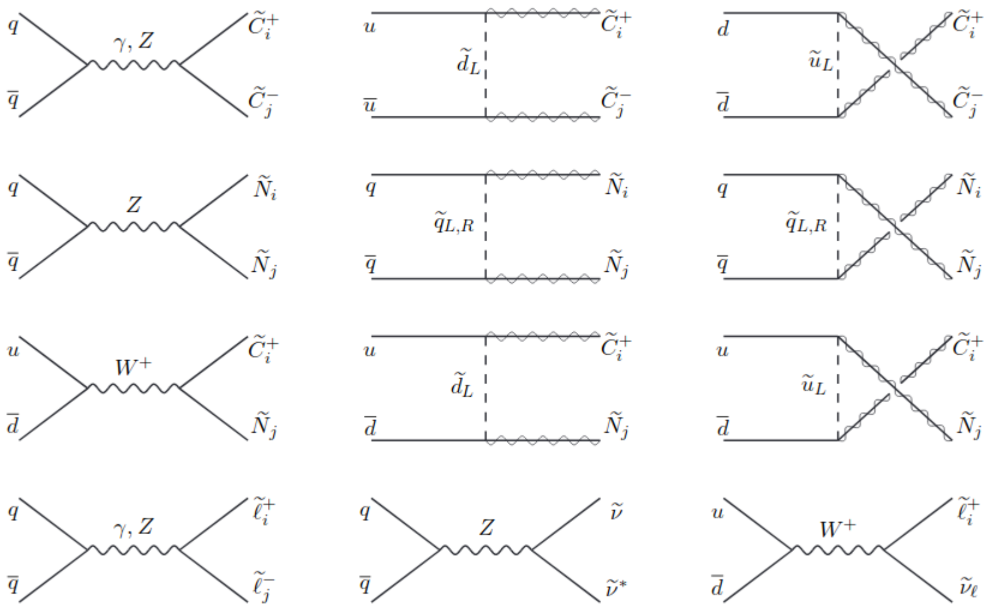

Figure 1.7: Feynman diagrams for electroweak production of sparticles from $q\bar{q}$ annihilation. Squark masses are supposed to be higher with respect to the chargino and neutralino ones, therefore the t-channel mediated production is assumed to be negligible, indeed dominated by the γ, Z and $W^{\pm}$ s-channels [16].

all of them could be an unrealistic undertaking.
The natural compromise between these two kinds of approaches is to start from a minimal subset of free parameters, corresponding to a specific parameter space, and

gradually to enlarge it until an interpretation of the collected data is found. A minimal model, having the simplest spectra compatible with SUSY-like signatures, is an ideal starting point. Such models are referred to as *simplified models* [71, 72] and the number of their free parameters is kept at a minimum by reducing the number of new particles being considered by the model itself; this will ensure that small variations to these parameters will produce large effects on the observables.
In a first characterization, these parameters are the most important ones to focus on in case of evidence for new physics. A simplified model allows to constrain several SUSY models alongside the one in which it has been formulated, since it relies on the phenomenology of SUSY particles, instead of a particular SUSY model, therefore being sensible to models with similar phenomenology[6].
A simplified model is obtained starting from a more general SUSY model and then proceeding to ignore the masses of particles[7] not of interest in the specific model considered, so they will not affect the physics involving the remaining SUSY particles in the model, whose masses are free parameters. This flexibility allows to focus a generic analysis on a specific model and then to reinterpret the obtained results in another model sharing a similar topology, resulting in a higher scanning efficiency of a selected mass plane.
The processes studied in this thesis are illustrated in Figure 1.8: the analysis is optimized to target the direct production of $\tilde{\chi}_1^{\pm}\tilde{\chi}_1^{\mp}$, where each chargino decays into an on-shell W boson and the LSP $\tilde{\chi}_1^0$ (Figure 1.8(a)) with a 100% branching ratio (BR). The chargino is assumed to be a pure wino state, while the $\tilde{\chi}_1^0$ pure bino. Finally, only the leptonic decay of the two Ws is considered, with a 10.7% BR factor for each leptonic flavor considered[8], generating a signature consisting of two opposite charged leptons and missing transverse energy.
The same analysis strategy is also applied to two other searches, all conserving lepton flavor:

- the direct production of $\tilde{\chi}_1^{\pm}\tilde{\chi}_1^{\mp}$, where each chargino decays into a slepton (charged slepton $\tilde{\ell}$ or sneutrino $\tilde{\nu}$) via the emission of a lepton (neutrino ν or charged lepton ℓ) and the slepton itself decays into a lepton and the LSP $\tilde{\chi}_1^0$ (Figure 1.8(b)). Here it is assumed that the scalar partners of the left-handed charged leptons and neutrinos are mass-degenerate and their masses are chosen to be midway between the mass of the chargino and that one of the $\tilde{\chi}_1^0$. Equal BR for the three slepton families are assumed and charginos decay into charged sleptons or sneutrinos with a BR of 50% to each;

- the direct pair production of sleptons, where each slepton decay into the corresponding lepton and the LSP $\tilde{\chi}_1^0$ (Figure 1.8(c)) with a 100% BR. Only $\tilde{e}$ and $\tilde{\mu}$ are considered in these models and and different assumptions about the masses of the superpartners of the left-handed and right-handed charged leptons, $\tilde{e}_{\mathrm{L}}$, $\tilde{e}_{\mathrm{R}}$, $\tilde{\mu}_{\mathrm{L}}$ and $\tilde{\mu}_{\mathrm{R}}$, are considered.

Figure 1.9(a) shows the exclusion limits at 95% of Confidence Level (CL) on chargino and neutralino masses set by all the SUSY electroweak searches of the ATLAS experiment [73] at the starting time of the analysis described, with results from Run I papers

[6]This peculiarity is not restricted to SUSY models; in principle, as long as a similar phenomenology is shared among other non-SUSY models, simplified models can be used to probe them.
[7]This is done by setting those masses to some unphysical multi-TeV values.
[8]In this analysis only final states with e and/or μ are considered.

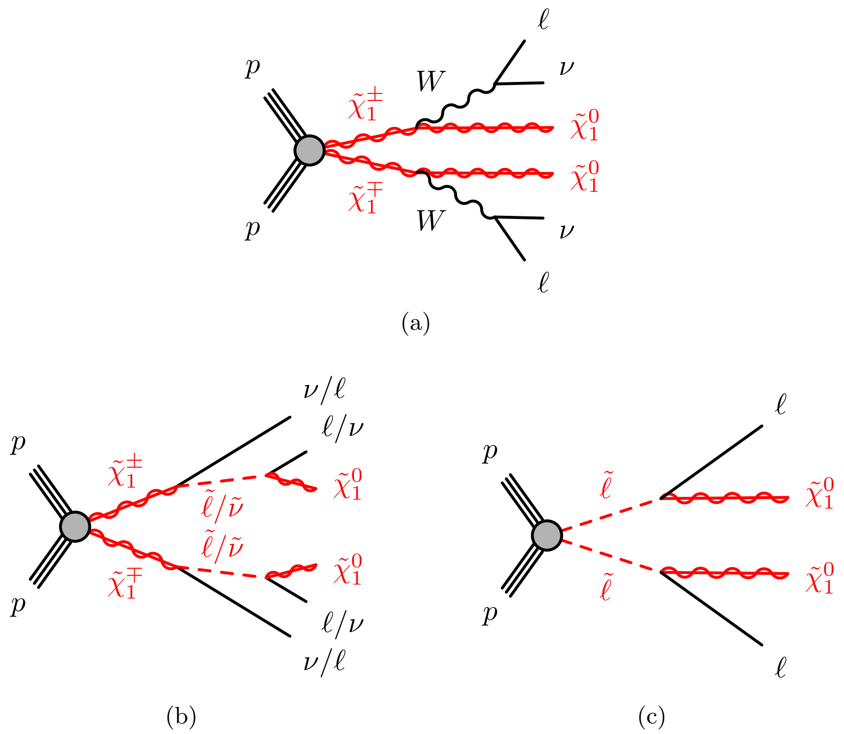

Figure 1.8: Diagrams of the supersymmetric models considered in this thesis, with two leptons in the final state: 1.8(a) $\tilde{\chi}_1^{\pm}\tilde{\chi}_1^{\mp}$ production with W-boson-mediated decays, 1.8(b) $\tilde{\chi}_1^{\pm}\tilde{\chi}_1^{\mp}$ production with slepton/sneutrino-mediated-decays and 1.8(c) slepton pair direct production. In the model with intermediate sleptons, all three flavors ($\tilde{e}$, $\tilde{\mu}$, $\tilde{\tau}$) are included, while only $\tilde{e}$ and $\tilde{\mu}$ are included in the direct slepton model. In the final state, ℓ stands for an electron or muon, which can be produced directly or, in the case of 1.8(a) and 1.8(b) only, via a leptonically decaying τ-lepton with additional neutrinos.

or 2015-2016 data taking years of Run II, while Figure 1.9(b) shows results [74] from data collected by the ATLAS experiment during 2015, 2016, 2017 corresponding to ~ 80 fb^{-1} . They were presented during the *26th International Conference on Supersymmetry and Unification of Fundamental Interactions* for the SUSY model reported in Figure 1.8(a).
The search described here extends the areas of the parameter space beyond those excluded by the previous searches by ATLAS [74–76] and CMS [77–82] Collaborations in the same channels.

1.4 Other SUSY searches

Although the SUSY search described in this thesis belongs to the electroweak sector, a glance on the main other fields of interest is provided in this chapter, in order to give a quite comprehensive picture of the global SUSY context.
If SUSY exists, the most abundantely produced supersymmetric particles have to be those ones resulting from the interaction with the proton constituents via the strong interaction. As it can be noticed in Figure 1.6 for a given particle mass, the first two squark generations, together with gluinos, are the sparticles expected to be mainly

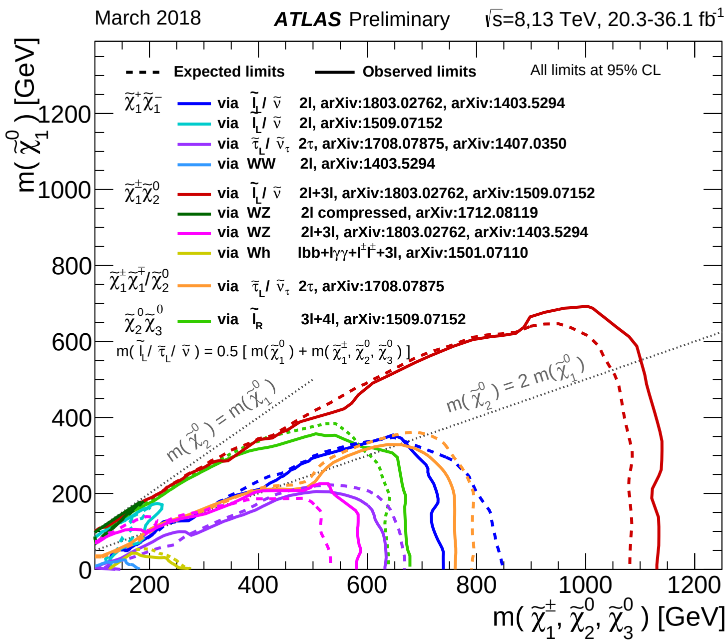

(a) The 95% CL exclusion limits on $\tilde{\chi}_1^+\tilde{\chi}_1^-$, $\tilde{\chi}_1^\pm\tilde{\chi}_2^0$ and $\tilde{\chi}_2^0\tilde{\chi}_3^0$ production with either SM-boson-mediated or $\tilde{\ell}$-mediated decays, as a function of the $\tilde{\chi}_1^\pm$, $\tilde{\chi}_2^0$ and $\tilde{\chi}_1^0$ masses.

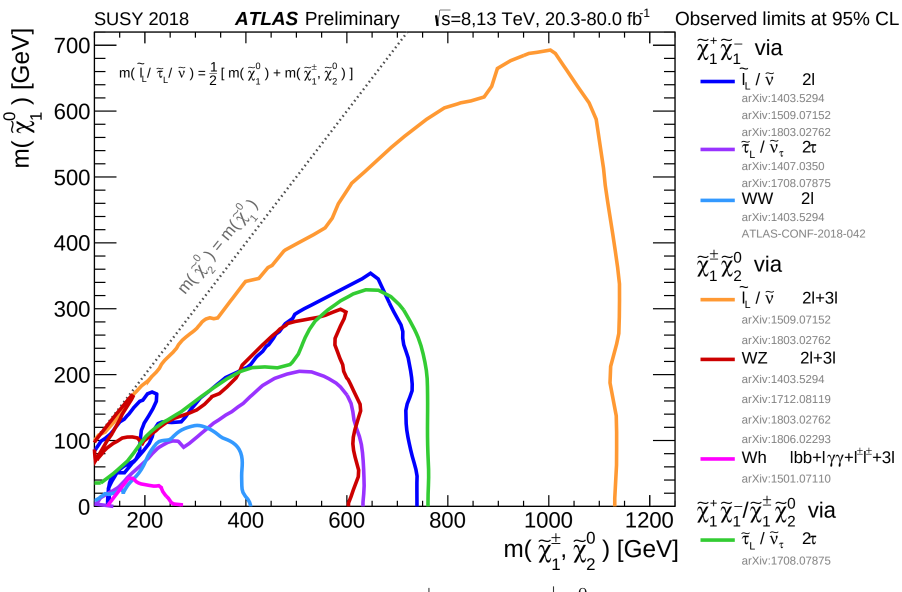

(b) The 95% CL exclusion limits on $\tilde{\chi}_1^+\tilde{\chi}_1^-$ and $\tilde{\chi}_1^\pm\tilde{\chi}_2^0$ production with either SM-boson-mediated or $\tilde{\ell}$-mediated decays, as a function of the $\tilde{\chi}_1^\pm$, $\tilde{\chi}_2^0$ and $\tilde{\chi}_1^0$ masses. Each individual exclusion contour represents one or more analysis in simple merged curves.

Figure 1.9: SUSY electroweak searches summary updated in March 2018 1.9(a) and July 2018 1.9(b).

produced at the LHC, because they can benefit from t-channel diagrams and, consequently, they have higher production cross sections. However, as already mentioned in Section 1.2.4, $\tilde{t}_1$ can be lighter than other squarks, making its production dominant at the LHC; moreover, from a naturalness point of view, a light top squark is largely hoped since it is responsible of the largest contributions to the Higgs mass correction at one-loop order. These two facts justify the large interests in $\tilde{t}_1$ direct production and dedicated searches are summarized in Figure 1.10.

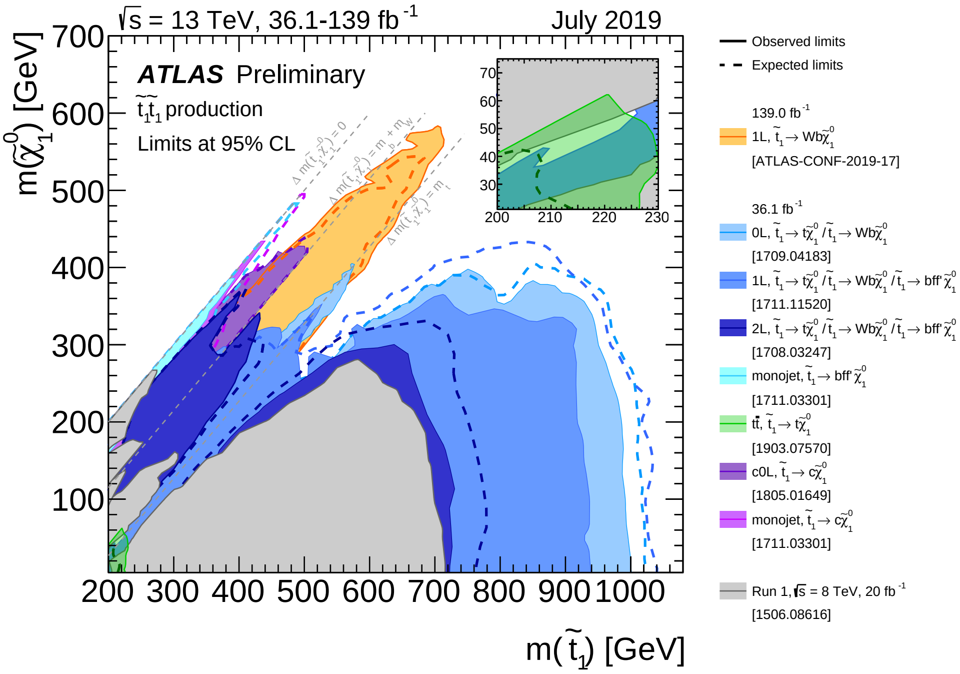

Figure 1.10: Summary of the dedicated ATLAS searches for top squark pair production based on pp collision data taken at $\sqrt{s} = 13$ TeV. Exclusion limits at 95% CL are shown in the $\tilde{t}_1$-$\tilde{\chi}_1^0$ mass plane. The dashed and solid lines show the expected and observed limits, respectively, including all uncertainties except the theoretical signal cross section uncertainty (PDF and scale). Four decay modes are considered separately with 100% BR: $\tilde{t}_1 \rightarrow t + \tilde{\chi}_1^0$ (2-body decay), $\tilde{t}_1 \rightarrow W + b + \tilde{\chi}_1^0$ (3-body decay for $m(\tilde{t}_1) < m(t) + m(\tilde{\chi}_1^0)$), $\tilde{t}_1 \rightarrow c + \tilde{\chi}_1^0$ and $\tilde{t}_1 \rightarrow f + f' + b + \tilde{\chi}_1^0$ (4-body decay). The latter two decay modes are superimposed [83].

Strictly related to $\tilde{t}_1$ searches, there are dedicated searches for $\tilde{b}_1$ direct production, summarized in Figure 1.11, completing third generation squark searches.
Concerning squarks and gluinos in general, the corresponding summary plots are shown in Figure 1.12.
Finally, a quick mention about long-lived particles: if a charged SUSY particle produced in a high-energy collider acquired a relatively long lifetime, it would leave multiple hits in the traversed detector tracking layers before decaying, allowing it to be reconstructed as a track segment in the innermost part of the detector. Therefore, a charged track arising from a long-lived particle can disappear, i.e. leave hits only in the innermost layers and no hits in the portion of the detector at higher radii. A summary plot for this kind of searches is shown in Figure 1.13.

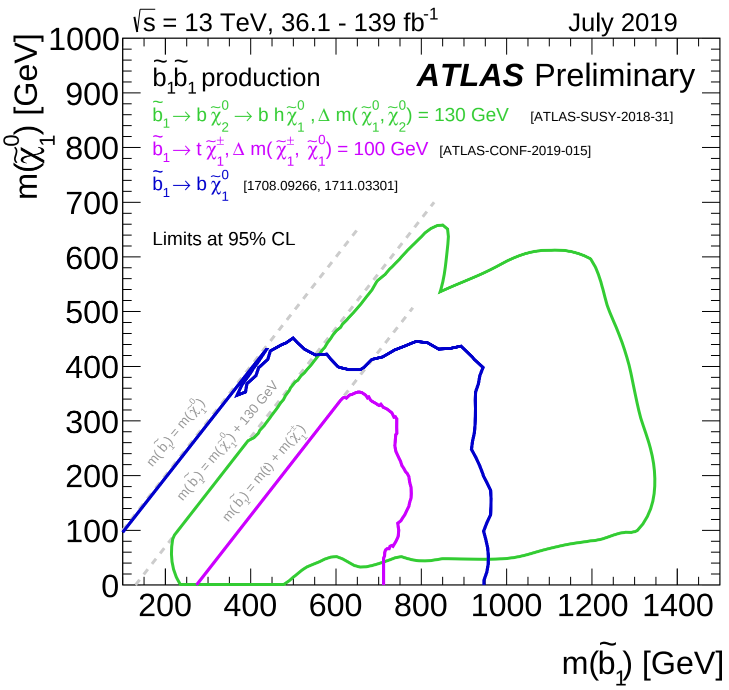

Figure 1.11: Exclusion limits at 95% CL in the $(\tilde{b}_1,\, \tilde{\chi}_1^0)$ mass plane for direct sbottom production. The lightest neutralino is assumed to be the lightest SUSY particle. Several different decay scenarios are shown, along with different parameterizations of the intermediate particles in the models [83].

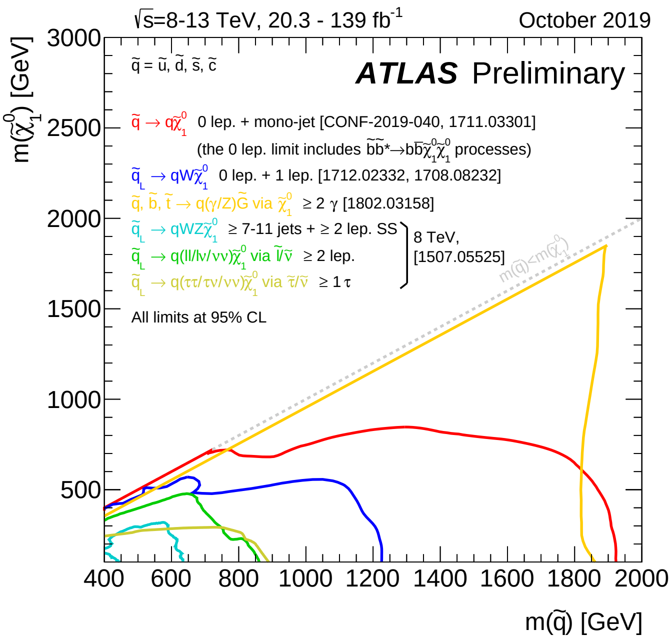

(a)

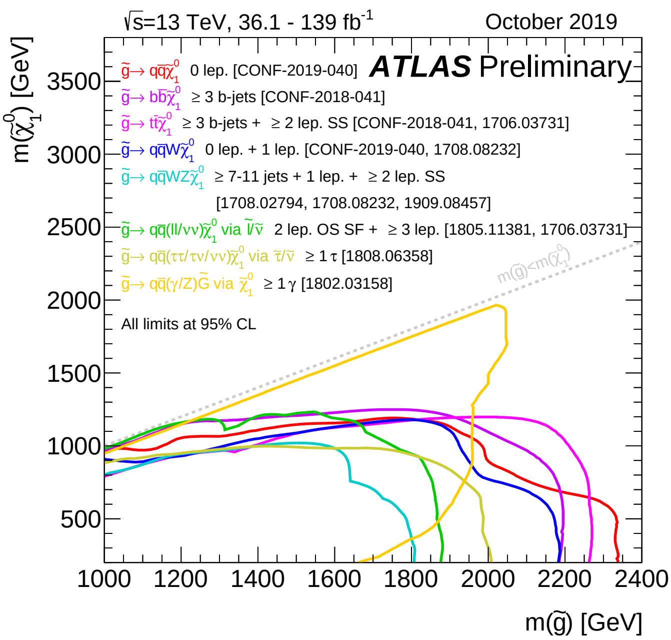

(b)

Figure 1.12: Exclusion limits at 95% CL based on 8 and 13 TeV data in the ($\tilde{q}$ or $\tilde{g}$, $\tilde{\chi}_1^0$) mass plane for different simplified models featuring the decay of squarks 1.12(a) or gluinos 1.12(b) to the lightest supersymmetric particle (lightest neutralino or gravitino) either directly or through a cascade chain featuring other SUSY particles with intermediate masses. For each line, the squark decay mode is reported in the legend and it is assumed to proceed with 100% branching ratio. Some limits depend on additional assumptions on the mass of the intermediate states, as described in the references provided in the plot [83].

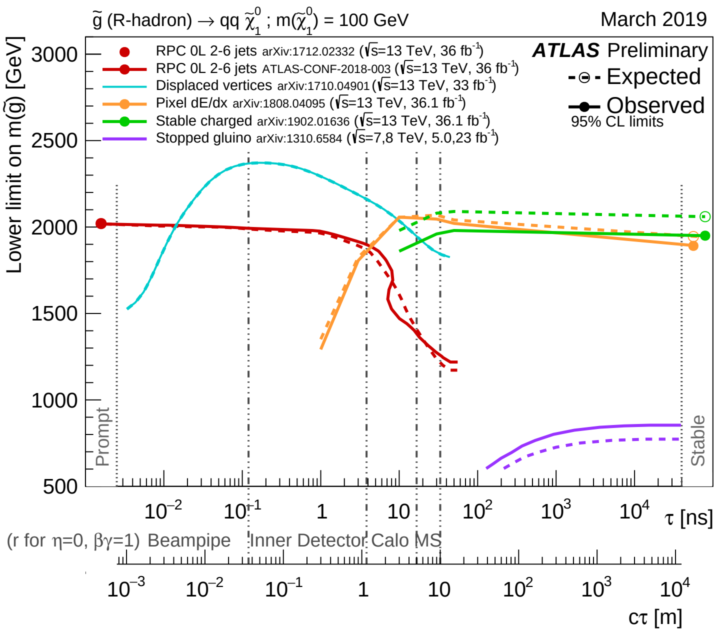

Figure 1.13: Constraints on the gluino mass-vs-lifetime plane for a split-supersymmetry model with the gluino R-hadron decaying into a gluon or light quarks and a neutralino with mass of 100 GeV. The solid lines indicate the observed limits, while the dashed lines indicate the expected limits. The area below the curves is excluded. For the displaced vertices result the expected and observed limits are identical. For the stopped gluino result the limit extends to larger lifetimes [84]. The analyses have sensitivity at lifetimes other than those shown, but only the limits at tested lifetimes are shown. The dots represent results for which the particle is assumed to be prompt or stable. In this context, stable means escaping the detector [83].

Chapter 2

The ATLAS experiment

The work described in this thesis was performed on data of proton-proton collision collected by the ATLAS[1] experiment [25] at the *Large Hadron Collider* (LHC) [51] at CERN[2] during the Run II operation, from 2015 to 2018, at a centre-of-mass energy ($\sqrt{s}$) of 13 TeV.
After a brief, general introduction about LHC, this chapter is mainly devoted to the description of the ATLAS experiment, in order to provide a complete overview of the experimental apparatus.
Finally, the last paragraph contains a general description of the ATLAS upgrade program and of the work done on the MicroMegas detector, which will be installed in the experiment before starting the Run III operation, in 2021.

2.1 The Large Hadron Collider

The Large Hadron Collider is an accelerating facility installed in the existing, 27 km long, tunnel initially built to host the *Lepton Electron-Positron* (LEP) machine [29] at CERN, dismissed in 2000. This tunnel is located underground between 45 and 170 m, on a plane inclined with a slope of 1.4%, at the frontier between France and Switzerland and it is made up of eight straight sections and eight arcs. LHC consists of superconducting magnets together with a series of accelerating structures devoted to increase the particle momentum along the way; thanks to this structure, LHC is able to accelerate protons or heavy ions.
LHC is designed to reach a centre-of-mass energy of 14 TeV, making it the most powerful accelerating machine for physics research ever built. It started its operation in 2008, collecting ~ 25 fb^{-1} of proton-proton (pp) collisions data from March 2010 to early 2013; the centre-of-mass energy was raised from the initial 7 TeV to 8 TeV in the last period of operation, called *Run I*. At the end of these first years of activity, the accelerator underwent a series of upgrades during the following two years (a period known as *Long Shutdown I*, or LS1), before starting again its operation in early 2015 for a second period of data taking, called *Run II*, at a centre-of-mass energy of 13 TeV. Run II ended in October 2018, after delivering ~ 158 fb^{-1} in more than three

[1] Acronym for *A Toroidal Lhc AppatuS*.

[2] Acronym for *Conseil Européen pour la Recherche Nucléaire*, with the initial convetion signed in 1953 by the 12 founding states Belgium, Denmark, France, the Federal Republic of Germany, Greece, Italy, the Netherlands, Norway, Sweden, Switzerland, the United Kingdom and Yugoslavia. Today CERN has 23 Member States.

years of activity. The second series of upgrade (a period known as *Long Shutdown II*, or LS2) is currently taking place during 2019-2020, before starting, in early 2021, the third period of data taking, called *Run III*, at a centre-of-mass energy of 14 TeV, whose end is scheduled in 2023. The final data taking period is called *High-Luninosity LHC* (HL-LHC) and it will start in early 2026, achieving instantaneous luminosity values up to $5 \div 10 \times 10^{34}$ cm^{-2} s^{-1}. A sketch of the current roadmap is shown in Figure 2.1.

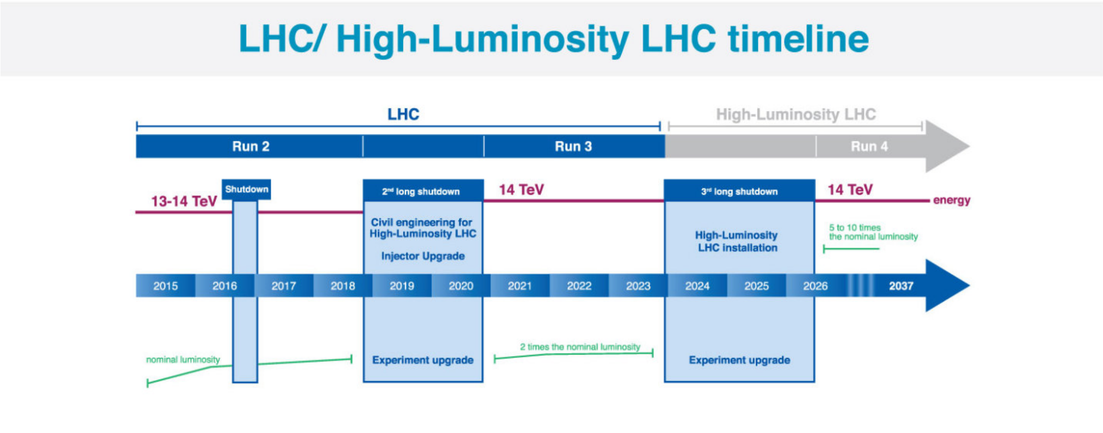

Figure 2.1: LHC schedule up to the HL-LHC phase [85].

LHC is the latest addition to CERN's accelerating complex, whose schematic view is reported in Figure 2.2.

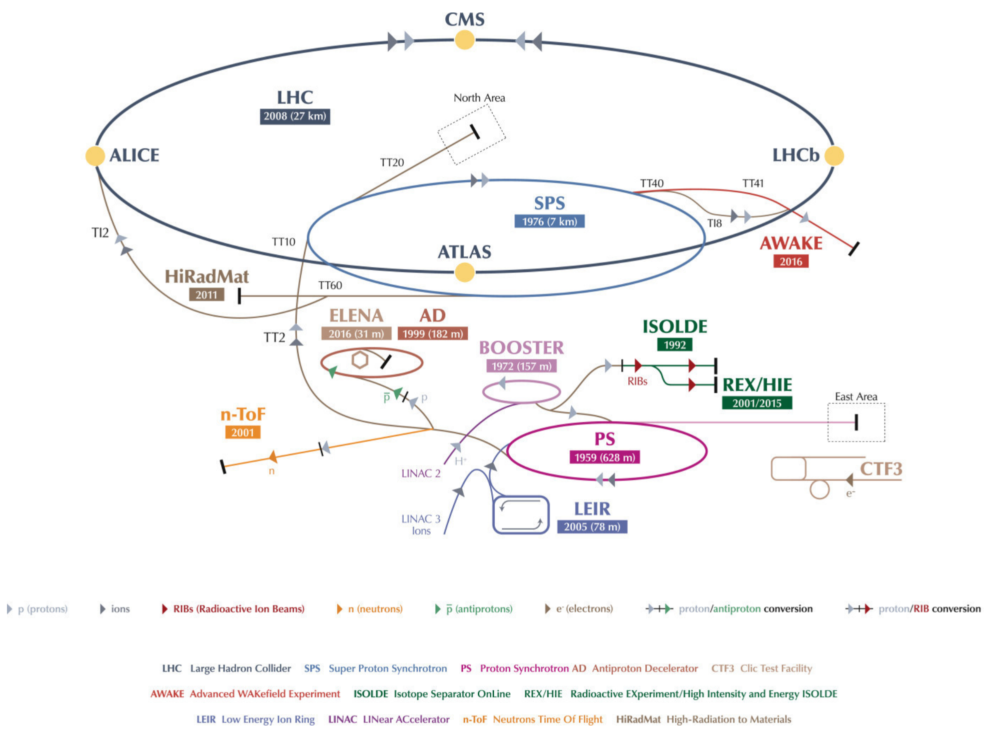

Figure 2.2: Overview of CERN accelerator complex [86].

An electric field is used to extract protons from hydrogen atoms, which are then injected in a linear accelerator, called *Linac 2*, boosting their energy to 50 MeV. The

beam is injected into the *Proton Synchrotron Booster* (PSB), which accelerates the protons to 1.4 GeV, then in the *Proton Synchrotron* (PS), obtaining a final energy of 25 GeV, and in the *Super Proton Synchrotron* (SPS), to furtherly accelerate the protons up to 450 GeV. Finally, they are injected in the LHC, and it takes 20 minutes for the *radiofrequency* (RF) cavities to boost protons to finally reach their nominal energy of 6.5 TeV in bunches of $\sim 10^{11}$ protons, with a nominal bunch separation of 25 ns.
Being a same sign particles collider, in LHC the two beams are counter-rotating in two separate pipes. Since the tunnel housing LHC was originally designed for LEP, it has longer straight sections than curved ones, in order to minimize the loss of energy due to synchrotron radiation which would have affected the lepton beams at LEP.
Strong magnetic field, up to ~ 8 T, is provided by superconducting electromagnets to properly bend the proton beams. Two kinds of magnets are used, dipole and quadrupole, in a continuous succession of bending and focusing stages for the two beams.
The tunnel in the arc sections has an internal diameter of 3.7 m, dimensions which made extremely difficult for two completely separated proton rings to fit in. The limited space available led to the adoption of twin-bore magnets [87], having coils and beam pipes hosted within the same mechanical structure and cryostat, as shown in Figure 2.3.

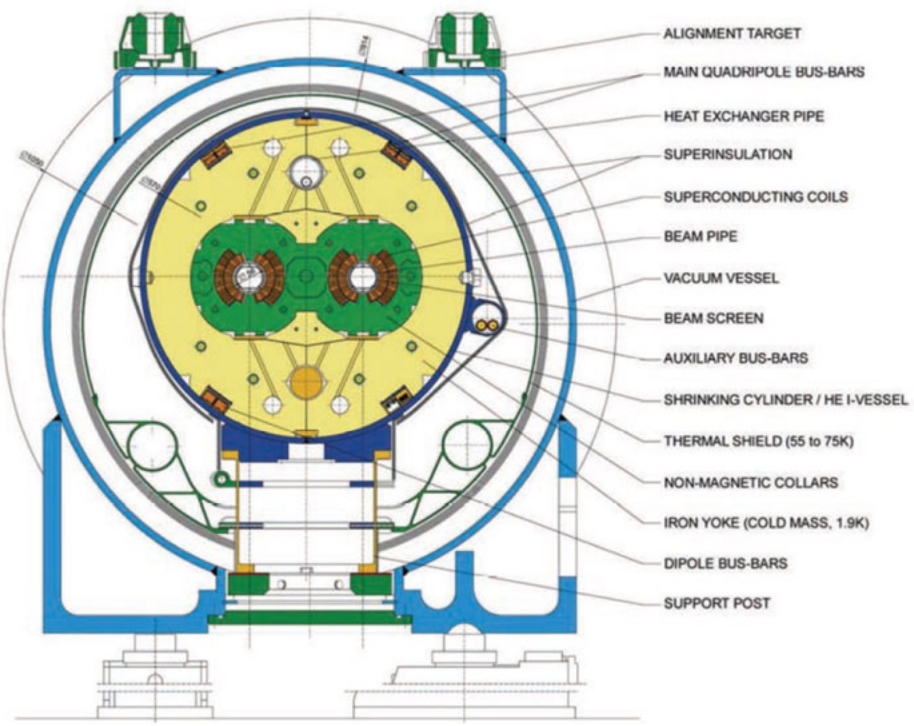

Figure 2.3: Cross-section of a cryodipole, the two-in-one LHC bending magnet. The two rings are hosted inside a single vacuum vessel to save space [87].

Along the accelerator ring four interaction points are present and around them the four major experiment, ALICE [88], ATLAS [25], CMS [53] and LHCb [89], are built to record the collisions delivered by the LHC. The basic layout of the LHC tunnel is sketched in Figure 2.4. The two largest experiments, ATLAS and CMS, are defined “general purpose”, since they are designed to investigate a wide range of physics processes; on the other hand, ALICE and LHCb are specialized experiments to focus on specific phenomena, i.e. heavy-ion collisions for ALICE and b-physics for LHCb.

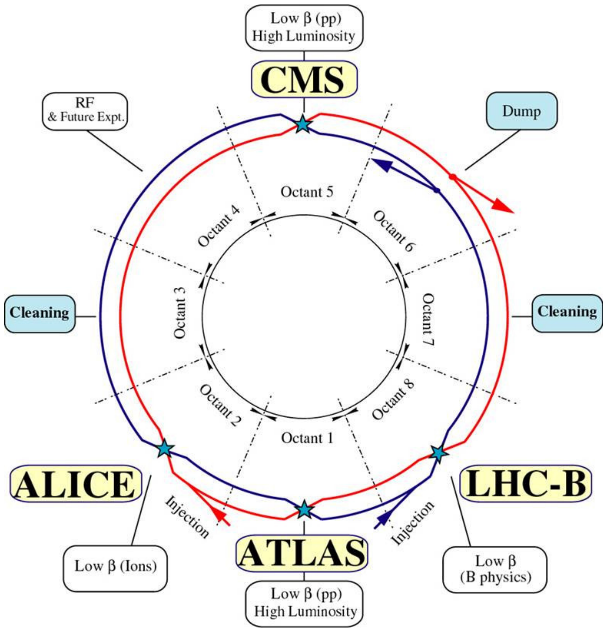

Figure 2.4: Schematic layout of the LHC [90].

2.1.1 Luminosity

In a collider experiment the quantity measuring the number of events per second, *rate* $R(t)$, is strictly related to the cross-section σ of the process itself, through a specific function called *instantaneous luminosity*:

$$R(t) = \mathcal{L}(t)\sigma. \tag{2.1}$$

The instantaneous luminosity is a quantity depending on the beams and the machine parameters. Assuming a Gaussian profile and the same bunch structure for the two beams, $\mathcal{L}(t)$ can be written as

$$\mathcal{L}(t) = f\frac{Nn_1n_2}{4\pi\sigma_x\sigma_y}, \tag{2.2}$$

where f is the revolution frequency, N the number of bunches per beam, n_1 and n_2 are the number of particles in the bunch for the two beams, whose transverse dimensions in the two direction orthogonal to the beam are represented by σ_x and σ_y.
Therefore, given an instantaneous luminosity $\mathcal{L}(t)$, the total number of events N_E produced during a generic time interval T for a process with cross-section σ is:

$$N_E = \sigma\int_0^T \mathcal{L}(t)\,dt \equiv \sigma L, \tag{2.3}$$

with L being the *integrated luminosity*.
The instantaneous luminosity per year delivered by LHC to ATLAS [91] during Run II operations is reported in Figure 2.5, reaching a peak value of $21.4 \cdot 10^{33}$ cm^{-2} s^{-1},

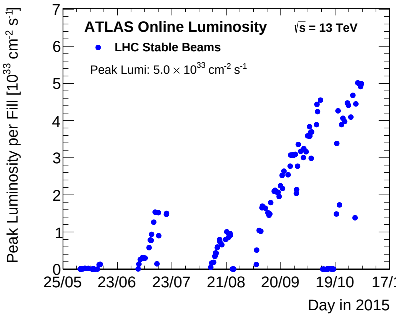

(a) 2015

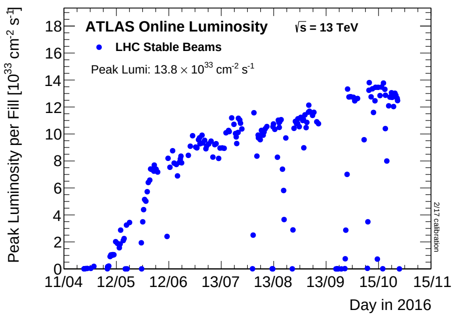

(b) 2016

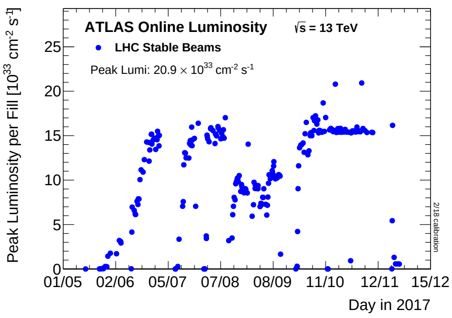

(c) 2017

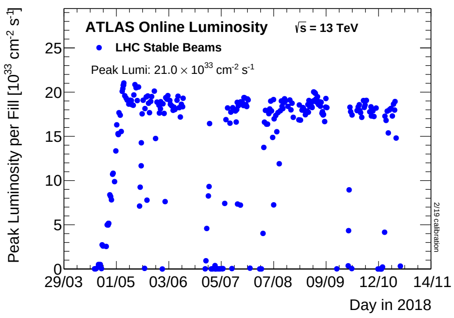

(d) 2018

Figure 2.5: The peak instantaneous luminosity delivered to ATLAS during stable beams for *pp* collisions at 13 TeV centre-of-mass energy, shown for each LHC fill as a function of time during Run II [91].

while the design value at $\sqrt{s} = 14$ TeV was 10^{34} cm^{-2}s^{-1}. The reached value is more than double of the nominal value expected.
Many processes are expected to occur in BSM physics scenarios in addition to the ones specific of the Standard Model, typically with a much lower cross-section. They can be observed with statistical significance only at high luminosity values. However, by increasing the instantaneous luminosity, the number of *pp* interactions per bunch crossing increases as well. The downside of this operation is related to several cross collisions which contaminate the hard scattering processes typically triggering the event; they complicate a lot the event reconstruction and identification and these collisions are referred to as *in-time pile-up* or, simply, *pile-up* (PU).
During Run II operations, the increase in the delivered luminosity (Figures 2.6(a) and 2.6(b)) produced an higher number of *pp* collisions per bunch crossing $\langle \mu \rangle$, as reported in Figure 2.6(c).
Pile-up represents a serious problem for all analyses and they must properly take into account the different PU condition in which the analyzed events were collected.

2.2 The ATLAS detector

The ATLAS detector was designed to perform high-accuracy measurements on a wide spectrum of physics processes and, at the same time, to maximize the sensitivity for potential discoveries of new physics. For this reason, ATLAS is a *general purpose* experiment. The detector is composed by different cylindric shells, each one corre-

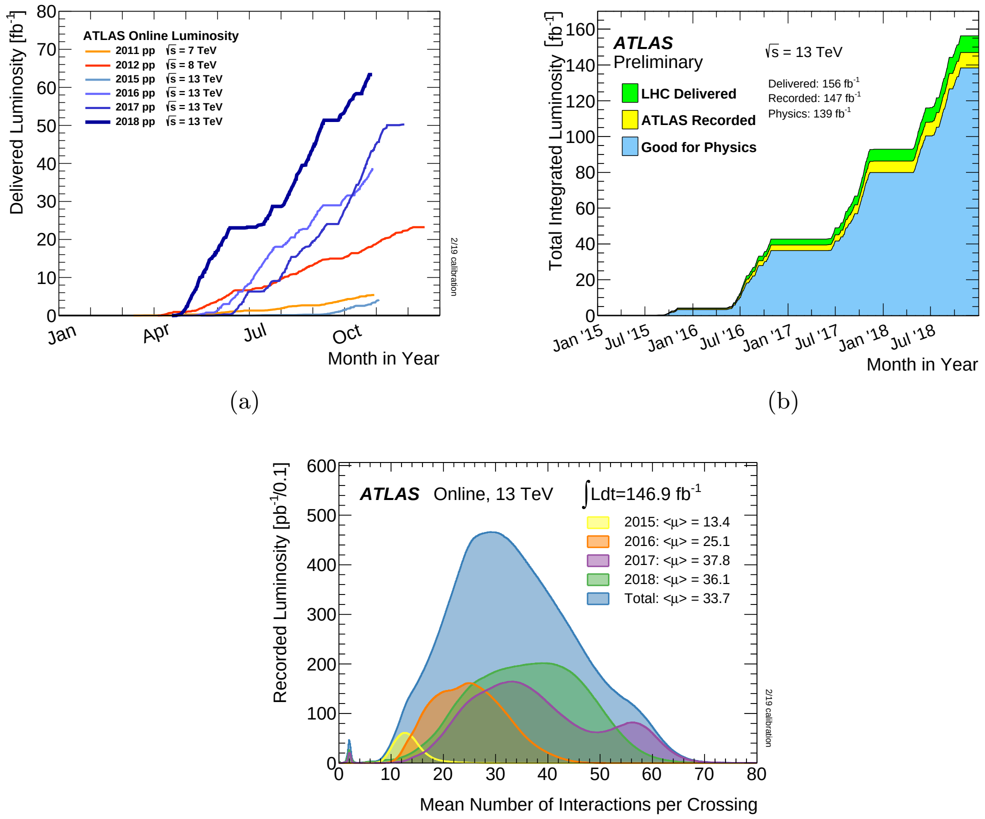

(a) (b)

(c)

Figure 2.6: LHC cumulative integrated luminosity [91] versus time delivered to ATLAS during stable beams for high energy pp collisions 2.6(a) and during Run II operations, divided in total one (green), recorded by ATLAS (yellow) and certified to be good quality data (blue) 2.6(b). Luminosity-weighted distribution 2.6(c) of the mean number of interaction per crossing from 2015 to 2018 is also reported.

sponding to a specific subdetector for a dedicated class of measurements, as shown in Figure 2.7.
The central part of the apparatus is called *barrel*, while the disks in the forward/backward regions are called *end caps*, enclosing the cylindrical volume. Before proceeding with the description of the detector components, it is useful to illustrate the coordinate system definition and the basic nomenclature that will be used.
ATLAS uses a right-handed coordinate system with its origin at the nominal interaction point (IP) in the centre of the detector and the z-axis along the beam pipe. The x-axis points from the IP to the centre of the LHC ring and the y-axis points upwards. In the x-y plane, called *trasverse* plane, the azimuthal angle ϕ is measured with respect to the positive x-axis direction and r is the radial distance. The polar angle θ is measured in the z-y plane starting from the z-axis positive direction. It is a common choice to express θ in terms of the *pseudorapidity* η, defined as:

$$\eta = -\ln\left(\tan\frac{\theta}{2}\right). \tag{2.4}$$

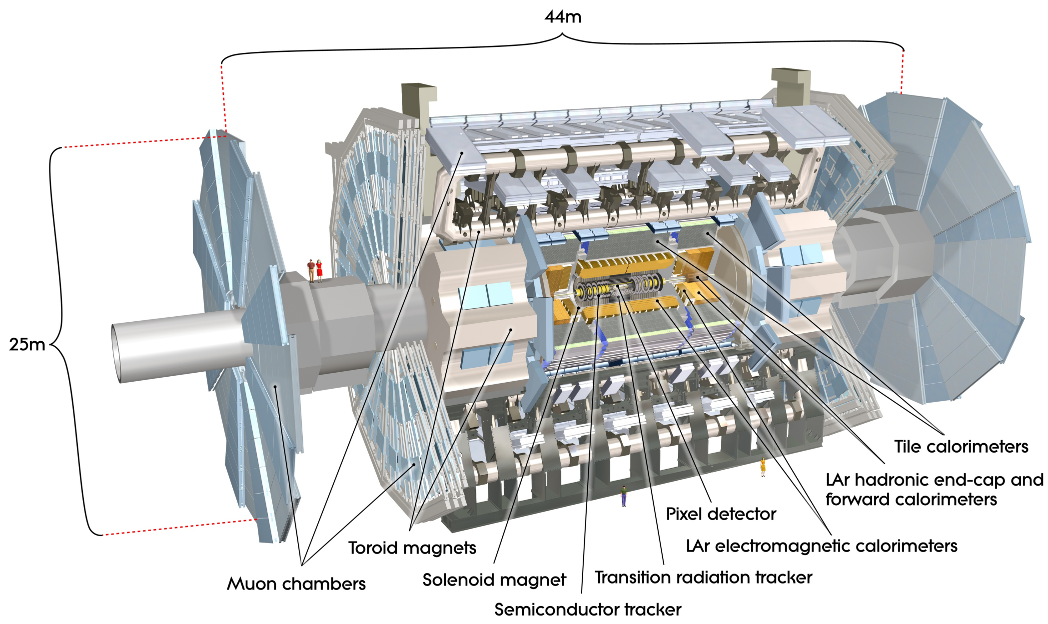

Figure 2.7: Schematic view of the ATLAS detector [25], whose dimensions are 25 m in height and 44 m in length. The overall weight of the entire structure is $\sim$ 7000 t.

For a particle with energy E and momentum $\mathbf{p} = (p_x, p_y, p_z)$, assuming $p \gg m$, η is approximately equal to the *rapidity* y [19]:

$$y = \frac{1}{2} \ln \left(\frac{E + p_z}{E - p_z} \right) . \tag{2.5}$$

At collider experiments, η is preferred over θ since differences in pseudorapidity are invariant under Lorentz boosts along the z-axis.
Starting from the IP, the *Inner Detector* (ID) is the innermost cylindric shell in ATLAS. It is immersed in a solenoidal magnetic field of 2 T, which allows to measure the trajectories and momenta of the charged particles, and it is composed of subdetectors employing different technologies: the *Pixel Detector*, the *Semi-Conductor Tracker* (SCT) and the *Transition Radiation Tracker* (TRT). The Inner Detector is surrounded by the *Calorimeter*, whose purpose is to measure the particle enegy. There are two specific substructures: the Electromagnetic Calorimeter, designed for electrons/positrons and photons, and the Hadronic Calorimeter, for charged and neutral hadrons. The outer shell of the apparatus is the *Muon Spectrometer* to perform muon identification, reconstruction and momentum measurement; it is located within a toroidal magnetic field with an intensity varying between 0.5 and 1 T.

2.2.1 Inner Detector

The ATLAS Inner Detector (ID) [92] is designed to provide high precision tracking and an excellent momentum resolution, relying on a robust pattern recognition for the majority of particles coming from the interaction point. The ID also provides both primary and secondary vertex measurements for charged particles within the pseudorapidity range $|\eta| < 2.5$, as well as electron identification in the same η-range.

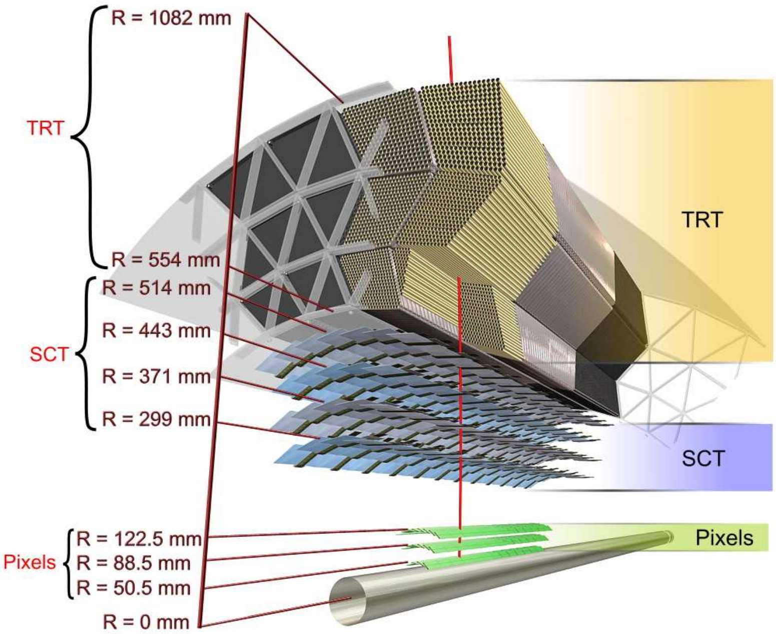

Figure 2.8: View of the ATLAS ID [25] showing the detector elements crossed by a charged particle (red line) coming from the interacion vertex at small $|\eta|$: after the beam pipe, the track crosses the Insertable B-Layer (made of silicon pixels), three cylindrical silicon-pixel layers, four cylindrical double layers of barrel SCT and approximately 36 layers of axial straw tubes contained in the barrel TRT modules.

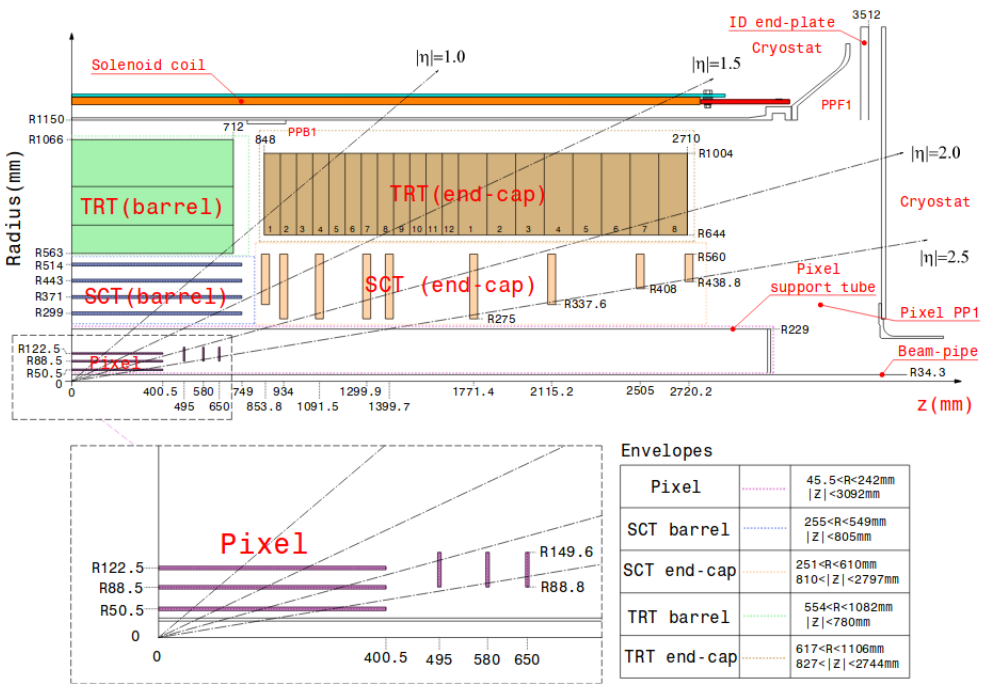

Figure 2.9: Side view of one quadrant of the ATLAS Inner Detector [93], showing each of the major detector elements with the relative dimensions and envelopes [25]. Insertable B-Layer is not shown.

Schematic views of the ID layout are reported in Figures 2.8 and 2.9.
The ID consists of three independent and complementary subdetectors, able to achieve an excellent resolution for charged particle momentum measurements:

$$\frac{\sigma_{p_{\mathrm{T}}}}{p_{\mathrm{T}}[\mathrm{GeV}]} = 0.05\%\ p_{\mathrm{T}} \oplus 1\%. \tag{2.6}$$

At inner radii, high resolution pattern recognition capabilities are ensured by using discrete space-points from silicon pixel layers and stereo pairs of silicon microstrip layers. On the other hand, at outer radii the transition radiation tracker comprises many layers of gaseous straw tubes interleaved with transition radiation material.

Pixel Detector

Close to the interaction point, a high detector granularity is achieved by the semiconductor *Pixel Detector* [94, 95]. This system needs to cope with a high track density and it provides very precise measurements over the full acceptance, mostly defining the ability of the ID to identify short-lived particles. In the barrel region four pixel layers are arranged on coaxial cylinders around the beam axis, while in the end-cap regions the pixel modules are mounted on three disks perpendicular to the beam axis. During LS1 an extra layer was inserted between the innermost of the three existing pixel detector layers and a new beam pipe with reduced radius, also inserted during LS1. This extra layer is called *Insertable B-Layer* (IBL) [96] and it contains ~ 13 million pixels with nominal size $50 \times 250\ \mu\mathrm{m}^2$; the nominal pixel size is $50 \times 400\ \mu\mathrm{m}^2$ for the ~ 80 million ones in the remaining layers.
The average resolution of IBL [97] is of 9.0 μm in the transverse plane and $\sim 60\ \mu$m along the z-axis. In the three outermost layers, the Pixel Detector is able to reach a nominal, spatial resolution of 10 μm in the azimuthal plane and 115 μm along the z-axis direction in the barrel and along the radial direction in the end-caps [98].

Semi-Conductor Tracker

The *Semi-Conductor Tracker* (SCT) [99, 100] surrounds the pixel detector and it consists of double-face silicon microstrip detectors, arranged in four cylindrical layers in the barrel and nine angular disks in each end-cap. The underlying technology is similar to the pixel detector one, the main difference being the arrangement structure (strips, instead of pixels) of the active material, with each sensitive element having a surface of $64 \times 64\ \mathrm{mm}^2$ with a strip pitch of 80 μm; in the end-caps the disks use wedge-shaped sensors of five slightly different sizes, with a strip pitch ranging from 57 to 90 μm [101]. These elementary units are glued back-to-back at a stereo angle of 40 mrad, in order to provide three-dimensional information from the hits.
The layout was designed in order to energetic charged particles will pass through at least four layers everywhere in the acceptance region. A nominal resolution of 580 μm is achieved in the z-axis direction in the barrel and in the radial direction in the end-caps, while a resolution of 17 μm is achieved in the azimuthal plane [98].

Transition Radiation Tracker

The *Transition Radiation Tracker* (TRT) [102] is the outermost part of the ID. The basic detector elements are about 300000 polyamide thin-walled proportional drift

tubes of 4 mm diameter, called *straws*. In the barrel they are 144 cm long and oriented parallel to the beam, while in the end-caps they are 37 cm in length and radially oriented. The anodes are ~ 30 μm gold-plated tungsten wires and a typical operating gas mixture is Xe:CO_2:O_2 (70:27:3). The detector geometry ensures that particles cross 35-40 straws in a pseudorapidity interval of $|\eta| < 2$.
TRT provides $r - \phi$ information with an intrinsic accuracy of 130 μm per straw [98], lower than the one of the silicon technology employed closer to the beam pipe. However, since the TRT can operate at very high rates at a higher average radius, the contribution provided to the momentum measurement of the charged particle is important.
In addition, TRT is able to perform electron identification, exploiting the so-called *transition radiation*, i.e. an electromagnetic radiation in the X-ray spectrum emitted when a relativistic charged particle crosses the boundaries between media with different electromagnetic properties. Having a lower mass with respect to other charged particle, electrons reach relativistic condition for the emission of the transition radiation at lower energies. The emitted photons are detected by the gas mixture in which straws are immersed, thus allowing a significant $e^{\pm}/\pi^{\pm}$ discrimination power between electrons and charged pions in the range of energies from 1 GeV up to ~ 100 GeV [103].

2.2.2 Calorimeters

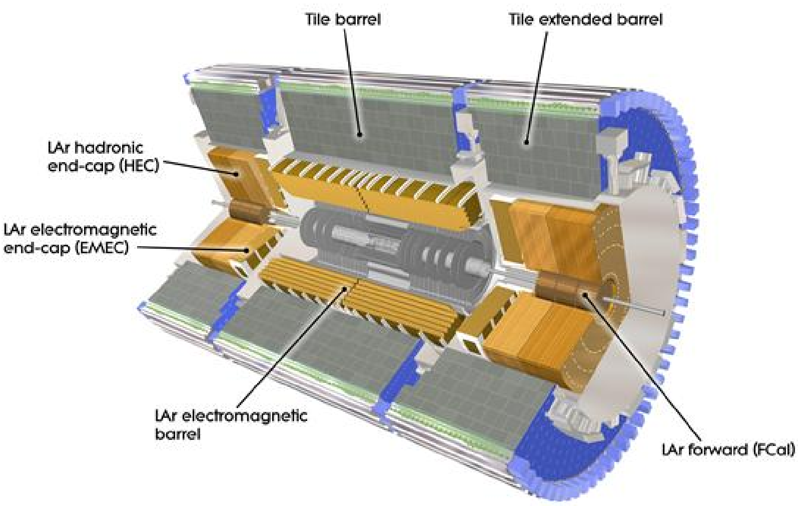

Figure 2.10: General view of the different components of the ATLAS calorimeter system [25].

The ATLAS calorimetric system [104] consists of a number of sampling detectors allowing to measure the energy of electrons, photons and hadrons entering the total sensitive volume, shown in Figure 2.10. The energy is deposited by the particles in the form of electromagnetic or hadronic *showers*. The features of the shower depend on the nature of the particle originating it and on its energy, providing fundamental information in order to perform particle identification.
The calorimetric system is one of the biggest component of the ATLAS detector, to fully contain the shower originated by one or more particles within the entire detector acceptance volume, and it covers a pseudorapidity region up to $|\eta| \simeq 4.9$. Only high-

energy muons and neutrinos are expected to escape it. A description of the two main calorimeter subcomponents is reported in the following paragraphs.

Electromagnetic Calorimeter

The first (inner) part of the ATLAS calorimeter is the *ElectroMagnetic* (EM) *Calorimeter* [105, 106], located immediately after the Inner Detector system. It is divided into a barrel part ($|\eta| < 1.475$) and two end-caps components ($1.375 < |\eta| < 3.2$), each one inserted in a dedicated cryostat. The barrel calorimeter consists of two identical half-barrels, separated by a small gap of 4 mm at $z = 0$. The length of each half-barrel is 3.2 m, while inner and outer diameters are 2.8 and 4 m, with an approximate weight of ~ 57 t each. Each end-cap calorimeter is mechanically divided in two coaxial wheels: an outer one covering the region $1.375 < |\eta| < 2.5$ and an inner one spanning the region $2.5 < |\eta| < 3.2$.

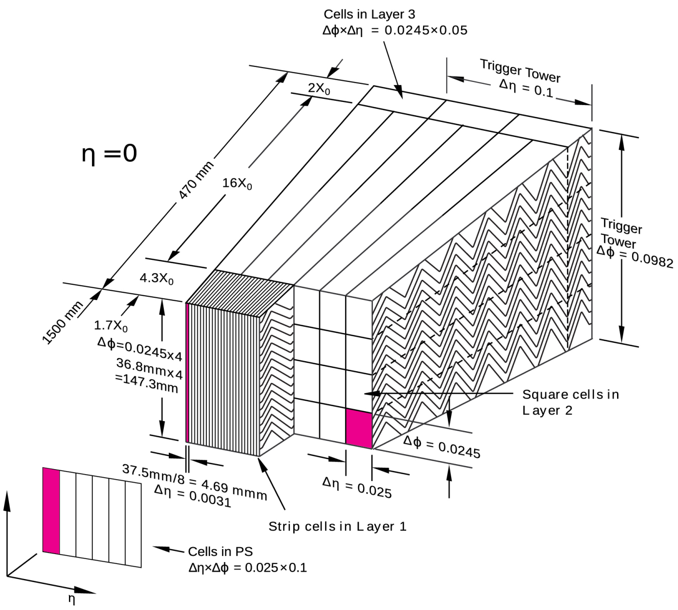

Figure 2.11: Longitudinal segmentation scheme in a barrel module where the different layers are visible with the ganging electrodes in the ϕ-direction. The granularity in η and ϕ for each of the three layers and for the trigger towers [25] is reported.

The EM Calorimeter uses Liquid Argon (LAr) as active material, accordion-shaped kapton electrodes and lead absorber plates over its full coverage volume. The accordion geometry provides complete ϕ symmetry without azimuthal cracks, as shown in Figure 2.11. In the barrel the accordion waves are axial, running in the ϕ-direction, and the folding angles of the waves vary with radius to keep the LAr gap constant. In the end-caps they are parallel to the radial direction, running axially.
The calorimeter is divided in towers which provides the position measurements of the energy deposited by electrons or photons (*cluster*). The cooling system exploits liquid Helium, sharing the cryostat with the solenoidal magnet.
Due to its low granularity, the EM Calorimeter cannot achieve high position resolutions, while the nominal energy resolution [25] is:

$$\frac{\sigma_E}{E} = \frac{10\%}{\sqrt{E[\text{GeV}]}} \oplus 0.7\%. \tag{2.7}$$

Hadronic Calorimeter

The second (outer) part of the ATLAS calorimeter is the *Hadronic Calorimeter*, dedicated to measure the energy of the hadronic jets coming from the hadronization processes of quarks and gluons. It has a composite structure: the *Tile Calorimeter* (TileCal), the *Hadronic End-cap Calorimeter* (HEC) and the *Forward Calorimeter* (FCal).

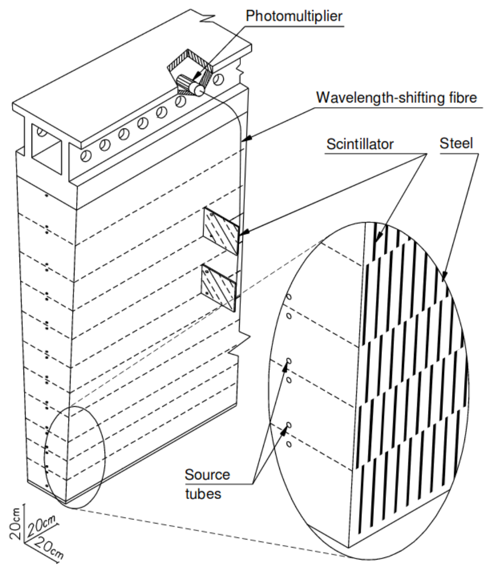

Figure 2.12: Schematic view of the ATLAS Tile Calorimeter and integration with the optical read-out [25].

The *Tile Calorimeter* [107] is located directly outside the EM Calorimeter envelope: its barrel component covers the region $|\eta| < 1$, while the two extended barrels the range $0.8 < |\eta| < 1.7$. It is a sampling calorimeter with steel plates as absorbers and plastic scintillating tiles, hence the name, as active material; the structure is shown in Figure 2.12.
The radial segmentation is done, in depth, in three layers. Two sides of the scintillanting tiles are read out by wavelength shifting fibers into two separates photomultiplier tubes. In the η-direction, the read-out cells, built by grouping the fibers into the photomultipliers, provide a pseudo-projection towards the interaction point.

The *Hadronic End-cap Calorimeter* [108] consists of two independent wheels per end-caps and exploits a LAr technology with copper plates, located directly behind the end-cap Electromagnetic Calorimeter, which shares the same LAr cryostats with. The pseudorapidity region covered by this structure is $1.5 < |\eta| < 3.2$.
Each wheel is built from 32 identical wedged-shaped modules, an example of which is shown in Figure 2.13, assembled with fixtures at the periphery and at the central bore. Each wheel is divided into two segments in depth, resulting in a total of 4 layers per end-cap. The wheels closest to the interaction point are built from 25 mm parallel copper plates, dimension increased to 50 mm for those further away.
The nominal energy resolution of TileCal and HEC is [25]:

$$\frac{\sigma_E}{E} = \frac{50\%}{\sqrt{E[\text{GeV}]}} \oplus 3\%. \tag{2.8}$$

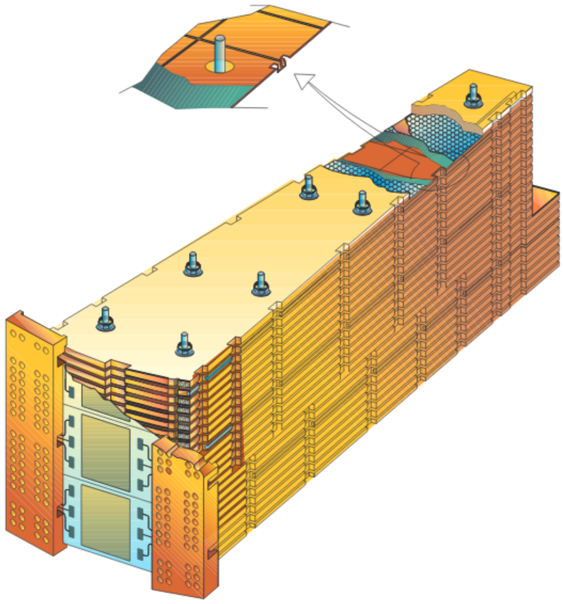

Figure 2.13: Schematic view of a HEC module with a cut-away showing the read-out structure and the active-pad electronics [25].

The *Forward Calorimeter* [109] is integrated in the end-cap cryostat structures and it covers the region $3.1 < |\eta| < 4.9$. Being located at high η, FCal modules are exposed to high particle fluxes. To overcome this situation, the design resulted in very small LAr gaps obtained by using an electrode structure of small-diameter rods placed centrally in tubes which are oriented parallel to the beam direction. Copper is used as passive material for the electromagnetic measurements, while tungsten for hadronic particle measurements. A view of the FCal layout is shown in Figure 2.14.

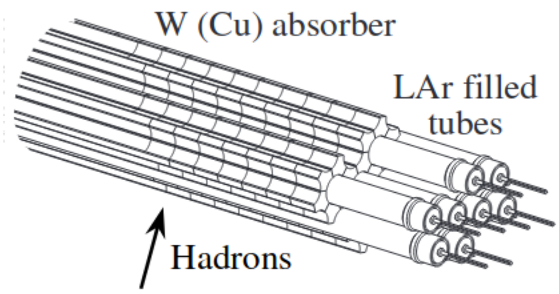

Figure 2.14: ATLAS Forward Calorimeter structure: tubes containing LAr are embedded in a copper or tungsten matrix [19].

The nominal energy resolution of FCal is [25]:

$$\frac{\sigma_E}{E} = \frac{100\%}{\sqrt{E[\text{GeV}]}} \oplus 10\%. \tag{2.9}$$

2.2.3 Muon Spectrometer

The ATLAS *Muon Spectrometer* [110] (MS) is the outermost layer of the ATLAS apparatus. It measures the momentum of the charged particles exiting the barrel and the end-cap calorimeters from the track deflection in the magnetic field generated by three air-core toroidal magnets, in the pseudorapidity range $|\eta| < 2.7$.
The design of the MS was driven by the request to achieve a transverse momentum resolution of

$$\frac{\sigma_{p_\mathrm{T}}}{p_\mathrm{T}} = 10\% \quad \text{at} \quad p_\mathrm{T} = 1 \text{ TeV}, \tag{2.10}$$

which corresponds to measure a muon sagitta in the magnetic field of ~ 500 μm with a resolution ≤ 50 μm. The two end-cap air toroids (each one covering the region $1.6 < |\eta| < 2.7$) are inserted in the barrel air toroid ($|\eta| < 1.4$) at both ends. The region with $1.4 < |\eta| < 1.6$ is usually referred to as transition region, where the deflection is provided by the overlapping of barrel and end-cap magnetic fields. The toroids provide a field mostly orthogonal to the muon trajectories, which are bent in the η-direction; this is opposite from what happens inside the ID, where charged particles are bent in the transverse plane.
In addition to the tracking capabilities, the MS is designed to trigger on muons in the region $|\eta| < 2.4$.
Muon momenta down to few GeV and up to few TeV can be measured by a system of chambers arranged as reported in Figure 2.15. In the barrel region, muon tracks are measured by chambers arranged in three cylindrical layers at radii of approximately 5 m, 7.5 m and 10 m around the beam axis (Figure 2.15(a)); in the transition and end-cap regions, chambers are installed in three layers (or wheels), located in planes perpendicular to the beam axis at distances of $|z| \approx 7.4$ m, 14 m and 21.5 m from the interaction point; due to the presence of the end-cap air toroid, another partial layer is located at $|z| \approx 10.8$ m (Figure 2.15(b)).
Over most of the η range ($|\eta| < 2.7$) a precision measurement of the track coordinate in the bending direction is provided by the *Monitored Drift Tubes* chambers (MDT). In the innermost end-cap layer the coverage is provided by the *Cathode-Strip Chambers* in the range $2.0 < |\eta| < 2.7$.
For the trigger system, *Resistive Plate Chambers* (RPC) and *Thin Gap Chambers* (TGC) are used, respectively, in the barrel and in the end-cap regions. Because of the stringent requirements on the momentum resolution at high momenta, a sophisticated optical alignment system has been designed to monitor the relative chamber positions and possible deformations and the chamber alignment with respect to the full detector, reaching a precision of a few tens of μm.

Monitored Drift Tubes

The *Monitored Drift Tubes* (MDT) [25, 111] chambers are crucial for the precision measurement of the muon trajectories. They consist of two multi-layers (3-4 layers) of aluminium drift tubes with a diameter of 30 mm. Tubes are filled with an Ar:CO_2 (93:7) gas mixture at an absolute pressure of 3 bar. Chambers are rectangulary-shaped in the barrel and trapezoidaly-shaped in the end-caps. The direction of the tubes both in the barrel and in the end-caps is along ϕ.
The MDT time-to-distance relation depends on several parameters (e.g. gas temperature, pressure, magnetic field, etc.), and continuous calibrations are needed. The

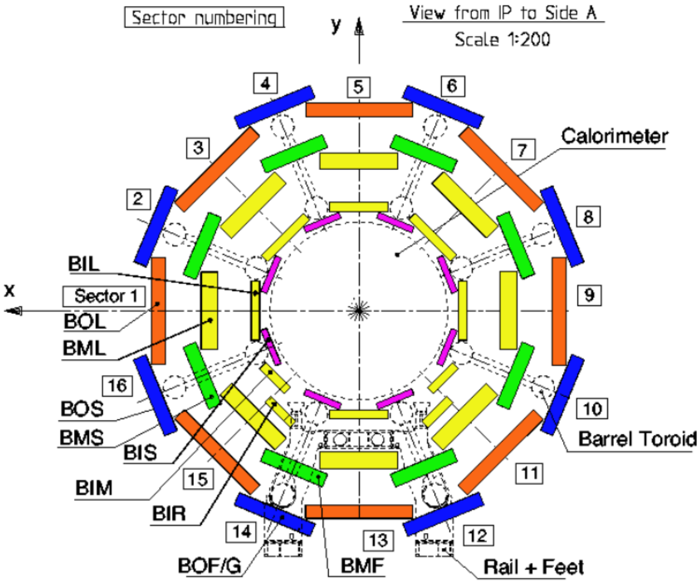

(a) Cross-section of the barrel muon system perpendicular to the z-axis, showing three concentric cylindrical layers of eight large and eight small chambers. A schematic view of the eight coils of the barrel air toroid is also shown.

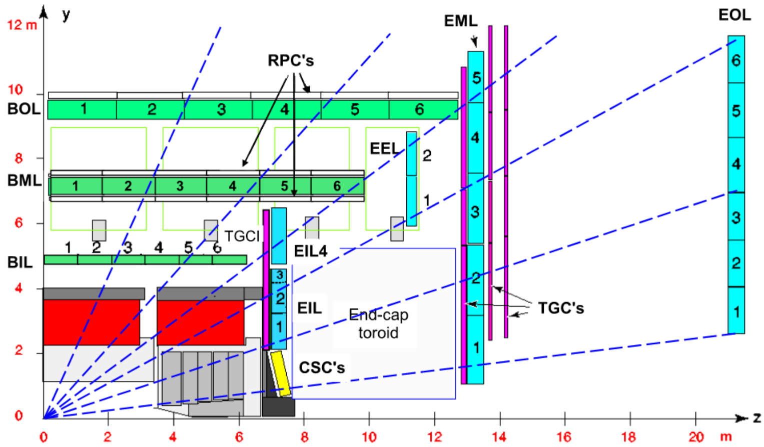

(b) Cross-section of the muon system in a plane containing the beam axis. Infinite-momentum muons would propagate along straight trajectories which are illustrated by the dashed lines, typically traversing three muon stations

Figure 2.15: Cross-sections in the non-bending 2.15(a) and bending 2.15(b) plane of the ATLAS MS [25]. Monitored Drift Tubes (MDT) detectors, in green and light blue boxes, Cathode-Strip Chambers (CSC), in yellow box, Thin-Gap Chambers (TGC), in purple boxes, and Resistive Plate Chambers (RPC), in white boxes, are reported in 2.15(b). CSC and EIL 1-3 stations constitute the so-called Small Wheel.

detector nominal resolution in the bending direction is $\sim 80\ \mu$m per single tube and $\sim 35\ \mu$m per chamber.

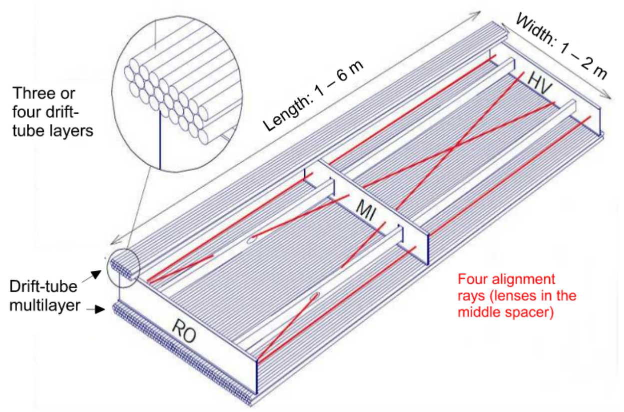

Figure 2.16: Schematic view of the mechanical structure of a MDT chamber [25].

Cathode-Strip Chambers

In the region $2.0 < |\eta| < 2.7$ *Cathode Strip Chambers* (CSC) replace MDT in the innermost muon tracking layer, due to their higher rate capability and time resolution, features needed in such critical region to cope with the high particle flux. The entire CSC system consists of two disks with eight chamber each, eight small and eight large. Each chamber contains four CSC planes, resulting in four indipendent measurements

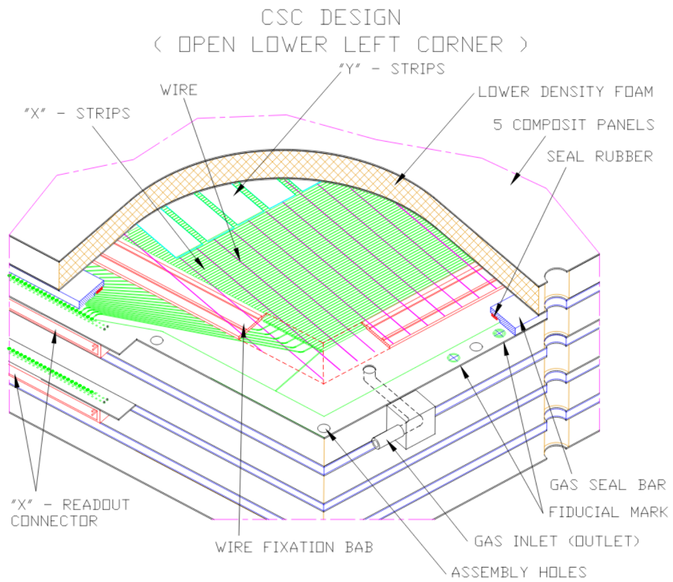

Figure 2.17: Structure of the CSC [25].

in η and ϕ for each track. CSC are multiwire proportional chambers with the wires oriented in the radial direction and an anode-cathode spacing equal to the anode wire pitch. The operating gas mixture is $Ar{:}CO_2$ (80:20); the absence of hydrogen reduces the neutron background. Both cathodes planes are segmented in strips with two different orientations: perpendicular to the wires, thus providing the precision coordinate R, and parallel to the wires, then providing the ϕ coordinate. The position of the track hits is obtained through an interpolation among the charges induced on the neighbouring cathode strips. The structure of a CSC is shown in Figure 2.17. The spatial resolution of a single chamber (4 layers combined) is $\sim 40\ \mu$m in R and ~ 5 mm in ϕ.

Resistive Plate Chamber

Resistive Plate Chambers (RPC) [25, 111] are used in the barrel region ($|\eta| < 1.06$) to trigger muons, given the time resolution $\sigma_t \leq 2$ ns which allows bunch-crossing identification and assignment. They are gaseous detectors with resistive parallel electrode-plates. The basic RPC unit is made by two Bakelite resistive plates, kept parallel to each other at a distance of 2 mm by insulating spacers to form a gap, as shown in Figure 2.18. The operating gas mixture in the gap is $C_2H_2F_4$:iC_4H_{10}:SF_6 (94.7:5:0.3).

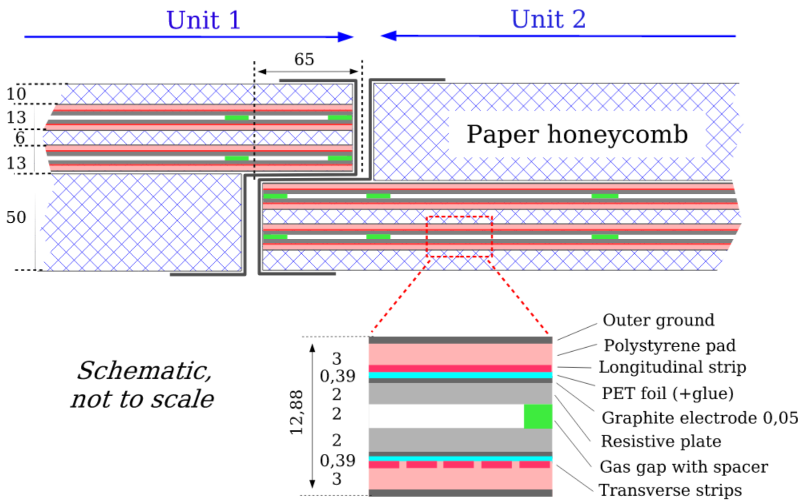

Figure 2.18: Section view of a RPC, where two units are joint to form a chamber. The sandwich structure (hashed) is made of paper honeycomb. The ϕ-strips are in the plane of the figure and the η-strips are perpendicular to it. Dimensions are given in mm [25].

When ionizing particles cross the gap, the strong electric field between the two plates allows the generation of the avalanche process, with the following drift towards the anode. The generated signal is read out via capacitive couplings to metallic strips, mounted on the outer sides of the resistive plates.
RPC also provide measurements of hits ϕ coordinate to the track reconstructing procedure, complementing the η measurement performed by MDT, since they can only measure the hit position on the z-axis. Spatial resolution is ~ 1 cm both in η- and ϕ-directions.

Thin Gap Chambers

Thin Gap Chambers [25] are multiwire proportional chambers, with the peculiarity to have the wire-to-cathode distance of 1.4 mm, smaller than the wire-to-wire distance of 1.8 mm, as shown in Figure 2.19, in order to achieve smaller drift times. The gas mixture is highly quenched, mainly composed of CO_2 and n-C_5H_{12}, with a high operating voltage of about 3 kV; these two features, together with the peculiar cell geometry, result in an operational saturated mode with very short drift times, leading to an excellent time resolution (a few ns) for the majority of tracks.

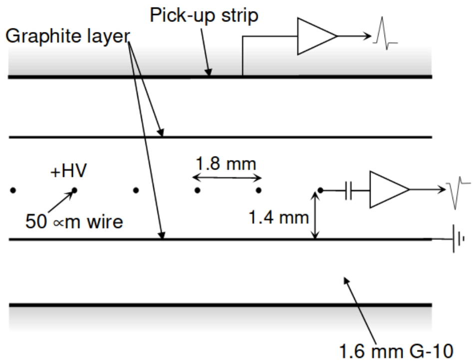

Figure 2.19: Schematic TGC structure [25].

TGC are arranged in circular disks, mounted in two concentric rings: an outer (or end-cap) one covering the pseudorapidity range $1.05 < |\eta| < 1.92$ and an inner (or forward) one for the region $1.92 < |\eta| < 2.4$.
TGC play a double role inside the end-cap MS, since they ensure muon trigger capability and determination of the second, azimuthal coordinate to complement the measurements of the precision tracking detectors in the bending plane. The middle wheel has three TGC station to complement the single layer of MDT, while only one TGC station is present in the inner layer. Spatial resolution of the TGC is of a few mm in both R- and ϕ-directions, respectively $(2 \div 6)$ and $(3 \div 7)$.

2.2.4 Trigger and Data Acquisition

The ATLAS trigger system [112] plays a key role in the experiment, given the high collision rate at the LHC. During Run I three different levels of trigger were used: *Level-1* (L1), *Level-2* (L2) and *Event-Filter* (EF). Conversely, during Run II operations the ATLAS trigger system was reduced to a hardware-based Level-1 trigger[3] paired with a software-based *High Level Trigger* (HLT) [113, 114] replacing L2 and EF, which has the task to reduce the rate from 100 kHz, output rate coming from L1, to ~ 1 kHz on average within a processing time of about 200 ms. The general scheme of the trigger system is reported in Figure 2.20.
The L1 trigger is activated by a broad range of high-momentum particles (electrons, muons, τ-leptons decaying into hadrons, photons, jets), as well as when the event shows large missing and total transverse energy. Its selection is performed by collecting information coming from a subset of detectors. High transverse momentum muons are identified by signals received from trigger chambers in the barrel and end-cap regions of the Muon Spectrometer. Calorimeter selections are based on the reduced-granularity information from all the calorimeters. Results from the L1 muon and calorimeter triggers are processed by the *Central Trigger Processor* (CPT), which implements a trigger menu containing combinations of different trigger selections. In each event, L1 defines one or more *Regions-of-Interests* (RoI) defined by the η and ϕ coordinates within the detector, regions where the selection process identified interesting features to be preserved. These kind of information also include, of course, the nature and the specific

[3]It is able to reduce the rate from 40 MHz to ~ 100 kHz, making trigger decision within an average time of 2.5 μs.

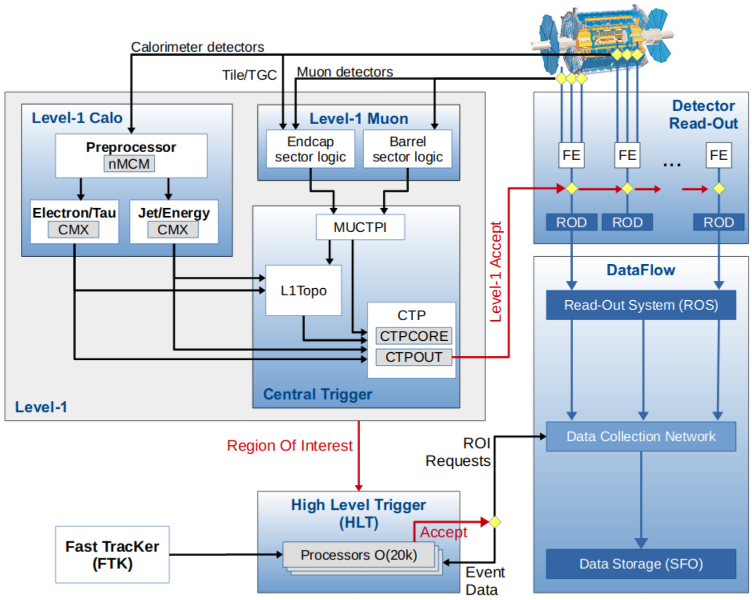

Figure 2.20: Schematic layout of the ATLAS trigger and data acquisition system in Run II [114].

criteria passed and, then, they are taken as seeds for the subsequent HLT processing. After the L1 trigger acceptance, surviving events are buffered in the *Read-Out System* (ROS) and processed by the HLT. In the HLT, events are processed considering the finer-granularity calorimeter clusters, in addition to the precision measurements coming from the Muon Spectrometer and the tracking information from the Inner Detector. Moreover, depending on the necessity, HLT reconstruction can be performed within the L1 RoI or considering the full detector.
Finally, events accepted by the HLT are transferred to local storage at the experimental site and exported to the *Tier-0* facility at CERN's computing center for offline reconstruction.

2.2.5 Forward detectors

Other minor detector systems cover the ATLAS forward region: their main purpose is to measure the luminosity delivered to ATLAS, to detect neutral particles in heavy-ion collisions and to perform beam monitoring.
LUminosity measurements Using Čerenkov Integrating Detector (LUCID) detects pp inelastic scattering in the forward region and it is the main online relative-luminosity monitor for ATLAS. *Absolute Luminosity For ATLAS* (ALFA) consists of scintillating fibre trackers designed to approach as close as 1 mm to the beam for absolute luminosity measurements. *Zero-Degree Calorimeter* (ZDC) is a fundamental system to determine the centrality of heavy-ion collisions. *Diamond Beam Monitor* (DBM), *Beam Condition Monitor* (BCM) and *Beam Loss Monitor* (BLM) are monitoring systems used to prevent serious damages to other detectors.
In the following, a short description of these detectors is reported.

LUCID

The original LUCID [25] detector used in Run I was upgraded for Run II operations [115], in order to cope with the new harsh LHC conditions. The detector consists of two identical modules, symmetrically located at a distance of ±17 m from the interaction point. Each module is installed on a carbon fiber cylindrical support tube surrounding the LHC beam pipe, at a radial distance of about 10 cm from the beam pipe, corresponding to $|\eta| \simeq 5.8$.
The active detectors consist of 16 photomultipliers and 4 optical quartz fibers: the photomultipliers are attached to the carbon fiber support, whose quartz windows act as a Čerenkov radiator, and they are placed inside the high radiation zone near the beam pipe; the optical quartz fibers also act as Čerenkov radiators, but they are read by 4 photomultipliers placed outside the high radiation region, at about 1 m from the detector.
Two different techniques can be employed by the LUCID system to measure luminosity: hit/event counting, which counts the hits produced as a result of one or several particles being inside the acceptance, after applying a threshold in amplitude to discriminate the electric signal, and particle flow, which registers the amplitude of the electric signal, proportional to the passage of one or more particles, if no threshold is applied. Independently of the approach chosen, LUCID is able to estimate the number of particles exiting the forward region due to *pp* inelastic scattering and to provide both a measurement of the integrated luminosity and the online monitoring of the beam conditions together with the instantaneous luminosity.

ALFA

The ALFA [25, 116] detector is located at a distance of ±240 m from the interaction point and it is used to measure the absolute luminosity via elastic scattering at small angles. However, this technique is efficient only for scattering angles ($\sim 3\ \mu$rad) smaller than the nominal beam divergence. Therefore, dedicated beams must be set up, with high beta and reduced emittance, to allow this kind of measurements; nevertheless, they can be also exploited for the calibration of LUCID detector. The ALFA scintillating fiber trackers are located inside Roman pots, which can be moved close to the beam down to a distance of 1 mm.

ZDC

The ATLAS ZDC [25, 117] is located at ±140 m and its primary purpose is the detection of forward neutron with $|\eta| > 8.3$ in heavy-ion collisions. It consists of two sampling calorimeters, each one composed of 4 modules: one electromagnetic and three hadronic. Tungsten plates are the absorber material and quartz rods the active medium for both calorimeters.
In addition to neutron detection, the ZDC system is used to reduce the background of beam-gas and beam-halo interactions by requiring a tight coincidence from the two detectors at the opposite sides of the interaction point.

DBM, BCM and BLM

The ATLAS [25] DBM [118], BCM [119, 120] and BLM [120] are three types of diamond detectors, symmetrically located at 0.93 m, 1.84 m and 3.45 m from the interaction point, respectively. Their main role is to protect the entire apparatus when several proton bunches hit the collimators in front of the detectors. In this situation, in addition to the accumulated radiation during normal days of operation, the huge instantaneous rate might cause severely detector damages. Therefore, this set of detectors is designed to identify this kind of events and trigger an abort in time to prevent serious damages to detectors.
BCM can also be used for luminosity determination, although it saturates when the instantaneous luminosity reaches $\sim 10^{34}$ cm^{-2}s^{-1}. Instead, thanks to its better segmentation, DBM can overcome this limitation.

2.2.6 Towards Run III and HL-LHC: the Muon Spectrometer upgrade

As already mentioned, in early 2021 the third data taking period will start with an expected instantaneous luminosity which will constantly increase with respect to Run II operations, value that will be enhanced further during HL-LHC period. This increase in the instantaneous luminosity will lead to an higher flux of particles throughout the ATLAS apparatus. The subdetectors which should be mainly affected by these new operating conditions are the ones closed to the beam pipe and the interaction point, namely the Inner Detector, the Forward Calorimeters and the innermost wheel of the Muon Spectrometer, called *Small Wheel*. For this reason, their upgrades are planned in two phases, taking place in the LHC long technical shutdowns. During the Long Shutdown II, in 2019-2020, the Small Wheel in the positive z-axis direction will be replaced by a new detector, called *New Small Wheel* (NSW) [121]; the remaining one will be replaced during Long Shutdown III.
This new detector will operate in an environment with very high particle rate (up to 15 kHz/cm^2, whereas currently installed detectors will become ineffective at hit rates of ~ 2 kHz/cm^2) and two detector technologies will be employed: *small-strip Thin Gap Chambers* (sTGC) [122, 123], primarily devoted to the Level-1 muon trigger, and *MicroMegas* (MM) [124], mainly dedicated to muon precision tracking. Nevertheless, each of the two technologies may be exploited for both tasks. Trigger information coming from the NSW will be matched with the existing TGC ones to reject muons not coming from the interaction point, then reducing muon trigger rates and allowing to run with lowered trigger thresholds. In order to reduce the muon Level-1 trigger rate to 20 kHz for muons with $p_{\mathrm{T}} > 20$ GeV, trigger track segments must be reconstructed satisfying the following quality criteria:

- angular resolution (in terms of RMS) of 1 mrad or better;
- granularity better than 0.04×0.04 in the $\eta - \phi$ plane, in order to match the one of the current muon trigger system;
- online track segment reconstruction efficiency $> 95\%$ in the full η coverage of the NSW trigger ($1.3 < |\eta| < 2.5$).

Concerning tracking, at high luminosity the performance of the new detector replacing the current one should be, at least, as good as the current detector at low luminosity is. In particular, the requests are:

- reconstruction of track segments with a position resolution in the bending plane better than 50 μm, to match the performance of the current MDT system. This will ensure that the Muon Spectrometer will have a momentum resolution better than 10% at $p_{\mathrm{T}} \sim 1$ TeV. The required resolution results in a resolution per plane better than 100 μm for a 4-layer multi-plane detector;
- segment finding efficiency better than 97% for muons with $p_{\mathrm{T}} > 10$ GeV;
- efficiency and resolution should not degrade at very high momenta or for a high background flux;
- measurement of the second coordinate with a resolution of $1-2$ mm, to match the Muon Spectrometer and the Inner Detector for the combined muon reconstruction.

The New Small Wheel

The New Small Wheel has been designed to meet all requirements previously listed. It consists of 16 detector planes arranged in two multilayers. The following baseline layout of the NSW has been defined:

- sTGC will act as primary trigger detectors and MM as primary precision tracking detectors;
- trigger acceptance in $1.3 < |\eta| < 2.5$;
- precision tracking acceptance in $1.3 < |\eta| < 2.7$;
- eight small and eight large sectors spanning the corresponding EM and EO MDT chambers sectors (see Figure 2.15(b)) in projective geometry for the precision tracking;
- planar detectors, i.e. no inclined chambers like the present CSC;
- eight layers of sTGC and eight of MM in each sector, with the following layer order in the z-direction: four layers of sTGC and four layers of MM, an optional spacer and support structure, four layers of MM and four layers of sTGC;
- 40 μm precision on the knowledge of the internal positions of the strips providing the precision coordinate;
- the re-use of the present disk shielding [125].

Concerning MM, each sector is segmented in two parts of different size, covering different regions in η. This division results in 4 subchambers (or *Modules*), as shown in Figure 2.21: two *Small Sectors Modules* (SM1 and SM2) and two *Large Sectors Modules* (LM1 and LM2). The chamber surface is ~ 2 m^2 for the Small Sectors and ~ 3 m^2 for the Large Sectors.
As previously mentioned, the MM precision tracking system is designed with eight independent layers. Muon tracks coming from the interaction point are expected to

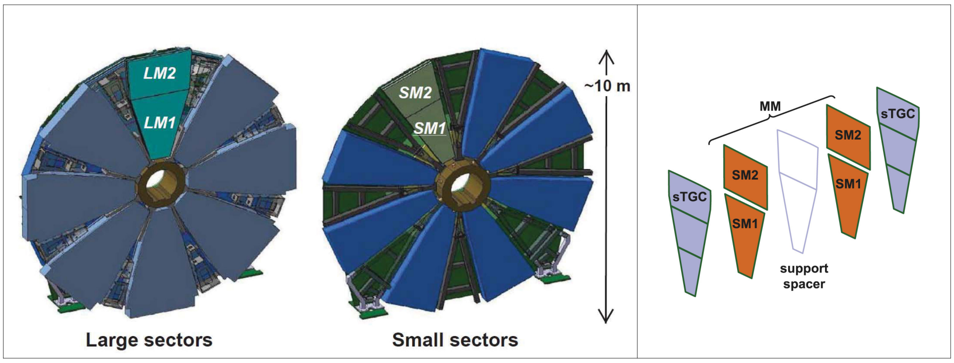

Figure 2.21: Overall view of the NSW. Left: views of the wheel, highlighting the large sectors LM1 and LM2 and the small ones SM1 and SM2. Right: exploded view of a SM1 module, with two sTGC chambers and two MM quadruplets [126].

impinge on each layer with angles in the range $\sim 0.14 \div 0.56$ rad with respect to the direction orthogonal to the layers. The two quadruplets provide eight precision points per muon track, with an overall lever arm of about 20 cm.

MicroMegas chambers: layout and construction scheme

The construction of the 32 SM1 chambers is under responsibility of the INFN sections of Cosenza, Frascati, Lecce, Napoli, Pavia, Roma Tre and Roma Sapienza.

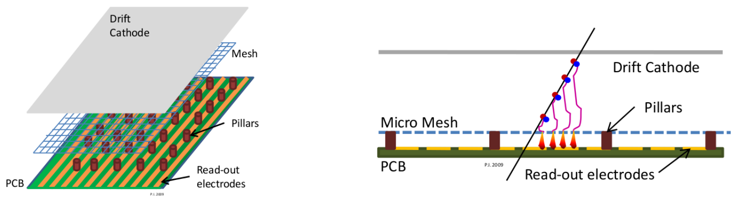

Figure 2.22: Basic layout and operating principle of a MM detector [121].

Figure 2.22 shows the structure of a single MM layer: a cathodic plane and a Printed Circuit Board (PCB) create a gap, filled with a gas mixture of Ar:CO_2 (93:7) at 3 mbar overpressure. The anode is made with copper resistive strips on a kapton layer, set on the PCB. A stainless steel stretched mesh is positioned on the top of 128 μm high insulating spacers, called pillars, which are deposited on the anode. The drift cathode, 5 mm apart from the mesh, is held at a negative High Voltage (HV), typically at -300 V, with respect to the mesh, which is grounded. The anode is held at a positive HV, typically around $500 \div 600$ V. As a result, two different electric field are in this layout: the first one in the 5 mm gas gap, called *Drift region*, corresponding to ~ 600 V/cm, and the second one in the mesh-anode gap, called *Amplification region*, corresponding to ~ 50 kV/cm.
Charged muons crossing the drift region ionize the gas and the electrons produced during the ionization process drift towards the mesh; since in the amplification region the electric field is 50-100 stronger than in the drift region, the mesh is almost transparent to the electrons, allowing more than 95% to pass. The avalanche multiplication process takes place in the amplification region and it occurs in a few nanoseconds, resulting in a fast signal pulse on the read-out strips; moreover, the small amplification gap provides

a fast evacuation of the positive ions ($\sim$ 100 ns). MM detectors work in proportional regime, but with this layout the total number of electrons in the avalanche may reach values of about 10^8 and, combining this value with the extremely thin amplification region, chambers can be particularly vulnerable to sparks which can damage both the detector and the read-out electronics. In addition, sparks can alter the chemical structure of the materials used to build the chamber, thus increasing the spark rate and the time needed to deplete the charge excess, leading to large dead times.
In order to prevent sparking, the read-out strips are protected by a thin layer of insulator, on top of which a layer of resistive strips is deposited, matching the pattern of the read-out strips. The charge produced by the avalanche process is read through capacitive couplings between the resistive and copper strips, preventing these ones to be directly exposed to the gas and to the sparks. The layout including the insulator is reported in Figure 2.23 and it makes MM a more robust detector, hence the name *resistive bulk micromegas* [127].

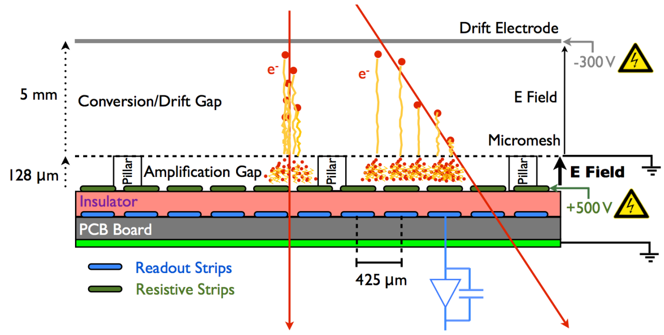

Figure 2.23: Layout of a resistive bulk micromegas, including examples of signal production and read-out [126].

The MM which will be installed on the NSW have a specific design: the read-out strips are 17 μm thick and 300 μm wide, with a strip pitch of 425 μm. On top of the copper strips a 25 μm thick layer of glue is deposited with a 50 μm kapton foil acting as insulator. The final carbon-based resistive strip layer is placed following the same geometry as the copper strip layer [128].
Each SM1 chamber is built as a quadruplet, each one being composed of five panels which give rise to four active gaps. Each panel has a trapezoidal shape 11.77 mm thick and 2210 mm high with the two extremities measuring 368 mm and 1187 mm, divided into 5 independent PCBs; the read-out panels have an extra border to host the front-end electronic boards and services, such that their dimensions extend to 500 mm and 1320 mm at the two sides (Figure 2.24(a)). As shown in Figure 2.24(b), out of five, three panels contain only cathodic planes and they are referred to as *drift panels*. In each drift panel the face directly exposed to the gas mixture is covered by a 17 μm layer of copper providing the conductivity of the cathodic plane. The remaining two panels are *read-out panels*; the strips of one of the panels are parallel to the chamber bases and the panel is called *eta panel*, since the read-out strips are orthogonal to the bending plane of the muon tracks in the toroid system. The remaining panel has its strips inclined by $\pm$26 mrad relatively to the strips of the eta panel and it is called *stereo panel*. This configuration allows for a precise determination of the η coordinate, mandatory for the measurement of the momentum, still retaining a less precise determination of the azimuthal coordinate ϕ.
Finally, in this configuration the mesh is mechanically floating (*floating mesh* tech-

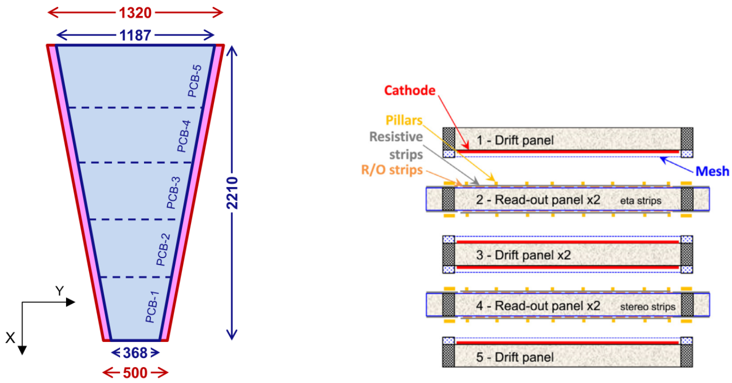

(a) A SM1 quadruplet. In blue the drift panels and in red the extensions of the read-out panels. Dimensions are in mm.

(b) A schematic view of the five panels of a MM quadruplet.

Figure 2.24: Dimensions and structure of a SM1 chamber [126].

nique [129, 130]), as it is not fixed on the read-out board, like in the bulk technology; this technique allows the detector to be re-opened again, essentially for cleaning purposes.

SM1 quadruplet validation at INFN Cosmic Ray Stand

In the MM construction team I took part in the SM1 quadruplet validation at the Cosmic Ray Stand in INFN National Laboratories of Frascati. More precisely, my work was dedicated to the adaptation and optimization of the reconstruction code used to analyze the cosmic data taken with SM1, in order to provide an estimate of quadruplet performance in terms of efficiency, dead channels and uniformity.
After joining the team, the second-produced SM1 (the so-called *Module 0.5*) chamber was available for testing. Figure 2.25(a) shows the experimental setup, also sketched in Figure 2.25(b).

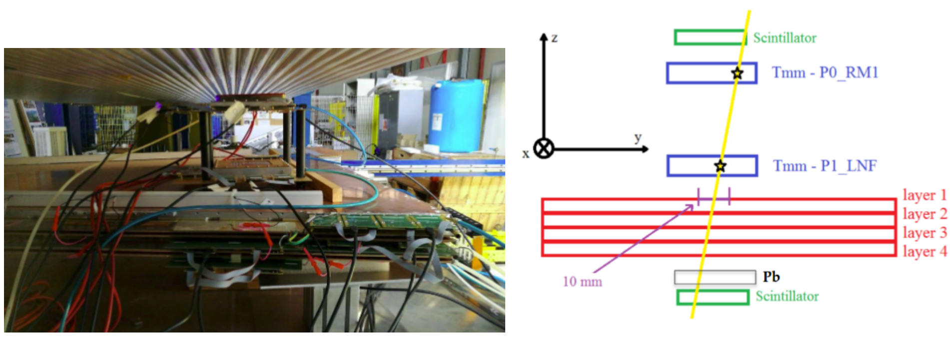

(a) Side view of the the setup

(b) Sketch of the telescope scheme.

Figure 2.25: View of the experimental setup of the Cosmic Ray Stand.

The chamber was filled with the usual Ar:CO_2 (93:7) gas mixture at atmospheric pressure with a flux rate of 20 l/h, constantly monitored by electronic mass flowmeters. Data were collected with the HV in the drift gap set at −300 V, while in the amplifi-

cation gap the HV value was 590 V. Two small dimension bulk MM chambers (Tmm[4]) with a two-dimensional coordinate read-out (X & Y) were used as a reference; for these two Tmm chambers the HV in the drift gap was set to −300 V as in the SM1 quadruplet, but in the amplification gap the HV value was fixed at 555 V. It is important to note that, in order to obtain the same gain, the operating voltage of the SM1 chamber has to be about 50 V larger than the voltage applied in bulk MM chambers, because of a larger effective size of the amplification gap.
Two plastic scintillators are placed above and below the Tmm-SM1 system, acting as a trigger, and their read-out system consisted of Silicon-PhotoMultipliers (Si-PM). A lead block was placed above the bottom scintillator in order to stop low-energy cosmic muons.
In the final NSW setup the MM read-out chain will be based on the *VMM* Application Specific Integrated Circuit (ASIC) [131] in order to fulfill the read-out requirements. Instead, on the cosmic ray stand the read-out electronics were composed of APV25 and SRS modules operating at 40 MHz, the same read-out used for all previous tests performed on smaller MM chambers. The APV25 [132] is a 128 channel chip, whose output data structure consists of the values of the charge collected in each sample, while the SRS (Scalable Readout System) [133] is a module used to interface the APV25 signal output[5]. For each event and channel, a total of 18 samples, one every 25 ns, was recorded in an acquisition time window of 450 ns.
Before starting processing raw data, the values of the charges in the single strips of the module are pedestral subtracted and corrected in order to consider known cross-talk effects between the electronic channels. The time of the signal is computed for each channel, by fitting the 18 charge samples as a function of time with a Fermi-Dirac distribution

$$Q(t) = \frac{Q_{max}}{1 + \exp\left[-(t - t_{FD})/\tau\right]} + B, \tag{2.11}$$

with four free parameters: Q_{max}, maximum charge collected by the strip, τ, slope of the raising edge of the time distribution, B, charge baseline value and t_{FD}. The half-height parameter of the function (t_{FD}) is considered as the time of the signal in the strip and used in the reconstruction. A group of nearby channels[6] with compatible times, possibly hit by the same track, and charges above a minimal threshold is identified as a *cluster*. The associated coordinate is measured as the cluster centroid, computed by weighting the position of each channel with its charge. The entire algorithm for the fitting procedure was optimized further to enhance the rejection of noisy strips without killing good signal ones; a similar optimization strategy was applied to the clusterization algorithm, taking into account charge, time and position of the strips.
The efficiency of the quadruplet was also studied. Starting from events with exactly one cluster reconstructed in both layers of the two Tmm chambers, for each layer of the SM1 module a one-dimensional interval of ±5 mm around the extrapolated position was defined. The layer was considered efficient if at least one strip with charge above a selected threshold was found within that interval; Figure 2.26 shows a preliminary efficiency for the four layers of the Module 0.5[7].

[4]The dimensions of the Tmm were 10×10 cm^2.
[5]Due to the large size of the SM1 quadruplet and the availability of APV25, only half of the PCB5 (see Figure 2.24(a)) was instrumented (an area corresponding to 512 strips), whose area was well

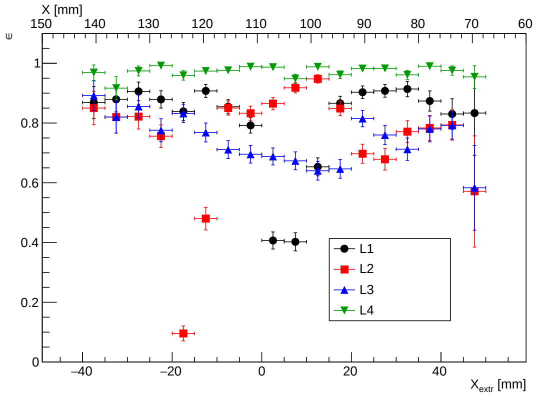

Figure 2.26: Preliminary software efficiency for each layer of the SM1 chamber.

The VMM read-out system

During my PhD I participated to a test beam which took place in the North Area of CERN SPS (see Figure 2.2), at the H8 beam line [134]. The primary purpose was to measure the performance of a SM2 quadruplet, as well as to test a VMM3 [135] board on a Tmm MM chamber (Figure 2.27).

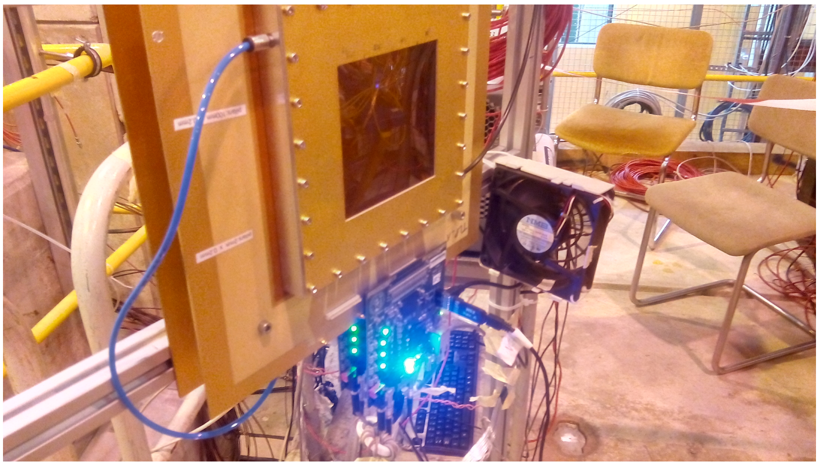

Figure 2.27: Experimental setup with VMM3 board connected to a Tmm chamber.

As already mentioned, the VMM will be used in the front-end read-out electronics of both MM and sTGC detectors of the NSW upgrade project. It consists of 64 linear front-end channels and a block diagram of one of the identical channels is shown in Figure 2.28.
A low-noise *charge amplifier* (CA) with adaptive feedback and test capacitor is integrated in each channel. The filter (*shaper*) is a third-order designed in delayed dissipative feedback [136] with adjustable configurations. Next to the shapers are the discriminators [131] with *Neighbour Enabling Logic* and individual threshold trimming,

covered by the Tmm chambers telescope.

[6] An APV25 channel was connected to each strip of the read-out panels, thus creating a one-to-one connection, although other different connection patterns have been tested.

[7] After the end of qualification task, a new cleaning and assembly protocol was established by the NSW Collaboration, allowing to obtain efficiency in agreement with the ATLAS requirements.

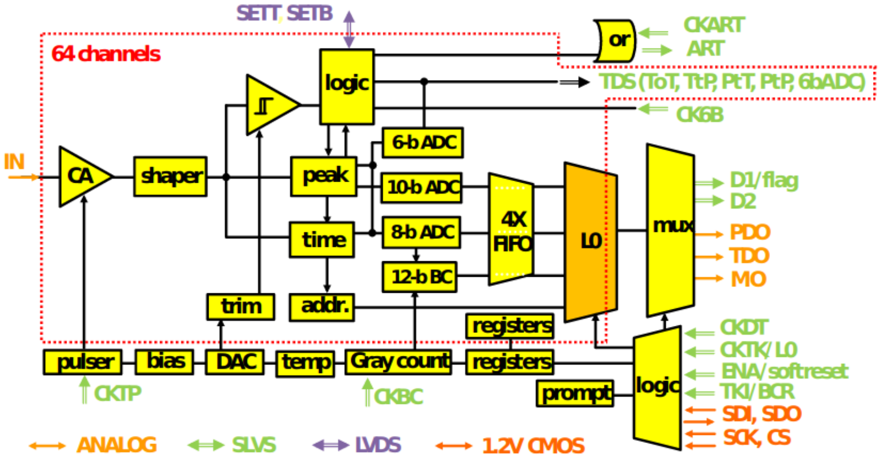

Figure 2.28: Architecture of the VMM3 [135].

the *Peak Detector* and the *Time Detector*. The neighbour channel logic forces the measurements from a channel neighbouring a triggered one, even if these channels did not exceed a specific set threshold, preventing possible losses of signals; the peak detector measures the timing using a *Time-to-Amplitude Converter* (TAC)[8], i.e. a voltage ramp that starts either at threshold crossing or at the time of the peak and it stops at a cycle of the external Bunch Crossing clock (CKBC)[9]. Finally, the VMM integrates analogue monitor capability to directly measure and control the global *Digital to Analogue Converters* (DAC) and every part of the board logic.
The ASIC can be read-out, mainly, in three different modes, although other ones are available but they are dedicated to trigger tasks. The main read-out mode used during the test beam was the so-called *Continuous mode* and it is shown in Figure 2.29.

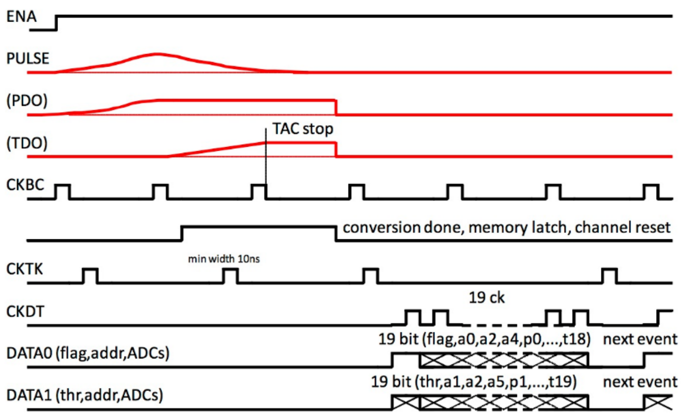

Figure 2.29: Data read-out of the VMM3 with DACs in the continuous mode [135].

In the continuous mode, there is a simultaneous read/write of data which is able to handle rates up to the maximum of 4 MHz per channel. Once the enable logic is activated, the peak and time detector outputs (PDO and TDO) convert the voltages into currents, routed to a 10-bit and 8-bit ADC, respectively; this second ADC provides

[8] Differently from APV25, VMM provides a time measurement within the ASIC.
[9] The total number of cycles, as well as the amplitude, can be chosen according to the needs of the measurement; a typical value is 40 MHz.

the conversion of the time measured using the TAC from to the time of the peak (or a set threshold) until an external stop signal (CKBC) is registered. The bunch crossing counter value at the TAC stop time is latched into a local 12-bit memory, thus providing a total of 20-bit deep time-stamp with a nanosecond resolution. Finally, the event enters a chain of FIFO chains to be sequentially multiplexed to the two digital output. During the test beam I learned a new read-out technology operating principles, being able to contribute in data taking operations and to monitor, at the same time, the acquisition process through an existing and dedicated graphical interface.

Chapter 3

Event reconstruction

After each bunch crossing, all particles originated in the interactions cross the various subdetectors in ATLAS and they produce several electric signals, which are acquired and processed by complex algorithms in order to identify and classify the originating particles, to determine their properties and, finally, to perform the full event reconstruction. This chapter is dedicated to the description of the procedures used in the experiment in order to define the fundamental "physical objects", i.e. electrons, muons, jets and missing transverse energy, which characterize the events studied in physics analyses and, more specifically, in the analysis described in this thesis.
The physical objects described in this Chapter are the ones provided by the recostruction of the event (*offline selection*), which can be different from the ones measured by HLT before accepting and storing the event (*online selection*), the latter being determined with a more limited set of information due to the reduced time to perform the decision.

3.1 Track and vertex reconstructions

The instantaneous luminosity reached during Run II resulted in a high abundance of events with high track occupancy. Starting from the end of Run I, the ATLAS track reconstruction software has been continuously evolving in order to cope with these harsh conditions. Particle tracking is one of the first task to be performed in the event reconstruction and it is used for electrons, muons, hadronic jet identification and missing transverse momentum measurement. It is performed in three main steps [137], described below.

3.1.1 Track finding (seeding)

The first step in the track reconstruction chain is the definition of the initial list of track candidates. Track *seeds* are defined as sets of three *space-points*, i.e. three-dimensional coordinates of hits, measured in the Pixel Detector and SCT, which are assembled into clusters. Drift times measured in the TRT are translated into calibrated drift circles by exploiting appropriate time-to-distance relations. Track *seeds* are built starting from the space-points passing specific cuts on p_{T} and on the impact parameter; finally, once the seeds are given, track candidates are selected by applying a pattern recognition algorithm based on the Kalman filtering procedure [138], which assumes the electron hypothesis to allow energy loss at each material surface, accounting for possible bremsstrahlung.

3.1.2 Ambiguity solving

In general, there is no unique and direct correspondence between a seed and a track; more often, multiple tracks are produced from a given seed, thus requiring an additional step to solve this ambiguity. The produced tracks are scored according to a number of parameters associated to the track quality (e.g. the number of disconnected track segments, the track χ^2 from the fit and $\log p_{\mathrm{T}}$). With the calculated score, the ambiguity is solved thanks to an Artificial Neural Network (ANN).

3.1.3 Track fitting

After solving the ambiguities, tracks are fitted for the final measurement of their parameters. The track fit procedure takes into account the multiple scattering and the energy losses in the various detector elements crossed by the track. After performing the vertex reconstruction, discussed in the following paragraph, the track parameters are computed again, including the vertex information as constraint for the fit.

3.1.4 Vertex reconstruction

A correct track reconstruction is a key element for the precise determination of the primary vertex [139], defined as the point where proton-proton interactions occurred. Moreover, the correct assignment of a generic charged particle track to the corresponding source vertex is fundamental in order to reconstruct the full kinematic properties of the hard-scattering interaction. The primary vertex reconstruction uses a subset of all the reconstructed tracks, selected with tight requirements to reduce contamination from fake tracks. The following steps are used for the determination of track vertices, once a set of tracks satisfying the selection and quality criteria is defined:

- a seed position for the first vertex is defined. The transverse position of the first seed is taken as the center of the beam spot. The z-coordinate of the seed is the mode of the z-coordinates of tracks at their respective points of closest approach to the reconstructed center of the beam spot;

- tracks and seed are used to fit the best vertex position. The fit is an iterative procedure and, in each iteration, the less compatible tracks are down-weighted and the vertex position is recomputed;

- after the vertex position is determined, all the incompatible tracks are removed from it and they are allowed to be used in the determination of another vertex. Vertices are required to have at least two associated tracks;

- the procedure is repeated until all of the tracks are associated to a vertex in the event or no additional vertex can be found in the remaining set of tracks.

3.2 Electrons and photons

Electrons and positrons, collectively referred to as electrons [140] in the ATLAS nomenclature, give rise to tracks in the Inner Detector and to energy deposits in the Electromagnetic Calorimeter (clusters); thus, electron identification and reconstruction must be based on signals coming from both these detectors. Several sets of identification criteria, with different levels of discrimination power, are applied on electron candidates in order to select the appropriate quality requested by the specific analysis, e.g. to reject non-prompt electrons originating mainly from photon conversions and heavy/light flavour hadron decays.
Photons are not considered in the analysis described in this thesis, however some details about their reconstruction and identification will be provided for completeness, since their signature is similar to the electron one and their reconstruction is performed in parallel with electrons.
In replacement of the sliding-window algorithm previously exploited in ATLAS for the reconstruction of fixed-size clusters of calorimeter cells [141–143], in 2017 the offline electron and photon reconstruction has been improved to use dynamic, variable-size clusters, called *superclusters*. This technique is employed for measurements and searches exploiting the complete LHC Run II dataset. While fixed-size clusters naturally provide a linear energy response and good stability as a function of pile-up, dynamic clusters change in size as needed to recover energy from bremsstrahlung photons or from electrons from photon conversions. The calibration techniques [144] exploit the advantage of this dynamic clustering algorithm, while achieving similar linearity and stability as for fixed-size clusters.
An electron is defined as an object consisting of a cluster built from energy deposits in the calorimeter (supercluster) and a matched track (or tracks). A converted photon is a cluster matched to a conversion vertex (or vertices), while an unconverted photon is a cluster not matched to an electron track or to a conversion vertex.
The reconstruction of electrons and photons with $|\eta| < 2.5$ proceeds through the steps shown in Figure 3.1.
In the first step the algorithm prepares the tracks and clusters which will be used: it selects clusters of energy deposits measured in topologically connected (topo-clusters) EM and Hadronic Calorimeter cells [145]; then, these clusters are matched to ID tracks, which are refitted accounting for bremsstrahlung. The algorithm also builds conversion vertices and matches them to the selected topo-clusters. Then, the electron and photon supercluster-building steps are performed separately using the matched clusters as input. After applying initial position corrections and energy calibrations to the resulting superclusters, the supercluster-building algorithm matches tracks to the electron superclusters and conversion vertices to the photon superclusters. The electron and photon objects to be used for analyses are then built, their energies are calibrated and discriminating variables used to separate electrons or photons from background are added. The single steps are described in more detail in the following paragraphs.

3.2.1 Topo-cluster reconstruction

The topo-cluster reconstruction algorithm [143, 145] begins by forming proto-cluster in the EM and Hadronic Calorimeters using a set of noise thresholds in which the cell

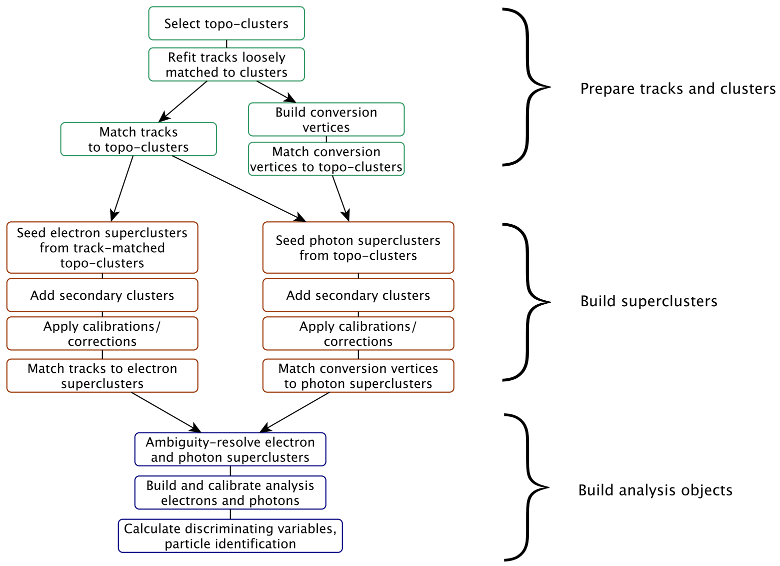

Figure 3.1: Algorithm flow diagram for the electron and photon reconstruction [140].

initiating the cluster is required to have significance $|\varsigma_{\text{cell}}^{\text{EM}}| \geq 4$, where

$$\varsigma_{\text{cell}}^{\text{EM}} = \frac{E_{\text{cell}}^{\text{EM}}}{\sigma_{\text{noise,cell}}^{\text{EM}}}. \tag{3.1}$$

$\varsigma_{\text{cell}}^{\text{EM}}$ is the cell energy at the basic signal scale, accounting correctly for the energy deposited in the calorimeter by electromagnetic showers and $\sigma_{\text{noise,cell}}^{\text{EM}}$ is the expected noise cell, which includes the known electronic noise and an estimate of the pile-up noise corresponding to the average instantaneous luminosity expected for Run II. The proto-clusters, then, collect neighbouring cells with significance $|\varsigma_{\text{cell}}^{\text{EM}}| \geq 2$. Each neighbour cell passing this threshold becomes a seed cell in the next iteration, collecting each of its neighbours in the enlarging proto-cluster. If two proto-clusters contain the same cell with $|\varsigma_{\text{cell}}^{\text{EM}}| \geq 2$ above the noise threshold, then these proto-clusters are merged. A crown of nearest-neighbour cells is added to the cluster independently on their energy. Electron and photon reconstruction starts from the topo-clusters, but only uses the energy from cells in the EM Calorimeter[1].

3.2.2 Track reconstruction, track-cluster matching and photon conversion reconstruction

Electron tracks in the Inner Detector are mainly reconstructed according to the general procedure described in Section 3.1. The standard ATLAS pattern recognition [146] uses the pion hypothesis for energy loss due to interactions with the detector material, complemented with another algorithm which uses the electron hypothesis allowing for up to 30% energy loss at each intersection of the track with the detector material due to possible bremsstrahlung effects. Then, track candidates are fitted using the pion or

[1]This procedure is not applied in the transition region of $1.37 < |\eta| < 1.63$, where the energy measured in the presampler and the scintillator between the calorimeter cryostats is also added.

electron hypothesis, in agreeement with the one used in the previous pattern recognition step, using the ATLAS Global χ^2 Track Fitter [147], allowing for additional energy loss when the standard track fit fails. This procedure has minimal interference with the main track reconstruction, while, at the same time, it improves the performance for electrons. If a track has no associated hits in the silicon detector, it is discarded from the procedure in order to reject photon conversions, while tracks with at least four silicon hits loosely matched to fixed-size clusters, are refitted using a *Gaussian Sum Filter* (GSF) [148] algorithm, a non-linear generalization of the Kalman filter, for improved track parameter estimation.
The loosely matched, refitted tracks are then matched to the EM topo-clusters described above. A track is considered matched if, with either momentum magnitude, $|\Delta\eta| < 0.05$ and $-0.10 < q \cdot (\phi_{\text{track}} - \phi_{\text{clus}}) < 0.05$, where q refers to the reconstructed charge of the track. The asymmetric requirement is because tracks sometimes miss some energy from radiated photons that clusters measure.
If multiple tracks are matched to a cluster, they are ranked with several criteria and the highest-ranked track is used to define the reconstructed electron properties.

For photon candidates, it is expected to observe a cluster in the calorimeter without any associated track, in case of no photon conversion, or with two tracks, in case of the photon converts in a $e^{\pm}e^{\mp}$ pair. Both tracks with silicon hits (Si tracks) and tracks reconstructed only in the TRT (TRT tracks) are used for the conversion reconstruction. Two-track conversion vertices are reconstructed from two opposite-charge tracks forming a vertex consistent with that one of a massless particle.
Changes were made with respect to the previous reconstruction software [142], mainly to improve the reconstruction efficiency of double-track Si conversions (conversions reconstructed with two Si tracks).
The conversion vertices are then matched to the EM topo-clusters. If there are multiple conversion vertices matched to a cluster, double-track conversions with two silicon tracks are preferred.

3.2.3 Supercluster reconstruction

The reconstruction of electron and photon superclusters proceeds independently, each one in two stages: in the first stage, EM topo-clusters are tested for use as seed cluster candidates, which form the basis of superclusters; in the second stage, EM topo-clusters near the seed candidates are identified as satellite cluster candidates, which may emerge from bremsstrahlung radiation or topo-cluster splitting. Satellite clusters are added to the seed candidates to form the final superclusters if they satisfy the necessary selection criteria.
In order to build superclusters, the initial list of EM topo-clusters is sorted according to descending E_{T}. The clusters are tested one by one in the sort order for a possible use as seed clusters. To become an electron supercluster seed, a cluster is required to have a minimum E_{T} of 1 GeV and to be matched to a track with at least four hits in the silicon tracking detectors. For photon reconstruction, a cluster must have E_{T} larger than 1.5 GeV to qualify as a supercluster seed, with no requirement made on any track or conversion vertex matching. A cluster cannot be used as a seed cluster if it has already been added as a satellite cluster to another seed cluster.
If a cluster meets the seed cluster requirements, the algorithm attempts to find satellite clusters, using the process summarized in Figure 3.2.
For both electrons and photons, a cluster is considered a satellite if it falls within a

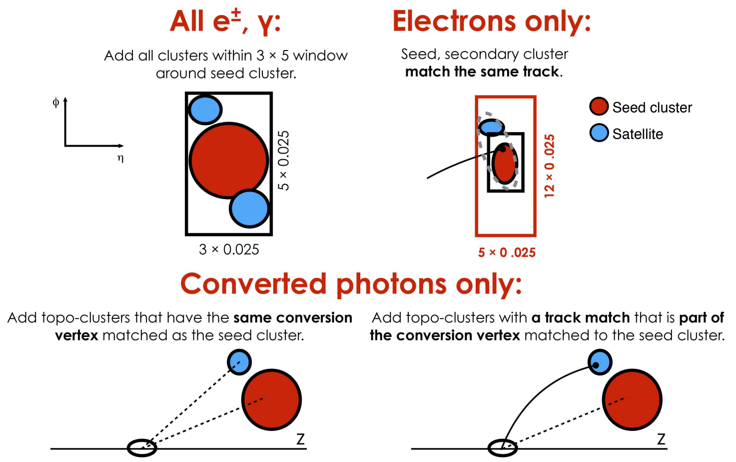

Figure 3.2: Diagram of the superclustering algorithm for electrons and photons. Seed clusters are shown in red, satellite clusters in blue [140].

window of $\Delta\eta \times \Delta\phi = 0.075 \times 0.125$ around the seed cluster barycentre, as these cases tend to represent secondary EM showers originating from the same initial electron or photon. For electrons, a cluster is also considered a satellite one if it is within a window of $\Delta\eta \times \Delta\phi = 0.125 \times 0.300$ around the seed cluster barycentre and its best-matched track is also the best-matched track for the seed cluster. For photons with conversion vertices made up only of tracks containing silicon hits, a cluster is added as a satellite one if its best-matched (electron) track belongs to the conversion vertex matched to the seed cluster. These steps rely on tracking information to discriminate distant radiative photons or conversion electrons from pile-up noise or other unrelated clusters.
The seed clusters with their associated satellite clusters are called superclusters.

Electron and photon candidates reconstruction

After the electron and photon superclusters are built, an initial energy calibration and position correction [140] is applied to them and tracks are matched to electron superclusters, while conversion vertices to photon superclusters. The matching is performed in the same way that the matching to EM topo-clusters, but using the superclusters instead. Because electron and photon superclusters are built independently, a given seed cluster can produce both an electron and a photon. In such cases, a discriminating procedure is applied. The purpose is that if a particular object can be easily identified only as a photon (a cluster with no good track attached) or only as an electron (a cluster with a good track attached and no good photon conversion vertex), then only a photon or an electron object is created for analyses; otherwise, both an electron and a photon object are created and these cases are marked as ambiguous, allowing the final classification of these objects to be determined taking into account the specific requirements of each analysis.
After another step of calibration depending on matched tracks and conversion vertices, shower shape parameters and other discriminating variables are obtained for electron and photon identification. The complete list is shown in Figure 3.3.

Category	Description	Name	Usage
Hadronic leakage	Ratio of E_T in the first layer of the hadronic calorimeter to E_T of the EM cluster (used over the ranges $\|\eta\| < 0.8$ and $\|\eta\| > 1.37$)	R_{had_1}	e/γ
	Ratio of E_T in the hadronic calorimeter to E_T of the EM cluster (used over the range $0.8 < \|\eta\| < 1.37$)	R_{had}	e/γ
EM third layer	Ratio of the energy in the third layer to the total energy in the EM calorimeter	f_3	e
EM second layer	Ratio of the sum of the energies of the cells contained in a 3×7 $\eta \times \phi$ rectangle (measured in cell units) to the sum of the cell energies in a 7×7 rectangle, both centred around the most energetic cell	R_η	e/γ
	Lateral shower width, $\sqrt{(\Sigma E_i \eta_i^2)/(\Sigma E_i) - ((\Sigma E_i \eta_i)/(\Sigma E_i))^2}$, where E_i is the energy and η_i is the pseudorapidity of cell i and the sum is calculated within a window of 3×5 cells	w_{η_2}	e/γ
	Ratio of the sum of the energies of the cells contained in a 3×3 $\eta \times \phi$ rectangle (measured in cell units) to the sum of the cell energies in a 3×7 rectangle, both centred around the most energetic cell	R_ϕ	e/γ
EM first layer	Total lateral shower width, $\sqrt{(\Sigma E_i (i - i_{\max})^2)/(\Sigma E_i)}$, where i runs over all cells in a window of $\Delta\eta \approx 0.0625$ and $i_{\max}$ is the index of the highest-energy cell	$w_{s\,\text{tot}}$	e/γ
	Lateral shower width, $\sqrt{(\Sigma E_i (i - i_{\max})^2)/(\Sigma E_i)}$, where i runs over all cells in a window of 3 cells around the highest-energy cell	$w_{s\,3}$	γ
	Energy fraction outside core of three central cells, within seven cells	f_{side}	γ
	Difference between the energy of the cell associated with the second maximum, and the energy reconstructed in the cell with the smallest value found between the first and second maxima	ΔE_s	γ
	Ratio of the energy difference between the maximum energy deposit and the energy deposit in a secondary maximum in the cluster to the sum of these energies	E_{ratio}	e/γ
	Ratio of the energy measured in the first layer of the electromagnetic calorimeter to the total energy of the EM cluster	f_1	e/γ
Track conditions	Number of hits in the innermost pixel layer	$n_{\text{innermost}}$	e
	Number of hits in the pixel detector	n_{Pixel}	e
	Total number of hits in the pixel and SCT detectors	n_{Si}	e
	Transverse impact parameter relative to the beam-line	d_0	e
	Significance of transverse impact parameter defined as the ratio of d_0 to its uncertainty	$\|d_0/\sigma(d_0)\|$	e
	Momentum lost by the track between the perigee and the last measurement point divided by the momentum at perigee	$\Delta p/p$	e
	Likelihood probability based on transition radiation in the TRT	eProbabilityHT	e
Track–cluster matching	$\Delta\eta$ between the cluster position in the first layer of the EM calorimeter and the extrapolated track	$\Delta\eta_1$	e
	$\Delta\phi$ between the cluster position in the second layer of the EM calorimeter and the momentum-rescaled track, extrapolated from the perigee, times the charge q	$\Delta\phi_{\text{res}}$	e
	Ratio of the cluster energy to the measured track momentum	E/p	e

Figure 3.3: Discriminating variables used for electron and photon identification [140].

3.2.4 Electron identification

Further quality criteria, called "identification selections" below, are used to improve the purity of selected electron and photon objects. The identification of prompt electrons relies on a *LikeliHood-based* (LH) discriminant constructed from quantities measured in the Inner Detector, the calorimeter and the combined Inner Detector and calorimeter.

The quantities used in the electron identification are chosen according to their ability to discriminate prompt isolated electrons from energy deposits coming from hadronic jets, from converted photons and from genuine electrons produced in the decays of

heavy-flavour hadrons. The variables can be grouped into properties of the primary electron track, the lateral and longitudinal development of the electromagnetic shower in the EM Calorimeter, and the spatial compatibility of the primary electron track with the reconstructed cluster.
Three level of identifications, or *Working Points* (WP), are typically provided for electron identification: with respect to the background rejection, they are referred to as *Loose*, *Medium* and *Tight*. These three working points are built using the same set of variables to define the LH discriminant, but a different selection is applied, such that the electrons classified as Tight are a subset of the ones selected as Medium, in turn being a subset of the Loose ones.
The performance of the LH identification algorithms are reported in Figure 3.4, as a function of E_{T} and $|\eta|$ using data recorded by the ATLAS experiment during 2015, 2016 and 2017. For typical electroweak processes they are, on average, 93%, 88% and

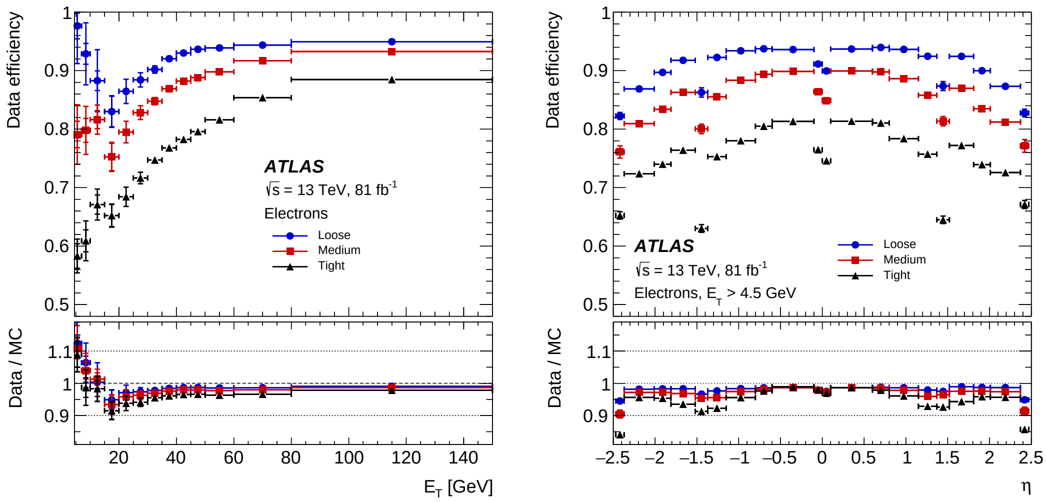

(a) (b)

Figure 3.4: Measured LH electron-identification efficiencies in $Z \to ee$ events for the Loose, Medium, and Tight operating points as a function of E_{T} (3.4(a)) and η (3.4(b)) using 81 fb^{-1} of data recorded $\sqrt{s} = 13$ TeV. For both plots, the bottom panel shows the data-to-simulation (Monte Carlo, MC) ratios [140]. The efficiencies in MC are obtained by applying data-to-simulation efficiency ratios that are measured in $J/\psi \to ee$ and $Z \to ee$ events to the $Z \to ee$ simulation. The uncertainties are statistical and (in the bottom panel) statistical and systematic uncertainties in the data-to-simulation efficiency ratio added in quadrature.

80% for the Loose, Medium and Tight operating points and gradually they increase from low to high E_{T}.

3.2.5 Photon identification

The photon identification criteria are designed to efficiently select prompt, isolated photons and reject backgrounds from hadronic jets. The photon identification is performed using the shower shape variables described in table shown in Figure 3.3. The variables using the first layer of the EM Calorimeter play a particularly important role in rejecting π^0 decays into two highly collimated photons. As for electrons, three levels

of identification are available: the primary identification selection is labelled as *Tight*, with less restrictive selections called *Medium* and *Loose*, which are used for trigger algorithms. Because the reconstruction of photons in the ATLAS trigger system does not differentiate between converted and unconverted photons, the Loose and Medium identification criteria are the same for converted and unconverted photons.
To assess the performance (in terms of E_{T} dependency) of the Tight photon identification on data, three photon efficiency measurements are performed using distinct data samples. The first uses an inclusive-photon production data selection, the second uses photons radiated from leptons in $Z \to \ell\ell\gamma$ decays and the third uses electrons from $Z \to ee$ decays, with a method transforming the electron shower shapes to resemble the photon shower shapes [142]. Obtained efficiencies are larger than 80% for $E_{\mathrm{T}} > 30$ GeV.

3.2.6 Electron and photon isolation

To enhance the discrimination between signal and background, most analyses require electrons to fulfill isolation requirements, in addition to the quality selections discussed above. The activity near leptons and photons can be quantified from the tracks of nearby charged particles or from energy deposits in the calorimeters, leading to the following two classes of isolation variables for this purpose.

- Calorimetric isolation: the energy isolation variable $E_{\mathrm{T}}^{\mathrm{cone}}$, built by summing the transverse energy of topological clusters whose barycentre falls within a cone centred around the electron or photon cluster barycentre, with some dedicated corrections accounting for the energy deposit of the candidate particle and pile-up effects. A cone size $\Delta R = \sqrt{\Delta\eta^2 + \Delta\phi^2} = 0.2$ is used for the electron working points whereas cone sizes $\Delta R = 0.2$ and 0.4 are used for photon working points.

- Track isolation: the track isolation variable $p_{\mathrm{T}}^{\mathrm{cone}}$, computed by summing the transverse momentum of selected tracks within a cone centred around the electron track or the photon cluster direction. Tracks matched to the electron or converted photon are excluded. Since for electrons produced in the decay of high-momentum heavy particles, other decay products can be very close to the electron direction, the track isolation for electrons is defined with a variable cone size ($p_{\mathrm{T}}^{\mathrm{varcone}}$), the cone shrinking for larger transverse momentum of the electron:

$$\Delta R = \min\left(\frac{10}{p_{\mathrm{T}}[\mathrm{GeV}]}, \Delta R_{\mathrm{max}}\right)$$

  where ΔR_{max} is the maximum cone size (typically 0.2).

The implementation of the isolation criteria is specific to the physics analysis needs, as it results from a compromise between a highly-efficient identification of prompt electrons, isolated or produced in a busy environment, and a good rejection of electrons from heavy-flavour decays or light hadrons misidentified as electrons. A variety of selection requirements is applied on the quantities $E_{\mathrm{T}}^{\mathrm{cone0.2}}/p_{\mathrm{T}}$ and $p_{\mathrm{T}}^{\mathrm{varcone0.2}}/p_{\mathrm{T}}$ for electrons. Table 3.1 reports the definition of the various working points: they can be defined in two different ways, targeting a fixed value of efficiency ϵ (*Gradient*) or with fixed cuts (FC) on the calorimeter and/or track isolation variables (*HighPtCaloOnly*, *Loose*, *Tight*).

Working point	Calorimeter Isolation	Track Isolation
Gradient	$\epsilon = 0.1143 \times p_{\mathrm{T}} + 92.14\%$	$\epsilon = 0.1143 \times p_{\mathrm{T}} + 92.14\%$
HighPtCaloOnly	$E_{\mathrm{T}}^{\mathrm{cone20}} < \max(0.015 \times p_{\mathrm{T}}, 3.5\ \mathrm{GeV})$	–
Loose	$E_{\mathrm{T}}^{\mathrm{cone20}}/p_{\mathrm{T}} < 0.20$	$p_{\mathrm{T}}^{\mathrm{varcone0.2}}/p_{\mathrm{T}} < 0.15$
Tight	$E_{\mathrm{T}}^{\mathrm{cone20}}/p_{\mathrm{T}} < 0.06$	$p_{\mathrm{T}}^{\mathrm{varcone0.2}}/p_{\mathrm{T}} < 0.06$

Table 3.1: Definition of the electron isolation working points. In the Gradient working point definition, the unit of p_{T} is GeV [140].

Analogously, three photon isolation operating points are defined using requirements on the calorimeter and track isolation variables, as summarized in Table 3.2.

Working point	Calorimeter Isolation	Track Isolation
Loose	$E_{\mathrm{T}}^{\mathrm{cone20}} < 0.065 \times E_{\mathrm{T}}$	$p_{\mathrm{T}}^{\mathrm{cone0.2}}/E_{\mathrm{T}} < 0.05$
Tight	$E_{\mathrm{T}}^{\mathrm{cone40}} < 0.022 \times E_{\mathrm{T}} + 2.45\ \mathrm{GeV}$	$p_{\mathrm{T}}^{\mathrm{cone0.2}}/E_{\mathrm{T}} < 0.05$
TightCaloOnly	$E_{\mathrm{T}}^{\mathrm{cone40}} < 0.022 \times E_{\mathrm{T}} + 2.45\ \mathrm{GeV}$	–

Table 3.2: Definition of the photon isolation working points [140].

3.3 Muons

Muons are precisely identified and reconstructed using the Muon Spectrometer and the Inner Detector, although the information coming from various subdetectors, calorimeters included, is also used [149, 150] in the final track reconstruction; in MS and ID tracking proceeds independently. Like any other charged particle, the muon track in the ID is reconstructed using the procedure described in Section 3.1.
In the Muon Spectrometer the first step is the search for hit patterns inside the MDT to form segments. Muon track candidates are then built by combining hits from segments in different layers. The algorithm performs a segment-seeded combinatorial search, with seeds being the segments generated in the middle layers of the detector, where more trigger hits are available. The search for segments is then extended to the outer and inner layers. The segment selection criteria are based on hit multiplicity and fit quality, while the segment matching is performed using their relative position and angles. At least two matching segments are required to build a track, the only exception being in the barrel-end-cap transition region, where a single high quality segment in η and ϕ can be used to build a track. The hits associated with each track candidate are fitted using a global χ^2 fit and the track candidate is accepted if the resulting χ^2 fulfills the selection criteria. Hits providing a large contribution to the χ^2 are removed and the track fit is repeated once again. A hit recovery procedure is performed looking for additional hits consistent with the candidate trajectory and, if found, the track candidate is refitted.
After the reconstruction in the MS, the combination of the muon information collected in the other subdetectors is performed, leading to the definition of four different types of muons, described below.

- Combined (CB): two independent track reconstructions are performed in the Inner Detector and Muon Spectrometer, building a combined track which uses hits from the two subdetectors with a global refit. The majority of muon candidates are CB muons, representing the best category in terms of hit purity and momentum resolution. Tracking is performed following an *outside-in* strategy, meaning that muons are firstly reconstructed in the MS, and then extrapolated inward to match an ID track. The *inside-out* reconstruction is used as a complementary strategy.

- Standalone (SA): the track is reconstructed in the MS only; the parameters at the interaction point are obtained after an extrapolation back to the point of closest approach to the beam axis, taking into account the expected energy loss and multiple scattering in the calorimeters. The purpose of this category is to extend the muon acceptance to the region defined by $2.5 < |\eta| < 2.7$, which is not covered by the ID.

- Segment-Tagged (ST): a track is identified and classified as muon in the ID if, once extrapolating it outward to the MS, it is associated to at least one local track segment in the precision tracking chambers. The aim of this category is to help in recovering those muons which crossed only one layer in the MS chambers, because of their low momentum or the reduced acceptance of a particular MS region.

- Calorimeter-Tagged (CT): using an approach similar to the ST category, a track in the ID is identified and classified as muon if it can be matched to an energy deposit in the calorimeter, this one being compatible with a minimum ionizing particle. This category has the lowest hit purity among the four, but it is used to recover the acceptance in the not-instrumented regions of the MS. The CT identification is optimized in the ranges $|\eta| < 0.1$ and $15 < p_{\mathrm{T}} < 100$ GeV.

When two muon categories share the same ID track, the preference to assign this track is given to CB muons, then to ST muons and, finally, to CT muons. The overlap with SA muons in the muon system itself is resolved through the analysis of the track hit content, giving preference to the track with better fit quality and larger number of hits.

3.3.1 Muon identification

As for electrons, muon identification is performed in order to select signal-like muons and suppress the background, mainly coming from pion and kaon decays, by applying track quality requirements. Several variables provide a good discrimination power in distinguishing prompt muons from background and they have been studied in simulated $t\bar{t}$ events. For CB tracks, the following three variables are used for prompt muon identification.

- q/p significance: it is defined as the absolute value of the difference between the ratio of the charge and momentum of muons measured in the ID and in the MS, divided by the sum in quadrature of the corresponding uncertainties.

- ρ': it is defined as the absolute value of the difference between the transverse momentum measurements in the ID and MS, respectively, divided by the p_{T} of the combined track.

- χ^2: the normalized value of the combined track fit.

Four different muon identification categories (or Working Points) are provided to address the specific needs of physics analyses: *Loose*, *Medium*, *Tight* and *High-*p_T. The first three categories are the main ones and they are inclusive, i.e. the muons identified with tighter requirements are also included in the categories with looser ones. A brief description of each category is provided below.

- Loose: it is designed to maximize the reconstruction efficiency while providing good-quality muon tracks. This working point was originally and specifically optimized for the reconstruction of muons coming from $H \to 4l$ decay channel. CT and ST muons are restricted to the $|\eta| < 0.1$ region.

- Medium: it is the default muon working point in ATLAS physics analyses, as it minimizes the systematic uncertainties assigned to the muon reconstruction and calibration. Only CB and SA muon tracks are used. In case of CB muons, a loose selection on the compatibility between the ID and MS momentum measurements is applied, in order to suppress the contamination of muons coming from in-flight charged hadron decays. The requested significance is $q/p < 7$.

- Tight: it is designed to maximize the purity of the selected muons, sacrifying the efficiency. Only CB muons satisfying the Medium requirements are considered, with the additional request of hits in at least two stations of the MS. A two-dimensional cut is performed on the ρ' and q/p significance variables as a function of the muon p_{T} and $|\eta|$ in order to reject background muons with p_{T} lower than 20 GeV.

- High-p_{T}: it is optimized to maximize the momentum resolution for tracks with $p_{\mathrm{T}} > 100$ GeV. Some regions in the MS are vetoed due to the not optimal alignment and hits in, at least, three stations are required. The reconstruction efficiency is reduced by 20%, while improving the p_{T} resolution for muons above 1.5 TeV.

Reconstruction efficiencies for signal and background muons obtained from $t\bar{t}$ simulation are reported in Table 3.3. A comparison of the efficiencies of the first three working

	$4 < p_{\mathrm{T}} < 20$ GeV		$20 < p_{\mathrm{T}} < 100$ GeV	
Selection	$\epsilon_{\mu}^{\mathrm{MC}}$ [%]	$\epsilon_{Hadrons}^{\mathrm{MC}}$ [%]	$\epsilon_{\mu}^{\mathrm{MC}}$ [%]	$\epsilon_{Hadrons}^{\mathrm{MC}}$ [%]
Loose	96.7	0.53	98.1	0.76
Medium	95.5	0.38	96.1	0.17
Tight	89.9	0.19	91.8	0.11
High-p_{T}	78.1	0.26	80.4	0.13

Table 3.3: Efficiency from prompt muons from W decays ($\epsilon_{\mu}^{\mathrm{MC}}$) and hadrons decaying in flight and misidentified as prompt muons ($\epsilon_{Hadrons}^{\mathrm{MC}}$). The results are computed using a $t\bar{t}$ MC sample [150].

points as functions of η is shown in Figure 3.5, based on the full pp collision dataset collected during the LHC Run II.

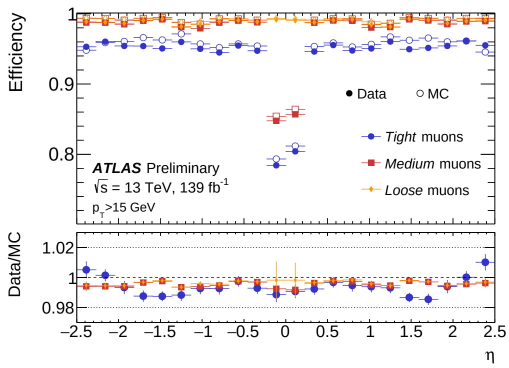

Figure 3.5: Muon reconstruction efficiencies for the Loose/Medium/Tight identification working points measured in $Z \to \mu\mu$ events as a function of the pseudorapidity for $p_{\mathrm{T}} > 15$ GeV muons. Reults on collision data (MC) are reported as full (empty) circles. The bottom panel shows the ratio between Data and MC efficiencies, i.e. the so-called efficiency scale factor. The errors in the bottom panel are the quadratic sum of statistical and systematic uncertainties [151].

3.3.2 Muon isolation

Muons originating from heavy particles decay, such as W, Z or Higgs bosons, are often produced isolated, thus well separated from other particles in the event. This is in contrast with muons coming from semileptonic decays, which are embedded in jets. The measurement of the detector activity around a muon candidate is referred to as muon isolation and it is a powerful tool to enhance background rejection in many physics analyses. As for electrons, two classes of variables are defined for muon isolation and listed below.

- Calorimetric isolation: the variable $E_{\mathrm{T}}^{\mathrm{topocone20}}$, defined as the sum of the transverse energy of clusters in a cone of size $\Delta R = 0.2$ around the muon, after subtracting corrections from energy deposity of the muon itself and from pile-up effects.
- Track isolation: the variable $p_{\mathrm{T}}^{\mathrm{varcone30}}$, defined as the scalar sum of the transverse momenta of the track with $p_{\mathrm{T}} > 1$ GeV in a cone size

$$\Delta R = \min\left(\frac{10}{p_{\mathrm{T}}^{\mu}[\mathrm{GeV}]}, 0.3\right)$$

around the muon transverse momentum, excluding the muon track itself.

Five main isolation working points are defined, each one optimized for different physics analyses, and they are listed in Table 3.4, with the corresponding discriminating variables and definition criteria.

3.4 Jets

Due to hadronization, colored particles emerging from the interaction point result in jets of colorless particles, reconstructed as multiple tracks in the Inner Detector and energy deposits in the Hadronic Calorimeter.

Isolation WP	Discriminating variable(s)	Definition
Loose	$p_{\mathrm{T}}^{\mathrm{varcone30}}/p_{\mathrm{T}}^{\mu}$, $E_{\mathrm{T}}^{\mathrm{topocone20}}/p_{\mathrm{T}}^{\mu}$	$\epsilon = 99\%$ in η and p_{T}
Tight	$p_{\mathrm{T}}^{\mathrm{varcone30}}/p_{\mathrm{T}}^{\mu}$, $E_{\mathrm{T}}^{\mathrm{topocone20}}/p_{\mathrm{T}}^{\mu}$	$\epsilon = 96\%$ in η and p_{T}
Gradient	$p_{\mathrm{T}}^{\mathrm{varcone30}}/p_{\mathrm{T}}^{\mu}$, $E_{\mathrm{T}}^{\mathrm{topocone20}}/p_{\mathrm{T}}^{\mu}$	$\epsilon \geq 90\%$ at $p_{\mathrm{T}} = 25$ GeV $\epsilon \geq 99\%$ at $p_{\mathrm{T}} = 60$ GeV
FixedCutTightTrackOnly	$p_{\mathrm{T}}^{\mathrm{varcone30}}/p_{\mathrm{T}}^{\mu}$	$p_{\mathrm{T}}^{\mathrm{varcone30}}/p_{\mathrm{T}}^{\mu} < 0.06$
FixedCutLoose	$p_{\mathrm{T}}^{\mathrm{varcone30}}/p_{\mathrm{T}}^{\mu}$, $E_{\mathrm{T}}^{\mathrm{topocone20}}/p_{\mathrm{T}}^{\mu}$	$p_{\mathrm{T}}^{\mathrm{varcone30}}/p_{\mathrm{T}}^{\mu} < 0.15$ $E_{\mathrm{T}}^{\mathrm{topocone20}}/p_{\mathrm{T}}^{\mu} < 0.30$

Table 3.4: Definition of the five main isolation working points. The discriminating variables are listed in the second column and the efficiency/criteria used in the definition are reported in the third column [150].

3.4.1 Jet reconstruction

Hadronic particles contained in a jet reach and deposit their energy in the EM and Hadronic Calorimeters. The calorimeter cells are grouped in *topological clusters* [152], following a similar procedure with respect to the one discussed in Section 3.2.1; since the reconstructed objects are jets, different thresholds may be applied.
For each cluster the relevant variables needed for the jet definition and the subsequent reconstruction are the sum of the energies of the cells in a cluster and the cluster direction with respect to the interaction point; from these variables it is possible to define a zero-mass four-vector to be used as input to the jet definition algorithm, whose task is to merge the clusters in jets.
The standard ATLAS jet clustering algorithm is the anti-k_t [153]: it introduces the concept of distance between entities (particles or clusters) and it associate them within a conic area of radius R, whose standard value adopted by ATLAS is 0.4. Once the jet algorithm has defined the final jet object, energies and momenta of the clusters belonging to it are added together.

3.4.2 Jet energy scale calibration

Figure 3.6 presents an overview of the ATLAS calibration scheme for jets, whose purpose is to determine, from the jet energy measured in the detector, the energy at particle-level, i.e. the *Jet Enegy Scale* (JES) [154].

- *Origin correction*: the measured four-momenta of jets are recomputed in order to point back to the hard-scatter primary vertex, instead of the center of the detector, but the jet energy is kept constant.

- *Pile-up correction*: the energy in excess due to in-time[2] and out-of-time[3] pile-up is removed. It consists of two components: an area-based p_{T} density subtraction [155], which is applied in each event, and a residual correction derived from MC simulation.

[2] Soft pp interactions that occur together with the hard-scattering collisions.
[3] Signals from collisions in different bunch crossings, happening if the detector and/or the electronics integration time is significantly larger than the time between two consecutive bunch crossings.

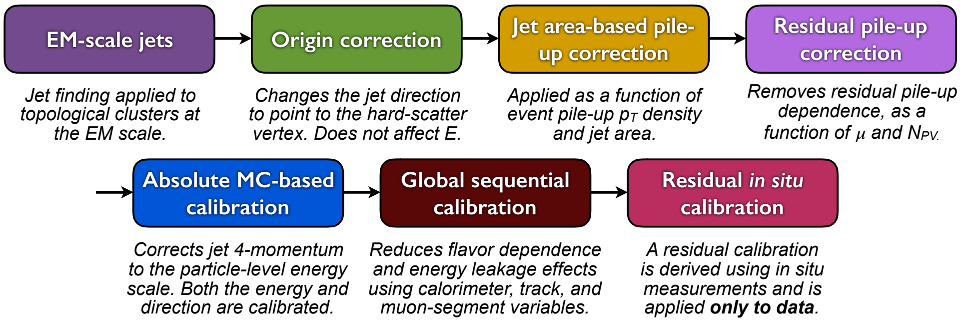

Figure 3.6: Calibration steps for jets. Other than the origin correction, each stage of the calibration is applied to the four-momentum of the jet [154].

- *Absolute JES calibration*: the four-momentum is corrected to the particle-level energy scale, as derived using truth jets in dijet MC events.
- *Global sequential calibration*: the reconstructed energy and related uncertainties are improved through the use of calorimeter, MS and track-based variables.
- *Residual in situ calibration*: the jet energy is corrected and the calibration procedure completed, by using well-measured reference objects, e.g. Z bosons and calibrated jets.

3.4.3 Jet Vertex Tagger and pile-up dependency

As previously mentioned, both in-time and out-of-time pile-up contributions are taken into account to correct the jet energy and they are typically subtracted on average. However, local fluctuations in the pile-up activity may lead to the reconstruction of spurious pile-up jets, not considered in the jet energy correction. The additional jets can be classified into two categories:

- *QCD pile-up jets*, where the particles in the central part of the jet mostly come from a single QCD process occuring in a single pile-up interaction;
- *stochastic jets* which combine particles from different interactions.

The *Jet-Vertex-Fraction* (JVF) [156] variable has been designed with the aim to help in effectively removing stochastic pile-up jets with requirements on it. It is defined as the scalar p_{T} sum of the tracks associated with the jet ($\sum_k p_{\mathrm{T}}^{\mathrm{trk}_k}(PV_0)$) and originated from the hard-scattering vertex (PV_0), divided by the scalar p_{T} sum of all associated tracks coming from any of the pile-up interactions, with vertices different from V_0, in the same bunch crossing ($\sum_{n\geq 1}\sum_l p_{\mathrm{T}}^{\mathrm{trk}_l}(PV_n) \equiv p_{\mathrm{T}}^{\mathrm{PU}}$):

$$\mathrm{JVF} = \frac{\sum_k p_{\mathrm{T}}^{\mathrm{trk}_k}(PV_0)}{\sum_l p_{\mathrm{T}}^{\mathrm{trk}_l}(PV_0) + \sum_{n\geq 1}\sum_l p_{\mathrm{T}}^{\mathrm{trk}_l}(PV_n)}. \tag{3.2}$$

Starting from JVF, the quantity *corrJVF* is defined in a similar way, but with the additional correction which takes into account the linear increase of the average $p_{\mathrm{T}}^{\mathrm{PU}}$

with the the total number of pile-up tracks in the event, $n_{\mathrm{trk}}^{\mathrm{PU}}$; for this reason $p_{\mathrm{T}}^{\mathrm{PU}}$ is divided by $(k \cdot n_{\mathrm{trk}}^{\mathrm{PU}})$, with $k = 0.01$:

$$\mathrm{corrJVF} = \frac{\sum_k p_{\mathrm{T}}^{\mathrm{trk}_k}(PV_0)}{\sum_l p_{\mathrm{T}}^{\mathrm{trk}_l}(PV_0) + [\sum_{n\geq 1}\sum_l p_{\mathrm{T}}^{\mathrm{trk}_l}(PV_n)]/(k \cdot n_{\mathrm{trk}}^{\mathrm{PU}})}. \tag{3.3}$$

corrJVT is set to -1 for jets without any associated track.
Another useful variable is $R_{p_{\mathrm{T}}}$, defined as the scalar sum of all the transverse momenta of the tracks associated with the jet and originated from the hard-scatter vertex, divided by the fully calibrated jet p_{T}, including pile-up subtraction:

$$R_{p_{\mathrm{T}}} = \frac{\sum_k p_{\mathrm{T}}^{\mathrm{trk}_k}(PV_0)}{p_{\mathrm{T}}^{\mathrm{jet}}} \tag{3.4}$$

$R_{p_{\mathrm{T}}}$ and corrJVF are combined to create a new multivariate discriminant called *Jet Vertex Tagger* (JVT): it is built as a 2-dimensional likelihood to correctly identify and remove pile-up jets, as shown in Figure 3.7 for hard-scatter and pile-up jets. It can be observed that the standard cut $|\mathrm{JVT}| > 0.59$, combined with a minimum one on $R_{p_{\mathrm{T}}}$, allows to reject the majority of pile-up jets.

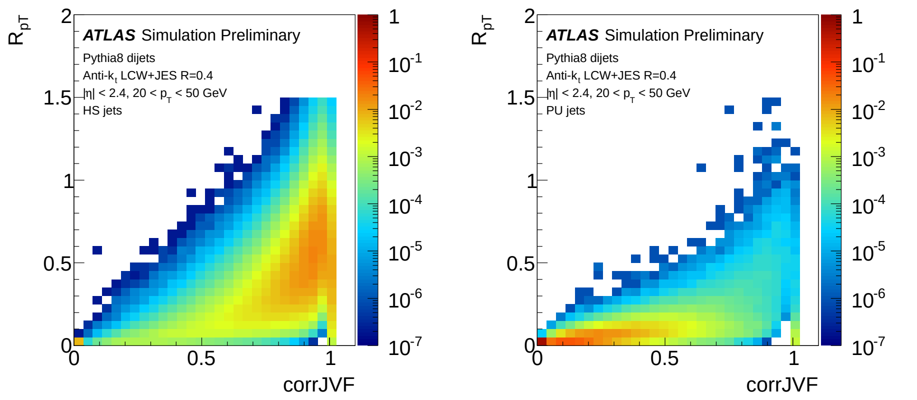

(a) (b)

Figure 3.7: 2-dimensional correlation of corrJVF and $R_{p_{\mathrm{T}}}$ for hard-scatter 3.7(a) and pile-up 3.7(b) jets [156].

In the pseudorapidity range $|\eta| > 2.5$ the identification of pile-up, or more generically *forward* [157], jets is more critical and crucial, due to the lack of track and vertex information. Moreover, the resolution of the missing transverse momentum ($E_{\mathrm{T}}^{\mathrm{miss}}$) components E_x^{miss} and E_y^{miss} (definitions and further details are given in Section 3.5) in Z +jets events is also affected by the presence of forward pile-up jets, because the inclusion of forward jets allows a more precise $E_{\mathrm{T}}^{\mathrm{miss}}$ calculation, but a more pronounced pile-up dependence, as shown in Figure 3.8.
The set of variables corrJVT and $R_{p_{\mathrm{T}}}$ are effective in suppressing stochastic pile-up jets, but they do not address QCD pile-up jets which are the dominant contribution in the forward region. A more comprehensive approach considers the total transverse momentum of tracks and jets associated with each reconstructed vertex independently: since the momentum conservation implies the total transverse momentum associated within each pile-up interaction should be conserved, any imbalance would be due to a

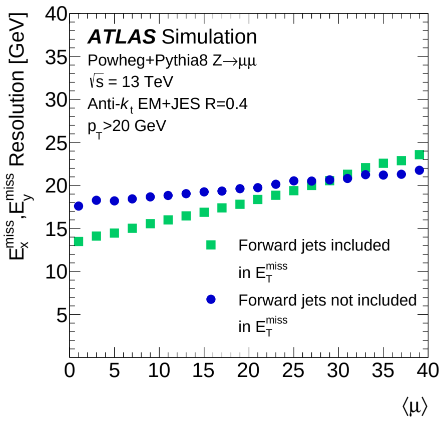

Figure 3.8: Resolution of $E_{\mathrm{T}}^{\mathrm{miss}}$ components E_x^{miss} and E_y^{miss} as a function of pile-up $\langle\mu\rangle$ [157].

forward jet from one of the interactions.
Starting from the JVF and $R_{p_{\mathrm{T}}}$ variables, a new procedure has been implemented and it is referred to as *forward Jet Vertex Tagging* (fJVT). The main parameters are the maximum JVT value, $\mathrm{JVT}_{\mathrm{max}}$, to reject central hard-scatter jets and the minimum of $\Delta R_{p_{\mathrm{T}}}$, the difference between the leading and median values of $R_{p_{\mathrm{T}}}$ for a central jet, requirement to guarantee the selected pile-up jets belong to the QCD category. The selected jets are, then, assigned to the vertex PV_i corresponding to the highest $R^i_{p_{\mathrm{T}}}$. For each pile-up vertex i the missing transverse momentum $\langle \mathbf{p}_{\mathrm{T},i}^{\mathrm{miss}} \rangle$ is calculated as the weighted vector sum of the jet and track transverse momenta. This quantity is used to build the fJVT discriminant defined as the normalized projection of the missing transverse momentum on the forward jet's transverse momentum $\mathbf{p}_{\mathrm{T}}^{\mathrm{fj}}$:

$$\mathrm{fJVT}_i = \frac{\langle \mathbf{p}_{\mathrm{T},i}^{\mathrm{miss}} \rangle \cdot \mathbf{p}_{\mathrm{T}}^{\mathrm{fj}}}{|\mathbf{p}_{\mathrm{T}}^{\mathrm{fj}}|^2} \tag{3.5}$$

The forward jet is tagged as pile-up if its fJVT value

$$\mathrm{fJVT} = \max_i(\mathrm{fJVT}_i) \tag{3.6}$$

is above a suitable threshold.

3.4.4 *b*-tagged jets

Among all jets produced in *pp* interactions, the capability to identify the ones arising from the hadronization of *b*-quarks (collectively, *b*-hadrons) is fundamental to relate them to specific physics processes, particularly the the top-quark decays. Jets containing *b*-hadrons are called *b*-tagged jets in the ATLAS nomenclature and the associate procedure for correctly identifying them is called *b*-tagging [158, 159]. The following three *b*-tagging classes of algorithms are used.

- *Impact parameter-based algorithms*: they exploit the long lifetime of *b*-hadrons ($c\tau \sim 450$ μm) by searching at least one displaced vertex with respect to the point where the hard-scatter took place. Two algorithms are employed, IP2D and IP3D, with the main difference being the discriminating variables used: the transverse impact parameter significance d_0/σ_{d_0} for IP2D or both the transverse and longitudinal $z_0 \sin\theta/\sigma_{z_0 \sin\theta}$ impact parameter significance for IP3D.

- *Secondary vertex finding algorithms*: this category explicitly reconstructs a displaced secondary vertex within the jet; all track pairs are tested for a two-track vertex hypothesis. If the vertex is found, it is rejected if its origin is compatible with the decay of long-lived particles or resonances, for instance K_L or Λ, otherwise, for each surviving vertex, a new vertex is fitted with all the other tracks which can be associated to it.

- *Decay chain multi-vertex reconstruction algorithm*: the topological structure of weak b-hadron decays inside the jet is used as the starting point to try the reconstruction of the full decay chain. A Kalman filter is applied in order to extract a common line connecting the primary and bottom vertices, corresponding approximatively to the b-hadron flight path, and the respective positions of these vertices.

The output of these three b-tagging algorithms is given as input to a Boosted Decision Tree (BDT)[4] [160] algorithm (MV2) [161] in order to achieve a combined performance, instead of considering the results of the three algorithms individually. The training of the multivariate classifier is performed on $t\bar{t}$+jets events, considering b-jets as signal and c-jets, together with light-flavour jets, as background. The kinematic properties of the jets (p_{T} and η) are included as training variables.
For training, the c-jet fraction in the background sample is set to 7%, with the remainder composed of light-flavour jets. The output discriminant of the MV2 algorithm for b-jets, c-jets and light-flavour jets, evaluated with the baseline $t\bar{t}$ simulated events, are shown in Figure 3.9.

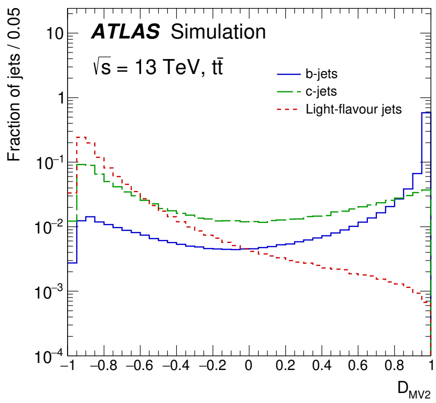

Figure 3.9: Distribution of the output discriminant of the MV2 b-tagging algorithm for b-jets, c-jets and light-flavoured jets in the baseline $t\bar{t}$ simulated events [161].

Operative working points are defined by a single cut on the BDT output and a specific working point is chosen on the basis of the b-jet efficiency in a $t\bar{t}$ sample. Working points for the MV2 tagger are reported in Table 3.5.

[4]The BDT algorithm is trained using the Root Toolkit for MultiVariate Analysis (Tmva)

ϵ_b	Selection	Rejection		
		c-jet	τ-jet	Light-flavour jet
60%	> 0.94	23	140	1200
70%	> 0.83	8.9	36	300
77%	> 0.64	4.9	15	110
85%	> 0.11	2.7	6.1	25

Table 3.5: Selection and c-jet, τ-jet and light-flavour jet rejections corresponding to the different b-jet tagging efficiency single-cut operating points for the MV2 b-tagging algorithm, evaluated on the baseline $t\bar{t}$ events [161].

Recently, several variants of the MV2 taggers have been developed as high-level taggers, combining the results of low-level taggers and using the multivariate classifier to maximize the b-tagging performance [162]:

- a reference version, based on the standard impact parameters (IP2D and IP3D) and secondary vertex-based input variables;
- an updated version, including in addition the *Soft Muon Tagger* (SMT) algorithm (MV2Mu);
- a full version, with the SMT and the *Recurrent Neural Networks Impact Parameter* (RNNIP) inputs, in addition to the standard variables (MV2MuRnn).

Furthermore, a new tagger (DL1) based on Artificial Deep Learning Neural Network has already started being widely used by several SUSY analyses in ATLAS. The DL1 NN algorithm has a multidimensional output, corresponding to the probabilities for a jet to be a b-, c- or light-flavour jet.

3.5 Missing Transverse Energy

Momentum conservation in the transverse plane requires that the sum of the momenta of all particles emerging from the interaction point should be zero, if the particle reconstruction and momentum measurement have been performed correctly. If some particles escaped the detector being undetected, it would expect to observe an imbalance in the sum of visible transverse momenta.
The quantity called *Missing transverse energy (momentum)* [163] and labelled as $E_{\mathrm{T}}^{\mathrm{miss}}$ is a fundamental observable which provides an experimental estimate of the transverse momentum carried by undetected particles produced in the collision. In each event its reconstruction is performed after all other objects, by using them as input. A non-zero value for the $E_{\mathrm{T}}^{\mathrm{miss}}$ may suggest the presence of weakly interacting particles in the detector, like neutrinos or BSM candidates, e.g. SUSY LSP.
In ATLAS, two contributions enter in the reconstructed $E_{\mathrm{T}}^{\mathrm{miss}}$ definition: the first one comes from the *hard event*, comprising fully reconstructed and calibrated particles and jets; the second contribution comes from *soft event*, consisting of reconstructed charged-particle tracks associated to the hard-scatter vertex, but not to any hard objects. Starting from the *x(y)*-axis components of the transverse momentum vectors

($\mathbf{p}_{\mathrm{T}}$) of the various contributions:

$$E_{x(y)}^{\mathrm{miss}} = - \sum_{i \in \{\mathrm{hard}\ \}} p_{x(y),i} - \sum_{j \in \{\mathrm{soft}\ \}} p_{x(y),j}, \tag{3.7}$$

where the vector $\mathbf{E}_{\mathrm{T}}^{\mathrm{miss}} = (E_x^{\mathrm{miss}}, E_y^{\mathrm{miss}})$ provides the magnitude of missing transverse momentum $E_{\mathrm{T}}^{\mathrm{miss}} = |\mathbf{E}_{\mathrm{T}}^{\mathrm{miss}}|$ and its direction in the transverse plane in terms of the azimuthal angle $\phi^{\mathrm{miss}} = \tan^{-1}(E_y^{\mathrm{miss}}/E_x^{\mathrm{miss}})$.
In the calculation of $E_{x(y)}^{\mathrm{miss}}$ the contributing objects to the hard event part need to be reconstructed from mutually exclusive detector signals. For the $E_{\mathrm{T}}^{\mathrm{miss}}$ reconstruction sequence from the hard-object contribution, the order commonly used starts with electrons, followed by photons, then hadronically decaying τ-leptons and finally jets. As already mentioned in Section 3.3, muons are mainly reconstructed from ID and MS tracks, with corrections based on their energy loss in the calorimeter, leading to little or no overlap with the other reconstructed particles in the calorimeter.
Regarding the soft term, there are two different ways to calculate the energy associated to it and they are described below.

- The most inclusive approach is performed starting from the calorimeter topo-clusters (Calorimeter Soft Term) not associated with reconstructed hard objects. The performance of this method is affected by a large dependence on pile-up.
- For each event, high-quality ID tracks emerging from the hard-scatter vertex but not associated to any electron, τ-lepton, muon or jet are considered (Track Soft Term). Since only reconstructed tracks associated with the hard-scatter vertex are used, the Track Soft Term is largely unaffected by pile-up effects, but it does not include contributions from any soft neutral particle.

Figure 3.10 shows the performance of $E_{\mathrm{T}}^{\mathrm{miss}}$ reconstruction in data and Monte Carlo simulation. The quality of the modelling of E_x^{miss}, E_y^{miss} and $E_{\mathrm{T}}^{\mathrm{miss}}$ is evaluated for an inclusive sample of $Z \to \mu\mu$ events by comparing the distributions of these observables in data recorded by the ATLAS experiment during 2015 and in Monte Carlo.

3.5.1 $E_{\mathrm{T}}^{\mathrm{miss}}$ Significance

In collider experiments like ATLAS, fake $E_{\mathrm{T}}^{\mathrm{miss}}$ can arise from particles which escape the acceptance of the detector or uncorrectly reconstructed or failed to be reconstructed altogether.
The degree of reliability of the reconstructed $E_{\mathrm{T}}^{\mathrm{miss}}$, i.e. how much it is consistent with momentum resolution and particle identification efficiencies, can be estimated by evaluating the $E_{\mathrm{T}}^{\mathrm{miss}}$ significance variable, labelled as $\mathcal{S}$ [164]. On an event-by-event basis, $\mathcal{S}$ is determined from the log-likelihood ratio that the reconstructed $E_{\mathrm{T}}^{\mathrm{miss}}$ is consistent with the null hypothesis of having zero real $E_{\mathrm{T}}^{\mathrm{miss}}$, given the full event composition. Therefore, high values of $\mathcal{S}$ can be an indication that the observed $E_{\mathrm{T}}^{\mathrm{miss}}$ in the event cannot be only explained by momentum resolution effects, suggesting the presence of undetected objects in the event, such as neutrinos or more exotic weakly interacting particles.
In more details, the $E_{\mathrm{T}}^{\mathrm{miss}}$ significance is defined to test the hypothesis that the total transverse momentum carried by invisible particles ($p_{\mathrm{T}}^{\mathrm{inv}}$) is equal to zero against the hypothesis that this quantity is different from zero. If $\mathcal{L} = (E_{\mathrm{T}}^{\mathrm{miss}}|p_{\mathrm{T}}^{\mathrm{inv}})$ is the likelihood

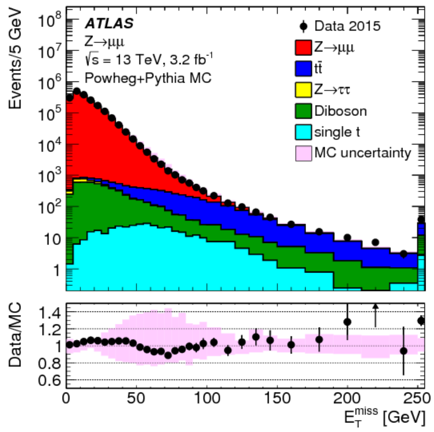

(a) $E_{\mathrm{T}}^{\mathrm{miss}}$

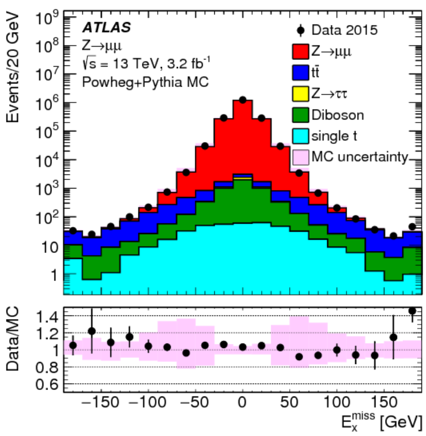

(b) E_x^{miss}

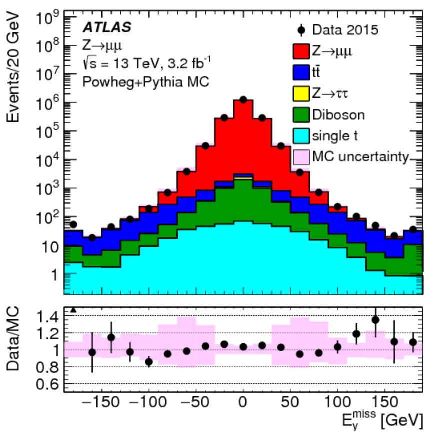

(c) E_y^{miss}

Figure 3.10: Distributions of $E_{\mathrm{T}}^{\mathrm{miss}}$, E_x^{miss} and E_y^{miss} for an inclusive sample of $Z \to \mu\mu$ extracted from data and compared to MC simulations including all relevant backgrounds. The last bin of each distribution includes the overflow, and the first bin contains the underflow in 3.10(b) and 3.10(c). The respective ratios between data and MC simulations are shown below the distributions, with the shaded areas showing the total uncertainty for MC simulations [163].

function of the 2D parameter $p_{\mathrm{T}}^{\mathrm{inv}}$ for a given value of measured $E_{\mathrm{T}}^{\mathrm{miss}}$, the log-likelihood ratio, corresponding to the significance $\mathcal{S}$, is defined as

$$\mathcal{S}^2 = 2 \ln \left(\frac{\max_{p_{\mathrm{T}}^{\mathrm{inv}} \neq 0} \mathcal{L}(E_{\mathrm{T}}^{\mathrm{miss}} | p_{\mathrm{T}}^{\mathrm{inv}})}{\max_{p_{\mathrm{T}}^{\mathrm{inv}} = 0} \mathcal{L}(E_{\mathrm{T}}^{\mathrm{miss}} | p_{\mathrm{T}}^{\mathrm{inv}})} \right), \tag{3.8}$$

where numerator and denominator are calculated maximizing on the parameters of the likelihood with the constraints $p_{\mathrm{T}}^{\mathrm{inv}} \neq 0$ and $p_{\mathrm{T}}^{\mathrm{inv}} = 0$, respectively. The likelihood function depends on the multiplicities, types and kinematics of the objects measured in each event.

3.6 Trigger

As already introduced at the beginning of this Chapter and in Chapter 2, the HLT object reconstruction occurs only to the extent required by the executed trigger algorithms, commonly referred to as online reconstruction. Events accepted by the HLT are, then, transferred to the Tier-0 computing facility for offline reconstruction. Event selections in the HLT are referred to as triggers and the collection of all triggers is called the trigger menu.
The trigger menu [165] strategy is based on the five building blocks described below.

- Primary triggers, used for physics measurements and typically run unprescaled[5]
- Support triggers, used for efficiency and performance measurements, background estimates or monitoring and typically run at small rate (~ 0.5 Hz each).
- Alternative triggers, which run alternative reconstruction algorithms complementary to the aforementioned two categories.
- Backup triggers, in case of too high rate of the primary triggers, consequently with tighter selections and lower expected rate.
- Calibration triggers, used for detector calibrations.

[5]For certain trigger chains the trigger rate may be too high to write every passing event to disk, therefore a *prescal factor* p may be introduced to reduce by a factor of $1/p$ the probability of a passing event to be recorded.

Chapter 4

Analysis strategy, results and interpretations

The analysis described in this thesis targets the search of electroweak production of the lightest chargino and slepton pairs in R-parity conserving SUSY scenarios. The analysis is optimized to target the direct production of chargino pairs, where each chargino decays into the lightest neutralino and an on-shell W boson. The neutralino is considered the LSP of the model, whose momentum contributes to $E_{\mathrm{T}}^{\mathrm{miss}}$ calculation, being undetected by the ATLAS apparatus. Only the leptonic decay of the W is considered, resulting in a final state with two charged leptons (electrons or muons) and large $E_{\mathrm{T}}^{\mathrm{miss}}$. The analysis strategy is based on the application of selection criteria on some discriminating variables in order to maximize the signal acceptance, while rejecting as much as possible the background of Standard Model events.
The analysis results are, then, reinterpreted in the context of other two searches, sharing a similar final state topology: the search for the direct production of charginos where each chargino decays into a slepton (charged slepton or sneutrino) via the emission of a lepton (neutrino or charged lepton) and the slepton itself decays into a lepton and the LSP; the search for direct pair production of sleptons where each slepton decays into a lepton and the LSP.
In order to avoid any bias due to previous results or theoretical expectations during the different analysis steps, a *Hidden Signal Box Blind Analysis* technique [166] is employed: a set of Signal Regions is defined where the significance of the SUSY model under study is maximized, but the data content of these regions is kept hidden until a reliable background estimate strategy is fully developed.
My contribution to the described analysis ranges from the Monte Carlo sample production and validation (both signals and backgrounds), through the finalization of the object definitions, the preliminary event selection, the Signal Regions, Control Regions and Validation Regions optimization, to the final evaluation of systematic uncertainties. In particular, the generation and test of all signal grids were fully or partially under my responsibility. Finally, I gave a general support to all analysis steps.

4.1 Data samples

The analysis uses data collected by the ATLAS experiment during the LHC Run II data taking period, i.e. from July 2015 to October 2018. The cumulative luminosity

collected during this period has already been shown in Figure 2.6(b). The delivered luminosity takes into account the luminosity starting from when the stable beam flag is raised, until the ATLAS detector is switched in a standby mode to allow beam dump or beam studies.
Several factors contribute to the differences between the delivered luminosity and the luminosity recorded by ATLAS: calibrations, trigger-specific data quality problems, the "warm start" procedure[1], DAQ inefficiencies. Finally, before being flagged as *good for physics*, all data must be checked for known detector issues, in order to avoid incomplete events. All luminosity blocks[2] passing this selection are inserted in a *Good Run List* (GRL) for the final luminosity estimation. The resulting integrated luminosity for the period from July 2015 to October 2018 corresponds to 139 fb^{-1} .
After passing the GRL requirements, several additional *cleaning cuts* are applied to data in order to completely remove all problematic events in the analyses:

- data events should not have raised error flags in the calorimeters, both Electromagnetic and Hadronic, and in the SCT;
- data events should not have been tagged as incomplete, i.e. events must contain information from all subdetector systems;
- a generic event is rejected if it is not found a primary vertex with at least two associated tracks;
- a generic event is rejected if a muon, tagged as cosmic, is found;
- a generic event is rejected if at least one jet in the event does not pass the *Loose* quality criterion [167], having $p_{\mathrm{T}} > 20$ GeV.

4.2 Monte Carlo samples

The hidden signal box blind analysis approach implies all choices concerning the Signal Region definitions have to be done without looking at the data yields. Monte Carlo simulations must be used to investigate the physics processes of interest, in order to find a suitable strategy to discriminate signals from the Standard Model processes sharing a similar signature; these simulations must be able to model, as much accurately as possible, both signals and backgrounds, as well as the detector response to them.
The first step of a Monte Carlo simulation is the computation of the proton-proton hard scattering cross section, which can be described by the parton interaction cross sections and the *Parton Distribution Functions* (PDF) [168] inside the proton itself

$$\sigma_{pp\to X} = \sum_{a,b} \int_0^1 dx_a \int_0^1 dx_b f_a(x_a, Q^2, \mu_F^2) f_b(x_b, Q^2, \mu_F^2) \sigma_{ab\to X}(s, \mu_F^2, \mu_R^2), \qquad (4.1)$$

with Q being the transferred momentum, $x_{a,b}$ the fractions of the proton energy carried by the two partons, $f_{a,b}$ the PDF and $\mu_{R,F}$ the renormalization and factorization

[1] When the stable beam flag is raised, the tracking detectors undergo this stage which includes a ramp of the high voltage and, for the pixel system, the turning on of pre-amplifiers.
[2] A luminosity block is a time interval (typically $\sim 1-2$ minutes) of data recording which assumes constant experimental conditions, especially the instantaneous luminosity.

scales for a generic final state X. Once a specific choice of $f_{a,b}$ and $\mu_{R,F}$ is performed, Equation 4.1 can be expressed as [169]:

$$\sigma_{ab\to X} = \sum_{k=0}^{\infty} \int d\Phi_{X+k} \left| \sum_{l=0}^{\infty} \mathcal{M}_{X+k}^{(l)} \right|^2 , \tag{4.2}$$

where the matrix element $\mathcal{M}_{X+k}^{(l)}$ is the probability amplitude for the final state $X+k$, with l one of the possible virtual loops and k one of the possible extra quarks or gluons emitted alongside the final state, before or after the hard scatter process, thus called *Initial State Radiation* (ISR) or *Final State Radiation* (FSR), respectively. Finally, Equation 4.2 holds at all orders.
To keep the numerical calculation feasible in a reasonable amount of time, some approximations are applied:

- $l = 0,\ k = 0$: *Leading Order* (LO) approximation for the final state X.
- $l = 0,\ k = n$: Leading Order approximation for the final state X, plus n jets.
- $k + l \leq n$: *Next*$^{(n)}$ *to Leading Order* (N$^{(n)}$LO) approximation for the final state X, also including the final state X plus 1 jet corresponding to N$^{(n-1)}$LO.

In order to apply the correct approximation and simulate the detector response, dedicated software is used. After the simulation of all particles produced in a collision, including the ones coming from the proton breakup but not participating to the hard scattering (the so-called *underlying event*), the hadronization process of quarks and gluons is performed, in a non-perturbative QCD regime, and then the final decay of QCD objects.

The next step is the simulation of particle interactions inside the ATLAS apparatus. The current standard full simulation (FullSim) relies on a detailed description of the detector geometry and of the interactions with the detector materials, based on Geant 4 [170]. This approach leads to very accurate results, however the CPU time required for each event to be processed is very high (several minutes) and more than 90% of this time is dedicated to the interactions with the calorimeters. To limit this long processing time, the FastCaloSim [171] tool has been developed and integrated in the Geant 4 simulations, in order to reproduce the reconstructed objects without the full calorimeter simulation, leading to the so-called Atlfast-II simulation[3].
The last step of Monte Carlo simulation is the emulation of the trigger response and, once this step is complete, simulated events are stored in a format similar to the data one, ready to be used by physics analyses. Another possibility is to use Monte Carlo samples before the reconstruction step takes place, i.e. just after the hadronization process: these samples are referred to as *Truth level* simulations and they can be used to check the effects of changing the generation parameters or to evaluate theoretical systematic uncertainties.

Despite the several, accurate steps involved in the reconstruction of Monte Carlo samples, some discrepancies may still be present when comparing their kinematic distributions to the ones measured in data. For this reason, the simulation undergoes

[3]More precisely, it is the combination of Geant 4 simulation of the Inner Detector and the Muon Spectrometer and the FastCaloSim. A variant is based on the combination of the fast calorimetric simulation together with the ATLAS fast track simulation Fatras [172] of the Inner Detector and the Muon Spectrometer, called Atlfast-IIF

the following additional calibrations whose result is the production of specific weights which must be applied on an event-by-event basis.
The additional sources of calibrations are the efficiencies of: trigger, identification and isolation working points for electron and muons, b-tagging, which can be, potentially, different in simulation and data. Then, several sets of *scale factors* are calculated for each calibration source, by computing ratios of the efficiencies on dedicated samples in data and Monte Carlo, and finally applied to simulations.
Pile-up is an important source of extra calibration, since its conditions are not constant during data taking periods: the corresponding event weight is calculated through the *pile-up reweighting* procedure and it has to be applied together with the other ones; the general idea behind this procedure is to scale the pile-up in the simulation to match the one of the considered data period.

4.2.1 Signal samples

The SUSY signal samples used in this analysis are generated from leading-order (LO) matrix elements with up to two extra partons using MadGraph5_aMC@NLO v2.6.1 [173] interfaced to Pythia 8.186 [174], with the A14 tune [175] for the modelling of the SUSY decay chain, parton showering [176], hadronization and the description of the underlying event. Parton luminosities are provided by the NNPDF2.3LO PDF set [177]. Jet-parton matching is performed following the CKKW-L prescription [178], with a matching scale set to one quarter of the mass of the pair-produced SUSY particles. Signal cross-sections are calculated to next-to-leading order (NLO) in α_s adding the resummation of soft gluon emission at next-to-leading-logarithm accuracy (NLO+NLL) [179–185]. The nominal cross-sections and their uncertainties are taken from an envelope of cross-section predictions using different PDF sets, factorization and renormalization scales [186].
The signal samples have been generated in the context of a simplified model with chargino/slepton/sneutrino and neutralino masses being the only free parameters. The $\tilde{\chi}_1^\pm$ is assumed to be pure wino and the $\tilde{\chi}_1^0$ pure bino. The decays $\tilde{\chi}_1^\pm \to W\tilde{\chi}_1^0$ and $\tilde{\ell} \to \ell\tilde{\chi}_1^0$ are assumed to happen with 100% branching ratios; for $\tilde{\chi}_1^\pm \to (\tilde{\ell}\nu)(\ell\tilde{\nu})$, equal branching ratios for the three slepton flavours are assumed and charginos decay into charged sleptons or sneutrinos with a branching ratio of 50% to each. It is also assumed, in this last case, that the sleptons are mass-degenerate, with their masses chosen to be midway between the mass of the chargino and that of the $\tilde{\chi}_1^0$. In models with direct $\tilde{\ell}\tilde{\ell}$ production each slepton decays into the corresponding lepton and a $\tilde{\chi}_1^0$ with a 100% branching ratio. Only $\tilde{e}$ and $\tilde{\mu}$ are considered in these models and different assumptions about the masses of the superpartners of the left-handed and right-handed charged leptons, $\tilde{e}_L$, $\tilde{e}_R$, $\tilde{\mu}_L$ and $\tilde{\mu}_R$, are considered. The cross-section for $\tilde{\chi}_1^+\tilde{\chi}_1^-$ production, each with a mass of 400 GeV, is 58.6 ± 4.7 fb, while the cross-section for $\tilde{\ell}\tilde{\ell}$ production, each with a mass of 500 GeV, is 0.47 ± 0.03 fb for each generation of left-handed sleptons and 0.18 ± 0.01 fb for each generation of right-handed sleptons.
Several signal samples have been generated in order to probe a vast region of the mass-parameter space; they are arranged in three different "grids" in the $[m(\tilde{\chi}_1^\pm, \tilde{\ell}), m(\tilde{\chi}_1^0)]$ plane, as shown in Figure 4.1.

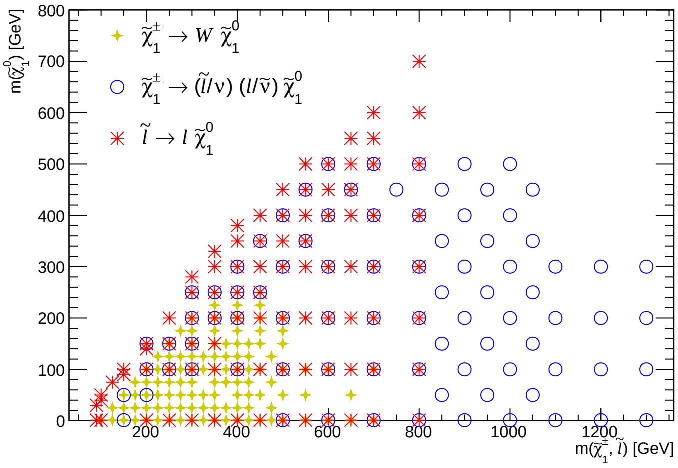

Figure 4.1: The three different grids of signal models considered in the analysis: the signal points related to the chargino pair production with W-boson-mediated decay are marked with yellow stars, the ones related to the chargino pair production with slepton-mediated decays with blue circles and the ones related to the direct slepton pair production with red sketched stars.

4.2.2 Background samples

For this analysis two charged leptons and missing transverse energy are expected in the final state. Several Standard Model processes produce this signature and, therefore, they must be considered as background processes. An important step of the analysis optimization procedure is the identification of the variables and the corresponding ranges where the SUSY signature emerges with respect to the background in a statistically significant way.
The background samples used in this analysis are reported below and they are listed in a compact view in Table 4.1, along with the MC generators, the relevant parton distribution function sets used by the generator and in the parton shower (PS), the configuration of the underlying event and hadronization parameters (tune) and the cross-section order in α_s used to normalize the event yields for these samples.

- Diboson (VV) processes: given the similarity of the chargino pair production with W-boson-mediated decay with the SM WW production and decay, a careful evaluation is needed. The diboson processes are generated with Powheg-Box v2 and split in WW, WZ and ZZ productions, with up to four charged leptons in the final state; these samples are interfaced to Pythia 8.210 for parton shower, with the AZNLO tune. Cross-sections are computed at NLO with CT10 NLO and CTEQ6L1 PDF sets for, respectively, generator and parton shower.

- top-quark processes: $t\bar{t}$ samples are generated with Powheg-Box v2, assuming a top-quark mass of 172.5 GeV, interfaced to Pythia 8.230 for parton shower. NNLO+NNLL cross-sections are used, with the A14 tune. The PDF used are NNPDF3.0NNLO for generator and NNPDF2.3LO for parton shower. Single-top-quark samples are produced with a similar setup, apart from the usage of NLO+NNLL cross-sections.

- Z/γ^*+jets: although this is not a primary source of background, they must be considered due to the high production cross-section. These samples are generated with SHERPA 2.2.1 with massive b/c-quarks for an improved treatment of the associated production of Z bosons with heavy flavour jets. Matrix elements are calculated for up to two partons at NLO and up to four partons at LO. The NNPDF3.0NNLO PDF set is used in association with a dedicated parton shower tuning developed by the SHERPA authors. Z production and Drell-Yan processes are included. A global k-factor [187] of 0.9751 is used to normalize the Z/γ^*+jets events to the NNLO QCD cross-sections. The samples are generated in non overlapping slices filtered on the basis of the vector boson p_{T} and of the presence of b- and c-jets.

- Other minor background processes are also considered: multiboson processes, such as triboson processes (WWW, WWZ, WZZ, ZZZ) with up to six charged leptons in the final states generated with SHERPA 2.2.2, $t\bar{t}$ production associated with W or Z generated with MADGRAPH5_aMC@NLO and Higgs boson processes with POWHEG-BOX v2 as generator.

Physics process	Generator	Parton shower	Normalization	Tune	PDF (generator)	PDF (PS)
$t\bar{t}$	POWHEG-BOX v2 [188–191]	PYTHIA 8.230 [192]	NNLO+NNLL [193]	A14 [175]	NNPDF3.0NLO [194]	NNPDF2.3LO [177]
$t\bar{t}+V$ ($V=W,Z$)	MADGRAPH5_aMC@NLO [173]	PYTHIA 8.210 [192]	NLO [173, 195]	A14	NNPDF3.0NLO	NNPDF2.3LO
$t\bar{t}+WW$	MADGRAPH5_aMC@NLO	PYTHIA 8.186 [174]	NLO [173]	A14	NNPDF3.0NLO	NNPDF2.3LO
$tZ, t\bar{t}t\bar{t}, tt\bar{t}$	MADGRAPH5_aMC@NLO	PYTHIA 8.230	NLO [173]	A14	NNPDF3.0NLO	NNPDF2.3LO
Single top (Wt)	POWHEG-BOX v2 [189, 190, 196]	PYTHIA 8.230	NLO+NNLL [197, 198]	A14	NNPDF3.0NLO	NNPDF2.3LO
$Z/\gamma^*(\rightarrow ll)$ +jets	SHERPA 2.2.1 [199–201]	SHERPA 2.2.1	NNLO [187]	SHERPA default [201]	NNPDF3.0NNLO [194]	NNPDF3.0NNLO [194]
WW, WZ, ZZ	POWHEG-BOX v2 [189, 190, 202, 203]	PYTHIA 8.210	NLO [202–204]	AZNLO [205]	CT10 NLO [206]	CTEQ6L1 [207]
VVV ($V=W,Z$)	SHERPA 2.2.2 [199, 200, 204]	SHERPA 2.2.2	NLO [200, 204]	SHERPA default [204]	NNPDF3.0NNLO	NNPDF3.0NNLO
Higgs boson	POWHEG-BOX v2 [189, 190, 208–211]	PYTHIA 8.186	NLO [212]	AZNLO	NNPDF3.0NLO [4]	CTEQ6L1

Table 4.1: Simulated background event samples with the corresponding matrix element and parton shower (PS) generators, cross-section order in α_{s} used to normalize the event yield, underlying-event tune and the generator PDF sets used [1].

Figure 4.2 shows a summary of the Standard Model total production cross-sections as measured by the ATLAS experiment [213].

4.3 Trigger

Since the request of two Opposite Sign (OS) leptons in the final state, dilepton triggers are used to select events. The considered lowest unprescaled trigger items are listed in Table 4.2 for different data taking periods together with a brief explanation of the trigger requests; for a given period, all trigger chains are applied in a logical OR. The trigger-level thresholds for the p_{T} of the leptons involved in the trigger decision are different according to the data-taking period. They are in the range 8-22 GeV for data collected in 2015 and 2016, while 8-24 GeV for data collected in 2017 and 2018. The trigger offline selection used in the analysis requires both leptons in the event to

[4] The PDF4LHC15 set have been used for some Higgs production processes, as via gluon-gluon fusion, VBF and VH.

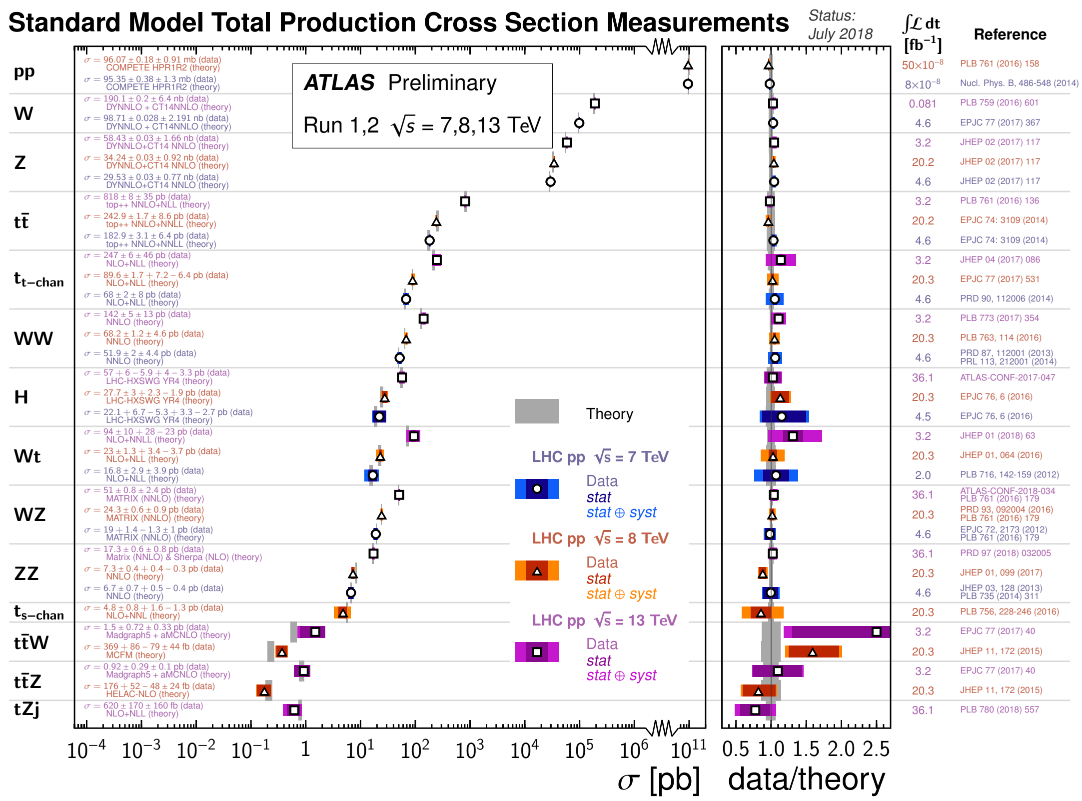

Figure 4.2: Summary of several Standard Model total production cross section measurements, corrected for leptonic branching fractions, compared to the corresponding theoretical expectations. All theoretical expectations were calculated at NLO or higher. The dark-color error bar represents the statistical uncertainty. The lighter-color error bar represents the full uncertainty, including systematics and luminosity uncertainties. The data/theory ratio, luminosity used and reference for each measurement are also shown. Uncertainties for the theoretical predictions are quoted from the original ATLAS papers [213].

have $p_{\mathrm{T}} > 25$ GeV, in order to efficiently select events triggered with the considered items.

4.4 Object definition

Following on the discussion of the specific objects in Chapter 3, several features can be requested to the objects used in a generic physics analysis. Table 4.3 reports these features in case of the analysis described in this thesis. Two sets of selection criteria are considered, *baseline* and *signal*, defined in such a way that the objects categorized as signal were selected with tighter criteria with respect to the baseline ones, representing a subset of them. Baseline objects are used in the analysis to compute $E_{\mathrm{T}}^{\mathrm{miss}}$ and $E_{\mathrm{T}}^{\mathrm{miss}}$ significance, in the procedure to solve ambiguities between objects themselves (overlap removal, see Section 4.4.1), in the estimation of the *fake-and-non-prompt* (FNP) lepton background. On the other hand, signal objects are used in the analysis final selection. Concerning $E_{\mathrm{T}}^{\mathrm{miss}}$, given the higher pile-up conditions during 2017 and 2018 data taking

Event Topology (channel)		Triggers
Di-electron	2015	HLT_2e12_lhloose_L12EM10VH – $2e^{\pm}$ with $E_{\mathrm{T}} > 12$ GeV, loose likelihood identification – Seeded by L1 trigger requiring two EM clusters with $E_{\mathrm{T}} > 10$ GeV
	2016	HLT_2e17_lhvloose_nod0 – $2e^{\pm}$ with $E_{\mathrm{T}} > 17$ GeV, very loose likelihood identification – No transverse impact parameter cut applied
	2017-2018	HLT_2e24_lhvloose_nod0 – $2e^{\pm}$ with $E_{\mathrm{T}} > 24$ GeV, very loose likelihood identification – No transverse impact parameter cut applied
Di-muon	2015	HLT_mu18_mu8noL1 – $2\mu^{\pm}$ with $p_{\mathrm{T}} > 18$ GeV and $p_{\mathrm{T}} > 8$ GeV – Reconstructed without L1 seed (full scan at HLT)
	2016-2017-2018	HLT_mu22_mu8noL1 – $2\mu^{\pm}$ with $p_{\mathrm{T}} > 22$ GeV and $p_{\mathrm{T}} > 8$ GeV – Reconstructed without L1 seed (full scan at HLT)
Electron-Muon	2015	HLT_e17_lhloose_mu14 – $E_{\mathrm{T}}^{e^{\pm}} > 17$ GeV, loose likelihood identification – $p_{\mathrm{T}}^{\mu^{\pm}} > 14$ GeV
	2016-2017-2018	HLT_e17_lhloose_nod0_mu14 – $E_{\mathrm{T}}^{e^{\pm}} > 17$ GeV, loose likelihood identification and no transverse impact parameter cut applied – $p_{\mathrm{T}}^{\mu^{\pm}} > 14$ GeV

Table 4.2: List of dilepton trigger items used in the analysis. Due to the increase of instantaneous luminosity and pile-up conditions during Run II, higher p_{T} thresholds or tighter trigger requests have been applied.

campaigns, the *Tight* working point is used. Tight $E_{\mathrm{T}}^{\mathrm{miss}}$ is calculated without including forward jets with $|\eta| > 2.4$ and $20 < p_{\mathrm{T}} < 30$ GeV, thus removing regions of phase space having more pile-up jets than hard scatter jets, in order to minimize the impact of pile-up jets in the $E_{\mathrm{T}}^{\mathrm{miss}}$ computation [214].
For jets with $|\eta| > 2.5$ and $p_{\mathrm{T}} < 60$ GeV, pile-up suppression is achieved through the fJVT algorithm, which exploits topological correlations between jet pairs. Since these jets can suffer of a relevant pile-up dependence, in the forward region they are not explicitly vetoed or selected in the analysis, but only included in the $E_{\mathrm{T}}^{\mathrm{miss}}$ calculation. Jets used as possible ISR/FSR candidates are required to have $|\eta| < 2.4$.

4.4.1 Overlap removal

The *overlap removal* procedure is applied in order to prevent that a single physics entry is reconstructed as multiple objects, being considered under multiple categories.

Physics Object		Definition
Electrons	Baseline	– ID: `LooseAndBLayerLLH` – $p_{\mathrm{T}} > 10$ GeV and $\lvert\eta\rvert < 2.47$ – $\lvert z_0 \sin\theta\rvert < 0.5$ mm
	Signal	– ID: `LLHTight` – Isolation: `FCLoose` ($p_{\mathrm{T}} < 200$ GeV) – Isolation: `FCHighPtCaloOnly` ($p_{\mathrm{T}} > 200$ GeV) – $\lvert d_0/\sigma_{d_0}\rvert < 5$
Muons	Baseline	– ID: `Medium` – $p_{\mathrm{T}} > 10$ GeV and $\lvert\eta\rvert < 2.7$ – $\lvert z_0 \sin\theta\rvert < 0.5$ mm
	Signal	– ID: `Medium` – Isolation: `FCLoose` – $\lvert d_0/\sigma_{d_0}\rvert < 3$
Jets	Baseline	– Reconstructed with anti-k_t algorithm, $R = 0.4$ – $p_{\mathrm{T}} > 20$ GeV and $\lvert\eta\rvert < 4.5$
	Signal	– JVT: $\lvert\mathrm{JVT}\rvert > 0.59$ with $p_{\mathrm{T}} < 120$ GeV and $\lvert\eta\rvert < 2.5$ – fJVT: jet $p_{\mathrm{T}} < 60$ GeV and $\lvert\eta\rvert > 2.5$ – ISR/FSR: $\lvert\eta\rvert < 2.4$ – b-tagging: *MV2* algorithm at 85% WP

Table 4.3: Summary of the objects used in the analysis: electrons, muons and jets are listed. Signal objets are a subset of the Baseline ones.

It is performed at the baseline objects level and applied as follows:

- jet candidates within $\Delta R' = \sqrt{\Delta y^2 + \Delta\phi^2} = 0.2$ of an electron candidate are discarded since they mostly originate from calorimeter energy deposits from electron showers or bremsstrahlung;
- jets with fewer than three tracks lying within $\Delta R' = 0.4$ of a muon candidate are removed;
- electrons and muons within $\Delta R' = 0.4$ of the remaining jets are discarded, in order to reject leptons from b- or c-hadron decays;
- electron candidates are rejected if sharing an ID track with a muon.

4.5 Search strategy

The analysis sensitivity to the searched signal model relies on the definition of the *Signal Regions* (SRs), i.e. regions where the signal/background ratio is maximized with respect to the kinematics and features of the SUSY signal. Usually, a null hypothesis is used to evaluate the statistical power of the SRs [215].
Given the null hypothesis $\mathcal{H}_b$, the yields observed (n_{obs}) in the SRs are supposed to be explained only by the presence of background processes, with μ_b the expected background yield. The alternative hypothesis $\mathcal{H}_{s+b}$ explains the same number of events by considering both signal and background contributions, being μ_s the expected signal

yield.
The p-value[5] of the analysis is the measure of its statistical power. If n_{obs} is large enough, the Poisson distribution describing the data in the $\mathcal{H}_{s+b}$ hypothesis can be approximated with a Gaussian distribution of mean $\mu = s + b$ and standard deviation $\sigma = \sqrt{s+b}$. In this context, the p-value can be correlated with the Z-value [216]:

$$Z = \Phi^{-1}(1-p); \qquad \Phi(Z) = \frac{1}{\sqrt{2\pi}} \int_{-\infty}^{z} \exp(-t^2/2)\, dt = \frac{1 + \text{erf}(Z/\sqrt{2})}{2}. \tag{4.3}$$

By calculating the p-value of the null hypothesis and assuming uncertainties on the background estimate to be Gaussian distributed, but positively truncated, the p_N[6] value is defined by the following set of equations:

$$\begin{aligned}
\Gamma(n, 0, x) &= \int_0^x t^{n-1} e^{-t}\, dt \\
p_{\text{P}} &= \sum_{j=n_{\text{obs}}}^{\infty} \frac{e^{-\mu_b} \mu_b^j}{j!} = \frac{\Gamma(n_{\text{obs}}, 0, \mu_b)}{\Gamma(n_{\text{obs}})}, \\
p_N &= \int p_{\text{P}}\, p(\mu_b)\, d\mu_b
\end{aligned} \tag{4.4}$$

where $\Gamma(n_{\text{obs}})$ is the usual and well-known Γ function, while $p(\mu_b)$ is the pdf encapsulating the results of the background measurement, assumed to be normalized following the procedure described in Section 4.7.2. The relative Z-value is called Z_N and it can be used to quantify the significance, defining a minimum value of Z_N above which the null hypothesis must be rejected.

4.5.1 Preliminary selection

After the trigger and the overlap removal requests, a preliminary event selection is applied, asking for exactly two oppositely charged signal leptons in the event, both with $p_{\text{T}} > 25$ GeV. To remove contributions from low-mass resonances, the invariant mass of the two leptons must be $m_{\ell_1 \ell_2} > 25$ GeV. Events are further required to have no reconstructed central[7] b-jets, to suppress contributions from processes with top-quarks. This set of criteria is summarized in Table 4.4.

4.5.2 The stransverse mass

The UA1 Collaboration [217] introduced the *transverse mass* variable in the search for the leptonic decay of the W boson [218], in order to evaluate the mass of a parent particle which decays into secondary particles, some of which, neutrinos in the UA1

[5] Considering a statistical variable X with the associate *probability density functions* (pdf, i.e. function describing the relative likelihood for a generic variable to take on a value in a generic interval) $f_b(X)$ for the null hypothesis and $f_{s+b}(X)$ for the alternative one, a critical value x_0 for X for which $\mathcal{H}_{s+b}$ is considered true, the p-value is defined as

$$p = \int_{X > x_0} f_b(X)\, dX$$

and this quantity is also known as the probability of a *type I* error.

[6] Here N stands for normal, as in the normal distribution.

[7] The attribute *central* refers directly to the signal jet criteria defined in Table 4.3.

Variable	Cut value
Number of signal leptons	$= 2$
Lepton charge	OS
Leading lepton p_{T} [GeV]	> 25
Subleading lepton p_{T} [GeV]	> 25
Invariant Mass $m_{\ell_1\ell_2}$ [GeV]	> 25

Table 4.4: Criteria defining the preliminary event selection.

case, undetected by the experimental apparatus. In events where a single produced particle P decays into an invisible particle with mass m_{miss}, carrying a transverse momentum $\mathbf{q}_{\mathrm{T}}^{\mathrm{invis}}$, and into a detected particle X with mass m_X and whose transverse momentum is $\mathbf{p}_{\mathrm{T}}^X$, then the transverse mass can be defined as:

$$m_{\mathrm{T}}^2 = m_X^2 + m_{\mathrm{miss}}^2 + 2(E_{\mathrm{T}}^X E_{\mathrm{T}}^{\mathrm{invis}} - \mathbf{p}_{\mathrm{T}}^X \cdot \mathbf{q}_{\mathrm{T}}^{\mathrm{invis}}) \simeq 2p_{\mathrm{T}}^X q_{\mathrm{T}}^{\mathrm{invis}}(1 - \cos\Delta\phi), \tag{4.5}$$

if $m_X \simeq 0$ and $m_{\mathrm{miss}} \simeq 0$, with $\Delta\phi$ being the difference in azimuthal angle between the two particle momenta. The kinematic endpoint of this variable is the mass of the parent particle: $m_{\mathrm{T}} \leq m_P$.
In case of two W bosons decaying leptonically in the event, the detectable part of the decay is represented by $(\mathbf{p}_{\mathrm{T},1-2})$, but there are also two neutrinos which prevent the usage of the transverse mass variable. However,

$$m_W \geq \max[m_{\mathrm{T}}(\mathbf{p}_{\mathrm{T},1}, \mathbf{q}_{\mathrm{T},1}), m_{\mathrm{T}}(\mathbf{p}_{\mathrm{T},2}, \mathbf{q}_{\mathrm{T},2})].$$

The two transverse momenta $\mathbf{q}_{\mathrm{T},1-2}$ of the two neutrinos can be combined together in

$$\mathbf{p}_{\mathrm{T}}^{\mathrm{miss}} = \mathbf{q}_{\mathrm{T},1} + \mathbf{q}_{\mathrm{T},2} \tag{4.6}$$

and, since the values of the neutrino momenta are unknown, the best obtainable information is:

$$m_W \geq \min_{\mathbf{q}_{\mathrm{T},1}+\mathbf{q}_{\mathrm{T},2}=\mathbf{p}_{\mathrm{T}}^{\mathrm{miss}}} \{\max[\, m_{\mathrm{T}}(\mathbf{p}_{\mathrm{T},1}, \mathbf{q}_{\mathrm{T},1}), m_{\mathrm{T}}(\mathbf{p}_{\mathrm{T},2}, \mathbf{q}_{\mathrm{T},2})\,]\} \equiv m_{\mathrm{T2}}(\mathbf{p}_{\mathrm{T},1}, \mathbf{p}_{\mathrm{T},2}, \mathbf{p}_{\mathrm{T}}^{\mathrm{miss}}), \tag{4.7}$$

where the minimization is performed over all the possible decompositions of $\mathbf{p}_{\mathrm{T}}^{\mathrm{miss}}$. The m_{T2} variable is called *stransverse mass* [219, 220].
The upper limit in Equation 4.7 can be fixed in the case of an ideal detector with perfect momentum resolution, where the only sources of $\mathbf{p}_{\mathrm{T}}^{\mathrm{miss}}$ are the two neutrinos, both originating from an on-shell W. In the real case, the calculation of $\mathbf{p}_{\mathrm{T}}^{\mathrm{miss}}$ can be affected by the detector resolution and the particles in the final state can come from off-shell W bosons, resulting in a not sharp value for this kinematic endpoint as it can be observed in Figure 4.3(a) for the two lepton system coming from $t\bar{t}$ and tW events.

In the case of WW process, the tail after the ideal endpoint is highly populated since the off-shell W does not have an upper bound at the top-quark mass like in the $t\bar{t}$ process, as shown in Figure 4.3(b).
In the case of R-parity conserving SUSY models such as the ones considered in this analysis, two LSPs are also present in the final states, complicating the decay chain. However, neutrinos and neutralinos can be grouped together in the calculation, which can be carried out in a similar way as the Standard Model case. The kinematic m_{T2}

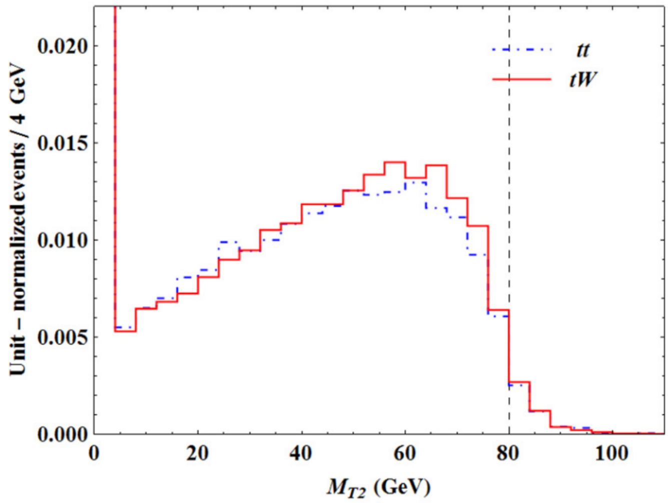

(a) m_{T2} distribution for $t\bar{t}$ and tW events. The dashed line indicates the expected endpoint of the $t\bar{t}$ system [221].

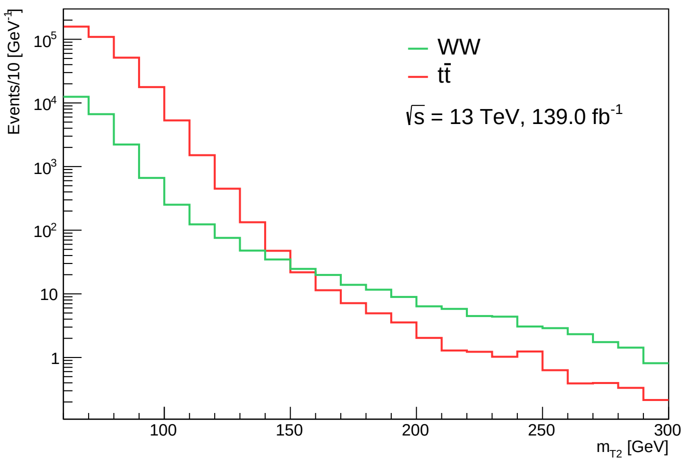

(b) m_{T2} distribution for WW and $t\bar{t}$ processes. The Monte Carlo samples are scaled and normalized to the total Run II luminosity (139 fb^{-1}). A preliminary event selection is considered, with the additional request of $m_{T2} > 60$ GeV.

Figure 4.3: m_{T2} distributions highlighting kinematical endpoints of $t\bar{t}$ samples compared to WW 4.3(b) and tW 4.3(a)events.

endpoint for these signal models is no longer the W-boson mass, expected from the dominant SM backgrounds, but the mass difference between the $\tilde{\chi}_1^{\pm}$ and the $\tilde{\chi}_1^0$. Therefore, these events are required to have high-m_{T2} values and this is a key feature for the SR definition.

4.6 Signal Region definition

As already discussed in Section 4.2.1, the SUSY signal samples used in the analysis cover a wide mass range for the two particles entering the model as free parameters. The kinematic of the final state is dependent on the splitting between the two masses,

making almost impossible to achieve a unique set of optimal cuts. For this reason, multiple Signal Regions are defined and arranged in two main categories: inclusive and exclusive.
The *exclusive SRs* are defined to be orthogonal with respect to all other regions in the analysis and they are optimized on the basis of the exclusion limits obtained via the CL_s prescription [222]; this method allows the likelihood fit (this procedure is decribed in more detailed in Section 4.7.2, when the background estimation is presented) to combine several Signal Regions in the likelihood function, providing more statistical information than a single region, by analyzing the shape[8] of the signal and of the background.
The *inclusive SRs* are defined focusing the attention on the discovery of SUSY particles and they do not have to be orthogonal, like the exclusive ones.
Following on the cuts defining the preliminary event selection shown in Table 4.4, a common set of additional kinematic cuts are applied to both sets of SRs:

- $m_{\ell_1\ell_2}$: to ensure good modelling of the SM background in all relevant regions, a cut on the invariant mass of the two lepton is required: $m_{\ell_1\ell_2} > 100$ GeV.
- *Flavour*: events are separated into "Same Flavour" (SF), i.e. $e^\pm e^\mp$ and $\mu^\pm\mu^\mp$, and "Different Flavour" (DF), i.e. $e^\pm\mu^\mp$, since the two classes of events have different background compositions, leading to the request of two set of cuts to reject the different classes of background events. In particular, in order to reduce the large background component of SF leptons resulting from the leptonic Z decays (Z+jets, ZZ and WZ diboson processes), SF events are required to have a dilepton invariant mass far from the Z mass peak; $m_{\ell_1\ell_2} > 121.2$ GeV.
- *Jets*: in the considered signal models no hadronic activity in the final state is expected, apart from Initial State Radiation jets. Following the veto on central b-tagged jets, central jets not tagged by the MV2C10 algorithm are limited to one, in order to take into account the possibility of an ISR jet which can boost the decay products to higher-$E_{\mathrm{T}}^{\mathrm{miss}}$ values.
- $E_{\mathrm{T}}^{\mathrm{miss}}$: since the signal is expected to have a high $E_{\mathrm{T}}^{\mathrm{miss}}$ coming from the two neutralinos, a cut on this variable is appropriate; however, it is kept low enough to retain sensitivity to lower mass points, i.e. $E_{\mathrm{T}}^{\mathrm{miss}} > 110$ GeV.
- $E_{\mathrm{T}}^{\mathrm{miss}}$ significance: this cut is designed to remove events where $E_{\mathrm{T}}^{\mathrm{miss}}$ is a result of mismeasurement of other objects or wrong reconstruction, e.g. Z+jets events. The object based definition of $E_{\mathrm{T}}^{\mathrm{miss}}$ significance is used and a large value is required: $\mathcal{S} > 10$.
- m_{T2}: the most powerful variable to discriminate signal from background is required to have values above the W-boson mass cut-off, leading to $m_{\mathrm{T2}} > 100$ GeV cut.

Different m_{T2} cuts and ranges are used to classify exclusive and inclusive SRs:

- *exclusive regions*: these regions are binned in m_{T2} so that the shape of this distribution can provide additional discrimination between signal and background. The binning procedure is optimized to give low statistics in each bin without

[8] This method is called *shape fit*.

statistical uncertainties become dominant. The non-uniform choice accounts for the broader m_{T2} tails expected in events with higher chargino and neutralino mass splitting, compared to sharper cut-off in events with a lower one. The m_{T2} values defining the lower bounds of the bins are: 100, 105, 110, 120, 140, 160, 180, 220 and 260 GeV; the last bin range does not include an upper threshold. The selection defining this set of exclusive SRs is reported in Table 4.5;

- *inclusive regions*: four regions are defined. Two are fully inclusive, with a different lower bound on m_{T2}, 100 and 160 GeV, to target different chargino or slepton mass regions, while two have both lower and upper bounds on m_{T2} to target models with lower endpoints. The selection defining this set of inclusive SRs is reported in Table 4.5.

Region	SR-DF-0J	SR-DF-1J	SR-SF-0J	SR-SF-1J
$n_{\text{non-b-tagged jets}}$	$= 0$	$= 1$	$= 0$	$= 1$
$m_{\ell_1\ell_2}$ [GeV]	> 100		> 121.2	
$E_{\mathrm{T}}^{\mathrm{miss}}$ [GeV]	> 110			
$\mathcal{S}$	> 10			
$n_{b\text{-tagged jets}}$	$= 0$			
Binned SRs				
m_{T2} [GeV]	$\in [100, 105)$			
	$\in [105, 110)$			
	$\in [110, 120)$			
	$\in [120, 140)$			
	$\in [140, 160)$			
	$\in [160, 180)$			
	$\in [180, 220)$			
	$\in [220, 260)$			
	$\in [260, \infty)$			
Inclusive SRs				
m_{T2} [GeV]	$\in [100, \infty)$			
	$\in [160, \infty)$			
	$\in [100, 120)$			
	$\in [120, 160)$			

Table 4.5: Definition of exclusive and inclusive Signal Regions. The bins labelled "DF" or "SF" refer to regions with different lepton flavour or same lepton flavour pair combinations, respectively, and the "0J" and "1J" labels refer to the multiplicity of non-b-tagged jets [1].

Table 4.6 shows the expected background (discussed in the next Section) yields and contributions from twelve benchmark points, four for each decay model, in the most inclusive SR, requiring $m_{\mathrm{T2}} \in [100, \infty)$.

4.7 Background estimation strategy

A careful evaluation of the expected backgrounds in the analysis event selection is crucial, both to assess for a possible signal evidence in the data or to exclude it.
The background entering the SRs can be classified in two categories, described below.

Region	SR-DF-0J	SR-DF-1J	SR-SF-0J	SR-SF-1J
$m(\tilde{\chi}_1^\pm, \tilde{\chi}_1^0) = (250, 1)$	36.47 ± 2.11	20.87 ± 1.05	33.11 ± 1.86	19.82 ± 1.12
$m(\tilde{\chi}_1^\pm, \tilde{\chi}_1^0) = (300, 50)$	26.41 ± 1.28	15.33 ± 0.72	25.40 ± 1.69	14.05 ± 0.68
$m(\tilde{\chi}_1^\pm, \tilde{\chi}_1^0) = (400, 1)$	14.48 ± 0.84	10.32 ± 0.51	13.72 ± 0.84	9.08 ± 0.61
$m(\tilde{\chi}_1^\pm, \tilde{\chi}_1^0) = (400, 100)$	12.43 ± 0.69	8.44 ± 0.46	14.34 ± 0.87	9.12 ± 0.63
$m(\tilde{\chi}_1^\pm, \tilde{\ell}, \tilde{\chi}_1^0) = (400, 250, 100)$	190.53 ± 9.53	135.05 ± 7.08	202.70 ± 10.96	144.86 ± 7.20
$m(\tilde{\chi}_1^\pm, \tilde{\ell}, \tilde{\chi}_1^0) = (600, 300, 1)$	53.79 ± 3.62	40.71 ± 2.93	55.97 ± 3.94	51.14 ± 2.50
$m(\tilde{\chi}_1^\pm, \tilde{\ell}, \tilde{\chi}_1^0) = (800, 600, 400)$	12.38 ± 0.70	8.29 ± 0.51	11.98 ± 0.75	10.93 ± 0.74
$m(\tilde{\chi}_1^\pm, \tilde{\ell}, \tilde{\chi}_1^0) = (1100, 600, 100)$	2.32 ± 0.18	1.91 ± 0.13	2.47 ± 0.17	22.84 ± 1.55
$m(\tilde{\ell}, \tilde{\chi}_1^0) = (300, 100)$	–	–	225.28 ± 12.05	136.39 ± 7.86
$m(\tilde{\ell}, \tilde{\chi}_1^0) = (400, 200)$	–	–	75.08 ± 4.29	8.76 ± 0.42
$m(\tilde{\ell}, \tilde{\chi}_1^0) = (500, 200)$	–	–	32.33 ± 2.22	41.70 ± 2.23
$m(\tilde{\ell}, \tilde{\chi}_1^0) = (600, 1)$	–	–	13.57 ± 1.11	2.08 ± 0.15
Total Expected SM	84.06 ± 10.87	69.77 ± 9.46	124.74 ± 8.53	112.70 ± 12.03
WW	59.94 ± 5.57	38.18 ± 4.82	57.66 ± 3.63	38.14 ± 2.99
WZ	1.29 ± 0.13	1.30 ± 0.17	9.10 ± 0.52	11.33 ± 0.75
ZZ	$0.00^{+0.16}_{-0.00}$	0.07 ± 0.01	32.51 ± 1.77	18.68 ± 1.24
$t\bar{t}$	16.32 ± 8.56	23.88 ± 7.85	15.16 ± 5.03	19.24 ± 9.31
Singletop	4.51 ± 2.45	3.37 ± 1.65	2.88 ± 1.69	3.99 ± 2.09
Others	0.24 ± 0.08	0.80 ± 0.13	2.07 ± 1.55	11.08 ± 4.06
FNP	1.77 ± 0.62	2.17 ± 0.60	5.37 ± 1.42	10.25 ± 1.51

Table 4.6: Expected yields in the most inclusive SRs for an integrated luminosity of 139 fb^{-1} . The expected signal contribution is also reported for three sets of benchmark points, whose masses are expressed in GeV. The "Other" background is comprehensive of all processes that contribute marginally, such as Higgs boson, Z+jets, multiboson production and $t\bar{t}$ produced in association with a gauge boson. The FNP lepton background is calculated using the data-driven matrix method. Statistical (for both signal and background samples) and systematic (only for background samples) uncertainties are included. Entries marked "–" indicate a negligible contribution.

- *Irreducible*: the same final state is shared between signal and background. If the expected contribution of the latter is small in the SR, the corresponding Monte Carlo yields can be a sufficiently accurate estimate.
- *Reducible*: the final state is different with respect to the signal one but, due to misidentification, errors in reconstruction, etc., the two signatures may become compatible, e.g. if at least one of the leptons in the final state is a misidentified jet or a non-prompt lepton emerging from decays of particles in jets. Also the $E_{\mathrm{T}}^{\mathrm{miss}}$ in the final state can be originated from objects mismeasured in the corresponding detectors.

For both reducible and irreducible backgrounds, an important point to highlight is that if the expected contribution in the SR is not negligible, dedicated procedure to evaluate them must be adopted. They will be described in the following paragraphs of this Section.

4.7.1 Reducible background: the Matrix Method

In this analysis the reducible background of FNP is estimated using a data-driven technique, known as *Matrix Method* [223]. This technique relies on the definition of two categories of leptons, *loose* and *tight*: for the current analysis they correspond to the baseline and signal lepton definitions reported in Table 4.3.
According to which identification criteria are fulfilled, three cases, with the corresponding labels, can occur:

- T (*Tight*): leptons pass the tight identification criteria.
- l (*exclusive loose*): leptons pass loose but not tight criteria.
- L (*inclusive loose*): leptons pass at least the loose identification criteria.

All the observed events containing two inclusive loose leptons are counted, ordered in p_{T}, and classified into four different categories, N_{TT}, N_{Tl}, N_{lT} and N_{ll}, where the first subscript index corresponds to the leading lepton, and the second one to the subleading. Based on this classification, two probabilities can be defined: the *real efficiency* r, i.e. the probability for a real lepton passing loose criteria to pass the tight ones as well, and the *fake rate* f, i.e. the probability for a fake[9] lepton passing loose criteria to pass the tight ones as well. If an event contains two leptons of opposite flavor ($e\mu$ or μe) four probabilities are needed, since the electron and muon probabilities are in general different. For the leading and subleading leptons real and fake probabilities are, respectively, r_1, r_2, f_1 and f_2.
From these inputs the number of events with two real (N_{LL}^{RR}), one real and one fake (N_{LL}^{RF} and N_{LL}^{FR}) and two fake (N_{LL}^{FF}) leptons can be estimate by inverting the following matrix:

$$\begin{pmatrix} N_{TT} \\ N_{Tl} \\ N_{lT} \\ N_{ll} \end{pmatrix} = \begin{pmatrix} r_1 r_2 & r_1 f_2 & f_1 r_2 & f_1 f_2 \\ r_1(1-r_2) & r_1(1-f_2) & f_1(1-r_2) & f_1(1-f_2) \\ (1-r_1)r_2 & (1-r_1)f_2 & (1-f_1)r_2 & (1-f_1)f_2 \\ (1-r_1)(1-r_2) & (1-r_1)(1-f_2) & (1-f_1)(1-r_2) & (1-f_1)(1-f_2) \end{pmatrix} \begin{pmatrix} N_{LL}^{RR} \\ N_{LL}^{RF} \\ N_{LL}^{FR} \\ N_{LL}^{FF} \end{pmatrix}, \tag{4.8}$$

[9]It is generically referred to both FNP leptons.

then obtaining:

$$N_{LL}^{RR} = \quad (1-f_1)(1-f_2)N_{TT} - [f_2(1-f_1)]\,N_{Tl} - [f_1(1-f_2)]\,N_{lT} + f_1 f_2 N_{ll} \quad (4.9a)$$
$$N_{LL}^{RF} = -(1-f_1)(1-r_2)N_{TT} + [r_2(1-f_1)]\,N_{Tl} + [f_1(1-r_2)]\,N_{lT} + f_1 r_2 N_{ll} \quad (4.9b)$$
$$N_{LL}^{RF} = -(1-f_2)(1-r_1)N_{TT} + [f_2(1-r_1)]\,N_{Tl} + [r_1(1-f_2)]\,N_{lT} + f_2 r_1 N_{ll} \quad (4.9c)$$
$$N_{LL}^{FF} = \quad (1-r_1)(1-r_2)N_{TT} - [r_2(1-r_1)]\,N_{Tl} - [r_1(1-r_2)]\,N_{lT} + r_1 r_2 N_{ll} \quad (4.9d)$$

These are the expected number of events with two, one and zero real leptons in a sample of two inclusive loose leptons. Since this analysis searches for new physics in the dilepton channel requiring two tight leptons in the final state, these numbers need to be translated into the corresponding yields for a sample containing two tight leptons. This is performed by multiplying Equations 4.9 by the appropriate probabilities:

$$N_{TT}^{RR} = r_1 r_2 N_{LL}^{RR} \quad (4.10a)$$
$$N_{TT}^{RF} = r_1 f_2 N_{LL}^{RF} \quad (4.10b)$$
$$N_{TT}^{FR} = f_1 r_2 N_{LL}^{FR} \quad (4.10c)$$
$$N_{TT}^{FF} = f_1 f_2 N_{LL}^{FF}. \quad (4.10d)$$

Then, the number of events with at least one fake lepton is obtained easily by summing up the three categories of events with a fake tight leptons, specifically Equations 4.10b, 4.10c and 4.10d. Additional details on the method are reported in Appendix A.

4.7.2 Irreducible background: the normalization procedure

The Signal Regions are tipically defined to cover a phase space which can feature extreme kinematics. However, Monte Carlo simulations are often tuned in regions more easily accessible, in order to speed up the testing of their predictions. Then, a connection between the background yields expected in these regions and the ones in the SRs is needed.
For this reason, it is a common method to use a semi-data-driven procedure which corrects the Monte Carlo yields on the basis of data observation in suitable regions. Such procedure relies on the definition of two additional sets of phase space regions, called *Control Regions* (CRs) and *Validation Regions* (VRs). These regions must be defined to be orthogonal to the SRs and among them and they should be as close as possible to the SRs, in order to have a similar kinematics.
For each irreducible dominant background in the SRs, one or more dedicated CRs are defined such as to be enriched in that particular background process under study; then, the Monte Carlo predictions in these regions are normalized to data using a likelihood fitting procedure. The obtained *normalization factors*[10] of the relevant backgrounds are validated in the VRs, which are not used to constrain the likelihood fit, but are used to verify the goodness of the fit in terms of the yields and of the shapes of the relevant kinematic distributions, which have to agree within uncertainties in regions of the phase space kinematically close to the SRs as well.
The full procedure is performed within the HistFitter package [224], the standard tool for SUSY searches performed by ATLAS. Internally, HistFitter uses the software packages HistFactory [225] and RooStats [226], which are based on RooFit [227] and Root [228, 229]. HistFitter extends these tools in four fundamental areas for a generic analysis:

[10] They are often referred to as *transfer factors* or, in a simpler naming convention, *scale factors*.

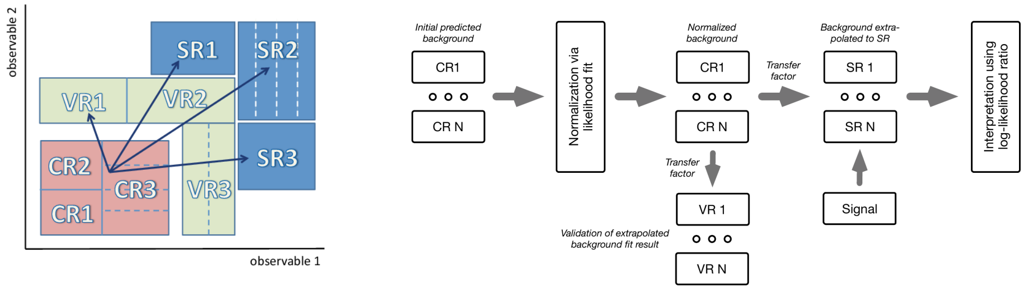

(a) Schematic view of an analysis strategy with multiple CRs, VRs and SRs. All regions can have single or multiple bins, with the dashed lines as separation. The extrapolation from CRs to SRs is verified in the VRs.

(b) Simplified overview of an analysis workflow within HistFitter: common normalization factors are applied to the backgrounds, whose yields are affected by a combination of the aforementioned factors with the nuisance parameters, with a procedure discussed in the following Paragraph.

Figure 4.4: Schematic summary of the procedure for the normalization of irreducible backgrounds [224].

- framework: it performs complete statistical analyses of preformatted input data within a coherent and programmable framework;
- analysis strategy: it has built-in concepts of CRs, VRs and SRs, used to constrain, extrapolate and validate data model predictions across an analysis;
- bookkeeping: it can keep track of numerous data models, performing statistical tests and model-parameter scans of all these models in an organized way;
- presentation and interpretation: it provides a collection of methods to determine the statistical significance of signal hypotheses and estimate the quality of likelihood fits, whose results are presented in suitable tables and plots.

Figure 4.4(a) shows a sketch of the extrapolation procedure from CRs to SRs, while Figure 4.4(b) represents a simplified analysis workflow within the HistFitter package.

Likelihood fit

Once the transfer factors μ_i have been calculated, they are used to rescale the irreducible components of the background. Therefore, the background contribution in a SR is approximately:

$$N_{\text{bkg}}(SR) \simeq \sum_{i\in\text{IR-bkg}} \mu_i N_i^{\text{exp}}(SR) + \sum_{j\in\text{bkg}} N_j^{\text{exp}}(SR), \tag{4.11}$$

where the index i runs on the list of the irreducible backgrounds entering the normalization procedure and j on the remaining ones, while the superscript "exp" refers to the purely MC background estimates. In a generic Control Region, the number of observed events in data can be related to the predictions for the various backgrounds with an Equation similar to 4.11. In principle, the calculation of the transfers factors could be done by defining a CR for each of the background components to be normalized and

then solving a system of equations. However, the drawback of this simplified approach is the poor treatment of the uncertainties on the background estimation since, for instance, correlations among them could not be taken into account correctly.
To overcome this issue, a *profile*, i.e. with an included description of uncertainties, likelihood fit is performed. In HistFitter the most general profile likelihood L is defined as the product of Poisson distributions for the event in CRs and SRs. Furthermore, this product takes into account the distributions representing the statistical constraint on uncertainties. The resulting formula[11] is

$$L(n, \boldsymbol{\theta}^0 | \mu_{\text{sig}}, \boldsymbol{s}, \boldsymbol{\mu}_{\text{bkg}}, \boldsymbol{b}, \boldsymbol{\theta}) = p_{\text{SR}} \times p_{\text{CR}} \times C(\boldsymbol{\theta}^0, \boldsymbol{\theta}) =$$
$$\prod_{i \in \text{SR}} p_i(n_i | \lambda_i(\mu_{\text{sig}}, s_i, \boldsymbol{\mu}_{\text{bkg}}, \boldsymbol{b}_i, \boldsymbol{\theta})) \times \prod_{j \in \text{CR}} p_j(n_j | \lambda_j(\mu_{\text{sig}}, s_j, \boldsymbol{\mu}_{\text{bkg}}, \boldsymbol{b}_j, \boldsymbol{\theta})) \times C(\boldsymbol{\theta}^0, \boldsymbol{\theta}) \tag{4.12}$$

The parameters entering this equation are:

- p_{SR} and p_{CR}: Poisson probabilities of observing n events, given the expected signal s and background $\boldsymbol{b}$ yields.
- μ_{sig} and $\boldsymbol{\mu}_{\text{bkg}}$: normalization factors on signal[12] and background processes.
- $\lambda_{i,j}$: expected Poisson values depending on both transfer factors (signal and background).
- $\boldsymbol{\theta}$ and $\boldsymbol{\theta}^0$: vector of *nuisance paramenters* with the corresponding central values. They are described by Normal distributions with mean zero, representing the nominal value, and width one, representing the *up* and *down* variations.
- $C(\boldsymbol{\theta}^0, \boldsymbol{\theta})$: function representing the additional constraint from the uncertainties, depending on the previous set of nuisance parameters.

The extraction of the normalization factors is performed through a maximization of the profile likelihood. However, the function used in this case is simplified with respect to the one in Equation 4.12 and it is obtained by neglecting all Poisson terms describing the SRs, as well as signal contributions by making the assumption $\mu_{\text{sig}} = 0$. In this case, the background-only hypothesis is assumed, hence the name of *background-only fit*, and it prevents any possible bias coming from the signal contamination in the CRs, which has to be supposed negligible. After the fit, the likelihood is normalized over $\boldsymbol{\mu}_{\text{bkg}}$ and $\boldsymbol{\theta}$.
Before safely applying the transfer factors to the SRs, the role of the VRs is to verify the agreement, in terms of the main kinematical variables used in the analysis and in comparing the yields, between data and MC after applying these corrections to all backgrounds.
The likelihood function and the parameters extracted during the maximization procedure can be used as input for the definition of the statistical estimator of the analysis significance, used in an enlarged fit procedure, this time including SRs. The estimator q_μ is built starting from the *profile likelihood ratio* [230], using both μ_{sig} and $\boldsymbol{\theta}$ as free parameters:

$$q_\mu = -2 \ln \lambda(\mu) \qquad \text{with} \qquad \lambda(\mu) = \frac{L(\mu_{\text{sig}}, \hat{\hat{\boldsymbol{\theta}}})}{L(\hat{\mu}_{\text{sig}}, \hat{\boldsymbol{\theta}})} \tag{4.13}$$

[11] All symbols highlighted in bold must be considered vectorial parameters.
[12] Another name of this (transfer) factor is *signal strength*: in case of $\mu_{\text{sig}} = 0$ the background-only hypothesis is assumed, while $\mu_{\text{sig}} = 1$ represents the full value predicted by the considered model.

with $\hat{\mu}_{\text{sig}}$ and $\hat{\boldsymbol{\theta}}$ the signal strength and nuisance parameters maximizing L; the $\hat{\hat{\boldsymbol{\theta}}}$ at the numerator is the specific value which maximizes the likelihood after choosing a fixed value for μ_{sig}. The presence of the nuisance parameters broadens the profile likelihood as a function of μ relative to what one would have if their values were fixed; this fact reflects the loss of information about μ due to systematic uncertainties.
By construction $0 < \lambda(\mu) < 1$, approaching the upper value once an agreement between the observation and the tested hypothesis has been found. On the other hand, $0 \leq \hat{\mu}_{\text{sig}} \leq \mu_{\text{sig}}$: the lower threshold is driven by the fact that the signal rate has to be positive, while the upper constraint is for a conservative purpose, to guarantee a one-sided confidence interval in order to avoid considering upward fluctuations of the data, such that $\hat{\mu}_{\text{sig}} > \mu_{\text{sig}}$, as signal evidence.
Introducing $f(q_\mu|\mu_{\text{sig}}, \boldsymbol{\theta})$ for the distribution of this test variable, the null hypothesis $\mathcal{H}_b$ implies a resulting p-value expressed by

$$p_b = \int_0^{Q_0} f(q_\mu|\mu_{\text{sig}} = 0, \boldsymbol{\theta})\, dq_\mu, \tag{4.14}$$

where $Q_0 \equiv q^{\text{obs}}_{\mu=0}$ is the value observed for the statistical test variable assuming $\mu_{\text{sig}} = 0$. This will lead to the exclusion of the background-only hypothesis when the corresponding Z-value is above the 5σ threshold.
The exclusion of the alternative hypothesis $\mathcal{H}_{s+b}$ has to be handled with much more care, preventing the exclusion of signal models for which the analysis has low sensitivity. The corresponding observed value is $Q_1 \equiv q^{\text{obs}}_{\mu=1}$ for the statistical test variable in the $\mu_{\text{sig}} = 1$ case and two p-values are estimated, for the signal+background (p_{s+b}) and the background-only hypotheses.

$$p_{s+b} = \int_{Q_1}^{\infty} f(q_\mu|\mu_{\text{sig}} = 1, \boldsymbol{\theta})\, dq_\mu \equiv CL_{s+b} \tag{4.15a}$$

$$p_b = \int_{-\infty}^{Q_1} f(q_\mu|\mu_{\text{sig}} = 0, \boldsymbol{\theta})\, dq_\mu \equiv 1 - CL_b \tag{4.15b}$$

The CL_s prescription [222] allows to define the variable:

$$CL_\text{s} = \frac{CL_{s+b}}{CL_b} = \frac{p_{s+b}}{1 - p_b} \tag{4.16}$$

and it is used to evaluate the $\mathcal{H}_{s+b}$ hypothesis, eventually excluding it for signal models whose CL_s is lower than a threshold. The choice of this value is usually function of the Confidence Level of the exclusion and a typical choice is to reject the model for $CL_\text{s} < 0.05$, corresponding to a Confidence Level of 95%.

4.8 Control Region definition

As can be observed in Table 4.6, the main Standard Model irreducible backgrounds in this analysis are due to the top-quark and the diboson productions; among them, WW is predominant, but WZ and ZZ are also important in SF events. Applying the previously described semi-data-driven method for the background estimate, a set of three dedicated Control Regions is defined for these backgrounds.
The WW and top-quark backgrounds depend on the leptonic decay of the W bosons with equivalent contributions in DF and SF Signal Regions. In WZ and ZZ the two

leptons in the final state mainly come from the decay of the Z boson and these processes give an important contribution to the SF Signal Regions. The cut $m_{\ell_1\ell_2} > 121.2$ GeV strongly reduce the on-shell Z bosons, while the majority of events entering the SR-SF selection comes from off-shell Z decays.
Three dedicated CRs are defined, each one targeting one of the aforementioned background category:

- *CR-WW*: this region targets the WW background, the most relevant in the analysis. A selection similar to the SR-DF-0J is applied, requiring events with DF leptons and no hadronic activity. In order to ensure orthogonality among regions, to keep high WW purity and a reasonable statistics, a low-m_{T2} range ($m_{\mathrm{T2}} \in [60, 65]$ GeV), $E_{\mathrm{T}}^{\mathrm{miss}} \in [60, 100]$ GeV and $E_{\mathrm{T}}^{\mathrm{miss}}$ significance $\mathcal{S} \in [5, 10]$ are requested.

- *CR-VZ*: this region targets the WZ and ZZ backgrounds with leptons mainly coming from Z boson decays. A selection similar to the SR-SF-0J is applied, requiring events with SF leptons and no hadronic activity. To enrich this region with Z decays, $m_{\ell_1\ell_2} \in [61.2, 121.2]$ is requested, which also ensures orthogonality with respect to the other CRs and SRs. The Z+jets background is removed requiring high $E_{\mathrm{T}}^{\mathrm{miss}}$ and $E_{\mathrm{T}}^{\mathrm{miss}}$ significance and finally, in order to define a region kinematically close to the SRs, a high cut on the stransverse mass is applied: $m_{\mathrm{T2}} > 120$ GeV.

- *CR-top*: this region targets both the $t\bar{t}$ and single-top-quark production. The region is enriched in the desired backgrounds by requiring one b-tagged jet in the final state, condition which ensures orthogonality. In order to keep the region close to the SR, $E_{\mathrm{T}}^{\mathrm{miss}}$ and $E_{\mathrm{T}}^{\mathrm{miss}}$ significance cuts are identical to the SRs ones and no additional hadronic activity is required. Loosening the cut on the stransverse mass ($m_{\mathrm{T2}} > 80$ GeV) ensures enough statistics, at the same time keeping low contamination from WW.

Table 4.7 reports the definition of the three Control Regions, while Table 4.8 shows the expected background yields and signal contamination from few benchmark points for each one of the signal models under study.

Region	CR-WW	CR-VZ	CR-top
Lepton flavour	DF	SF	DF
$n_{b\text{-tagged jets}}$	$= 0$	$= 0$	$= 1$
$n_{\text{non-}b\text{-tagged jets}}$	$= 0$	$= 0$	$= 0$
m_{T2} [GeV]	$\in [60, 65]$	> 120	> 80
$E_{\mathrm{T}}^{\mathrm{miss}}$ [GeV]	$\in [60, 100]$	> 110	> 110
$\mathcal{S}$	$\in [5, 10]$	> 10	> 10
$m_{\ell_1\ell_2}$ [GeV]	> 100	$\in [61.2, 121.2]$	> 100

Table 4.7: Control Region definitions for extracting normalization factors for the dominant background processes. “DF” or “SF” refer to regions with different lepton flavour or same lepton flavour pair combinations, respectively [1].

Finally, Figure 4.5 shows that the signal contamination, reported as a percentage of the total expected Standard Model background yield for all points of the grid of the

Region	CR-WW	CR-VZ	CR-top
$m(\tilde{\chi}_1^{\pm}, \tilde{\chi}_1^0) = (250, 1)$	3.94 ± 0.45	13.34 ± 0.63	2.05 ± 0.34
$m(\tilde{\chi}_1^{\pm}, \tilde{\chi}_1^0) = (300, 50)$	1.44 ± 0.19	8.50 ± 0.58	1.24 ± 0.15
$m(\tilde{\chi}_1^{\pm}, \tilde{\chi}_1^0) = (400, 1)$	0.46 ± 0.07	3.71 ± 0.28	0.88 ± 0.25
$m(\tilde{\chi}_1^{\pm}, \tilde{\chi}_1^0) = (400, 100)$	0.65 ± 0.18	3.15 ± 0.14	0.46 ± 0.08
$m(\tilde{\chi}_1^{\pm}, \tilde{\ell}, \tilde{\chi}_1^0) = (400, 250, 100)$	7.15 ± 1.06	48.03 ± 3.26	6.88 ± 0.79
$m(\tilde{\chi}_1^{\pm}, \tilde{\ell}, \tilde{\chi}_1^0) = (600, 300, 1)$	0.32 ± 0.10	4.82 ± 0.60	3.09 ± 0.39
$m(\tilde{\chi}_1^{\pm}, \tilde{\ell}, \tilde{\chi}_1^0) = (800, 600, 400)$	0.19 ± 0.05	1.43 ± 0.08	0.54 ± 0.09
$m(\tilde{\chi}_1^{\pm}, \tilde{\ell}, \tilde{\chi}_1^0) = (1100, 600, 100)$	0.01 ± 0.01	0.07 ± 0.00	0.14 ± 0.02
$m(\tilde{\ell}, \tilde{\chi}_1^0) = (300, 100)$	–	29.95 ± 1.66	–
$m(\tilde{\ell}, \tilde{\chi}_1^0) = (400, 200)$	–	8.20 ± 0.83	–
$m(\tilde{\ell}, \tilde{\chi}_1^0) = (500, 200)$	–	1.77 ± 0.14	–
$m(\tilde{\ell}, \tilde{\chi}_1^0) = (600, 1)$	–	0.46 ± 0.03	–
Total Expected SM	875.82 ± 55.43	687.26 ± 12.01	384.93 ± 13.43
WW	528.16 ± 4.67	15.14 ± 0.62	4.34 ± 2.06
WZ	9.92 ± 0.38	158.20 ± 1.62	0.27 ± 0.13
ZZ	0.24 ± 0.05	486.56 ± 4.88	–
$t\bar{t}$	210.26 ± 53.61	2.16 ± 1.51	327.20 ± 10.55
Singletop	106.54 ± 5.44	0.79 ± 0.43	46.68 ± 2.77
Others	0.17 ± 0.06	19.40 ± 7.36	2.21 ± 0.20
FNP	20.52 ± 8.52	$5.02^{+5.73}_{-5.02}$	4.24 ± 2.16

Table 4.8: Expected yields in the three CRs for an integrated luminosity of 139 fb^{-1} . The expected signal contribution is also reported for three sets of benchmark points, whose masses are expressed in GeV. The "Other" background is comprehensive of all processes that contribute marginally, such as Higgs boson, Z+jets, multiboson production and $t\bar{t}$ produced in association with a gauge boson. The FNP lepton background is calculated using the data-driven matrix method. Statistical (for both signal and background samples) and systematic (only for background samples) uncertainties are included. Entries marked "–" indicate a negligible contribution.

chargino with W-boson-mediated decay, is low as requested to apply the background-only fit procedure. A similar check was performed on the other two signal grids, finding negligible percentages as well.

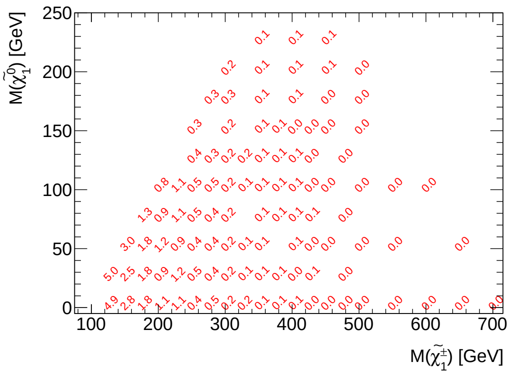

(a) CR-WW

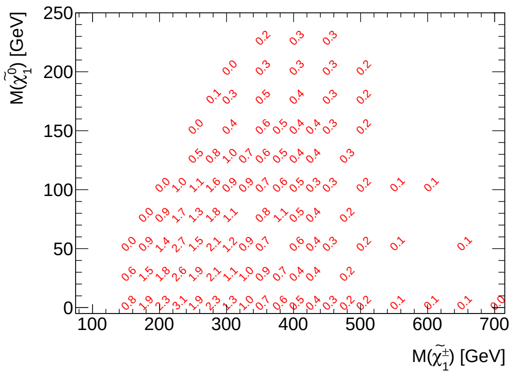

(b) CR-VZ

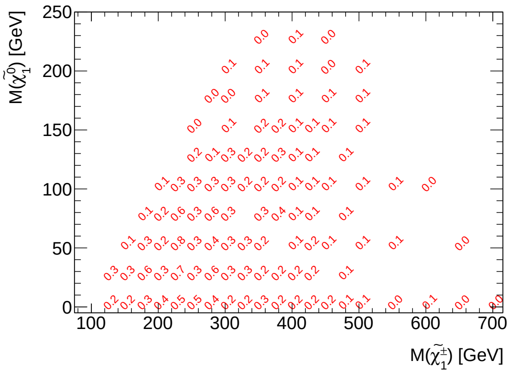

(c) CR-top

Figure 4.5: Signal contamination from the chargino with W-boson-mediated decay as a percentage of the total expected Standard Model background for CR-WW 4.5(a), CR-VZ 4.5(b) and CR-top 4.5(c).

4.9 Validation Region definition

Once the transfer factors have been derived, the next step is to validate the normalization procedure performed in a set of dedicated Validation Regions, as already discussed in Section 4.7.2. The aim of these regions is to assess the correctness of the background-only fit results by comparing data and MC predictions, in terms of yields and shapes of the relevant kinematic distributions.
Two categories of VRs are defined in this analysis: one requires a two lepton selection, the other one a three lepton selection.

4.9.1 Validation Regions with a two lepton selection

Six VRs are defined using a two lepton selection: half of them are used to validate WW and VZ diboson processes, while the remaining half is devoted to the validation of the $t\bar{t}$ and Wt in different regions of $E_{\mathrm{T}}^{\mathrm{miss}}$ and m_{T2}, since the contributions from top-quark backgrounds in the VRs for WW are not negligible:

- *VR-WW-0J*: this region is dedicated to the validate of the WW normalization provided by CR-WW. For this reason, the event selection is similar to the CR, requiring DF leptons, no hadronic activity and same invariant mass selections. m_{T2} is required to be in a range closer to the SRs: $m_{\mathrm{T2}} \in [65, 100]$ GeV. $E_{\mathrm{T}}^{\mathrm{miss}}$ and $E_{\mathrm{T}}^{\mathrm{miss}}$ significance cuts are made looser than in the SRs in order to gain in statistics: $E_{\mathrm{T}}^{\mathrm{miss}} > 60$ GeV and $\mathcal{S} > 5$.
- *VR-WW-1J*: this region is dedicated to validate the WW normalization in presence of exactly one central light jet, while all other cuts are kept identical to the VR-WW-0J ones. It is defined in order to validate the transfer factor extrapolation to the SRs where the presence of an ISR jet is allowed.
- *VR-VZ*: this region is dedicated to the validation of the WZ and ZZ normalization. The selection is similar to the corresponding CR-VZ, requiring events with SF leptons close to the Z-peak, no hadronic activities, same cuts on $E_{\mathrm{T}}^{\mathrm{miss}}$ and $E_{\mathrm{T}}^{\mathrm{miss}}$ significance. The orthogonality with respect to the CR is ensured by changing the cut on the stransverse mass ($m_{\mathrm{T2}} \in [100, 120]$ GeV).
- *VR-top-low*: this region is dedicated to the validation of the top-quark normalization in the low-m_{T2} range ($m_{\mathrm{T2}} \in [80, 100]$ GeV), as in VR-WW-0J and VR-WW-1J. The selection is similar to CR-top, requiring one b-tagged jet to enrich it with the desired background. The cut on $E_{\mathrm{T}}^{\mathrm{miss}}$ significance is loosened.
- *VR-top-high*: this region is also dedicated to the validation of top-quark background, but in a higher stransverse mass region. It requires $m_{\mathrm{T2}} > 100$ GeV, providing validation in the high-m_{T2} region where the the SRs are defined. The request of an additional central light jet is applied to ensure orthogonality with respect to CR-top;
- *VR-top-WW*: the aim of this region is to validate the top-quark background performing a selection similar to the CR-WW. In fact, it requires the same $E_{\mathrm{T}}^{\mathrm{miss}}$, $E_{\mathrm{T}}^{\mathrm{miss}}$ significance and m_{T2} as CR-WW, providing validation of the modelling of top-quark production in this region. The orthogonality with CR-WW is guaranteed by requesting hadronic activity in the event.

Table 4.9 reports the definition of the six Validation Regions, while Table 4.10 shows the expected background yields and signal contamination from few benchmark points for each one of the signal models under study.

Region	VR-WW-0J	VR-WW-1J	VR-VZ	VR-top-low	VR-top-high	VR-top-WW
Lepton flavour	DF	DF	SF	DF	DF	DF
$n_{b\text{-tagged jets}}$	$= 0$	$= 0$	$= 0$	$= 1$	$= 1$	$= 1$
$n_{\text{non-}b\text{-tagged jets}}$	$= 0$	$= 1$	$= 0$	$= 0$	$= 1$	$= 1$
m_{T2} [GeV]	$\in [65, 100]$	$\in [65, 100]$	$\in [100, 120]$	$\in [80, 100]$	> 100	$\in [60, 65]$
$E_{\mathrm{T}}^{\mathrm{miss}}$ [GeV]	> 60	> 60	> 110	> 110	> 110	$\in [60, 100]$
$\mathcal{S}$	> 5	> 5	> 10	$\in [5, 10]$	> 10	$\in [5, 10]$
$m_{\ell_1\ell_2}$ [GeV]	> 100	> 100	$\in [61.2, 121.2]$	> 100	> 100	> 100

Table 4.9: Validation region definitions used to study the modelling of the SM backgrounds. "DF" or "SF" refer to regions with different lepton flavour or same lepton flavour pair combinations, respectively [1].

Finally, Figure 4.6 shows that the signal contamination, reported as a percentage of

Region	VR-WW-0J	VR-WW-1J	VR-VZ	VR-top-low	VR-top-high	VR-top-WW
$m(\tilde{\chi}_1^{\pm}, \tilde{\chi}_1^0) = (250, 1)$	37.67 ± 2.00	21.33 ± 0.81	6.39 ± 0.46	0.06 ± 0.01	0.51 ± 0.15	$0.04^{+0.15}_{-0.04}$
$m(\tilde{\chi}_1^{\pm}, \tilde{\chi}_1^0) = (300, 50)$	18.92 ± 1.17	10.34 ± 0.53	2.85 ± 0.50	0.04 ± 0.01	0.80 ± 0.13	–
$m(\tilde{\chi}_1^{\pm}, \tilde{\chi}_1^0) = (400, 1)$	5.12 ± 0.33	3.99 ± 0.20	0.87 ± 0.11	–	0.75 ± 0.12	–
$m(\tilde{\chi}_1^{\pm}, \tilde{\chi}_1^0) = (400, 100)$	7.01 ± 0.42	2.87 ± 0.24	0.82 ± 0.09	–	0.71 ± 0.13	–
$m(\tilde{\chi}_1^{\pm}, \tilde{\ell}, \tilde{\chi}_1^0) = (400, 250, 100)$	73.41 ± 4.91	46.63 ± 4.66	5.56 ± 0.89	–	7.21 ± 0.80	–
$m(\tilde{\chi}_1^{\pm}, \tilde{\ell}, \tilde{\chi}_1^0) = (600, 300, 1)$	1.68 ± 0.13	1.45 ± 0.12	0.03 ± 0.02	–	0.60 ± 0.08	–
$m(\tilde{\chi}_1^{\pm}, \tilde{\ell}, \tilde{\chi}_1^0) = (800, 600, 400)$	9.22 ± 0.40	4.28 ± 0.37	0.28 ± 0.10	–	1.74 ± 0.39	–
$m(\tilde{\chi}_1^{\pm}, \tilde{\ell}, \tilde{\chi}_1^0) = (1100, 600, 100)$	0.15 ± 0.01	0.09 ± 0.02	–	–	0.13 ± 0.03	–
$m(\tilde{\ell}, \tilde{\chi}_1^0) = (300, 100)$	–	–	3.87 ± 0.25	–	–	–
$m(\tilde{\ell}, \tilde{\chi}_1^0) = (400, 200)$	–	–	–	–	–	–
$m(\tilde{\ell}, \tilde{\chi}_1^0) = (500, 200)$	–	–	0.37 ± 0.08	–	–	–
$m(\tilde{\ell}, \tilde{\chi}_1^0) = (600, 1)$	–	–	–	–	–	–
Total Expected SM	2669.95 ± 125.43	3015.50 ± 329.44	360.09 ± 39.93	223.20 ± 19.20	61.74 ± 8.50	1023.89 ± 70.35
WW	1229.62 ± 44.14	790.23 ± 58.26	13.96 ± 1.33	1.63 ± 0.52	2.04 ± 1.05	12.77 ± 1.50
WZ	28.80 ± 1.27	22.75 ± 1.73	83.80 ± 6.99	$0.04^{+0.15}_{-0.04}$	$0.13^{+0.47}_{-0.13}$	0.45 ± 0.11
ZZ	0.42 ± 0.05	0.33 ± 0.05	225.92 ± 18.97	–	–	$0.01^{+0.02}_{-0.01}$
$t\bar{t}$	960.22 ± 106.75	1699.71 ± 304.60	12.68 ± 3.77	189.56 ± 17.54	48.98 ± 8.08	790.35 ± 67.15
Singletop	406.36 ± 21.46	462.22 ± 34.11	2.64 ± 1.64	29.42 ± 2.71	5.55 ± 1.66	219.93 ± 9.28
Others	0.92 ± 0.30	2.06 ± 0.52	$20.86^{+26.98}_{-20.86}$	0.28 ± 0.06	3.20 ± 0.20	0.39 ± 0.11
FNP	43.63 ± 22.80	38.21 ± 21.48	$0.23^{+2.09}_{-0.23}$	2.27 ± 1.45	1.84 ± 0.46	–

Table 4.10: Expected yields in the six VRs for an integrated luminosity of 139 fb^{-1} . The expected signal contribution is also reported for three sets of benchmark points, whose masses are expressed in GeV. The "Other" background is comprehensive of all processes that contribute marginally, such as Higgs boson, Z+jets, multiboson production and $t\bar{t}$ produced in association with a gauge boson. The FNP lepton background is calculated using the data-driven matrix method. Statistical (for both signal and background samples) and systematic (only for background samples) uncertainties are included. Entries marked "–" indicate a negligible contribution.

the total expected Standard Model background yield for all points of the grid involving the chargino with W-boson-mediated decay, is low. A similar check was performed on the other two signal grids, finding negligible percentages as well.

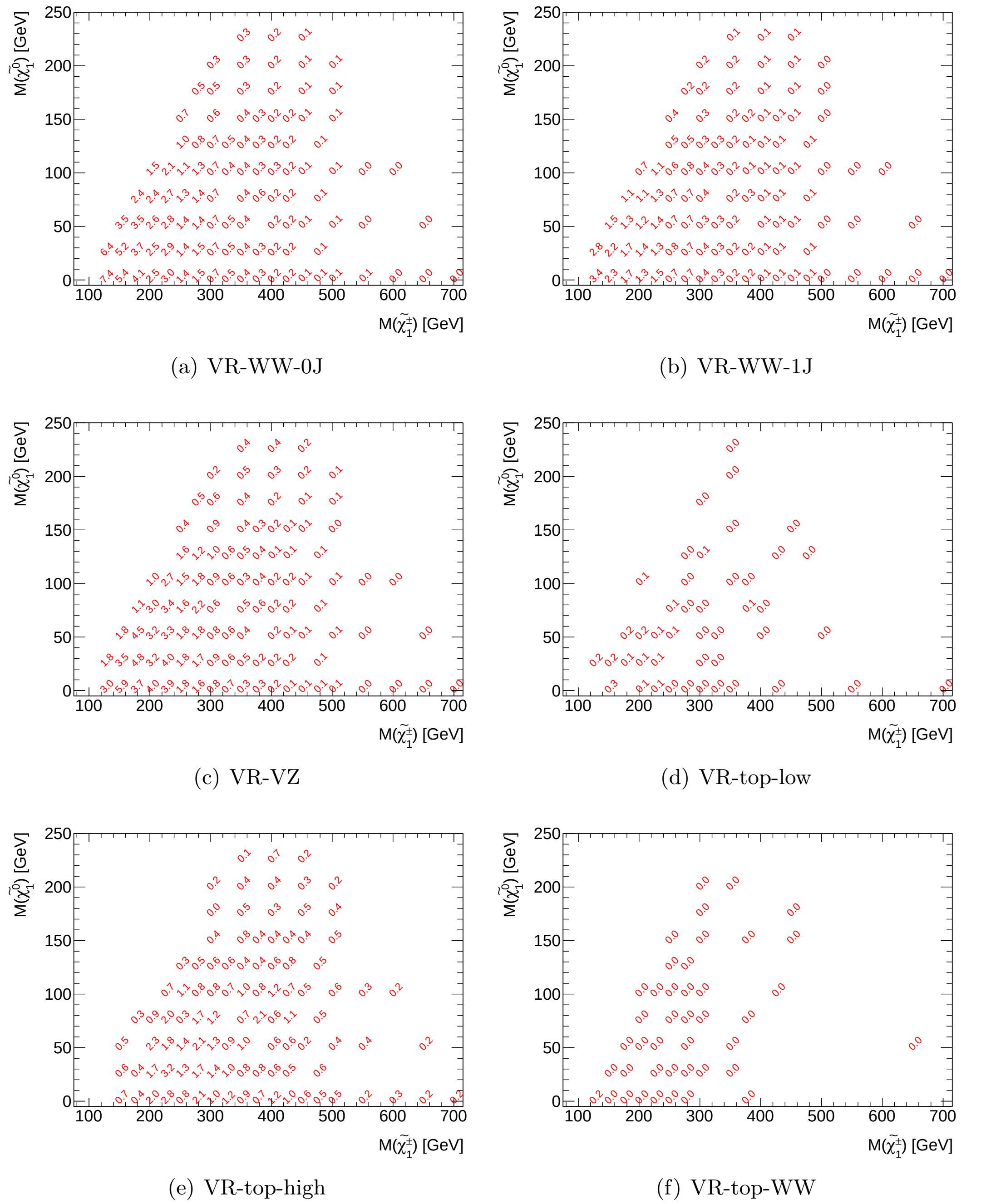

(a) VR-WW-0J

(b) VR-WW-1J

(c) VR-VZ

(d) VR-top-low

(e) VR-top-high

(f) VR-top-WW

Figure 4.6: Signal contamination from the chargino with W-boson-mediated decay SUSY model as a percentage of the total expected Standard Model backround for VR-WW-0J 4.6(a), VR-WW-1J 4.6(b), VR-VZ 4.6(c), VR-top-low 4.6(d), VR-top-high 4.6(e) and VR-top-WW 4.6(f).

4.9.2 Validation Regions with a three lepton selection

The diboson WW background is the dominant contribution at high stransverse mass, but both the CRs and VRs are defined in a relatively low-m_{T2} range. This is due to the difficulty to find a region to validate the WW modelling at high-m_{T2} values without retaining a significant signal contamination. For this reason, a region with a three lepton event selection is used to validate the modelling in the high-m_{T2} region of the WW background, closer to the SRs. The procedure applied is described in the following steps.

- Events are selected to have exactly three signal leptons in the final state, assumed to come from the decay of a WZ diboson process. Among the three leptons, the two ones supposed to come from the decay of the Z form a SF pair with opposite charges (SFOS), having an invariant mass within 10 GeV with respect to the Z peak ($|m_{ell_1\ell_2} - m_Z| < 10$ GeV). In case of ambiguity in the choice, the pair with the invariant mass closest to the Z mass is chosen.

- The transverse momentum of the lepton belonging to the SFOS pair and having the same charge as the third lepton (assumed to come from the decay of the W boson) is added to a recalculation of the $E_{\mathrm{T}}^{\mathrm{miss}}$. For sufficiently high energy leptons like the ones in the analysis, this procedure allows to consider it as a neutrino in a WW event. The resulting selected class of events is called *pseudo-twoLep* events.

- The pseudo-twoLep category of events is normalized to data in a region where the original $E_{\mathrm{T}}^{\mathrm{miss}}$ coming from the three lepton event is $E_{\mathrm{T}}^{\mathrm{miss}} \in [40, 170]$ GeV, to minimize possible overlaps with the SRs defined for other SUSY models having three leptons as final state signature, while being consistent with the preliminary event selection of this analysis; in addition, a b-jet veto is applied and the number of central light jets is requested to be at least one to emulate the Signal Regions, the p_{T} of both OS leptons and their invariant mass larger than 25 GeV;

- The resulting m_{T2} and $E_{\mathrm{T}}^{\mathrm{miss}}$ distributions are compared to data to validate the diboson modelling. Since, with this selection, there is a good agreement between the shapes of the m_{T2} distributions observed in data and simulation, no additional systematic uncertainty is applied to the WW background at high m_{T2}.

4.10 Sources of uncertainty

The background and signal predictions provided by MC are affected by several sources of uncertainty, mainly divided in two categories: *experimental* and *theoretical* uncertainties. Both of them are taken into account by varying the physical quantities provided by MC and affected by each uncertainty.
The experimental uncertainties try to estimate the effects which can impact on the final analysis objects, in reconstruction or identification, due to the ATLAS detector. The dominant sources of theoretical uncertainty are related to the uncertainties in the MC modelling, e.g. to the choice of a particular generator.

4.10.1 Experimental uncertainties

- **Electrons**: the two main sources of uncertainty considered in this analysis are the ones related to the electron energy resolution and energy scale, both calculated by applying $\pm 1\sigma$ variations to the relative factors.

- **Muons**: as for electrons, the two main sources of uncertainty taken into account are the ones on the muon momentum resolution and on the momentum scale. Concerning resolution, uncertainties are calculated by applying $\pm 1\sigma$ variations on the Inner Detector and Muon Spectrometer tracks, while for momentum scale they are calculated from $\pm 1\sigma$ variations on the scale of the muon momentum.

- **Lepton Scale Factors**: for both electrons and muons, uncertainties related to the scale factors for reconstruction, identification, isolation and trigger efficiencies are computed by considering $\pm 1\sigma$ errors on the corresponding scale factors, applied as event-based weights.

- **Jets**: two main categories of uncertainty are considered for jets.
  - **Energy**: it includes uncertainties on Jet Energy Scale (JES) and Jet Energy Resolution (JER). Concerning JES, several sources of uncertainty are taken into account: the $\pm 1\sigma$ variations are derived using a combination of data and simulation, through measurements of the transverse momentum balance between a jet and reference object in dijet events, Z+jets, γ+jets and multi-jet events. Propagation of single particle and test beam, pile-up, flavour related, punch-through and Monte Carlo non-closure uncertainties are considered as well. Regarding JER, $\pm 1\sigma$ uncertainties are calculated through a smearing process of Monte Carlo jets to data in dijet events.
  - **Scale Factors**: it is related to the scale factors associated with flavour-tagging and JVT efficiencies. Flavour-tagging ones are evaluated considering $\pm 1\sigma$ variations on the error on the scale factor, which accounts for differences between data and simulation in the b-jet identification efficiency. The uncertainties on JVT efficiencies account for both the statistical uncertainty and the error on the estimation of the residual contamination from pile-up jets after pile-up suppression.

- **Missing Transverse Energy**: in addition to the uncertainties directly coming from all the object categories entering the respective $E_{\mathrm{T}}^{\mathrm{miss}}$ term calculations, the uncertainties on the resolution and the scale of the track soft-term are included. Both are evaluated taking into account the $\pm 1\sigma$ variations on the different predictions considering 2015 data and Monte Carlo samples from different generators (POWHEG+PYTHIA 8 and MADGRAPH) and the effect of using the FULLSIM with respect to the ATLFAST-II simulation.

- **Luminosity**: a 1.7% uncertainty [231] in the measurement of the combined luminosity for the entire Run II is applied. The total uncertainties on the integrated luminosities for each individual year of data-taking range from 2.0-2.4%, being partially correlated among years.

- **Pile-up**: it is the uncertainty on the pile-up reweighting procedure used to evaluate the discrepancy between the observed distribution of the average number of collisions per bunch crossing in the Monte Carlo samples with respect to data.

- **Fake Estimation**: several sources of uncertainty are taken into account in the final estimate of FNP leptons from the Matrix Method. The main contributions are:
  - **Statistics**: it is the uncertainty related to the limited statistics in Control Regions where fake rates and real efficiencies are calculated. The uncertainty is calculated by varying fake rates and real efficiencies $\pm 1\sigma$ around the nominal value and the final estimates from these variations are then compared with the nominal ones.
  - **Weights**: it is the uncertainty on the weight for each fake component. It is extracted by examining six different regions. Standard baseline selection is applied to all of the six regions, but, on top of that, there is one additional cut applied for each region, meant to mimic the Signal Regions. The extreme values of the FNP estimates are taken as the downward and upward uncertainties coming from the weights.
  - **Numbers of N_{TT}, N_{Tl}, N_{lT} and N_{ll} events**: this contribution is calculated by taking the sum of the squared weights in each region.
  - **Subtraction of real leptons**: it is the uncertainty coming from the real lepton contamination in the Heavy Flavour Control Regions. Each MC process is scaled up and down 10% of the nominal and the corresponding fake rates are calculated and separate estimations are carried out using these fake rates. The spread in the estimations, compared with the nominal, is used to estimate the uncertainty.

4.10.2 Theoretical uncertainties

Several sources of theoretical uncertainty in the modelling of the dominant backgrounds are considered. They are described in the following two paragraphs.

Top-quark uncertainties

The $t\bar{t}$ background is affected by uncertainties associated to the parton shower, the MC generator and the amount of Initial and Final State Radiation (ISR/FSR). The systematic effect due to the parton shower is evaluated by comparing the difference between the predictions of the nominal POWHEG-BOX interfaced to either PYTHIA 8.186 or HERWIG 7.04.
The uncertainty associated with the choice of event generator is estimated by comparing the nominal POWHEG+PYTHIA 8 samples with the samples generated with aMC@NLO+PYTHIA.
The $t\bar{t}$ uncertainty coming from the modelling of Initial and Final State Radiation is calculated by comparing the predictions of the nominal sample with two alternative samples, generated with POWHEG-BOX interfaced to PYTHIA 8.186 but with the radiation settings varied.
For the single-top-quark production (Wt process) an uncertainty is assigned to the treatment of the interference between the Wt and $t\bar{t}$ samples. This is done by comparing the nominal samples generated using the *Diagram Removal* (DR) method with samples generated using the *Diagram Subtraction* method (DS) [232].
Plots representing the different contributions for $t\bar{t}$ and Wt processes, taken into account in the theoretical uncertainty estimations, are shown in Figure 4.7.

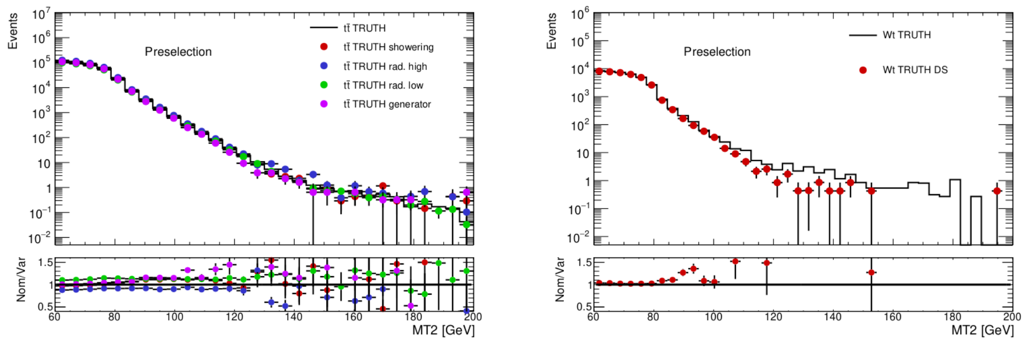

(a) (b)

Figure 4.7: Comparison of the m_{T2} distributions between the nominal $t\bar{t}$ 4.7(a) and Wt 4.7(b) samples with respect to the systematic variations used in the theoretical uncertainties estimation. A preliminary event selection is considered, with the request of $m_{\mathrm{T2}} > 60$ GeV.

Monte Carlo simulations are produced with a large, but finite, number of events. In the high-m_{T2} selection, corresponding to the SR definition in the analysis, the effect of the Monte Carlo fluctuations due to the limited statistics can be relevant, as it can be observed in Figure 4.7. Theoretical uncertainties are evaluated changing internal parameters of the simulation, or the generator itself, then comparing the relative predictions at truth level.
Being designed to be used by multiple analyses, nominal samples are designed to be produced with very high number of events, with minimal uncertainties coming from the Monte Carlo statistics. On the other hand, alternative samples are often produced with a reduced statistics with respect to the nominal ones, leading to higher statistical errors than the fluctuations due to the variations of the wanted parameters and, therefore, resulting in a not accurate estimate of the theoretical uncertainties. This effect is very important in the exclusive SRs in the analysis, because of the limited statistics.
To overcome this problem, the systematic variation is performed in the most inclusive region ($m_{\mathrm{T2}} > 100$ GeV), then applied to each of the exclusive SRs, to reduce statistical fluctuations. In addition, $E_{\mathrm{T}}^{\mathrm{miss}}$ significance requirements are relaxed for all regions, leaving only an inclusive requirement of $\mathcal{S} > 5$ applied. Since both $t\bar{t}$ and Wt processes are normalized in the CRs, the same normalization must be applied in the computation of the variations. For a generic region R, the percentage uncertainty in this region is calculated using the formula

$$\sigma_{\mathrm{syst.}}^{\mathrm{top}}(R) = \left(\frac{N^{\mathrm{Nom.}}(R)}{N^{\mathrm{Nom.}}(CR)} - \frac{N^{\mathrm{Var.}}(R)}{N^{\mathrm{Var.}}(CR)} \right) \left(\frac{N^{\mathrm{Nom.}}(CR)}{N^{\mathrm{Nom.}}(R)} \right). \tag{4.17}$$

Diboson uncertainties

For the POWHEG diboson samples, uncertainties in the Monte Carlo modelling are estimated by varying the renormalization and factorization scales used to generate the samples, as well as the PDF sets. Different PDF sets are implemented in the samples and a combination of all available variations is considered, in order to build a coherent uncertainty. A comparison at the level of a preliminary event selection is shown in Figure 4.8.

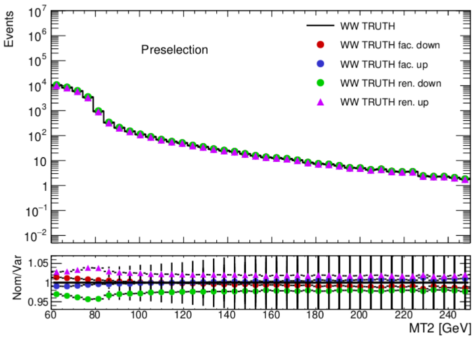

(a) WW process.

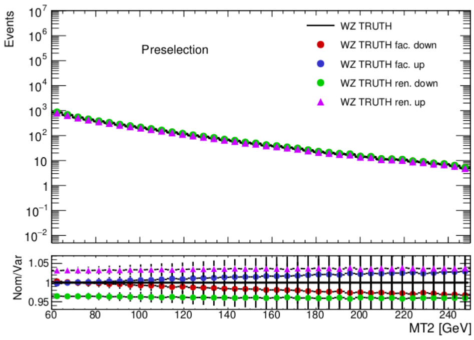

(b) WZ process.

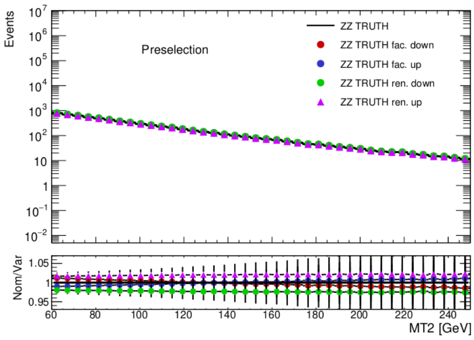

(c) ZZ process.

Figure 4.8: Comparison of the m_{T2} distributions between the nominal diboson samples for WW 4.8(a), WZ 4.8(b) and ZZ 4.8(c) processes and the systematic variations used in the theoretical uncertainties estimation. A preliminary event selection is considered, with the request of $m_{\mathrm{T2}} > 60$ GeV.

In order to account for the effects due to the choice of the generator, the nominal Powheg diboson samples are compared with Sherpa diboson samples, having a different matrix element calculation and parton shower simulation. Since Sherpa samples are classified using the final state composition, they do not allow the differentiation of the WW, WZ and ZZ processes, so it is not possible to separate the three processes and to perform the normalization as done for the Powheg sample. Sherpa DF events are then normalized to Powheg WW+WZ+ZZ in CR-WW, where the WZ and ZZ contributions are small, obtaining a scale factor μ_{DF}. Sherpa SF events are normalized to Powheg WW+WZ+ZZ in CR-VZ, where the WW contribution is small, obtaining a scale factor μ_{SF}.
To account for a different composition in each region, a scale factor weighted (μ_w) with the region fraction of WW, $N(WW)$, and WZ or ZZ, generically $N(VZ)$, events is defined as follows:

$$\mu_w = \frac{\mu_{\mathrm{DF}} \cdot N(WW) + \mu_{\mathrm{SF}} \cdot N(VZ)}{N(WW + WZ + ZZ)}. \tag{4.18}$$

This obtained scale factor is then applied to the corresponding Sherpa yield. The final uncertainty is computed as

$$\sigma^{\mathrm{VV}}_{\mathrm{syst.}}[\%] = \frac{N(\textsc{Powheg}) - N(\textsc{Sherpa})}{N(\textsc{Powheg})}. \tag{4.19}$$

Region	CR-WW	CR-VZ	CR-top
Observed events	962	811	321
Fitted backgrounds	962 ± 31	811 ± 28	321 ± 18
Fitted WW	670 ± 60	19.1 ± 1.9	5.5 ± 2.7
Fitted WZ	11.8 ± 0.7	188 ± 7	0.32 ± 0.15
Fitted ZZ	0.29 ± 0.06	577 ± 23	–
Fitted $t\bar{t}$	170 ± 50	1.8 ± 1.3	270 ± 16
Fitted single top	88 ± 8	0.65 ± 0.35	38.6 ± 2.6
Other backgrounds	0.17 ± 0.06	19 ± 7	2.21 ± 0.20
FNP leptons	21 ± 8	5^{+6}_{-5}	4.2 ± 2.2
Simulated WW	528	15.1	4.3
Simulated WZ	9.9	158	0.27
Simulated ZZ	0.24	487	–
Simulated $t\bar{t}$	210	2.2	327
Simulated single top	107	0.8	46.7
Transfer Factors	1.25 ± 0.11	1.18 ± 0.05	0.82 ± 0.06

Table 4.11: Observed event yields and predicted background yields from the fit in the CRs. For backgrounds with a normalization extracted from the fit, the yield expected from the simulation before the fit is also shown. “Other backgrounds” include the non-dominant background sources, i.e. $t\bar{t}+V$, Higgs boson and Drell–Yan events. A “–” symbol indicates that the background contribution is negligible. Transfer factors are also reported [1].

4.11 Background-Only Fit results

The results of the background-only fit are discussed in this Section. Three transfer factors are obtained from the fit: μ_{WW} for the WW process, μ_{VZ} for the WZ and ZZ processes and μ_t for $t\bar{t}$ and single-top-quark productions. They are reported in Table 4.11 for the three CRs, together with the observed data, the predicted background yields after the normalization procedure, the non-normalized background expected yields and the expected MC yields for the normalized backgrounds.
The distributions of m_{T2} in CR-VZ and CR-top and of $E_{\mathrm{T}}^{\mathrm{miss}}$ in CR-WW are shown in Figure 4.9. The shapes of the kinematic distributions are well reproduced by the simulation in each CR. In addition to the background predictions and observed events, three signal samples are overlaid for comparison, each one representative of the corresponding SUSY model considered in the analysis.
Figure 4.10 shows the final estimate for the free parameters considered in the background-only fit, while the correlation matrix between the transfer factors and the nuisance parameters of the likelihood fit is shown in Figure 4.11. Both figures show no evidence of anomaly in the normalization procedure.
Concerning Validation Regions, the number of observed events and the predicted background yields after the normalization procedure in each VR are shown in Table 4.12, together with the expected non-normalized background yields. For backgrounds with a normalization extracted from the fit, the expected yield from simulated samples before the fit is also shown. Figure 4.12 shows a selection of kinematic distributions for data and the estimated SM backgrounds in the VRs; good agreement is observed overall.

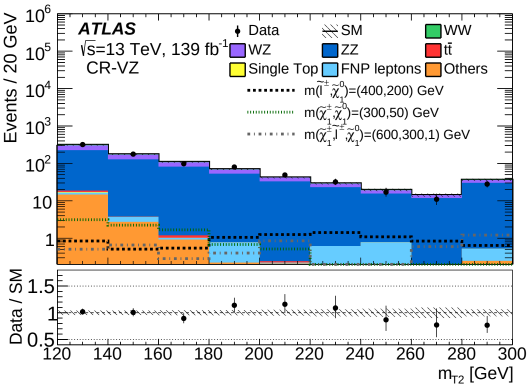

(a) m_{T2} in CR-VZ

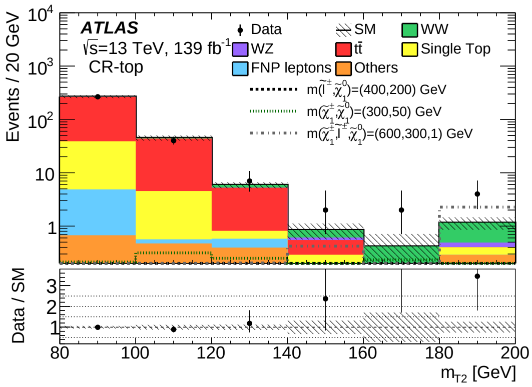

(b) m_{T2} in CR-top

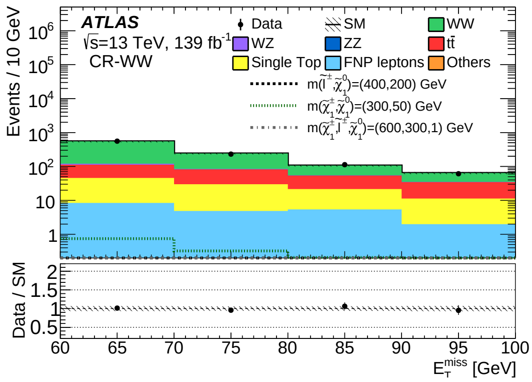

(c) $E_{\mathrm{T}}^{\mathrm{miss}}$ in CR-WW

Figure 4.9: Distributions of m_{T2} in 4.9(a) CR-VZ and 4.9(b) CR-top and 4.9(c) $E_{\mathrm{T}}^{\mathrm{miss}}$ in CR-WW for data and the estimated SM backgrounds. The normalization factors extracted from the corresponding CRs are used to rescale the $t\bar{t}$, single-top-quark, WW, WZ and ZZ backgrounds. The FNP lepton background is calculated using the data-driven matrix method. Negligible background contributions are not included in the legends. The uncertainty band includes systematic and statistical errors from all sources and the final bin in each histogram includes the overflow. Distributions for three benchmark signal points are overlaid for comparison. The lower panels show the ratio of data to the SM background estimate [1].

In addition to the background predictions and observed events, three different signal samples are overlaid for comparison, each one representative of the corresponding SUSY model considered in the analysis. Finally, Figure 4.13 shows the results of the background-only fit in all the VRs and good agreement, within about one standard deviation, is observed for all of them.
Concerning the validation with the three lepton selection, Figure 4.14 shows the m_{T2} distributions of the pseudo-twoLep events after the normalization procedure, in case of electron-muon and di-muon events. The observed data and Monte Carlo predictions agree within 1σ.
After extrapolating the transfer factors to the SRs, the results of the background-only fit in the CRs together with the observed data in the binned SRs are shown in Figure 4.15, where each bin of the histogram corresponds to one of the exclusive SRs. Figure 4.16 shows the m_{T2} distribution for the data and estimated Standard Model

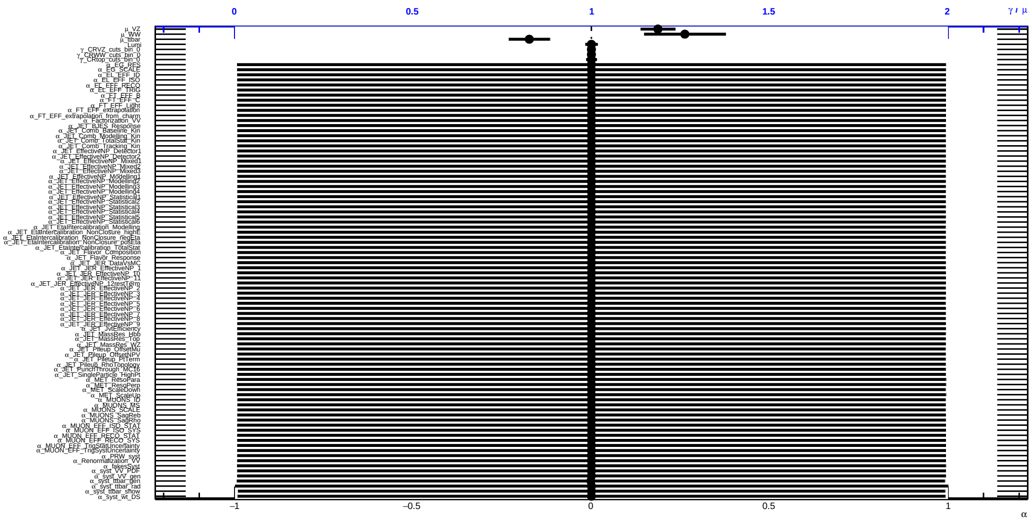

Figure 4.10: Final estimate of the fit parameters. No profiling is observed: all nuisance parameters related to the systematic uncertainties (labeled with an $\alpha\_$ prefix) are centered in 0 with an error close to 1. The nuisance parameters related to the statistical uncertainties in CRs (labeled with γ) have values centered in 0 with an uncertainty compatible to the statistical uncertainties associated to the CR.

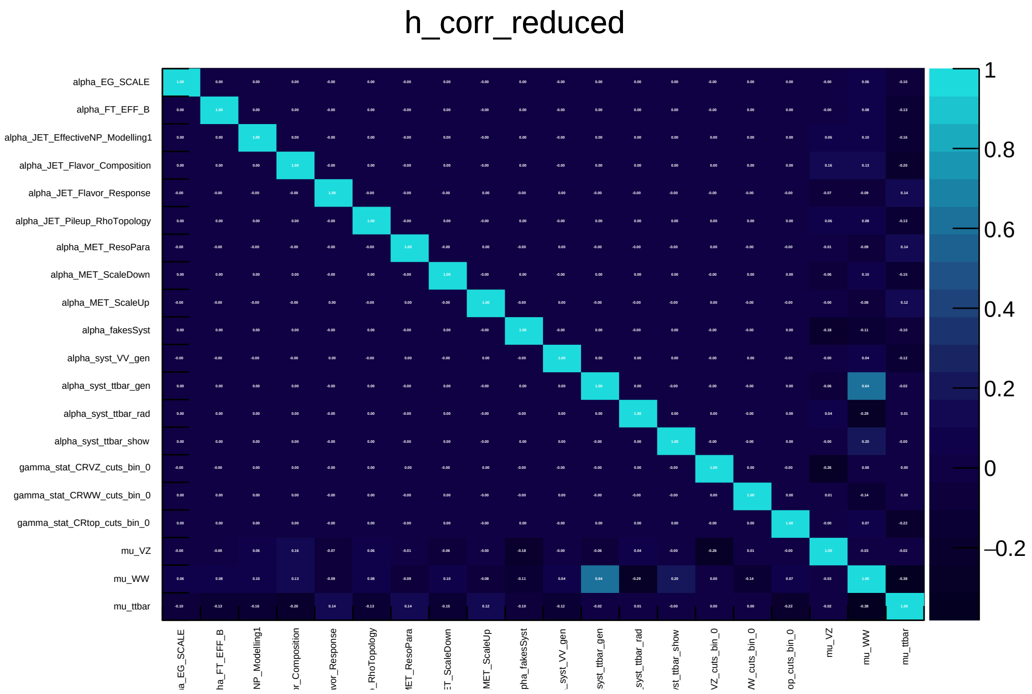

Figure 4.11: Correlation matrix between the transfer factors and the nuisance parameters of the likelihood fit. Only non-zero correlation values are shown.

backgrounds for events in the most inclusive SRs. Along with the background predictions and observed events, three signal samples are overlaid for comparison, each one belonging to one of the three different SUSY model considered in the analysis.
No significant deviation from the SM expectations is observed in any of the SRs considered, as shown in Figures 4.15 and 4.16.

Regions	VR-WW-0J	VR-WW-1J	VR-VZ	VR-top-low	VR-top-high	VR-top-WW
Observed events	2742	2671	464	190	50	953
Fitted backgrounds	2760 ± 120	2840 ± 250	420 ± 40	185 ± 17	53 ± 7	850 ± 80
Fitted WW	1550 ± 150	990 ± 120	17.6 ± 2.2	2.1 ± 0.7	2.6 ± 1.4	16.1 ± 2.5
Fitted WZ	34.2 ± 2.0	27.0 ± 2.3	99 ± 9	$0.05^{+0.17}_{-0.05}$	$0.2^{+0.6}_{-0.2}$	0.53 ± 0.13
Fitted ZZ	0.50 ± 0.06	0.39 ± 0.07	268 ± 25	–	–	$0.01^{+0.03}_{-0.01}$
Fitted $t\bar{t}$	790 ± 110	1400 ± 270	10.5 ± 3.2	157 ± 15	40 ± 7	650 ± 70
Fitted single top	336 ± 32	380 ± 40	2.2 ± 1.4	24.3 ± 2.6	4.6 ± 1.4	182 ± 15
Other backgrounds	0.92 ± 0.30	2.1 ± 0.5	21^{+27}_{-21}	0.28 ± 0.06	3.20 ± 0.20	0.39 ± 0.11
FNP leptons	44 ± 23	38 ± 21	$0.2^{+2.1}_{-0.2}$	2.3 ± 1.4	1.8 ± 0.5	–
Simulated WW	1230	790	14.0	1.6	2.0	12.8
Simulated WZ	28.8	22.8	84	0.04	0.1	0.45
Simulated ZZ	0.42	0.33	226	–	–	0.01
Simulated $t\bar{t}$	960	1700	13	190	49	790
Simulated single top	406	462	2.6	29.4	5.6	220

Table 4.12: Observed event yields and predicted background yields in the VRs. For backgrounds with a normalization extracted from the fit in the CRs, the yield expected from the simulation before the fit is also shown. "Other backgrounds" include the non-dominant background sources, i.e. $t\bar{t}+V$, Higgs boson and Drell–Yan events. A '–' symbol indicates that the background contribution is negligible [1].

After performing the likelihood fit, a summary of the impact of the systematic uncertainties on the background yields in the inclusive SRs with $m_{\mathrm{T2}} > 100$ GeV is shown in Table 4.13. The dominant sources of systematic uncertainty are related to theoretical uncertainties in the MC modelling, with values up to 8%, while the largest source of experimental uncertainties are related to the jet energy scale (JES) and resolution (JER), but both below 4% of uncertainty in each inclusive SR. Systematic uncertainties on the signal acceptance and shape, due to scale and parton shower variations, are found to be negligible.

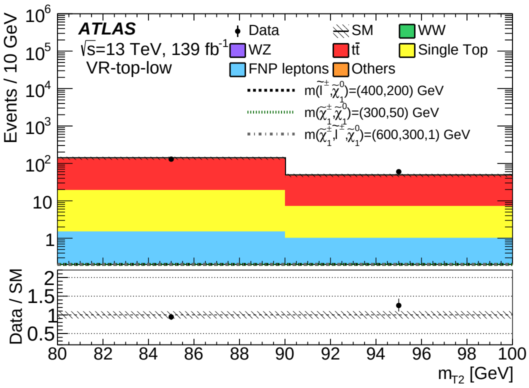

(a) m_{T2} in VR-top-low

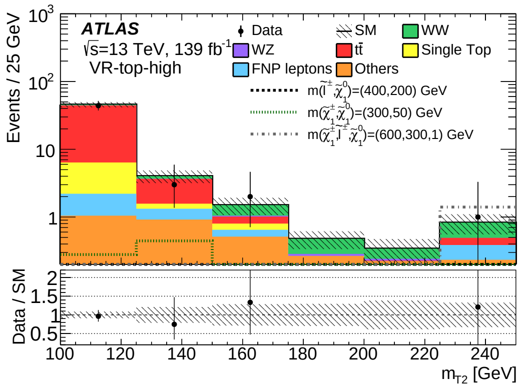

(b) m_{T2} in VR-top-high

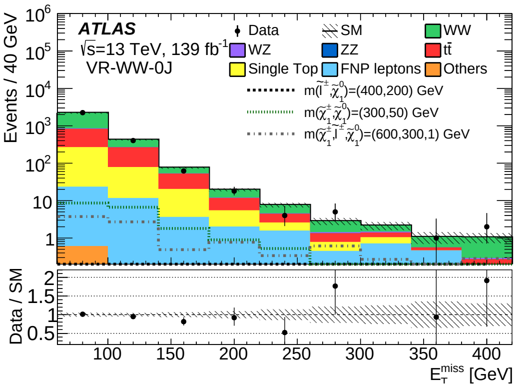

(c) $E_{\mathrm{T}}^{\mathrm{miss}}$ in VR-WW-0J

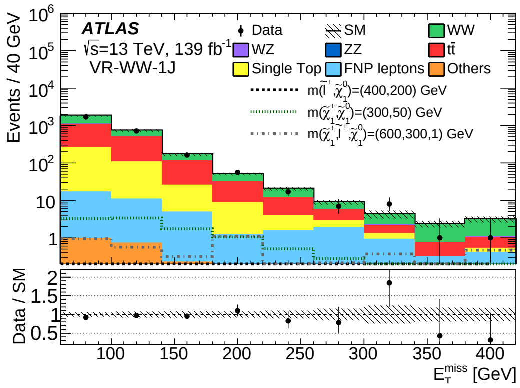

(d) $E_{\mathrm{T}}^{\mathrm{miss}}$ in VR-WW-1J

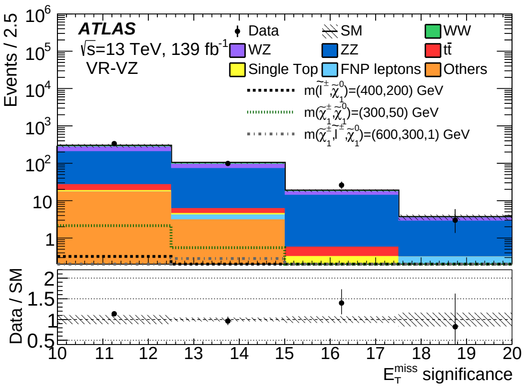

(e) $E_{\mathrm{T}}^{\mathrm{miss}}$ significance in VR-VZ

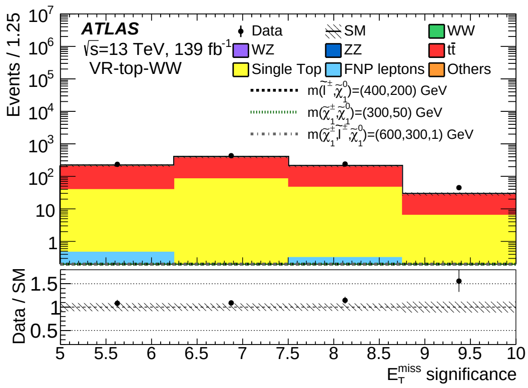

(f) $E_{\mathrm{T}}^{\mathrm{miss}}$ significance in VR-top-WW

Figure 4.12: Distributions of m_{T2} in 4.12(a) VR-top-low and 4.12(b) VR-top-high, $E_{\mathrm{T}}^{\mathrm{miss}}$ in 4.12(c) VR-WW-0J and 4.12(d) VR-WW-1J, and $E_{\mathrm{T}}^{\mathrm{miss}}$ significance in 4.12(e) VR-VZ and 4.12(f) VR-top-WW, for data and the estimated SM backgrounds. The normalization factors extracted from the corresponding CRs are used to rescale the $t\bar{t}$, single-top-quark, WW, WZ and ZZ backgrounds. The FNP lepton background is calculated using the data-driven matrix method. Negligible background contributions are not included in the legends. The uncertainty band includes systematic and statistical errors from all sources and the last bin includes the overflow. Distributions for three benchmark signal points are overlaid for comparison. The lower panels show the ratio of data to the SM background estimate [1].

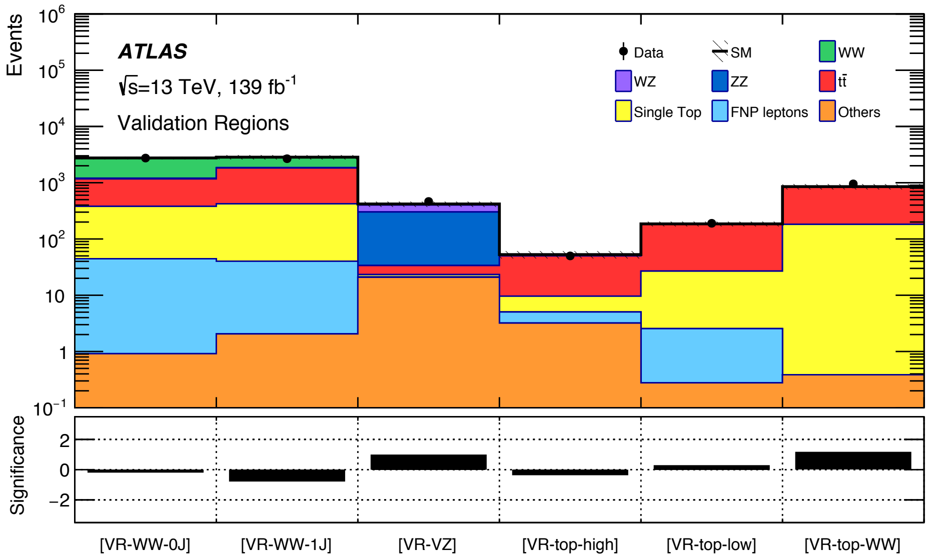

Figure 4.13: The upper panel shows the observed number of events in each of the VRs defined in Table 4.9, together with the expected SM backgrounds obtained after the background-only fit in the CRs. The shaded band represents the total uncertainty in the expected SM background. The lower panel shows the corresponding significance [1, 216].

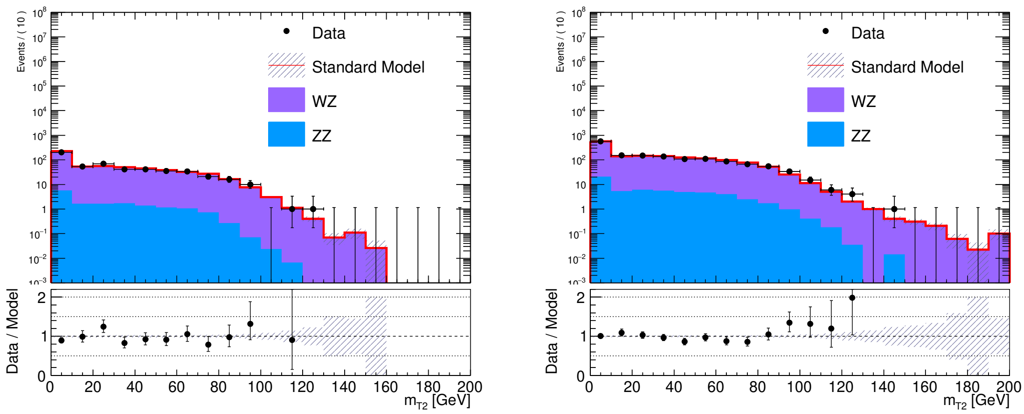

(a) Electron-Muon events. (b) Muon-Muon events.

Figure 4.14: Distributions of m_{T2} for the diboson Monte Carlo samples and data pseudo-twoLep events after the normalization procedure for the validation using the three lepton selection. The electron-muon 4.14(a) and di-muon 4.14(b) channels are shown. Statistical and systematic uncertainties are included.

4.12 Exclusion Fit results

In absence of a statistically significant excess in any of the SRs considered, limits can be calculated both on the SUSY models under study and, more generally, on the presence of BSM physics processes.

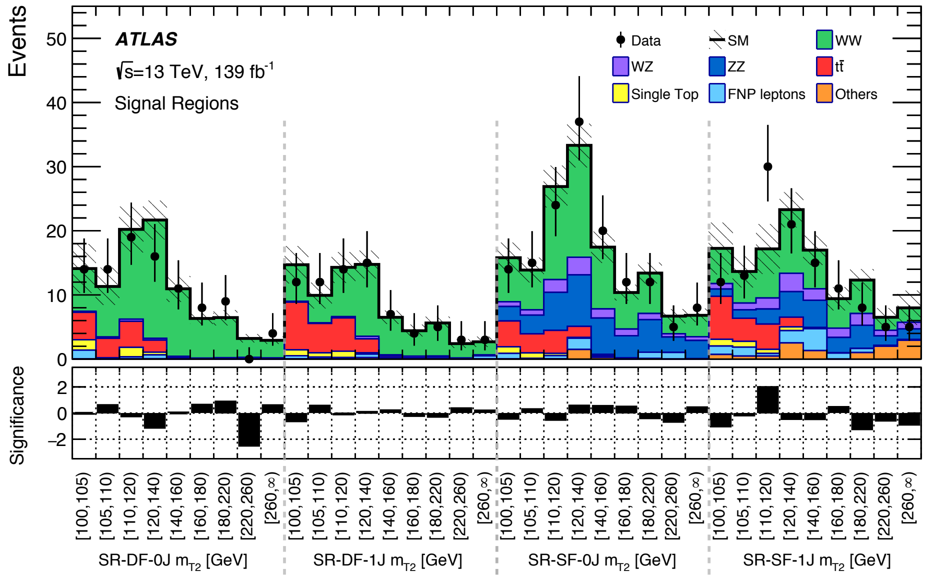

Figure 4.15: The upper panel shows the observed number of events in each of the SRs defined in Table 4.5, together with the expected SM backgrounds obtained after the background-only fit in the CRs. The shaded band represents the total uncertainty in the expected SM background. The lower panel shows the corresponding significance [1, 216].

4.12.1 Model-Dependent upper limits

The $\mathrm{CL_s}$ prescription is used to exclude the signal+background hypothesis for each of the signal models shown in Figure 1.8; exclusion limits at 95% CL are set on the masses of chargino, neutralino and sleptons. These limits are obtained including the exclusive SRs and the CRs in the simultaneous likelihood fit. For the models involving chargino pair production, both the SF and DF SRs are included in the fit, whilst for testing the direct slepton production only the SF SRs are included.

In the mass parameter space of the simplified model considered, an exclusion plot can be obtained, where all mass values with $\mathrm{CL_s}$ lower than 0.05 are included in the contour and are, therefore, excluded. The results are shown in Figure 4.17.

In the model of direct chargino pair production with decays via W bosons with a massless $\tilde{\chi}_1^0$, $\tilde{\chi}_1^{\pm}$ masses up to 420 GeV are excluded at 95% CL. In the model of direct chargino pair production with decays via sleptons or sneutrinos with a massless $\tilde{\chi}_1^0$, $\tilde{\chi}_1^{\pm}$ masses up to 1 TeV are excluded at 95% CL. Finally, in the model of direct slepton pair production with a massless $\tilde{\chi}_1^0$, slepton masses up to 700 GeV are excluded at 95% CL.

For direct slepton production, exclusion limits are also set for selectrons and smuons separately, by including only the di-electron and di-muon SF SRs in the likelihood fit, respectively. These are shown in 4.18 for single slepton species $\tilde{e}_{\mathrm{L}}$, $\tilde{e}_{\mathrm{R}}$, $\tilde{\mu}_{\mathrm{L}}$ and $\tilde{\mu}_{\mathrm{R}}$, along with combined limits for mass-degenerate $\tilde{e}_{\mathrm{L,R}}$ and $\tilde{\mu}_{\mathrm{L,R}}$.

The observed limit for $\tilde{\ell}_{\mathrm{L}}$ is shown on the exclusion plot for chargino pair production with slepton-mediated decays in Figure 4.17(b) for comparison. However, since there is no strong dependence of the sensitivity on the slepton mass hypothesis for a broad range of slepton masses [75], these results are applicable for many models not excluded

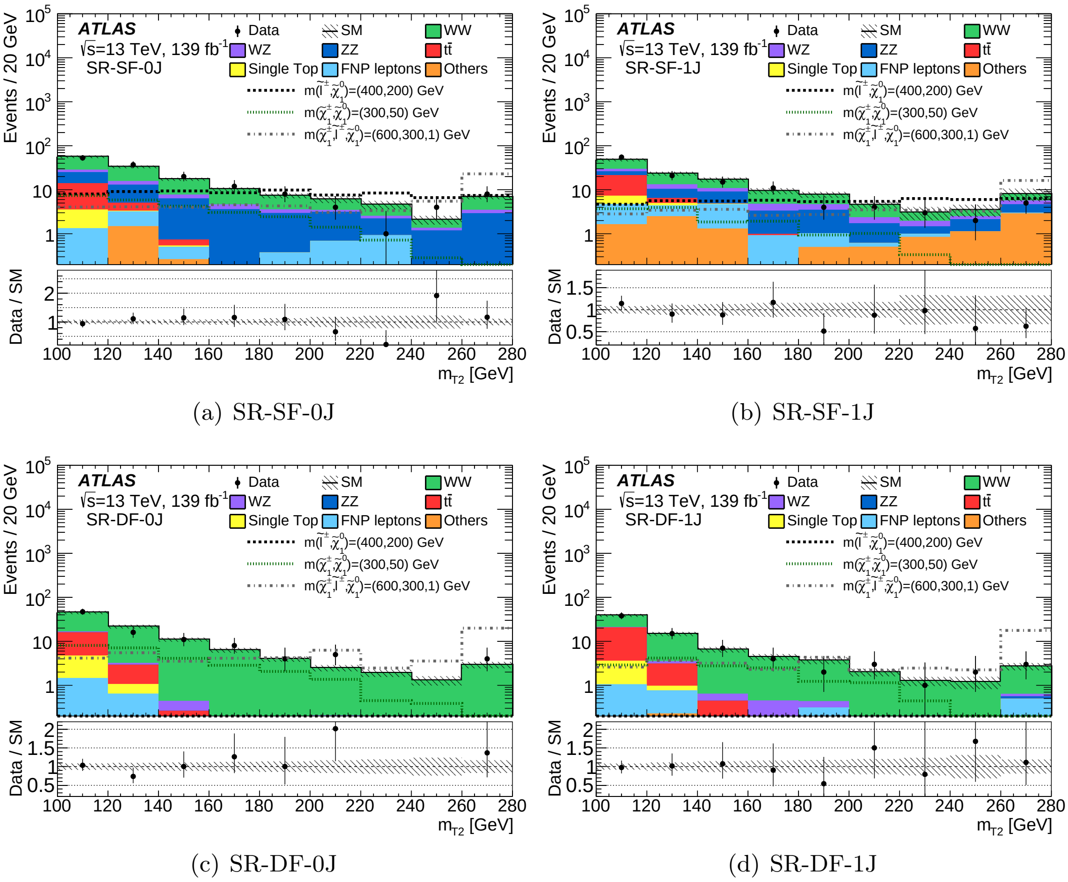

(a) SR-SF-0J (b) SR-SF-1J (c) SR-DF-0J (d) SR-DF-1J

Figure 4.16: Distributions of m_{T2} in 4.16(a) SR-SF-0J, 4.16(b) SR-SF-1J, 4.16(c) SR-DF-0J and 4.16(d) SR-DF-1J, for data and the estimated SM backgrounds. The normalization factors extracted from the corresponding CRs are used to rescale the $t\bar{t}$, single-top-quark, WW, WZ and ZZ backgrounds. The FNP lepton background is calculated using the data-driven matrix method. Negligible background contributions are not included in the legends. The uncertainty band includes systematic and statistical errors from all sources and the last bin includes the overflow. Distributions for three benchmark signal points are overlaid for comparison. The lower panels show the ratio of data to the SM background estimate [1].

by the direct slepton limits.

4.12.2 Model-Independent upper limits

The inclusive SRs can be used to set upper limits on BSM physics, independently from the three SUSY model considered. For this purpose, a dummy signal with no associated error can be injected in a likelihood for each of the inclusive SRs: the observed yield in the SR is a fit constraint and the dummy signal yield in the SR a free parameter. Then, the number of signal events N_s is varied and, given the total background estimates with their errors and the observed data, the number of signal events (S^{95}_{obs}) needed to the dummy signal to be excluded at 95% CL is evaluated. This information, together with the $\mathrm{CL_s}$ prescription, is used to set model-independent

Region m_{T2} [GeV]	SR-DF-0J $\in [100, \infty)$	SR-DF-1J $\in [100, \infty)$	SR-SF-0J $\in [100, \infty)$	SR-SF-1J $\in [100, \infty)$
Total background expectation	96	75	144	124
MC statistical uncertainties	3%	3%	2%	3%
WW normalisation	7%	6%	4%	3%
VZ normalisation	$< 1\%$	$< 1\%$	1%	1%
$t\bar{t}$ normalisation	1%	2%	$< 1\%$	1%
Diboson theoretical uncertainties	7%	7%	4%	3%
Top theoretical uncertainties	7%	8%	3%	6%
$E_{\mathrm{T}}^{\mathrm{miss}}$ modelling	1%	1%	$< 1\%$	2%
Jet energy scale	2%	3%	2%	2%
Jet energy resolution	1%	2%	1%	2%
Pile-up reweighting	$< 1\%$	1%	$< 1\%$	$< 1\%$
b-tagging	$< 1\%$	2%	$< 1\%$	1%
Lepton modelling	1%	1%	1%	3%
FNP leptons	1%	1%	1%	1%
Total systematic uncertainties	15%	12%	8%	10%

Table 4.13: Summary of the dominant systematic uncertainties in the background estimates in the inclusive SRs requiring $m_{\mathrm{T2}} > 100$ GeV after performing the profile likelihood fit. The individual uncertainties can be correlated, and do not necessarily add in quadrature to the total background uncertainty. The percentages show the size of the uncertainty relative to the total expected background. "Top theoretical uncertainties" refers to $t\bar{t}$ theoretical uncertainties and the uncertainty associated with Wt–$t\bar{t}$ interference added in quadrature [1].

upper limits at 95% CL on the visible signal cross-section[13] $\sigma_{\mathrm{obs}}^{0.95}$ of BSM processes, computed as the ratio between S_{obs}^{95} and the integrated luminosity used in the analysis. It is also possible to evaluate the expected upper limit on the number S_{exp}^{95} of signal events considering the N_s value needed to have an expected $\mathrm{CL_s}$ lower than 0.05.
The observed ($S_{\mathrm{obs}}^{0.95}$) and expected ($S_{\mathrm{exp}}^{0.95}$) limits at 95% CL on the numbers of events from processes beyond the SM in the inclusive SRs, together with $\sigma_{\mathrm{obs}}^{0.95}$, are reported in Tables 4.14 and 4.15 for the DF and SF inclusive SRs, respectively, alongside the observed events and the total background predictions. The p_0-values are also provided and they represent the probability of the SM background alone to fluctuate to the observed number of events or higher. They are capped at $p_0 = 0.50$.
Finally, Figures 4.19, 4.20, 4.21 and 4.22 show the scan on the number of signal events for the inclusive SRs in order to obtain the upper limits $S_{\mathrm{obs}}^{0.95}$ and $S_{\mathrm{exp}}^{0.95}$.

[13] It is defined as the product of the cross-section σ of the process, the reconstruction efficiency ϵ_{SR} in the SRs and the acceptance $\mathcal{A}$ of the kinematic cuts in the SR. ϵ_{SR} is defined as $N_{\mathrm{reco}}/N_{\mathrm{truth}}$, i.e. the ratio between the number of reconstructed signal events, N_{reco}, and the number of signal events at truth level, N_{truth}. $\mathcal{A}$ is defined as $N_{\mathrm{truth}}/N_{\mathrm{gen}}$, with N_{gen} being the total number of generated events.

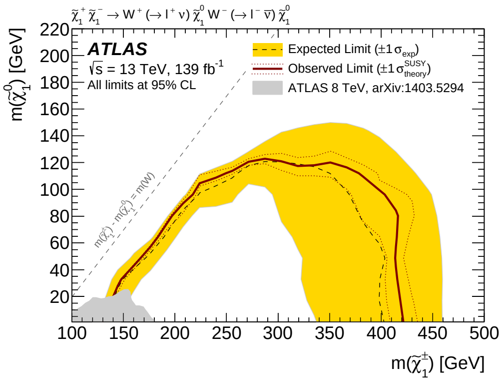

(a) $\tilde{\chi}_1^+\tilde{\chi}_1^-$ production with W-boson-mediated decays

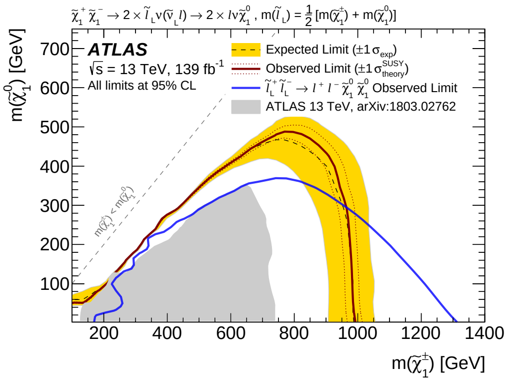

(b) $\tilde{\chi}_1^+\tilde{\chi}_1^-$ production with $\tilde{\ell}/\tilde{\nu}$-mediated decays

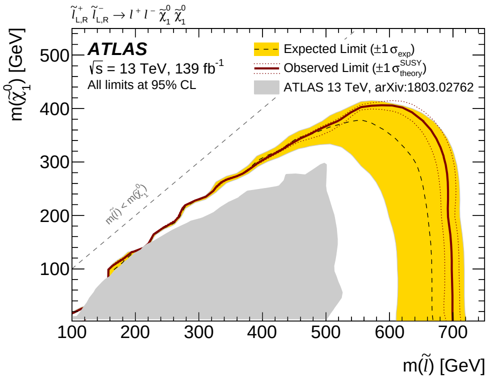

(c) $\tilde{\ell}\tilde{\ell}$ production

Figure 4.17: Observed and expected exclusion limits on SUSY simplified models for chargino-pair production with 4.17(a) W-boson-mediated decays and 4.17(b) slepton/sneutrino-mediated decays, and 4.17(c) for slepton-pair production [1]. In Figure 4.17(b) all three slepton flavours ($\tilde{e}$, $\tilde{\mu}$, $\tilde{\tau}$) are considered, while only $\tilde{e}$ and $\tilde{\mu}$ are considered in Figure 4.17(c). The observed (solid thick line) and expected (thin dashed line) exclusion contours are indicated. The upper shaded band corresponds to the $\pm 1\sigma$ variations in the expected limit, including all uncertainties except theoretical uncertainties in the signal cross-section. The dotted lines around the observed limit illustrate the change in the observed limit as the nominal signal cross-section is scaled up and down by the theoretical uncertainty. The blue line in 4.17(b) corresponds to the observed limit for $\tilde{\ell}_{\mathrm{L}}$ projected into this model for the chosen slepton mass hypothesis (slepton masses midway between the mass of the chargino and that of the $\tilde{\chi}_1^0$). All limits are computed at 95% CL. The observed limits obtained by ATLAS in previous searches are also shown (lower shaded areas) [75, 76].

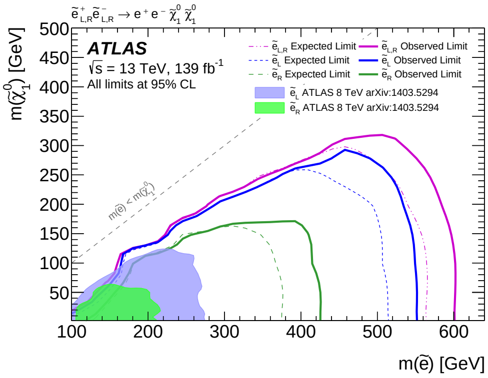

(a) $\tilde{e}\tilde{e}$ production

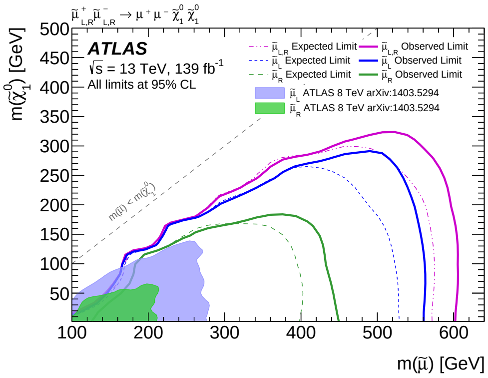

(b) $\tilde{\mu}\tilde{\mu}$

Figure 4.18: Observed and expected exclusion limits on SUSY simplified models for 4.18(a) direct selectron production and 4.18(b) direct smuon production [1]. In Figure 4.18(a) the observed (solid thick lines) and expected (dashed lines) exclusion contours are indicated for combined $\tilde{e}_{\mathrm{L,R}}$ and for $\tilde{e}_{\mathrm{L}}$ and $\tilde{e}_{\mathrm{R}}$. In Figure 4.18(b) the observed (solid thick lines) and expected (dashed lines) exclusion contours are indicated for combined $\tilde{\mu}_{\mathrm{L,R}}$ and for $\tilde{\mu}_{\mathrm{L}}$ and $\tilde{\mu}_{\mathrm{R}}$. All limits are computed at 95% CL. The observed limits obtained by ATLAS in previous searches are also shown in the shaded areas [76].

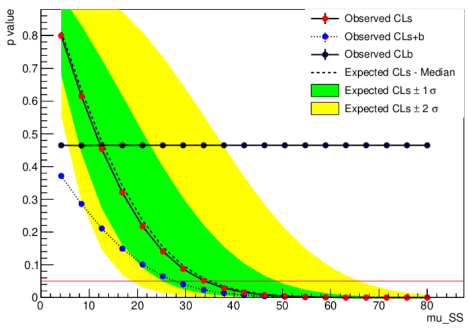

(a) $m_{\mathrm{T2}} > 100$ GeV

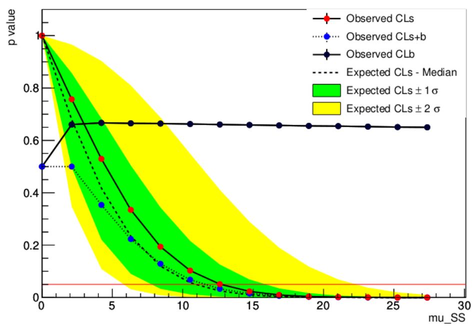

(b) $m_{\mathrm{T2}} > 160$ GeV

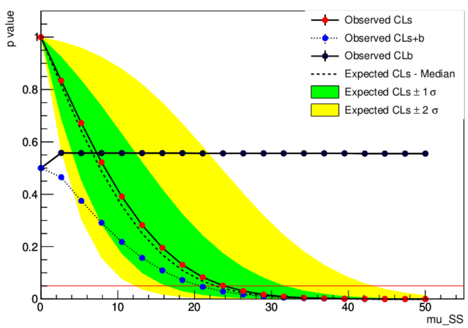

(c) $m_{\mathrm{T2}} \in [100, 120)$ GeV

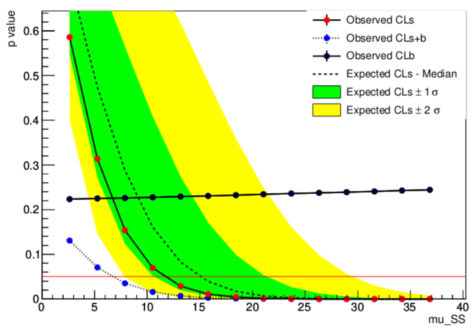

(d) $m_{\mathrm{T2}} \in [120, 160)$ GeV

Figure 4.19: Scan on a dummy signal used for the estimation of the upper limits on the visible cross-section in the inclusive region SR-DF-0J. The observed $\mathrm{CL_s}$, $\mathrm{CL_b}$ and $\mathrm{CL_{s+b}}$ are reported, alongside the expected $\mathrm{CL_s}$ with the associate $\pm 1\sigma$ and $\pm 2\sigma$ error bands.

Region m_{T2} [GeV]	SR-DF-0J $\in [100, \infty)$	SR-DF-0J $\in [160, \infty)$	SR-DF-0J $\in [100, 120)$	SR-DF-0J $\in [120, 160)$
Observed events	95	21	47	27
Fitted backgrounds	96 ± 15	18.8 ± 2.4	45 ± 9	33 ± 5
Fitted WW	76 ± 10	18.2 ± 2.4	29 ± 4	29 ± 4
Fitted WZ	1.53 ± 0.17	0.40 ± 0.07	0.66 ± 0.11	0.47 ± 0.07
Fitted ZZ	$0.00^{+0.19}_{-0.00}$	0.14 ± 0.03	$0.06^{+0.23}_{-0.06}$	< 0.04
Fitted $t\bar{t}$	13 ± 7	–	11 ± 6	2.1 ± 1.2
Fitted single top	3.7 ± 2.0	–	3.3 ± 1.8	0.42 ± 0.25
Other backgrounds	0.24 ± 0.08	0.07 ± 0.02	0.08 ± 0.02	0.09 ± 0.05
FNP leptons	1.8 ± 0.6	–	1.4 ± 0.4	0.47 ± 0.17
$S^{0.95}_{\text{obs}}$	34.1	12.7	23.8	11.8
$S^{0.95}_{\text{exp}}$	$35.2^{+13.9}_{-10.0}$	$11.0^{+4.9}_{-3.2}$	$22.8^{+9.1}_{-6.5}$	$15.1^{+6.3}_{-4.5}$
$\sigma^{0.95}_{\text{obs}}$ [fb]	0.24	0.09	0.17	0.08
p_0	0.50	0.33	0.44	0.50

Region m_{T2} [GeV]	SR-DF-1J $\in [100, \infty)$	SR-DF-1J $\in [160, \infty)$	SR-DF-1J $\in [100, 120)$	SR-DF-1J $\in [120, 160)$
Observed events	75	15	38	22
Fitted backgrounds	75 ± 9	15.1 ± 2.7	39 ± 6	21.3 ± 2.8
Fitted WW	48 ± 8	13.4 ± 2.6	17.7 ± 2.6	17.1 ± 2.8
Fitted WZ	1.54 ± 0.21	0.53 ± 0.12	0.43 ± 0.09	0.59 ± 0.11
Fitted ZZ	0.08 ± 0.01	$0.07^{+0.24}_{-0.07}$	< 0.04	0.01 ± 0.00
Fitted $t\bar{t}$	20 ± 7	0.09 ± 0.03	17 ± 6	2.4 ± 0.9
Fitted single top	2.8 ± 1.4	–	2.6 ± 1.3	0.21 ± 0.13
Other backgrounds	0.80 ± 0.13	0.25 ± 0.05	0.19 ± 0.10	0.34 ± 0.04
FNP leptons	2.2 ± 0.6	0.71 ± 0.16	0.87 ± 0.29	0.59 ± 0.16
$S^{0.95}_{\text{obs}}$	25.1	10.2	16.8	12.3
$S^{0.95}_{\text{exp}}$	$25.3^{+10.3}_{-7.2}$	$10.3^{+4.6}_{-3.0}$	$17.6^{+7.3}_{-5.1}$	$11.9^{+5.2}_{-3.3}$
$\sigma^{0.95}_{\text{obs}}$ [fb]	0.18	0.07	0.12	0.09
p_0	0.50	0.50	0.50	0.45

Table 4.14: Observed event yields and predicted background yields from the fit for the DF inclusive SRs. The model-independent upper limits at 95% CL on the observed and expected numbers of beyond-the-SM events $S^{0.95}_{\text{obs/exp}}$ and on the effective beyond-the-SM cross-section $\sigma^{0.95}_{\text{obs}}$ are also shown. The $\pm 1\sigma$ variations on $S^{0.95}_{\text{exp}}$ are also provided. The last row shows the p_0-value of the SM-only hypothesis. For SRs where the data yield is smaller than expected, the p_0-value is capped at 0.50. "Other backgrounds" include the non-dominant background sources, i.e. $t\bar{t} + V$, Higgs boson and Drell–Yan events. A "–" symbol indicates that the background contribution is negligible [1].

Region m_{T2} [GeV]	SR-SF-0J $\in [100, \infty)$	SR-SF-0J $\in [160, \infty)$	SR-SF-0J $\in [100, 120)$	SR-SF-0J $\in [120, 160)$
Observed events	147	37	53	57
Fitted backgrounds	144 ± 12	37.3 ± 3.0	56 ± 6	51 ± 5
Fitted WW	73 ± 8	18.1 ± 2.1	27.6 ± 3.0	27 ± 4
Fitted WZ	10.8 ± 0.8	3.08 ± 0.27	3.55 ± 0.29	4.2 ± 0.5
Fitted ZZ	38.6 ± 2.6	13.8 ± 1.0	11.1 ± 0.8	13.7 ± 1.5
Fitted $t\bar{t}$	13 ± 4	–	11 ± 4	1.9 ± 0.7
Fitted single top	2.4 ± 1.4	–	2.2 ± 1.3	0.15 ± 0.09
Other backgrounds	2.1 ± 1.5	$0.10^{+0.33}_{-0.10}$	$0.2^{+1.4}_{-0.2}$	1.76 ± 0.30
FNP leptons	5.4 ± 1.4	2.2 ± 0.4	1.1 ± 0.6	2.0 ± 0.5
$S^{0.95}_{\mathrm{obs}}$	35.5	14.3	17.8	23.5
$S^{0.95}_{\mathrm{exp}}$	$33.6^{+13.6}_{-9.3}$	$14.5^{+6.3}_{-4.2}$	$20.0^{+8.1}_{-5.6}$	$18.7^{+7.8}_{-5.3}$
$\sigma^{0.95}_{\mathrm{obs}}$ [fb]	0.25	0.10	0.13	0.17
p_0	0.44	0.50	0.50	0.25

Region m_{T2} [GeV]	SR-SF-1J $\in [100, \infty)$	SR-SF-1J $\in [160, \infty)$	SR-SF-1J $\in [100, 120)$	SR-SF-1J $\in [120, 160)$
Observed events	120	29	55	36
Fitted backgrounds	124 ± 12	36 ± 5	48 ± 8	40 ± 4
Fitted WW	48 ± 6	14.1 ± 2.1	18.1 ± 2.4	16.0 ± 2.2
Fitted WZ	13.4 ± 1.1	5.2 ± 0.6	3.62 ± 0.33	4.7 ± 0.5
Fitted ZZ	22.2 ± 1.8	9.1 ± 1.1	4.8 ± 0.5	8.2 ± 0.9
Fitted $t\bar{t}$	16 ± 8	$0.07^{+0.10}_{-0.07}$	14 ± 7	1.6 ± 0.8
Fitted single top	3.3 ± 1.7	–	2.6 ± 1.4	0.7 ± 0.4
Other backgrounds	11.1 ± 4.0	5.6 ± 2.1	$1.7^{+2.4}_{-1.7}$	3.8 ± 1.3
FNP leptons	10.3 ± 1.5	1.80 ± 0.34	3.1 ± 0.6	5.3 ± 0.7
$S^{0.95}_{\mathrm{obs}}$	30.6	11.2	27.3	12.6
$S^{0.95}_{\mathrm{exp}}$	$33.5^{+13.3}_{-9.3}$	$15.3^{+6.5}_{-4.5}$	$21.9^{+9.0}_{-6.2}$	$15.5^{+6.5}_{-4.2}$
$\sigma^{0.95}_{\mathrm{obs}}$ [fb]	0.22	0.08	0.19	0.09
p_0	0.50	0.50	0.26	0.50

Table 4.15: Observed event yields and predicted background yields from the fit for the SF inclusive SRs. The model-independent upper limits at 95% CL on the observed and expected numbers of beyond-the-SM events $S^{0.95}_{\mathrm{obs/exp}}$ and on the effective beyond-the-SM cross-section $\sigma^{0.95}_{\mathrm{obs}}$ are also shown. The $\pm 1\sigma$ variations on $S^{0.95}_{\mathrm{exp}}$ are also provided. The last row shows the p_0-value of the SM-only hypothesis. For SRs where the data yield is smaller than expected, the p_0-value is capped at 0.50. "Other backgrounds" include the non-dominant background sources, i.e. $t\bar{t}+V$, Higgs boson and Drell–Yan events. A "–" symbol indicates that the background contribution is negligible [1].

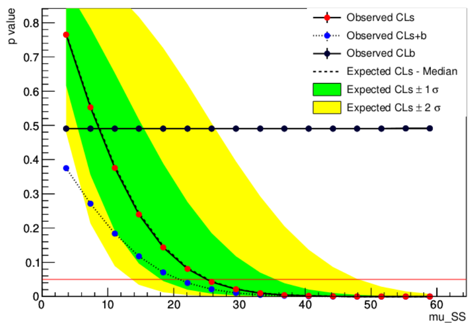

(a) $m_{\mathrm{T2}} > 100$ GeV

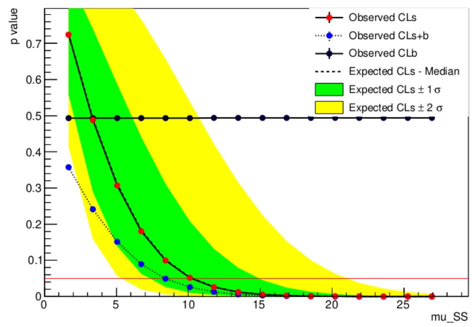

(b) $m_{\mathrm{T2}} > 160$ GeV

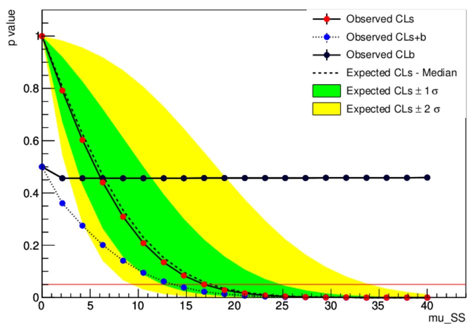

(c) $m_{\mathrm{T2}} \in [100, 120)$ GeV

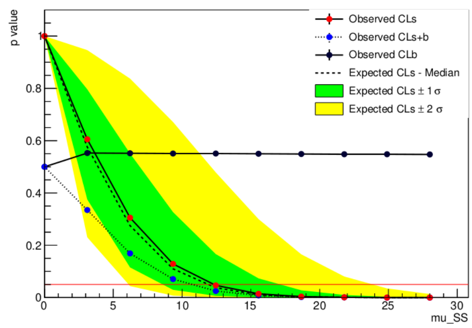

(d) $m_{\mathrm{T2}} \in [120, 160)$ GeV

Figure 4.20: Scan on a dummy signal used for the estimation of the upper limits on the visible cross-section in the inclusive region SR-DF-1J. The observed $\mathrm{CL_s}$, $\mathrm{CL_b}$ and $\mathrm{CL_{s+b}}$ are reported, alongside the expected $\mathrm{CL_s}$ with the associate $\pm 1\sigma$ and $\pm 2\sigma$ error bands.

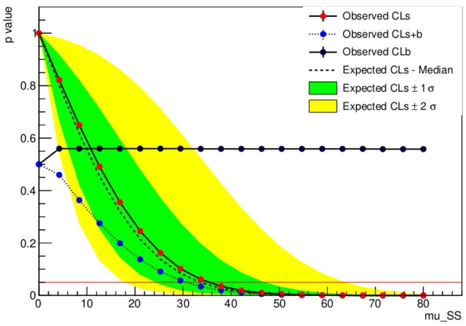

(a) $m_{\mathrm{T2}} > 100$ GeV

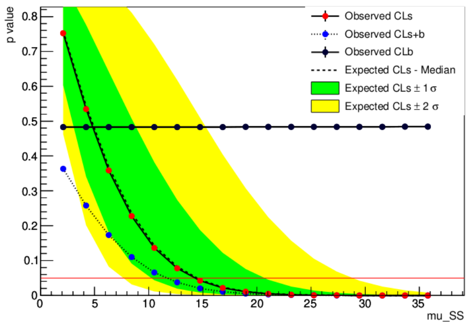

(b) $m_{\mathrm{T2}} > 160$ GeV

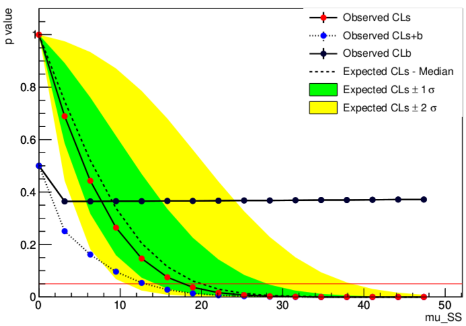

(c) $m_{\mathrm{T2}} \in [100, 120)$ GeV

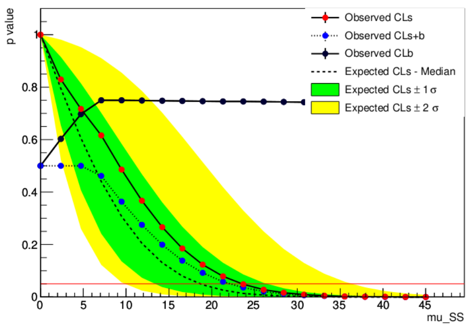

(d) $m_{\mathrm{T2}} \in [120, 160)$ GeV

Figure 4.21: Scan on a dummy signal used for the estimation of the upper limits on the visible cross-section in the inclusive region SR-DF-0J. The observed $\mathrm{CL_s}$, $\mathrm{CL_b}$ and $\mathrm{CL_{s+b}}$ are reported, alongside the expected $\mathrm{CL_s}$ with the associate $\pm 1\sigma$ and $\pm 2\sigma$ error bands.

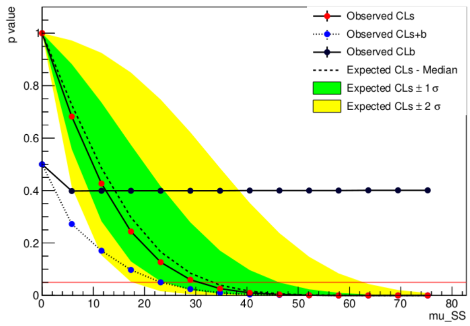

(a) $m_{\mathrm{T2}} > 100$ GeV

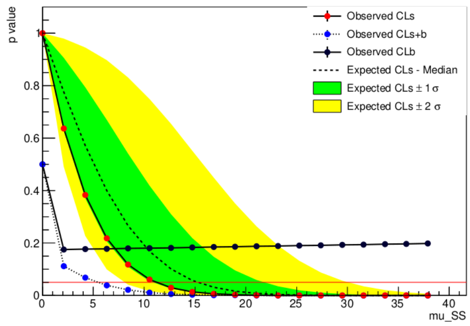

(b) $m_{\mathrm{T2}} > 160$ GeV

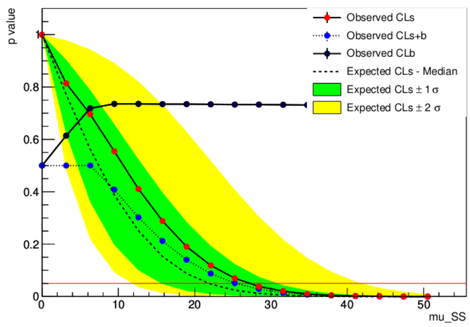

(c) $m_{\mathrm{T2}} \in [100, 120)$ GeV

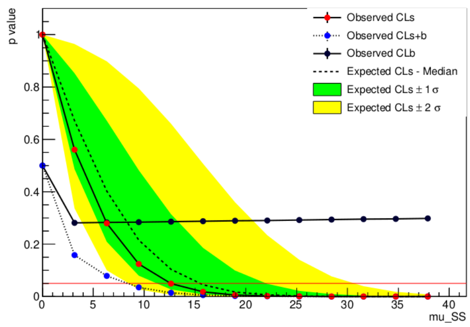

(d) $m_{\mathrm{T2}} \in [120, 160)$ GeV

Figure 4.22: Scan on a dummy signal used for the estimation of the upper limits on the visible cross-section in the inclusive region SR-DF-1J. The observed $\mathrm{CL_s}$, $\mathrm{CL_b}$ and $\mathrm{CL_{s+b}}$ are reported, alongside the expected $\mathrm{CL_s}$ with the associate $\pm 1\sigma$ and $\pm 2\sigma$ error bands.

Chapter 5

Current and future developments

The analysis described so far in this thesis targets a phase space characterized by a medium/high $E_{\mathrm{T}}^{\mathrm{miss}}$, $E_{\mathrm{T}}^{\mathrm{miss}}$ significance and m_{T2} in the SR definition, aiming to search for SUSY evidences in events at high-m_{T2} values, mainly located in the tails of the variable distribution.
However, from the exclusion contours shown in Figure 4.17 it is evident the "compressed region" close to the diagonals $m(\tilde{\chi}_1^{\pm}) - m(\tilde{\chi}_1^0) = m(W)$ is not excluded by the cut&count and shape fit combined approach used in the analysis.
Then, new developments of this analysis have already started in the context of the second round of ATLAS SUSY searches with the Run II data collected at LHC, to target chargino pair production with $\tilde{\chi}_1^{\pm} - \tilde{\chi}_1^0$ mass splittings near the electroweak scale, using non-conventional approaches. This chapter will provide a glance at some preliminary aspects of the analysis setup, which have been mostly developed by me. In particular, I was responsible of the signal generation and generation, as well as MultiVariate Analysis design and implementation.

5.1 Signal samples

As in the first round of analysis, the SUSY models considered are the ones reported in Figure 1.8, but the following sections will focus on the chargino production with W-boson-mediated decays.
An important difference with respect to the already described analysis is the choice of the Monte Carlo generator for the new signal samples. Previously, MadGraph5_aMC@NLO generator interfaced to Pythia was used, being the mass differences between chargino and neutralino larger than 100 GeV. In analogy with the previous generation, the signal samples for this second analysis round are generated from leading-order matrix elements with up to two additional partons using MadGraph5_aMC@NLO v2.6.2., but both charginos were decayed using MadSpin[1] [233]. In fact, while the decay of the chargino into a virtual W boson and the subsequent leptonic decay should be performed within MadGraph (since Pythia does not treat spin correlation and the angular distributions of the final states appropriately), when including spin correlation and off-shell effects it is not possible to perform the full decay chain within MadGraph, since the procedure is very CPU and time consuming, therefore not feasible when several millions of events have to be generated. Instead, MadSpin is able to keep

[1] MadSpin is implemented as a generic tool in the MadGraph framework.

a reasonable timescale while ensuring a good accuracy in terms of spin correlation[2] and off-shell effects[3].
Finally, these new signal samples, organized in order to probe a vast region of the compressed mass-parameter space, are arranged in a new grid, shown in Figure 5.1, and divided in two different areas: "compressed points" with $m(\tilde{\chi}_1^{\pm}) - m(\tilde{\chi}_1^0) < 100$ GeV highlighted in green, where the majority of W bosons are expected to be in the off-shell regime and for which MadSpin is used in generation, and "connection points", highlighted in red and still not excluded or on the edge of the current exclusion, whose main purpose is the creation of a connection belt between the contour shown in Figure 4.17(a) and the new signal grid. MadSpin does not apply to signal points highlighted in red. MadGraph with MadSpin is interfaced with Pythia 8.212 [192], with the A14 tune for the modelling of the SUSY decay chain, parton showering, hadronization and the description of the underlying event. Parton luminosities are provided by the NNPDF2.3LO PDF set.
As in the previous signal generation, the decay $\tilde{\chi}_1^{\pm} \to W\tilde{\chi}_1^0$ is assumed to happen with 100% branching ratio, while the Standard Model W decays into leptons with the usual branching ratios.

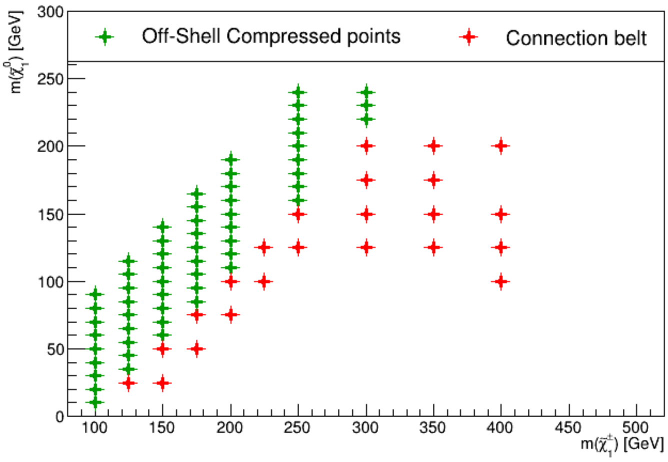

Figure 5.1: The new signal grid for the chargino pair production with W-boson-mediated decays: the points in the compressed region are marked with green stars, while the ones marked with red stars are generated in order to establish a continuity with the grid used for the previous analysis and keeping in mind the exclusion contour shown in Figure 4.17(a).

The second important difference with respect to the signal grid used in the previously described analysis is the choice of the filter to be applied at the generator level. The

[2]Many theories beyond the Standard Model predict the existence of unstable particles (or resonances) at TeV scale; they are not observed directly, but they iniziate a cascade of decays (the so-called *decay branch*) ending up with particles which may be observed in the detector. Such processes lead to a rich phenomenology, because the spin of the heavy resonances and the type of couplings to other fields imply non-trivial angular corrections among the final state particles inside a given decay branch (*decay spin correlation effects*) or among the particles from distinct decay brances (*production spin correlation effects*).

[3]The off-shell effects imply that the masses of some external particles in the undecayed event with some specific kinematics are altered, requiring to modify the external momenta in such a way that energy and momentum are still conserved. This modification is sometimes called *momentum reshuffling*.

role of the filter is to introduce a minimal event selection during the generation process, but avoiding any bias in the generated sample; this prevents the assignment of abnormally high normalization event weights to the events surviving the analysis selection due to the limited statistics of inclusive samples, at the same time reducing the statistical error.
In the signal samples described in Section 4.2.1, a filter requiring the existence in each event of at least two leptons in the final state (electrons or muons, directly coming from the off-shell W or from τ decays) with $p_{\mathrm{T}} > 8$ GeV and $|\eta| < 2.8$ is applied. This filter choice is referred to as 2L8 and it was adopted coherently with the choice of dilepton triggers, with $p_{\mathrm{T}} > 25$ GeV offline threshold on both lepton in the analysis.
However, leptons in the low mass-splitting region are expected to be softer, which makes the approach used in the previous analysis not suitable. Two alternatives have been taken into account.
The first alternative is to use of an $E_{\mathrm{T}}^{\mathrm{miss}}$-based filter requiring $E_{\mathrm{T}}^{\mathrm{miss}} > 100$ GeV ($m100$), which is a quite conventional approach in exploring compressed signatures. In order to test $m100$, two different signal points, with $m(\tilde{\chi}_1^{\pm}, \tilde{\chi}_1^0) = (125, 100)$ GeV and $m(\tilde{\chi}_1^{\pm}, \tilde{\chi}_1^0) = (175, 150)$ GeV have been generated with 2L8 and $m100$ filters to compare their effectiveness in these low mass-splittings scenarios. Then, loose offline cuts on the filtered events have been defined thinking of the trigger selection to be perfomed on these samples, i.e. dilepton triggers (as reported in Table 4.2) for 2L8 and $E_{\mathrm{T}}^{\mathrm{miss}}$ triggers (whose thresholds are around 100 GeV) for $m100$, leading to: two opposite sign leptons with $p_{\mathrm{T}} > 25$ GeV for 2L8 and $E_{\mathrm{T}}^{\mathrm{miss}} > 250$ GeV for $m100$.
The most important difference observed between the two filters, together with the previously defined offline cuts, comes from the jet multiplicity in the event, as shown in Figure 5.2.

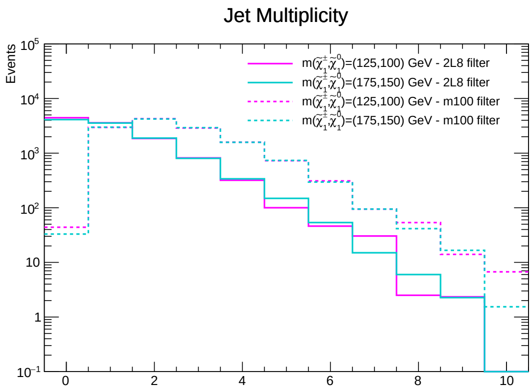

Figure 5.2: Distribution of the jet multiplicity for two generated "compressed" signal points, comparing a lepton (2L8) and a $E_{\mathrm{T}}^{\mathrm{miss}}$-based ($m100$) filter; the offline cuts associated are reported in the text.

The distribution of the jet multiplicity for 2L8-filtered samples is shown with the solid lines and it is peaked at low values of jet multiplicity, as expected from the final state signature under study (also considering the possible presence of an ISR/FSR jet). On the opposite, the $m100$-filtered samples are shown with dashed lines and the corresponding distributions tend to have higher values, since the $E_{\mathrm{T}}^{\mathrm{miss}}$ cut select events with ISR/FSR jets which, boosting the chargino system, are responsible of the higher-$E_{\mathrm{T}}^{\mathrm{miss}}$ values. Then, finally, $m100$ induces a bias on the filtered events which would reduce them drastically with respect to the expected signal signature.

The second alternative consists in looking forward to a trigger selection based on single lepton triggers, which allows for an offline asymmetric p_{T} selection: the leading lepton p_{T} may have a higher threshold requested, while a very loose one can be applied on the subleading lepton.
For this reason, two other filters have been compared: one requires at least one lepton with $p_{\mathrm{T}} > 20$ GeV (1L20), while the latter at least two soft lepton with $p_{\mathrm{T}} > 3$ GeV in a logical AND with the condition of at least one hard lepton with $p_{\mathrm{T}} > 20$ GeV (1L202L3). A common request of $|\eta| < 2.8$ is also applied to the lepton.

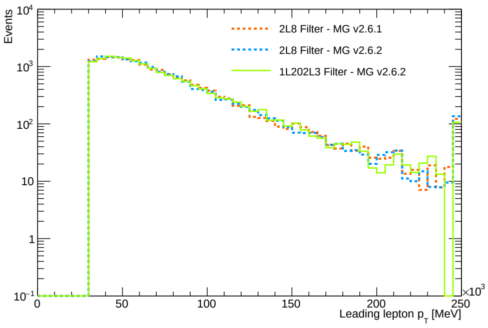

(a) Leading lepton p_{T}

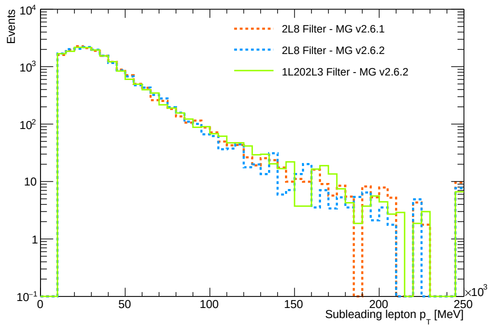

(b) Subleading lepton p_{T}

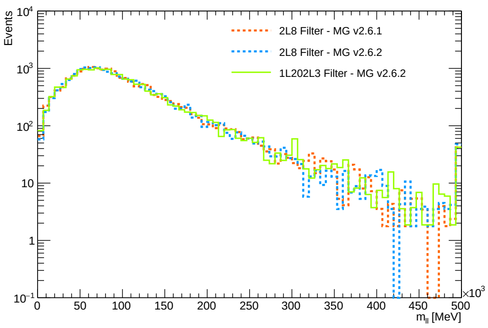

(c) Dilepton invariant mass

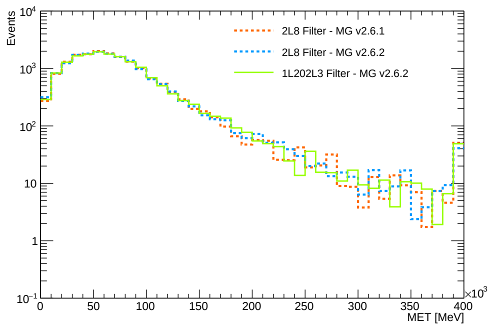

(d) Missing Transverse Energy

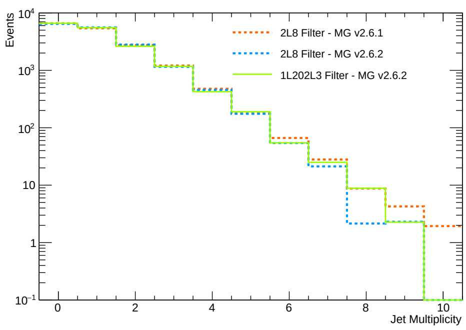

(e) Jet Multiplicity

Figure 5.3: Kinematic distributions at truth level comparing two filters, 2L8 and 1L202L3, and two MadGraph versions using the same offline selection $p_{\mathrm{T}}^{\ell_1} > 30$ GeV and $p_{\mathrm{T}}^{\ell_2} > 10$ GeV for the signal point $m(\tilde{\chi}_1^{\pm}, \tilde{\chi}_1^0) = (150, 50)$ GeV.

An offline selection requiring $p_{\mathrm{T}}^{\ell_1} > 30$ GeV and $p_{\mathrm{T}}^{\ell_2} > 10$ GeV is applied. Some kinematic distributions are shown in Figure 5.3 to compare the two filters (and also 2L8 applied to two different MadGraph versions, v2.6.1 and v2.6.2) for the signal point $m(\tilde{\chi}_1^{\pm}, \tilde{\chi}_1^0) = (150, 50)$ GeV.

Filter	Selection [GeV]	Yield
2L8	$p_T^{\ell_{1,2}} > 25$	6.30 ± 0.57
	$p_T^{\ell_1} > 30$ and $p_T^{\ell_2} > 10$	23.04 ± 1.10
1L20	$p_T^{\ell_1} > 30$ and $p_T^{\ell_2} > 10$	24.59 ± 0.89
	$p_T^{\ell_1} > 30$ and $p_T^{\ell_2} > 5$	36.82 ± 1.09
1L202L3	$p_T^{\ell_1} > 30$ and $p_T^{\ell_2} > 10$	22.14 ± 0.63
	$p_T^{\ell_1} > 30$ and $p_T^{\ell_2} > 5$	33.57 ± 0.78

Table 5.1: Comparison of 2L8, 1L20 and 1L202L3 filters after generating 10000 events per each filter for the very compressed point $m(\tilde{\chi}_1^{\pm}, \tilde{\chi}_1^0) = (200, 190)$, representative of the minimum mass splitting in the new grid.

As it can be observed in Table 5.1, the 2L8 filter with the preliminary selection $p_T > 25$ GeV on both leptons (the request performed in the previous analysis) has a limited acceptance in this so-compressed scenario. For the three filters with the selection $p_T^{\ell_1} > 30$ GeV and $p_T^{\ell_2} > 10$ GeV, as expected, the same numbers of events survive within errors, but 1L202L3 is the best choice because of the higher offline selection efficiency, which results in a reduced statistical uncertainty on the final selected event yield. Although the requirements $p_T^{\ell_1} > 30$ GeV and $p_T^{\ell_2} > 5$ GeV cannot be applied in case of the 2L8 filter, the situation is different for the other two possible choices: the aforementioned selection results in a relevant gain ($\sim 30\%$) if compared to the one with a 10 GeV threshold on the subleading lepton p_T, with 1L202L3 ensuring a lower statistical error, as expected.

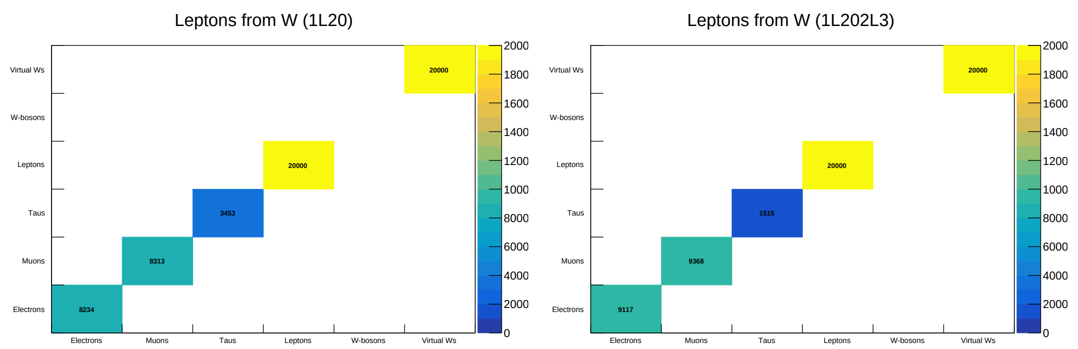

(a) 1L20 filter (b) 1L202L3 filter

Figure 5.4: Comparison of the lepton flavour coming from the leptonic W boson decays with the 1L20 and 1L202L3 filters. The latter shows a reduced contribution of hadronically decaying τ-leptons.

Moreover, looking at the truth origin of the leptons, hadronically decaying τ-leptons are significantly rejected by requiring the presence of a second lepton in the filter definition, alongside imposing a minimal cut on its p_T, as in 1L202L3 filter and shown in Figure 5.4.
Such motivations have justified the submission of the official request of the signal grid

shown in Figure 5.1 for the chargino production with W-boson-mediated decays in the compressed region asking for the application of a 1L202L3 filter in generation. Accordingly to this choice, the implemented trigger selection is based on the lowest unprescaled single lepton trigger items, as shown in Table 5.2.

5.2 MultiVariate Analysis approach

Nowadays the crucial need to extract as much information as possible from data coming from several fields, especially when searching for rare events in large datasets, leads to use multivariate classification methods based on machine learning algorithms. Tuning and combining multivariate classifiers to gain in performance has become a fundamental ingredient in analizing data in recent years.
In general, a *classification* problem corresponds to a *discretized regression* problem, where a regression is the process of estimating the parameter values of a function which, in turn, predicts the value of a response variable or function, the *classifier*[4]. The process depends on a set of *input* variables which are provided to the algorithm. For instance, a typical regression problem is the estimation of a calorimeter cluster energy starting from the individual electromagnetic cell energies. This problem is not trivial, becoming much more complicated in case of a multi-dimensional parameter space.
All multivariate techniques may be included in the more general family of *supervised learning* algorithms. They make use of training events, for which the output is well-known, to determine a mapping function either describing a decision boundary (in case of a *classification* task) or an approximation of the underlying functional behavior defining the target values (for a *regression* task). The mapping function can include various degrees of approximation and may be a single, global function or a set of local models.
For a classification problem of events into the two standard signal and background categories, the best choice of the decision boundary relies on the knowledge of the pdf associated with the null $\mathcal{H}_b$ and the alternative $\mathcal{H}_{s+b}$ hypotheses. Unfortunately, in a real-world problem these quantities are unknown, hence the need to approximate them with some other functions. Monte Carlo simulations are, therefore, used to have an estimation of the probability density functions for signal and background event category. Of course, an accurate Monte Carlo tuning to reproduce the real data is an absolutely essential condition to ensure the reliability of the entire procedure.
A typical analysis, using a multivariate approach to classify events in the "signal" and "background" categories, needs two main steps which are described below.

- *Training*: this is the "learning" phase, where the chosen algorithm uses events which are known to belong to signal or background to determine the mapping function. Simulated events are split in two statistically independent subcategories:
  - training events, which are used to estimate the mapping function, as well as a region where emphasizing separation of signal from background;
  - testing events, used to validate the mapping function determined by the training ones on a statistically independent sample.

[4]Classifiers can be a mono- or multi-dimensional quantities.

Event Topology (channel)		Triggers
Electron	2015	HLT_e24_lhmedium_L1EM20VH – $1e^{\pm}$ with $E_{\mathrm{T}} > 24$ GeV, medium likelihood identification – Seeded by L1 trigger requiring one EM clusters with $E_{\mathrm{T}} > 20$ GeV HLT_e60_lhmedium – $1e^{\pm}$ with $E_{\mathrm{T}} > 60$ GeV, medium likelihood identification HLT_e120_lhloose – $1e^{\pm}$ with $E_{\mathrm{T}} > 120$ GeV, loose likelihood identification
	2016	HLT_e24_lhtight_nod0_ivarloose – $1e^{\pm}$ with $E_{\mathrm{T}} > 24$ GeV, tight likelihood identification – No transverse impact parameter cut applied – Loose isolation criteria applied
	2016-2017-2018	HLT_e140_lhloose_nod0 – $1e^{\pm}$ with $E_{\mathrm{T}} > 140$ GeV, loose likelihood identification – No transverse impact parameter cut applied HLT_e300_etcut – $1e^{\pm}$ with $E_{\mathrm{T}} > 300$ GeV, no likelihood identification
	2017-2018	HLT_e26_lhtight_nod0_ivarloose – $1e^{\pm}$ with $E_{\mathrm{T}} > 26$ GeV, tight likelihood identification – No transverse impact parameter cut applied – Loose isolation criteria applied HLT_e60_lhmedium_nod0 – $1e^{\pm}$ with $E_{\mathrm{T}} > 60$ GeV, medium likelihood identification – No transverse impact parameter cut applied
Muon	2015	HLT_mu20_iloose_L1MU15 – $1\mu^{\pm}$ with $p_{\mathrm{T}} > 20$ GeV – Loose isolation criteria applied – Seeded by L1 trigger requiring $1\mu^{\pm}$ with $p_{\mathrm{T}} > 15$ GeV
	2015-2016	HLT_mu40 – $1\mu^{\pm}$ with $p_{\mathrm{T}} > 40$ GeV
	2015-2017-2018	HLT_mu60_0eta105_msonly – $1\mu^{\pm}$ with $p_{\mathrm{T}} > 60$ GeV – Muon Spectrometer standalone chain, barrel region
	2016	HLT_mu24_ivarloose – $1\mu^{\pm}$ with $p_{\mathrm{T}} > 24$ GeV – Loose isolation criteria applied HLT_mu24_ivarmedium – $1\mu^{\pm}$ with $p_{\mathrm{T}} > 24$ GeV – Medium isolation criteria applied
	2016-2017-2018	HLT_mu26_ivarmedium – $1\mu^{\pm}$ with $p_{\mathrm{T}} > 26$ GeV – Medium isolation criteria applied HLT_mu50 – $1\mu^{\pm}$ with $p_{\mathrm{T}} > 50$ GeV

Table 5.2: Preliminary list of single lepton trigger items used in the second round of the analysis. Due to the compressed scenarios targeted, alongside the increase of instantaneous luminosity and pile-up conditions during Run II, higher p_{T} thresholds or tighter trigger requests have been applied on the leading lepton.

- *Application*: this is the subsequent classification of any given event (or sample, e.g. in data) into signal or background categories, exploiting the mapping function determined in the training.

In order to rely on the application results, an accurate validation of the training procedure plays a crucial role, mainly guaranteeing the subsequent reproducibility of the training results with any unknown sample. The following tests deserve a particular mention.

- *Overtraining*: it occurs when a machine learning problem has too few degrees of freedom, deriving from the introduction in the algorithm of too many model parameters which are, then, adjusted to too few data points. The sensitivity to the overtraining depends on the chosen algorithm (or, more generically, machine learning method) and on the available event statistics available for the training. In general, the overtraining has the effect that the classification performance measured on the training sample is different (higher) than the one really achievable on an independent generic sample.

- *Kolmogorov-Smirnov test*: this test is based on the maximum difference between an empirical, cumulative distribution function of a sample x [234] $\tilde{P}_n(x)$ and the model distribution function $P(x)$, representative of the null hypothesis $\mathcal{H}_0$: $\tilde{P}_n(x) = P(x)$. The test statistic is the maximum distance between these distributions
$$D_n = \sup_x |\tilde{P}_n(x) - P(x)| \tag{5.1}$$
The smaller the distance D_n, the better the agreement between $\tilde{P}_n$ and P, pointing to the acceptance of $\mathcal{H}_0$. In the specific case, the two functions are the classifier distributions for the training and testing samples and this test is used to verify the null hypothesis, i.e. the two distributions belong to the same parent distribution. An important feature of the Kolmogorov-Smirnov test is that the two samples of events are treated in separated ways, without any interference, since an internal division between training and testing samples is performed at the beginning of the classification procedure.

- *Receiver Operating Characteristic* (ROC): it quantifies the performance of the classification and it usually shows the true positive rate (signal efficiency) versus the false positive rate, as they result from the different trainings. In a signal-background classification, it usually reports the background rejection as a function of the signal efficiency.

5.2.1 Software tools

In this section a short description of the software packages used to implement a, still preliminary, MVA approach in the search for chargino production with W-boson-mediated decays in the low mass-splitting region, is presented. The *Toolkit for MultiVariate Analysis* [160] (TMVA) provides a general environment, integrated in the ROOT computing framework, for the processing, parallel evaluation and application of multivariate classification and regression techniques. The software package consists of abstract, object-oriented implementations in C++/ROOT for a broad range of multivariate analysis methods, as well as auxiliary tools for performance evaluation and visualization. In order to make available in TMVA additional external methods, PyMVA is the interface, based on Python, to powerful external libraries, easily accessible with

a direct integration into the Tmva workflow.
The framework to train the machine learning classifier chosen to distinguish between Standard Model background and signal is based on an artificial *Deep Neural Network* (DNN) built with the python library Keras [235] with the Theano [236] backend and the Adam [237] optimizer. Although this method is not directly included in Tmva framework, the training and predictions steps of the Keras python package are interfaced to it, so that the entire procedure can be done within the Tmva environment: a model must be generated with Keras first, then it can be loaded and trained in the Tmva framework. It is important to stress that the decision to use this external method has been taken after a detailed investigation about the discrimination powers of several BDT [238] methods. They are directly available in Tmva and often used in other analysis; after comparing them with Keras, it has been noticed being more performing in terms of signal-background discrimination. As an example, a direct comparison is performed in Table 5.5, after the explanation of the technique adopted for this kind of analysis.

5.2.2 Monte Carlo samples

The background samples in this analysis are mostly the same as the ones reported in Section 4.2.2, the only difference being the usage of diboson samples (VV) generated with Sherpa v2.2.1 or v2.2.2 [200] generators, depending on the process. Fully leptonic and semileptonic final states are generated using matrix element at NLO accuracy in QCD for up to one additional parton and at LO accuracy for up to three additional parton emission. Samples for the loop-induced processes $gg \to VV$ are generated using LO-accurate matrix elements for up to one additional parton emission for both cases of fully leptonic and semileptonic final states. The matrix element calculations are matched and merged with the Sherpa parton shower based on Catani-Seymour dipole [239, 240] using the MEPS@NLO prescription [241–244]. The virtual QCD correction are provided by the Open-Loops library [245, 246]. The NNPDF3.0NNLO set of PDF is used [194], along with the dedicated set of tuned parton-shower parameters developed by the Sherpa authors.
In order to train the method using as much statistics as possible, a few privately generated truth signal samples, $m(\tilde{\chi}_1^{\pm}, \tilde{\chi}_1^0) = (150, 100)$, $(200, 100)$ and $(200, 150)$ GeV having one million of events each[5], have been used. In these samples a smearing procedure is applied on the truth events, using a framework which is based on dedicated smearing functions, all derived from detailed studies by the ATLAS performance groups. From these studies, the parametrizations of reconstruction and identification efficiencies in ATLAS are determined. Energies of truth objects are smeared with a Gaussian term using a standard deviation corresponding to the energy resolution of the detector, with a dependence on p_{T}, η and on the reconstructed physics object type. The smearing is applied on all key objects of the analysis at generator level. Preliminary studies have shown that the relevant (for the analysis) kinematic distributions of the signals generated, as just described, are in reasonable agreement with the ones of the corresponding signals generated with the standard simulation procedure, as shown in Figure 5.5 for the signal point $m(\tilde{\chi}_1^{\pm}, \tilde{\chi}_1^0) = (200, 100)$ GeV.

[5] In big collaborations for high energy particle physics research, such high statistics cannot be requested without an appropriate or dedicated justification.

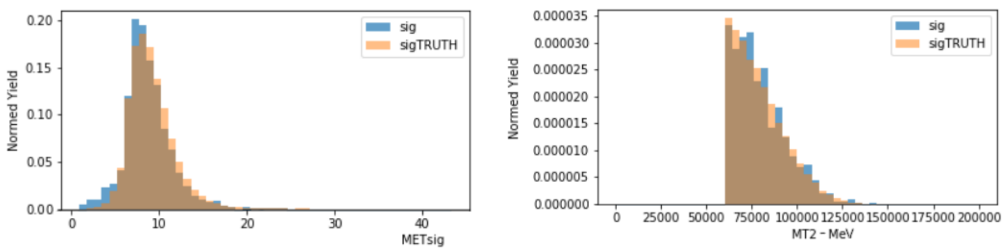

(a) $E_{\mathrm{T}}^{\mathrm{miss}}$ significance (b) m_{T2}

Figure 5.5: Distributions of $E_{\mathrm{T}}^{\mathrm{miss}}$ significance 5.5(a) and m_{T2} 5.5(b) for the reconstructed signal point $m(\tilde{\chi}_1^{\pm}, \tilde{\chi}_1^0) = (200, 100)$ GeV and the truth-smeared one. The enlarged preselection $p_{\mathrm{T}}^{\ell_1} > 30$ GeV, $p_{\mathrm{T}}^{\ell_2} > 25$ GeV, $m_{\ell_1\ell_2} > 11$ GeV, $m_{\mathrm{T2}} > 65$ GeV, $\mathcal{S} > 3$ is applied.

5.2.3 Analysis setup

The general object definitions mostly resemble the ones reported in Section 4.4, although the optimization is still in progress. Concerning the trigger to select the events, as already discussed, the major difference is the adoption of single lepton trigger strategy. This choice implies the usage of a different preliminary event selection with respect to the one described in Section 4.5.1. Exactly two opposite charged leptons are required, the leading one with $p_{\mathrm{T}} > 30$ GeV, while the subleading one with $p_{\mathrm{T}} > 9$ GeV. This last cut is not optimal, since the general idea in this analysis is to target softer subleading leptons to increase the signal acceptance for low mass splittings. However, the background samples currently used in this analysis have a dedicated and minimal selection on the leptons, corresponding to the threshold applied to the subleading lepton. The production of Monte Carlo samples with suitable cuts for this analysis is under investigation.

Variable	Cut value
Number of signal leptons	$= 2$
Lepton charge	OS
Leading lepton p_{T} [GeV]	> 30
Subleading lepton p_{T} [GeV]	> 9
Invariant Mass $m_{\ell_1\ell_2}$ [GeV]	> 11
Number of central b-jets	$= 0$
Number of central light jets	$= 0$
$\lvert\cos\theta^*_{\ell_1\ell_2}\rvert$	< 0.8
$E_{\mathrm{T}}^{\mathrm{miss}}$ [GeV]	> 30
$\mathcal{S}$	> 3

Table 5.3: Preliminary cuts in the event selection for the compressed analysis.

To avoid contributions from low-mass resonances, the invariant mass of the two leptons must be $m_{\ell_1\ell_2} > 11$ GeV. Events are further required to have no reconstructed b-jet and no central light jet. $\cos\theta^*_{\ell_1\ell_2} \equiv \tanh[(\eta_{\ell_1} - \eta_{\ell_2})/2]$ is an interesting variable [247], being sensitive to the polar angle in direct slepton pair production. Moreover, it is invariant under boosts along the beam axis, therefore it can be used despite the fact that the longitudinal boost of the centre-of-mass frame cannot be determined. On this variable,

the cut $|\cos\theta^*_{\ell_1\ell_2}| < 0.8$ is applied, in order to ensure a reasonably good modelling of the Standard Model background. No separate optimization is performed for Different and Same lepton Flavour, but in case of Same Flavour events $|m_{\ell_1\ell_2} - m_Z| > 20$ GeV is requested (Z veto). Minimal requirements are applied on $E_{\mathrm{T}}^{\mathrm{miss}}$ and $E_{\mathrm{T}}^{\mathrm{miss}}$ significance in order to reduce Z+jets contribution: $E_{\mathrm{T}}^{\mathrm{miss}} > 30$ GeV and $\mathcal{S} > 3$. This set of preliminary cuts is summarized in Table 5.3.
The truth-smeared sample of the signal point $m(\tilde{\chi}_1^{\pm}, \tilde{\chi}_1^0) = (200, 150)$ GeV, assumed as a benchmark point, has been trained against the full background. A list of 14 variables, including several angular-related quantities, have been chosen as input variables for the training phase:

- leading and subleading lepton p_{T};
- dilepton invariant mass $m_{\ell_1\ell_2}$;
- $E_{\mathrm{T}}^{\mathrm{miss}}$ and $E_{\mathrm{T}}^{\mathrm{miss}}$ significance;
- stransverse mass m_{T2};
- leading and subleading lepton η;
- absolute difference between the two lepton ϕ-coordinates: $\Delta\phi_{12} \equiv |\phi_{\ell_1} - \phi_{\ell_2}|$;
- absolute difference between the lepton ϕ-coordinates and the ϕ-component of the missing transverse momentum: $\Delta\phi^{\mathrm{miss}}_{\ell_{(1,2)}} \equiv |\phi_{\ell_{(1,2)}} - \phi_{\mathrm{T}}^{\mathrm{miss}}|$;
- lepton transverse mass: $m_{\mathrm{T}}^{\ell_{(1,2)}} \equiv \sqrt{2p_{\mathrm{T}}^{\ell_{(1,2)}} E_{\mathrm{T}}^{\mathrm{miss}}[1 - \cos(\phi_{\ell_{(1,2)}} - \phi_{\mathrm{T}}^{\mathrm{miss}})]}$;
- $\cos\theta^*_{\ell_1\ell_2}$.

Figure 5.6 shows some input variable distributions at the preliminary event selection level. It is important to stress that the FNP contamination is not taken into account in these distributions, since it is expected to be evaluated later with a data-driven method.
The training is performed on 70% of all background events, while the residual 30% is defined as the test set. Table 5.4 shows the relevant settings of the neural network.

Parameter	Setting
Number of layers	3
Activation function	relu [248]
Learning rate	Default
Weight initialization	Glorot normal [249]
Batch size	32 [250]
Batch normalization [251]	Yes

Table 5.4: Properties and parameters of the neural network.

After the training phase, the goodness and reliability of the training itself can be roughly evaluated through the two plots in Figure 5.7. Figure 5.7(a) shows the classifier distributions for signal and background events for training and testing samples. By TMVA convention, signal (background) events accumulate at large (small) classifier values. Hence, retaining events with classifier values larger than a given cut selects

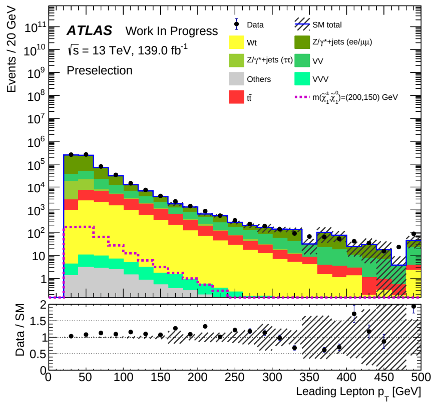

(a) Leading lepton p_{T}

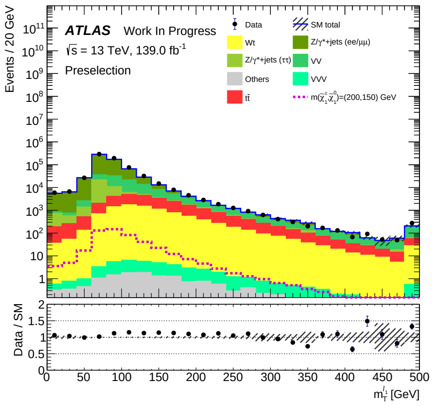

(b) Leading lepton transverse mass m_{T}

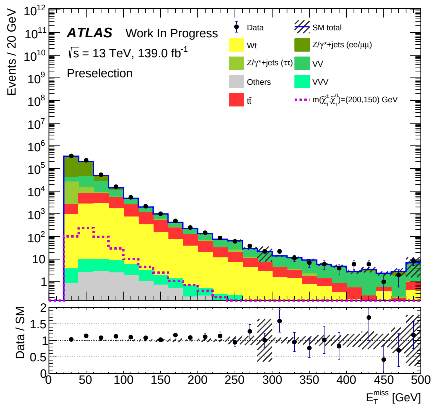

(c) $E_{\mathrm{T}}^{\mathrm{miss}}$

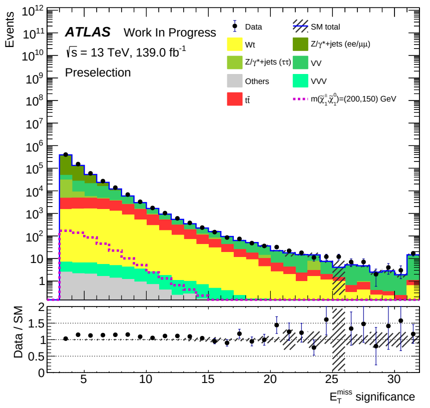

(d) $E_{\mathrm{T}}^{\mathrm{miss}}$ significance

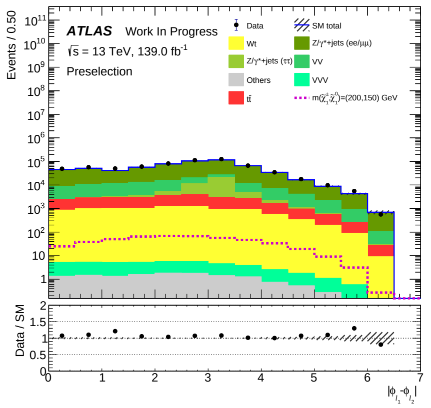

(e) $\Delta\phi_{12}$

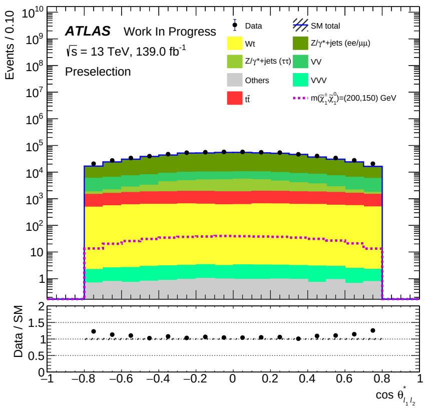

(f) $\cos\theta^*_{\ell_1\ell_2}$

Figure 5.6: Distributions of some kinematic variables used as input for the machine learning algorithm at the preliminary event selection level. The uncertainty band includes statistical errors only. Distribution of the truth-smeared signal point is overlaid for comparison. The lower panel show the ratio of data to the SM background estimate.

the signal with efficiencies/purities that, respectively, decrease/increase with increasing the cut value. The resulting background rejection versus signal efficiency is shown in Figure 5.7(b) which reports the Receiver Operating Characteristic curve.

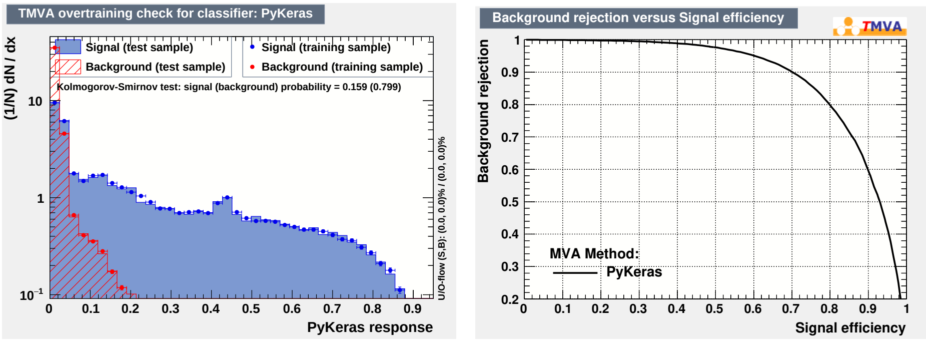

(a) Signal and background distributions for the trained classifier (testing and training samples are superimposed to probe overtraining), alongside the results of the Kolmogorov-Smirnov test.

(b) Background rejection versus signal efficiency achievable with the training (ROC curve from the testing sample).

Figure 5.7: Standard test distributions to evaluate the training.

The results of the training phase, i.e. the mapping function definition, are stored in a weight file which is used to classify any unknown (from Monte Carlo or, in the future stages of the analysis, from data) given event as signal or background. For each Monte Carlo sample in the analysis a resulting distribution of the classifier output is produced starting from this weight file. The further step is the definition of the best cut on the classifier value which maximizes the significance function (`RooStats::NumberCountingUtils::BinomialExpZ`) [216, 252, 253]. Due to the presence in the present samples of few off-shell Z+jets events with large weights associated, the resulting overall significance and sensitivity in the SF channel are severely harmed. Nevertheless, the Different Flavour channel looks promising, as shown in Figure 5.8. The cuts applied are the ones reported in Table 5.3, with the best cut on the classifier value. The achieved significance is shown in case of an additional 0% or 20% flat systematic uncertainty is applied, on top of the statistical one. Table 5.5 shows the best cut on classifier value and the corresponding significance, alongside the signal and dominant background event yields in both cases. The bottom part of the table also reports the results obtained using a BDT classifier without any optimization on the internal parameters of the method, but with the same preliminary event selection and training variables used for the DNN. This consistent comparison supports the choice of a DNN as primary analysis tool.

General and specific improvements are under evaluation at this stage of the analysis, other signal points are needed in order to perform new trainings according to $\Delta m(\tilde{\chi}_1^{\pm}, \tilde{\chi}_1^0)$ and the significance through the full new signal grid must be evaluated. However the usage of machine learning algorithms could be promising in the search for chargino pair production with W-boson-mediated decays in a compressed scenario, where the analysis described in Chapter 4, based on the cut&count and shape fit combined approach, did not show sensitivity.

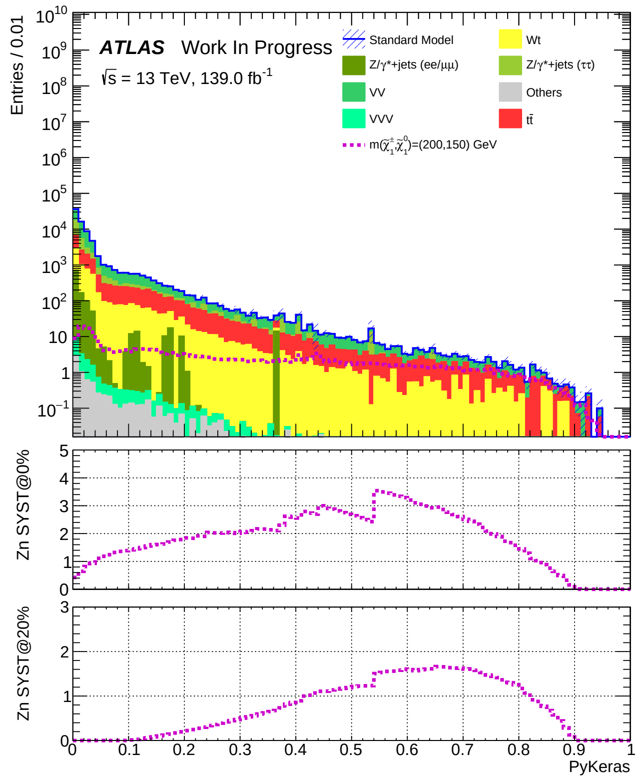

Figure 5.8: Distribution of the classifier for the Monte Carlo backgrounds and the truth-smeared benchmark signal sample overlaid. Only DF events are shown, after the preliminary selection. The uncertainties are statistical only. The achievable significance, as a function of the cut on the classifier value, is also reported, both in case of no systematic uncertainty applied (middle panel) and in case of a 20% flat systematic included (bottom panel).

	0% systematic uncertainty	20% systematic uncertainty
	DNN (PyKeras)	
Classifier cut	0.54	0.65
Significance	3.53	1.66
Background yields	Wt: 13.4 ± 1.3 $t\bar{t}$: 40.7 ± 1.6 VV: 40.0 ± 2.0	Wt: 6.96 ± 0.97 $t\bar{t}$: 18.74 ± 1.14 VV: 18.05 ± 1.29
Signal yield	39.5 ± 0.4	22.60 ± 0.32
	BDT	
Classifier cut	0.02	–
Significance	0.60	–
Background yields	Wt: 3277.7 ± 21.3 $t\bar{t}$: 6492.8 ± 20.3 VV: 23742.9 ± 56.7 Z+jets: 2763.0 ± 185.0	– – – –
Signal yield	165.7 ± 0.9	–

Table 5.5: Best cuts on classifier value, in case of applying an additional 0% or 20% flat systematic uncertainty, and the related significance. Signal and dominant background yields after the cuts are also reported. A comparison between a DNN and a BDT is shown: because of the poor performance of the latter method, only the case with 0% flat systematic uncertainty is reported.

Conclusions

This thesis describes the search for the electroweak pair production of charginos and sleptons. The analysis strategy is optimized to study the decay of the lightest chargino into an on-shell W boson and the lightest neutralino (assumed to be the LSP). The signature of the final state requires two isolated, opposite in charge, highly energetic leptons (electron or muons) coming from the decay of the W bosons and large values of missing transverse energy. At least one light jet is allowed in the final state.
The analysis results are interpreted in two other SUSY scenarios: the search for the direct production of lightest-chargino pairs, where each chargino decays into a slepton via the emission of a lepton and the slepton itself decay into a lepton and the LSP; and the search of direct pair production of sleptons, where each slepton decays into a lepton and the LSP. Different assumptions about the masses of the superpartners of the left-handed and right-handed charged leptons are considered. Lepton flavour is conserved in all processes. The interpretation of the results is based on simplified models for all processes.
The search is performed on data collected in LHC proton-proton collisions from 2015 to 2018, the entire LHC Run II operating period, by the ATLAS experiment at $\sqrt{s} = 13$ TeV, resulting in an integrated luminosity of 139 fb^{-1} .
The irreducible Standard Model diboson background, particularly the WW component, makes this search challenging because of its similarity with the signal models under study. The analysis strategy is mainly driven by the usage of high stransverse mass values, alongside hard cuts on missing transverse energy and significance. Two sets of m_{T2}-based Signal Regions are defined: exclusive Signal Regions, optimized through the maximization of the exclusion limits with a shape fit strategy adopted, and inclusive Signal Regions, optimized to maximize the probability to discover physics processes beyond the Standard Model.
The main background contributions in these regions are diboson and top-quark production. They are carefully evaluated using a semi-data-driven estimation relying on dedicated Control Regions, in order to normalize the Monte Carlo predictions to the observed data through a likelihood fit procedure. The extracted transfer factors are, then, validated in suitably defined Validation Regions before being applied to the Signal Regions.
No statistically significant excess is observed in none of the Signal Regions after the fit. Therefore, the exclusive Signal Regions are used to calculate exclusion limits in the $[m(\tilde{\chi}_1^{\pm}, \tilde{\ell}), m(\tilde{\chi}_1^0)]$ mass plane. In the model of direct chargino pair production with W-boson-mediated decays, chargino masses up to 420 GeV are excluded for a massless lightest neutralino. In the scenario of direct chargino pair production with decays via sleptons or sneutrinos, chargino masses up to 1 TeV are excluded for a massless lightest neutralino. In the model of direct slepton pair production, slepton masses up to 700 GeV are excluded for a massless lightest neutralino. All exclusion limits are computed

at 95% Confidence Level. These results significantly extend the previous exclusion limits for the same scenarios. Furthermore, upper limits on the visible cross-section of possible Beyond Standard Model physics are also calculated.
This analysis has been described, and its results reported, in the paper: *Search for electroweak production of charginos and sleptons decaying into final states with two leptons and missing transverse momentum in* $\sqrt{s} = 13$ *TeV pp collisions using the ATLAS detector*. It has been published on European Physics Journal C [1] on February 2020.
The strategy used in this analysis is optimized to target signals with intermediate/large ($\geq W$ mass) splitting between the chargino and the lightest neutralino masses and, in general, for intermediate/large chargino and slepton masses. It does not show sensitivity in the region close to the diagonal $m(\tilde{\chi}_1^{\pm}) - m(\tilde{\chi}_1^0) \simeq m(W)$, leaving this "compressed" region a perfect target for a new round of analysis, which has already started. A new set of signal models in the compressed region is ready to be investigated with a MultiVariate analysis approach. Preliminary results obtained using machine learning techniques are encouraging.

Appendix A

Additional details on the FNP estimation

The reducible background of fake-and-non-prompt leptons is derived using a data-driven technique called Matrix Method. Additional details concerning the estimation of fake rate and real efficiencies are given here, completing the description provided in Section 4.7.1.

A.1 Real efficiency

The real efficiency is calculated as a function of p_{T} and η in a dedicated Control Region extrated from $Z \to \ell^{\pm}\ell^{\mp}$, defined by requiring two opposite charged leptons with an invariant mass within 10 GeV from the Z peak. Figure A.1 shows the p_{T} distributions for loose electrons and muons in this region, separated per data taking campaign. As expected, the region is totally dominated by leptons from Z decays.
The corresponding real efficiencies extracted from data are shown in Figure A.2: they are calculated using the bidimensional dependence on both p_{T} and η, considering each data taking campaign separately when estimating the fake lepton background.

A.2 Fake rate

The fake rate for leptons come from different sources: decay of *Light-Flavoured* (LF) and *Heavy-Flavoured* (HF) hadrons and *Photon Conversions* (CO). All these sources share a common (p_{T}, η) dependence and individual contributions are combined together into a global weighted-averaged fake rate, given by

$$f_{tot}(p_{\mathrm{T}}, \eta) = \sum_i f_i(p_{\mathrm{T}}, \eta) w_i(p_{\mathrm{T}}, \eta), \qquad \text{(A.1)}$$

with the index i running over the different types considered, each component having an efficiency f_i. The weight w_i reflects the relative amount of each fake source in a signal-like region; this fraction is estimated after applying the preliminary event selection of the analysis in a set of regions as a function of m_{T2}.
The m_{T2}-dependence on the fake composition is shown in the upper panels of Figure A.3, as an example, for opposite charged electron-muon events in four different

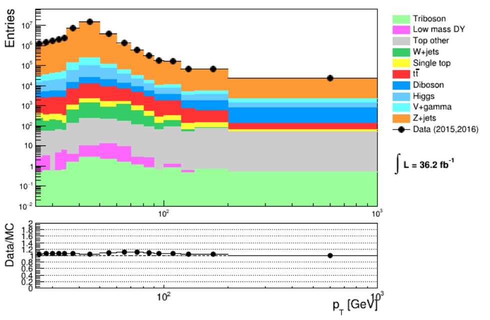

(a) Loose electrons (Data 2015-2016)

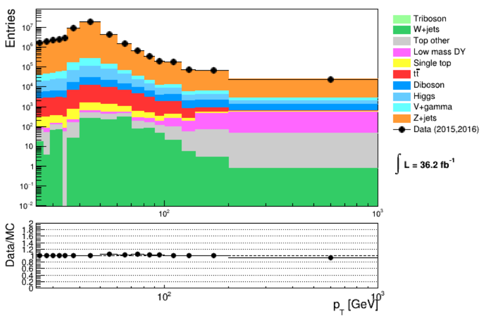

(b) Loose muons (Data 2015-2016)

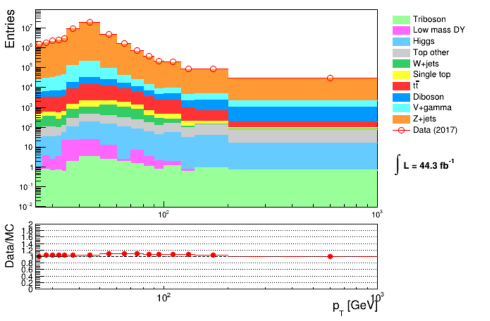

(c) Loose electrons (Data 2017)

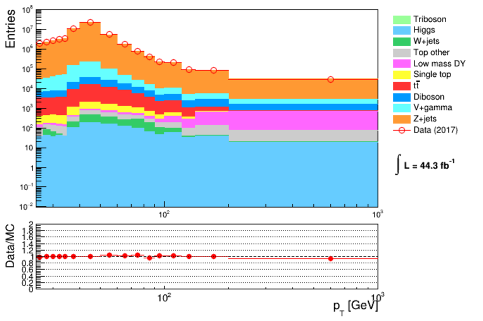

(d) Loose muons (Data 2017)

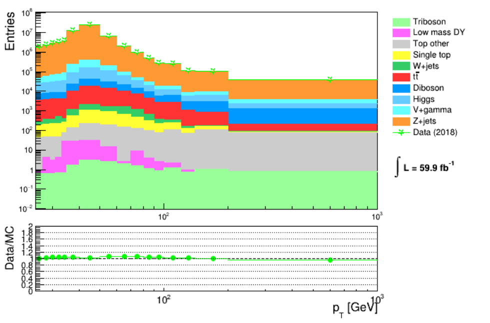

(e) Loose electrons (Data 2018)

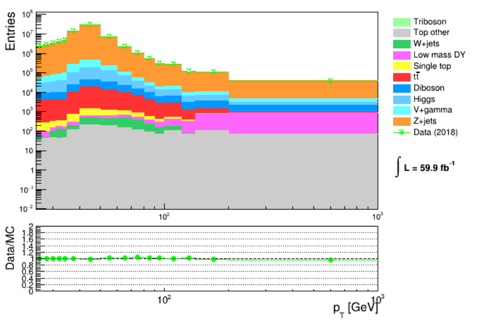

(f) Loose muons (Data 2018)

Figure A.1: p_{T} distributions for the Loose electrons (left) and muons (right) in the Control Region used for the real efficiency estimation. The distribution are divided per data taking campaign.

regions; the lower panel indicates the main Monte Carlo processes contributing to the fake leptons in each region for five different m_{T2} bins. They include preliminary event selection cuts ($p_{\mathrm{T}}^{\ell_{1,2}} > 25$ GeV and $m_{\ell_1\ell_2} > 25$ GeV) and a b-jet veto, together with additional cuts reported in each case.
The relative composition is used to compute the relatively importance of each fake source, whilst the difference in the estimate for all the regions is considered as a source of global uncertainty, i.e. for the estimation itself.
The three different sources of fake leptons have all the same importance for the electron fake rate estimate, while the decay of Heavy-Flavoured hadrons is the dominant contribution in the fake rate for muons. For the latter category, the Monte Carlo truth samples are used to subtract the contamination of real leptons in the dedicated Con-

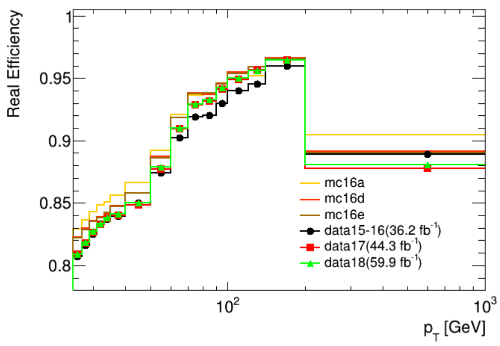

(a) Electrons

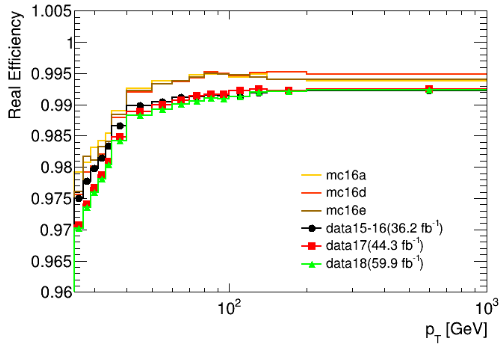

(b) Muons

Figure A.2: The real efficiencies for electrons (left) and muons (right) as a function of p_{T} for the different data taking periods, compared with the efficiency from the total Monte Carlo.

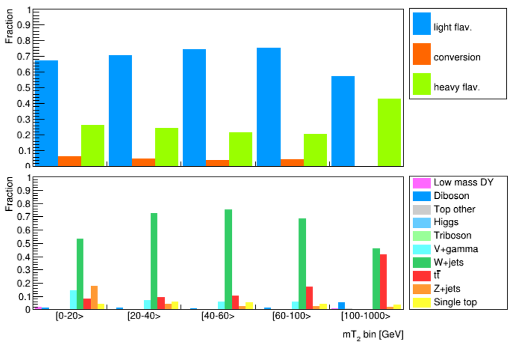

(a) Preliminary event selection

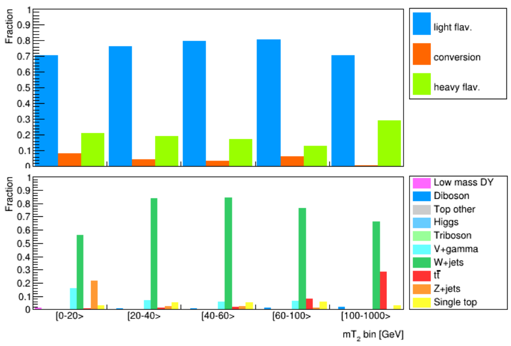

(b) Central jet veto

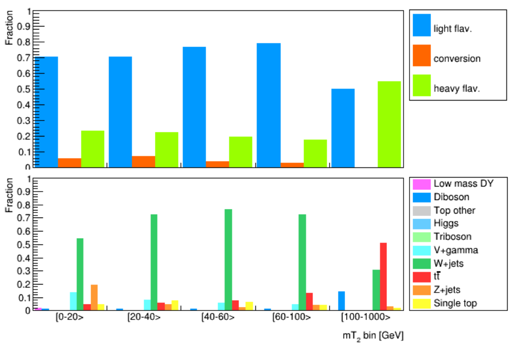

(c) One central jet

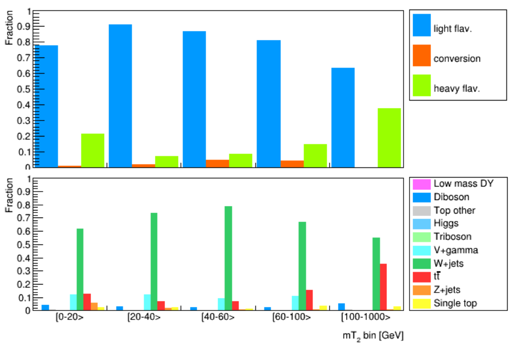

(d) $E_{\mathrm{T}}^{\mathrm{miss}}$ significance $\mathcal{S} > 10$

Figure A.3: Relative composition of the fake lepton sources (upper panel) and the contributing Monte Carlo processes (lower panel) as a function of m_{T2} for opposite charged electron-muon events. Four different regions are shown and, in addition to the preliminary event selection (Table 4.4) and a b-jet veto, the cuts applied are indicated in the relative caption.

trol Region. In absence of a Control Region pure enough in fake electrons from LF hadron decays, the corresponding fake rate for this source is extracted using Monte Carlo truth samples. Figure A.4 shows the final fake rate for electrons and muons.

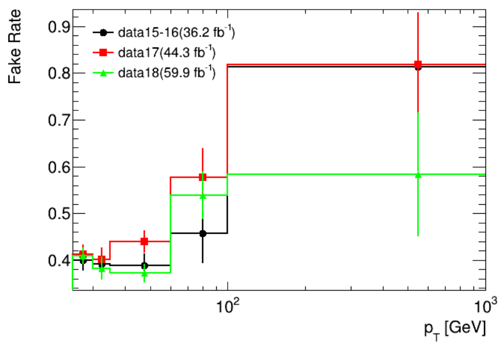

(a) CO fake rate.

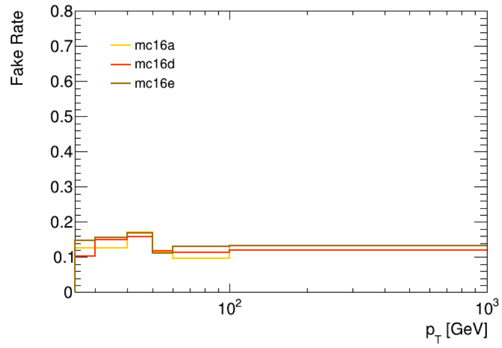

(b) LF fake rate.

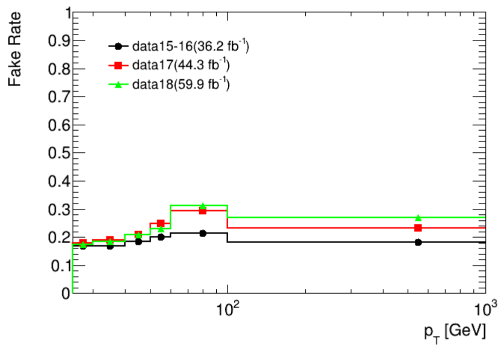

(c) HF fake rate (Electrons).

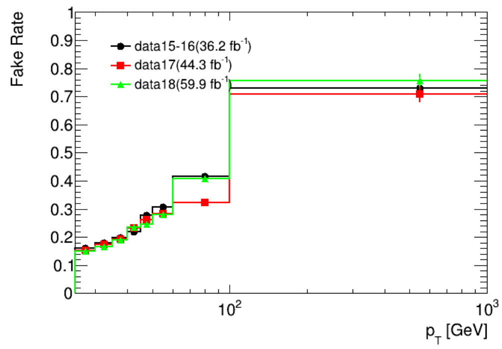

(d) HF fake rate (Muons).

Figure A.4: p_{T} distributions of the final fake rates for electrons and muons. The corresponding fake lepton source is also reported.

A.3 Validation

The final fake estimate is validated in a region requiring two same charged signal leptons, where the contribution from FNP electrons is expected to dominate, $m_{\mathrm{T2}} > 60$ GeV, Z-peak ($|m_{\ell_1\ell_2} - m_Z| > 20$ GeV) and b-jet vetoes. For same sign electrons, the additional cut $E_{\mathrm{T}}^{\mathrm{miss}} > 40$ GeV is applied to reduce the contamination from charge-flipping.

Figures A.5, A.6 and A.7 show the invariant mass, $E_{\mathrm{T}}^{\mathrm{miss}}$ and m_{T2} distributions in the di-electron, electron-muon and di-muon channels, respectively. Statistical and systematic uncertainties from the Matrix Methods are included. The predictions of the method agree with the observed data within uncertainties.

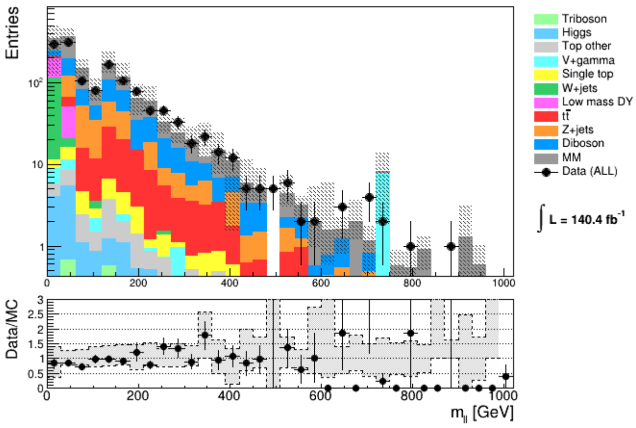

(a) Invariant mass

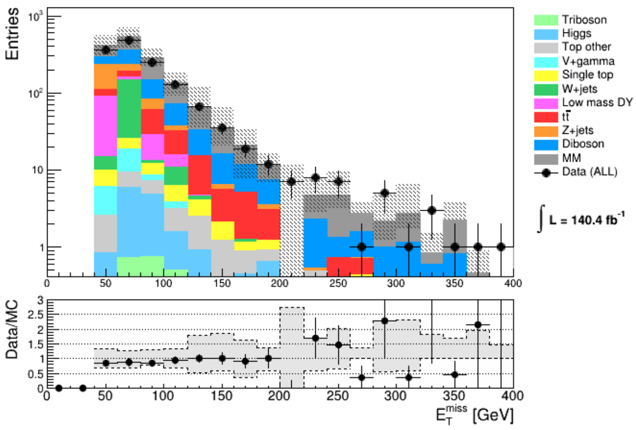

(b) $E_{\mathrm{T}}^{\mathrm{miss}}$

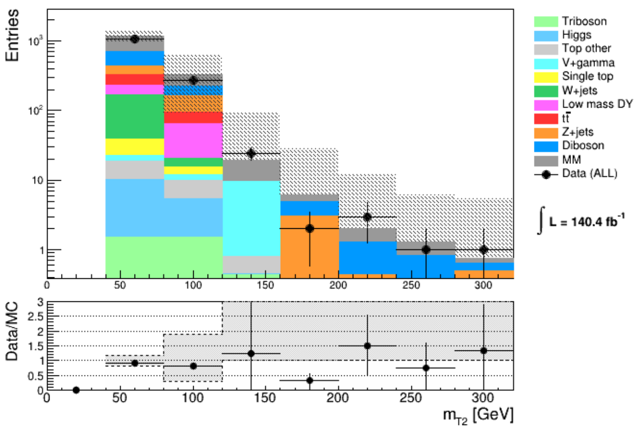

(c) m_{T2}

Figure A.5: Validation distributions for the final fake estimation in the same sign di-electron channel. Invariant mass, $E_{\mathrm{T}}^{\mathrm{miss}}$ and m_{T2} distributions are shown.

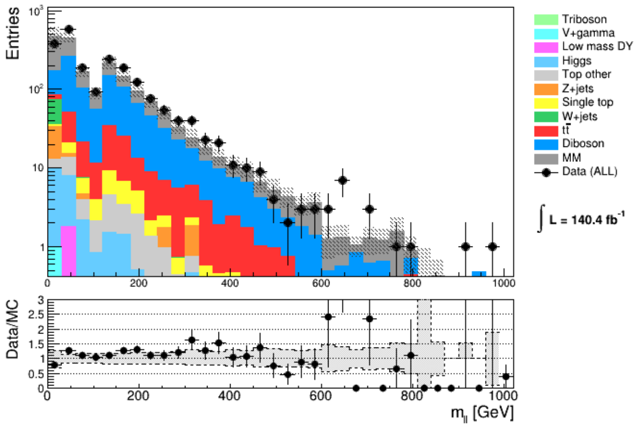

(a) Invariant mass

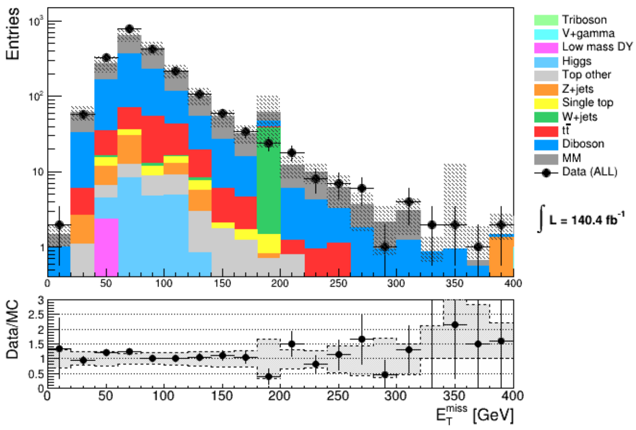

(b) $E_{\mathrm{T}}^{\mathrm{miss}}$

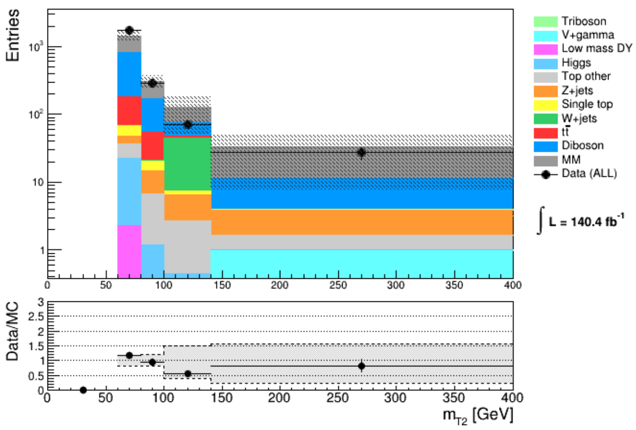

(c) m_{T2}

Figure A.6: Validation distributions for the final fake estimation in the same sign electron-muon channel. Invariant mass, $E_{\mathrm{T}}^{\mathrm{miss}}$ and m_{T2} distributions are shown.

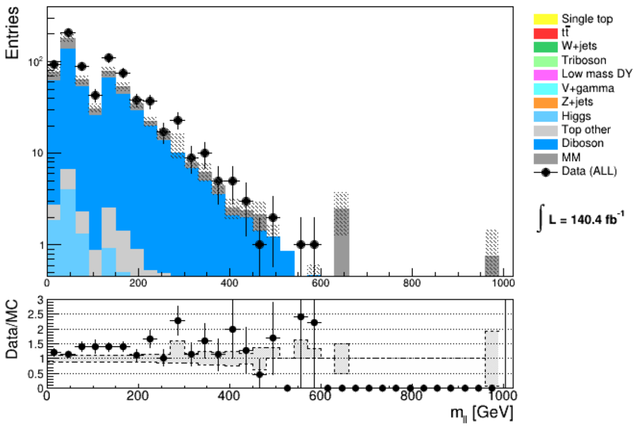

(a) Invariant mass

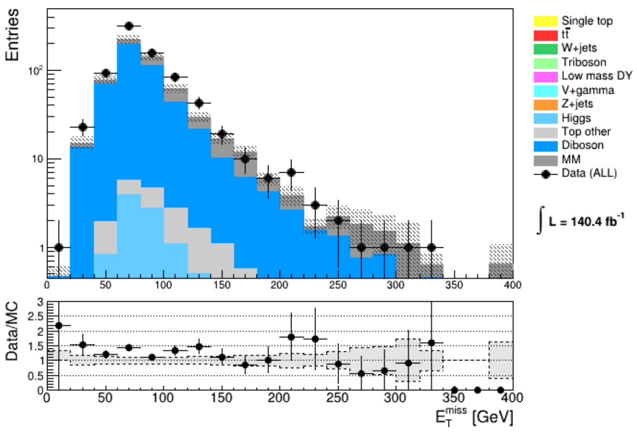

(b) $E_{\mathrm{T}}^{\mathrm{miss}}$

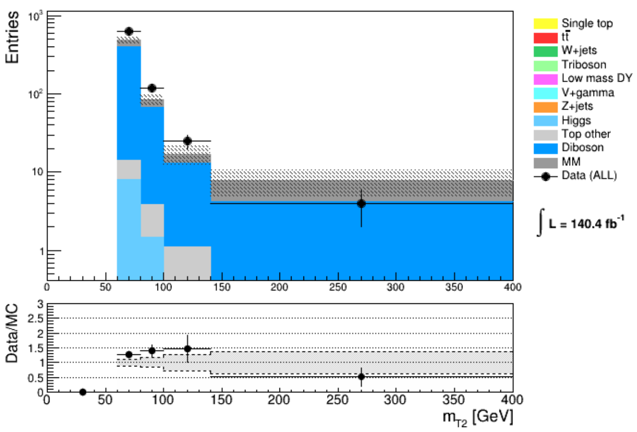

(c) m_{T2}

Figure A.7: Validation distributions for the final fake estimation in the same sign di-muon channel. Invariant mass, $E_{\mathrm{T}}^{\mathrm{miss}}$ and m_{T2} distributions are shown.

Appendix B

Breakdown of systematic uncertainties

Tables B.1, B.2, B.3, B.4, B.5, B.6 and B.7 report the breakdown of systematic uncertainties in CRs, VRs and inclusive SRs after performing the background-only fit.

Uncertainty of channel	CR-top	CR-WW	CR-VZ
Total background expectation	321.00	961.87	811.00
Total statistical ($\sqrt{N_{\mathrm{exp}}}$)	±17.92	±31.01	±28.48
Total background systematic	±17.91 [5.58%]	±31.00 [3.22%]	±28.48 [3.51%]
mu_ttbar	±21.45 [6.7%]	±18.24 [1.9%]	±0.17 [0.02%]
gamma_stat_CR-top_cuts_bin_0	±4.65 [1.4%]	±0.00 [0.00%]	±0.00 [0.00%]
alpha_JET_Flavor_Composition	±4.15 [1.3%]	±4.02 [0.42%]	±5.22 [0.64%]
alpha_JET_EffectiveNP_Modelling1	±3.28 [1.0%]	±3.11 [0.32%]	±2.15 [0.26%]
alpha_MET_ScaleDown	±3.21 [1.00%]	±3.12 [0.32%]	±1.70 [0.21%]
alpha_JET_Flavor_Response	±3.05 [0.95%]	±2.85 [0.30%]	±2.42 [0.30%]
alpha_MET_ResoPara	±2.88 [0.90%]	±2.61 [0.27%]	±0.52 [0.06%]
alpha_FT_EFF_B	±2.69 [0.84%]	±2.63 [0.27%]	±0.03 [0.00%]
alpha_JET_Pileup_RhoTopology	±2.67 [0.83%]	±2.55 [0.27%]	±1.89 [0.23%]
alpha_syst_VV_gen	±2.59 [0.81%]	±0.01 [0.00%]	±0.03 [0.00%]
alpha_MET_ScaleUp	±2.56 [0.80%]	±2.48 [0.26%]	±0.25 [0.03%]
alpha_EG_SCALE	±2.19 [0.68%]	±2.00 [0.21%]	±0.03 [0.00%]
alpha_fakesSyst	±2.15 [0.67%]	±8.46 [0.88%]	±5.69 [0.70%]
alpha_MET_ResoPerp	±2.07 [0.65%]	±2.09 [0.22%]	±0.15 [0.02%]
alpha_JET_JER_EffectiveNP_3	±1.52 [0.47%]	±1.65 [0.17%]	±1.33 [0.16%]
alpha_JET_Pileup_OffsetNPV	±0.98 [0.30%]	±0.78 [0.08%]	±1.10 [0.14%]
alpha_JET_JER_EffectiveNP_10	±0.89 [0.28%]	±0.99 [0.10%]	±1.14 [0.14%]
alpha_PRW_syst	±0.88 [0.27%]	±0.88 [0.09%]	±0.99 [0.12%]
alpha_FT_EFF_Light	±0.78 [0.24%]	±0.72 [0.07%]	±0.05 [0.01%]
alpha_JET_JER_EffectiveNP_6	±0.73 [0.23%]	±0.76 [0.08%]	±0.34 [0.04%]
alpha_EG_RES	±0.66 [0.21%]	±0.55 [0.06%]	±0.18 [0.02%]
alpha_JET_JER_EffectiveNP_1	±0.65 [0.20%]	±0.71 [0.07%]	±0.73 [0.09%]
alpha_JET_JER_EffectiveNP_2	±0.65 [0.20%]	±0.66 [0.07%]	±0.08 [0.01%]
alpha_JET_JER_EffectiveNP_11	±0.63 [0.20%]	±0.63 [0.07%]	±0.02 [0.00%]
alpha_JET_Pileup_OffsetMu	±0.62 [0.19%]	±0.74 [0.08%]	±1.40 [0.17%]
alpha_MUONS_SCALE	±0.56 [0.17%]	±0.58 [0.06%]	±0.03 [0.00%]
mu_WW	±0.49 [0.15%]	±60.21 [6.3%]	±1.73 [0.21%]
alpha_JET_JER_EffectiveNP_5	±0.44 [0.14%]	±0.41 [0.04%]	±0.93 [0.11%]
alpha_JET_JER_EffectiveNP_4	±0.43 [0.13%]	±0.39 [0.04%]	±0.92 [0.11%]
alpha_JET_EffectiveNP_Mixed2	±0.42 [0.13%]	±0.41 [0.04%]	±0.15 [0.02%]
alpha_MUONS_MS	±0.39 [0.12%]	±0.41 [0.04%]	±0.05 [0.01%]
alpha_JET_EffectiveNP_Statistical2	±0.37 [0.12%]	±0.30 [0.03%]	±0.19 [0.02%]
alpha_JET_JvtEfficiency	±0.37 [0.11%]	±0.29 [0.03%]	±0.52 [0.06%]
alpha_syst_VV_PDF	±0.33 [0.10%]	±0.00 [0.00%]	±0.65 [0.08%]
alpha_JET_EffectiveNP_Mixed1	±0.32 [0.10%]	±0.34 [0.04%]	±0.23 [0.03%]
alpha_JET_JER_EffectiveNP_9	±0.28 [0.09%]	±0.28 [0.03%]	±0.50 [0.06%]
alpha_JET_EffectiveNP_Statistical1	±0.26 [0.08%]	±0.26 [0.03%]	±0.04 [0.00%]
alpha_JET_EtaIntercalibration_TotalStat	±0.25 [0.08%]	±0.18 [0.02%]	±0.07 [0.01%]
alpha_EL_EFF_ISO	±0.24 [0.07%]	±0.39 [0.04%]	±0.17 [0.02%]
alpha_JET_Pileup_PtTerm	±0.21 [0.07%]	±0.25 [0.03%]	±0.87 [0.11%]
alpha_JET_EtaIntercalibration_Modelling	±0.19 [0.06%]	±0.01 [0.00%]	±1.28 [0.16%]
alpha_JET_JER_EffectiveNP_7	±0.18 [0.06%]	±0.07 [0.01%]	±0.86 [0.11%]
alpha_JET_EffectiveNP_Detector1	±0.17 [0.05%]	±0.16 [0.02%]	±0.28 [0.03%]
alpha_FT_EFF_C	±0.17 [0.05%]	±0.14 [0.01%]	±0.01 [0.00%]
alpha_JET_EffectiveNP_Modelling2	±0.16 [0.05%]	±0.08 [0.01%]	±0.20 [0.02%]
alpha_JET_JER_EffectiveNP_12restTerm	±0.13 [0.04%]	±0.27 [0.03%]	±0.05 [0.01%]
alpha_JET_EffectiveNP_Statistical6	±0.12 [0.04%]	±0.10 [0.01%]	±0.14 [0.02%]
alpha_EL_EFF_ID	±0.11 [0.03%]	±0.09 [0.01%]	±0.22 [0.03%]
Lumi	±0.11 [0.03%]	±0.35 [0.04%]	±0.41 [0.05%]
alpha_MUONS_SagReb	±0.11 [0.03%]	±0.01 [0.00%]	±0.89 [0.11%]
alpha_MUONS_SagRho	±0.10 [0.03%]	±0.01 [0.00%]	±0.11 [0.01%]
alpha_MUON_EFF_RECO_SYS	±0.10 [0.03%]	±0.12 [0.01%]	±0.09 [0.01%]
alpha_JET_JER_DataVsMC	±0.10 [0.03%]	±0.17 [0.02%]	±0.67 [0.08%]
alpha_JET_EffectiveNP_Statistical5	±0.07 [0.02%]	±0.05 [0.00%]	±0.17 [0.02%]
alpha_JET_JER_EffectiveNP_8	±0.06 [0.02%]	±0.02 [0.00%]	±0.89 [0.11%]
alpha_Renormalization_VV	±0.05 [0.02%]	±0.10 [0.01%]	±0.08 [0.01%]
alpha_JET_EffectiveNP_Modelling3	±0.05 [0.02%]	±0.03 [0.00%]	±0.17 [0.02%]
alpha_JET_EtaIntercalibration_NonClosure_posEta	±0.05 [0.02%]	±0.05 [0.01%]	±0.02 [0.00%]
alpha_JET_EffectiveNP_Detector2	±0.04 [0.01%]	±0.04 [0.00%]	±0.00 [0.00%]
alpha_Factorization_VV	±0.03 [0.01%]	±0.33 [0.03%]	±0.25 [0.03%]
alpha_MUONS_ID	±0.03 [0.01%]	±0.04 [0.00%]	±0.09 [0.01%]
alpha_JET_EffectiveNP_Statistical4	±0.02 [0.00%]	±0.04 [0.00%]	±0.16 [0.02%]
alpha_JET_EffectiveNP_Modelling4	±0.02 [0.00%]	±0.02 [0.00%]	±0.00 [0.00%]
alpha_JET_EffectiveNP_Mixed3	±0.01 [0.00%]	±0.01 [0.00%]	±0.00 [0.00%]
mu_VZ	±0.01 [0.00%]	±0.49 [0.05%]	±31.20 [3.8%]
alpha_FT_EFF_extrapolation	±0.01 [0.00%]	±0.01 [0.00%]	±0.00 [0.00%]
alpha_EL_EFF_RECO	±0.01 [0.00%]	±0.01 [0.00%]	±0.04 [0.00%]
alpha_JET_PunchThrough_MC16	±0.01 [0.00%]	±0.01 [0.00%]	±0.01 [0.00%]
alpha_JET_EtaIntercalibration_NonClosure_negEta	±0.01 [0.00%]	±0.00 [0.00%]	±0.02 [0.00%]
alpha_MUON_EFF_ISO_STAT	±0.01 [0.00%]	±0.01 [0.00%]	±0.01 [0.00%]
alpha_JET_EffectiveNP_Statistical3	±0.01 [0.00%]	±0.01 [0.00%]	±0.20 [0.02%]
alpha_MUON_EFF_TrigStatUncertainty	±0.00 [0.00%]	±0.02 [0.00%]	±0.04 [0.00%]
alpha_MUON_EFF_RECO_STAT	±0.00 [0.00%]	±0.00 [0.00%]	±0.02 [0.00%]
alpha_MUON_EFF_ISO_SYS	±0.00 [0.00%]	±0.00 [0.00%]	±0.04 [0.00%]
alpha_syst_wt_DS	±0.00 [0.00%]	±3.75 [0.39%]	±0.32 [0.04%]
alpha_syst_ttbar_rad	±0.00 [0.00%]	±16.84 [1.8%]	±0.70 [0.09%]
gamma_stat_CR-VZ_cuts_bin_0	±0.00 [0.00%]	±0.00 [0.00%]	±8.08 [1.00%]
gamma_stat_CR-WW_cuts_bin_0	±0.00 [0.00%]	±8.38 [0.87%]	±0.00 [0.00%]
alpha_syst_ttbar_show	±0.00 [0.00%]	±11.68 [1.2%]	±0.24 [0.03%]
alpha_syst_ttbar_gen	±0.00 [0.00%]	±38.13 [4.0%]	±0.88 [0.11%]

Table B.1: Breakdown of the dominant systematic uncertainties on background estimates in the CRs after the background-only fit. Note that the individual uncertainties can be correlated and do not necessarily add up quadratically to the total background uncertainty. The percentages show the size of the uncertainty relative to the total expected background.

Uncertainty of channel	VR-WW-0J	VR-WW-1J	VR-VZ
Total background expectation	2755.03	2844.19	418.87
Total statistical ($\sqrt{N_{\mathrm{exp}}}$)	±52.49	±53.33	±20.47
Total background systematic	±115.83 [4.20%]	±250.99 [8.82%]	±43.77 [10.45%]
mu_WW	±140.11 [5.1%]	±89.51 [3.1%]	±1.59 [0.38%]
mu_ttbar	±78.13 [2.8%]	±124.05 [4.4%]	±0.88 [0.21%]
alpha_syst_ttbar_gen	±65.68 [2.4%]	±215.60 [7.6%]	±1.86 [0.44%]
alpha_syst_VV_gen	±51.21 [1.9%]	±60.71 [2.1%]	±26.21 [6.3%]
alpha_syst_ttbar_show	±48.50 [1.8%]	±60.54 [2.1%]	±0.21 [0.05%]
alpha_JET_Flavor_Composition	±28.16 [1.0%]	±42.10 [1.5%]	±18.11 [4.3%]
alpha_fakesSyst	±22.65 [0.82%]	±21.33 [0.75%]	±2.08 [0.50%]
alpha_syst_VV_PDF	±17.35 [0.63%]	±18.22 [0.64%]	±4.62 [1.1%]
gamma_stat_VR-WW-0J_cuts_bin_0	±14.37 [0.52%]	±0.00 [0.00%]	±0.00 [0.00%]
alpha_JET_Flavor_Response	±14.30 [0.52%]	±8.07 [0.28%]	±6.42 [1.5%]
alpha_JET_Pileup_RhoTopology	±14.27 [0.52%]	±35.82 [1.3%]	±4.70 [1.1%]
alpha_MET_ResoPerp	±14.21 [0.52%]	±15.27 [0.54%]	±1.18 [0.28%]
alpha_JET_EffectiveNP_Modelling1	±12.95 [0.47%]	±23.40 [0.82%]	±7.31 [1.7%]
alpha_MET_ScaleUp	±12.24 [0.44%]	±17.90 [0.63%]	±1.85 [0.44%]
alpha_FT_EFF_B	±11.71 [0.42%]	±123.56 [4.3%]	±0.17 [0.04%]
alpha_MET_ScaleDown	±10.66 [0.39%]	±14.72 [0.52%]	±6.31 [1.5%]
alpha_syst_wt_DS	±10.66 [0.39%]	±1.70 [0.06%]	±1.08 [0.26%]
alpha_syst_ttbar_rad	±7.53 [0.27%]	±19.65 [0.69%]	±2.12 [0.51%]
alpha_MET_ResoPara	±6.48 [0.24%]	±9.08 [0.32%]	±0.75 [0.18%]
alpha_JET_Pileup_OffsetNPV	±5.64 [0.20%]	±17.02 [0.60%]	±5.69 [1.4%]
alpha_JET_JER_EffectiveNP_2	±4.58 [0.17%]	±11.25 [0.40%]	±8.90 [2.1%]
alpha_JET_JER_EffectiveNP_4	±4.48 [0.16%]	±6.15 [0.22%]	±0.94 [0.22%]
alpha_MUONS_SagRho	±4.47 [0.16%]	±1.08 [0.04%]	±0.04 [0.01%]
alpha_MUONS_SagReb	±4.46 [0.16%]	±0.84 [0.03%]	±2.38 [0.57%]
alpha_Factorization_VV	±4.09 [0.15%]	±13.43 [0.47%]	±2.25 [0.54%]
alpha_JET_JER_EffectiveNP_5	±4.02 [0.15%]	±7.45 [0.26%]	±0.57 [0.14%]
alpha_JET_JER_EffectiveNP_10	±3.69 [0.13%]	±3.13 [0.11%]	±0.67 [0.16%]
alpha_Renormalization_VV	±3.54 [0.13%]	±17.98 [0.63%]	±0.06 [0.01%]
alpha_MUONS_SCALE	±3.49 [0.13%]	±2.43 [0.09%]	±0.43 [0.10%]
alpha_JET_JvtEfficiency	±2.97 [0.11%]	±7.84 [0.28%]	±0.40 [0.10%]
alpha_EG_SCALE	±2.81 [0.10%]	±0.49 [0.02%]	±2.22 [0.53%]
alpha_JET_JER_EffectiveNP_6	±2.59 [0.09%]	±6.46 [0.23%]	±0.50 [0.12%]
alpha_JET_Pileup_PtTerm	±2.46 [0.09%]	±4.31 [0.15%]	±0.19 [0.04%]
alpha_JET_JER_EffectiveNP_11	±2.16 [0.08%]	±2.24 [0.08%]	±4.17 [1.00%]
alpha_JET_EtaIntercalibration_Modelling	±2.00 [0.07%]	±16.58 [0.58%]	±4.87 [1.2%]
alpha_FT_EFF_Light	±1.94 [0.07%]	±13.48 [0.47%]	±0.03 [0.01%]
alpha_EG_RES	±1.93 [0.07%]	±2.69 [0.09%]	±0.77 [0.18%]
alpha_PRW_syst	±1.70 [0.06%]	±7.75 [0.27%]	±1.62 [0.39%]
mu_VZ	±1.41 [0.05%]	±1.12 [0.04%]	±14.99 [3.6%]
alpha_JET_JER_EffectiveNP_7	±1.09 [0.04%]	±0.38 [0.01%]	±2.14 [0.51%]
alpha_MUONS_MS	±1.08 [0.04%]	±2.87 [0.10%]	±1.48 [0.35%]
alpha_JET_JER_EffectiveNP_1	±1.06 [0.04%]	±1.35 [0.05%]	±7.10 [1.7%]
alpha_JET_JER_EffectiveNP_3	±1.01 [0.04%]	±6.05 [0.21%]	±3.38 [0.81%]
alpha_JET_JER_DataVsMC	±0.79 [0.03%]	±0.29 [0.01%]	±0.00 [0.00%]
alpha_JET_EffectiveNP_Mixed1	±0.78 [0.03%]	±1.70 [0.06%]	±0.40 [0.09%]
alpha_JET_JER_EffectiveNP_12restTerm	±0.78 [0.03%]	±0.31 [0.01%]	±3.62 [0.86%]
Lumi	±0.75 [0.03%]	±0.68 [0.02%]	±0.36 [0.09%]
alpha_EL_EFF_ID	±0.73 [0.03%]	±1.54 [0.05%]	±0.49 [0.12%]
alpha_JET_EtaIntercalibration_NonClosure_negEta	±0.59 [0.02%]	±0.49 [0.02%]	±0.42 [0.10%]
alpha_JET_JER_EffectiveNP_8	±0.43 [0.02%]	±0.45 [0.02%]	±1.19 [0.28%]
alpha_JET_Pileup_OffsetMu	±0.42 [0.02%]	±11.70 [0.41%]	±4.64 [1.1%]
alpha_JET_EtaIntercalibration_TotalStat	±0.35 [0.01%]	±5.32 [0.19%]	±1.89 [0.45%]
alpha_FT_EFF_C	±0.35 [0.01%]	±5.26 [0.18%]	±0.02 [0.00%]
alpha_JET_JER_EffectiveNP_9	±0.35 [0.01%]	±1.64 [0.06%]	±1.55 [0.37%]
alpha_JET_EffectiveNP_Statistical6	±0.32 [0.01%]	±1.04 [0.04%]	±0.42 [0.10%]
alpha_JET_EffectiveNP_Modelling2	±0.23 [0.01%]	±5.52 [0.19%]	±0.57 [0.13%]
alpha_JET_EffectiveNP_Statistical1	±0.21 [0.01%]	±1.91 [0.07%]	±0.47 [0.11%]
alpha_JET_EffectiveNP_Detector1	±0.19 [0.01%]	±0.83 [0.03%]	±0.59 [0.14%]
alpha_EL_EFF_ISO	±0.18 [0.01%]	±1.96 [0.07%]	±1.13 [0.27%]
alpha_JET_EffectiveNP_Statistical3	±0.18 [0.01%]	±1.24 [0.04%]	±0.09 [0.02%]
alpha_JET_EffectiveNP_Modelling4	±0.13 [0.00%]	±0.02 [0.00%]	±0.13 [0.03%]
alpha_MUON_EFF_TrigStatUncertainty	±0.12 [0.00%]	±0.10 [0.00%]	±0.11 [0.03%]
alpha_JET_EffectiveNP_Statistical4	±0.12 [0.00%]	±1.57 [0.06%]	±0.01 [0.00%]
alpha_JET_EffectiveNP_Statistical2	±0.11 [0.00%]	±3.73 [0.13%]	±0.75 [0.18%]
alpha_JET_EffectiveNP_Mixed3	±0.10 [0.00%]	±0.59 [0.02%]	±0.14 [0.03%]
alpha_JET_EtaIntercalibration_NonClosure_posEta	±0.10 [0.00%]	±0.07 [0.00%]	±0.02 [0.01%]
alpha_MUON_EFF_RECO_SYS	±0.09 [0.00%]	±0.31 [0.01%]	±0.22 [0.05%]
alpha_JET_EffectiveNP_Mixed2	±0.09 [0.00%]	±0.25 [0.01%]	±0.53 [0.13%]
alpha_EL_EFF_RECO	±0.06 [0.00%]	±0.12 [0.00%]	±0.02 [0.01%]
alpha_JET_EffectiveNP_Modelling3	±0.04 [0.00%]	±3.48 [0.12%]	±0.01 [0.00%]
alpha_MUONS_ID	±0.04 [0.00%]	±2.56 [0.09%]	±0.68 [0.16%]
alpha_JET_PunchThrough_MC16	±0.04 [0.00%]	±0.07 [0.00%]	±0.01 [0.00%]
alpha_JET_EffectiveNP_Statistical5	±0.02 [0.00%]	±0.81 [0.03%]	±0.01 [0.00%]
alpha_FT_EFF_extrapolation	±0.02 [0.00%]	±0.08 [0.00%]	±0.00 [0.00%]
alpha_MUON_EFF_ISO_SYS	±0.02 [0.00%]	±0.01 [0.00%]	±0.07 [0.02%]
alpha_JET_EffectiveNP_Detector2	±0.01 [0.00%]	±0.18 [0.01%]	±0.02 [0.00%]
alpha_MUON_EFF_ISO_STAT	±0.01 [0.00%]	±0.04 [0.00%]	±0.03 [0.01%]
alpha_JET_Comb_TotalStat_Kin	±0.00 [0.00%]	±0.00 [0.00%]	±0.01 [0.00%]
alpha_JET_Comb_Tracking_Kin	±0.00 [0.00%]	±0.00 [0.00%]	±0.01 [0.00%]
alpha_JET_Comb_Baseline_Kin	±0.00 [0.00%]	±0.00 [0.00%]	±0.01 [0.00%]
alpha_JET_SingleParticle_HighPt	±0.00 [0.00%]	±0.00 [0.00%]	±0.01 [0.00%]
alpha_JET_Comb_Modelling_Kin	±0.00 [0.00%]	±0.00 [0.00%]	±0.01 [0.00%]
alpha_JET_MassRes_Hbb	±0.00 [0.00%]	±0.00 [0.00%]	±0.01 [0.00%]
alpha_MUON_EFF_RECO_STAT	±0.00 [0.00%]	±0.00 [0.00%]	±0.02 [0.00%]
alpha_FT_EFF_extrapolation_from_charm	±0.00 [0.00%]	±0.05 [0.00%]	±0.00 [0.00%]
alpha_JET_EtaIntercalibration_NonClosure_highE	±0.00 [0.00%]	±0.01 [0.00%]	±0.00 [0.00%]
gamma_stat_VR-WW-1J_cuts_bin_0	±0.00 [0.00%]	±14.45 [0.51%]	±0.00 [0.00%]
gamma_stat_VR-VZ_cuts_bin_0	±0.00 [0.00%]	±0.00 [0.00%]	±18.98 [4.5%]

Table B.2: Breakdown of the dominant systematic uncertainties on background estimates in the diboson VRs after the background-only fit. Note that the individual uncertainties can be correlated and do not necessarily add up quadratically to the total background uncertainty. The percentages show the size of the uncertainty relative to the total expected background.

Uncertainty of channel	VR-top-low	VR-top-high	VR-top-WW
Total background expectation	185.49	52.80	852.24
Total statistical ($\sqrt{N_{\mathrm{exp}}}$)	±13.62	±7.27	±29.19
Total background systematic	±17.23 [9.29%]	±7.37 [13.96%]	±84.50 [9.92%]
mu_WW	±0.19 [0.10%]	±0.23 [0.44%]	±1.46 [0.17%]
mu_ttbar	±12.56 [6.8%]	±3.13 [5.9%]	±58.03 [6.8%]
alpha_syst_ttbar_gen	±1.86 [1.0%]	±0.30 [0.57%]	±33.68 [4.0%]
alpha_syst_VV_gen	±0.50 [0.27%]	±1.36 [2.6%]	±0.00 [0.00%]
alpha_syst_ttbar_show	±0.58 [0.31%]	±0.60 [1.1%]	±29.49 [3.5%]
alpha_JET_Flavor_Composition	±10.36 [5.6%]	±0.33 [0.62%]	±2.12 [0.25%]
alpha_fakesSyst	±1.44 [0.77%]	±0.45 [0.85%]	±0.00 [0.00%]
alpha_syst_VV_PDF	±0.28 [0.15%]	±0.69 [1.3%]	±0.00 [0.00%]
alpha_JET_Flavor_Response	±4.38 [2.4%]	±0.75 [1.4%]	±4.63 [0.54%]
alpha_JET_Pileup_RhoTopology	±3.88 [2.1%]	±1.55 [2.9%]	±4.69 [0.55%]
alpha_MET_ResoPerp	±0.14 [0.08%]	±0.62 [1.2%]	±4.45 [0.52%]
alpha_JET_EffectiveNP_Modelling1	±4.29 [2.3%]	±1.25 [2.4%]	±0.18 [0.02%]
alpha_MET_ScaleUp	±0.65 [0.35%]	±0.85 [1.6%]	±8.36 [0.98%]
alpha_FT_EFF_B	±1.50 [0.81%]	±0.85 [1.6%]	±11.17 [1.3%]
alpha_MET_ScaleDown	±0.10 [0.05%]	±1.31 [2.5%]	±17.24 [2.0%]
alpha_syst_wt_DS	±0.20 [0.11%]	±0.93 [1.8%]	±1.80 [0.21%]
alpha_syst_ttbar_rad	±0.63 [0.34%]	±5.60 [10.6%]	±20.26 [2.4%]
alpha_MET_ResoPara	±0.10 [0.05%]	±0.20 [0.39%]	±2.58 [0.30%]
alpha_JET_Pileup_OffsetNPV	±1.02 [0.55%]	±0.42 [0.79%]	±1.08 [0.13%]
alpha_JET_JER_EffectiveNP_2	±1.16 [0.63%]	±0.40 [0.75%]	±3.67 [0.43%]
alpha_JET_JER_EffectiveNP_4	±1.19 [0.64%]	±0.10 [0.19%]	±0.23 [0.03%]
alpha_MUONS_SagRho	±0.88 [0.47%]	±0.10 [0.19%]	±1.08 [0.13%]
alpha_MUONS_SagReb	±0.88 [0.47%]	±0.12 [0.22%]	±1.06 [0.12%]
alpha_Factorization_VV	±0.03 [0.02%]	±0.07 [0.14%]	±0.09 [0.01%]
alpha_JET_JER_EffectiveNP_5	±0.83 [0.45%]	±0.17 [0.33%]	±3.12 [0.37%]
alpha_JET_JER_EffectiveNP_10	±0.49 [0.26%]	±0.54 [1.0%]	±0.46 [0.05%]
alpha_Renormalization_VV	±0.02 [0.01%]	±0.03 [0.06%]	±0.02 [0.00%]
alpha_MUONS_SCALE	±0.34 [0.18%]	±0.05 [0.09%]	±0.64 [0.08%]
alpha_JET_JvtEfficiency	±0.32 [0.17%]	±0.16 [0.30%]	±3.36 [0.39%]
alpha_EG_SCALE	±0.44 [0.24%]	±0.66 [1.2%]	±8.43 [0.99%]
alpha_JET_JER_EffectiveNP_6	±0.12 [0.06%]	±0.36 [0.69%]	±4.07 [0.48%]
alpha_JET_Pileup_PtTerm	±0.10 [0.05%]	±0.23 [0.44%]	±1.38 [0.16%]
alpha_JET_JER_EffectiveNP_11	±0.28 [0.15%]	±0.08 [0.15%]	±0.75 [0.09%]
alpha_JET_EtaIntercalibration_Modelling	±4.72 [2.5%]	±0.14 [0.26%]	±4.70 [0.55%]
alpha_FT_EFF_Light	±0.39 [0.21%]	±0.15 [0.28%]	±2.12 [0.25%]
alpha_EG_RES	±0.52 [0.28%]	±0.15 [0.29%]	±2.04 [0.24%]
alpha_PRW_syst	±1.49 [0.80%]	±0.37 [0.70%]	±4.61 [0.54%]
mu_VZ	±0.00 [0.00%]	±0.01 [0.01%]	±0.02 [0.00%]
alpha_JET_JER_EffectiveNP_7	±0.67 [0.36%]	±0.61 [1.1%]	±1.46 [0.17%]
alpha_MUONS_MS	±0.25 [0.14%]	±0.17 [0.32%]	±1.86 [0.22%]
alpha_JET_JER_EffectiveNP_1	±4.00 [2.2%]	±0.25 [0.47%]	±6.30 [0.74%]
alpha_JET_JER_EffectiveNP_3	±0.16 [0.09%]	±0.25 [0.47%]	±4.52 [0.53%]
alpha_JET_JER_DataVsMC	±1.38 [0.75%]	±0.37 [0.70%]	±3.75 [0.44%]
alpha_JET_EffectiveNP_Mixed1	±0.09 [0.05%]	±0.08 [0.15%]	±0.76 [0.09%]
alpha_JET_JER_EffectiveNP_12restTerm	±0.88 [0.47%]	±0.33 [0.62%]	±1.85 [0.22%]
Lumi	±0.04 [0.02%]	±0.09 [0.16%]	±0.01 [0.00%]
alpha_EL_EFF_ID	±0.13 [0.07%]	±0.07 [0.14%]	±0.33 [0.04%]
alpha_JET_EtaIntercalibration_NonClosure_negEta	±0.23 [0.12%]	±0.02 [0.04%]	±0.37 [0.04%]
alpha_JET_JER_EffectiveNP_8	±0.34 [0.18%]	±0.88 [1.7%]	±0.95 [0.11%]
alpha_JET_Pileup_OffsetMu	±3.53 [1.9%]	±0.34 [0.65%]	±3.45 [0.41%]
alpha_JET_EtaIntercalibration_TotalStat	±1.40 [0.75%]	±0.24 [0.46%]	±1.69 [0.20%]
alpha_FT_EFF_C	±0.08 [0.04%]	±0.03 [0.06%]	±0.84 [0.10%]
alpha_JET_JER_EffectiveNP_9	±1.47 [0.79%]	±0.27 [0.51%]	±1.58 [0.18%]
alpha_JET_EffectiveNP_Statistical6	±0.24 [0.13%]	±0.10 [0.19%]	±0.03 [0.00%]
alpha_JET_EffectiveNP_Modelling2	±0.38 [0.21%]	±0.29 [0.55%]	±1.78 [0.21%]
alpha_JET_EffectiveNP_Statistical1	±0.42 [0.22%]	±0.19 [0.35%]	±0.46 [0.05%]
alpha_JET_EffectiveNP_Detector1	±0.46 [0.25%]	±0.05 [0.09%]	±0.04 [0.01%]
alpha_EL_EFF_ISO	±0.18 [0.10%]	±0.10 [0.19%]	±0.40 [0.05%]
alpha_JET_EffectiveNP_Statistical3	±0.08 [0.04%]	±0.11 [0.20%]	±0.54 [0.06%]
alpha_JET_EffectiveNP_Modelling4	±0.17 [0.09%]	±0.06 [0.11%]	±0.09 [0.01%]
alpha_MUON_EFF_TrigStatUncertainty	±0.00 [0.00%]	±0.00 [0.00%]	±0.01 [0.00%]
alpha_JET_EffectiveNP_Statistical4	±0.06 [0.03%]	±0.18 [0.34%]	±0.87 [0.10%]
alpha_JET_EffectiveNP_Statistical2	±0.53 [0.28%]	±0.25 [0.47%]	±0.86 [0.10%]
alpha_JET_EffectiveNP_Mixed3	±0.20 [0.11%]	±0.08 [0.15%]	±0.18 [0.02%]
alpha_JET_EtaIntercalibration_NonClosure_posEta	±0.09 [0.05%]	±0.08 [0.16%]	±0.16 [0.02%]
alpha_MUON_EFF_RECO_SYS	±0.07 [0.04%]	±0.08 [0.15%]	±0.12 [0.01%]
alpha_JET_EffectiveNP_Mixed2	±0.39 [0.21%]	±0.12 [0.23%]	±0.02 [0.00%]
alpha_EL_EFF_RECO	±0.00 [0.00%]	±0.00 [0.01%]	±0.04 [0.01%]
alpha_JET_EffectiveNP_Modelling3	±0.02 [0.01%]	±0.33 [0.62%]	±1.10 [0.13%]
alpha_MUONS_ID	±0.67 [0.36%]	±0.19 [0.36%]	±2.48 [0.29%]
alpha_JET_PunchThrough_MC16	±0.01 [0.01%]	±0.00 [0.00%]	±0.03 [0.00%]
alpha_JET_EffectiveNP_Statistical5	±0.06 [0.03%]	±0.13 [0.25%]	±0.05 [0.01%]
alpha_FT_EFF_extrapolation	±0.00 [0.00%]	±0.00 [0.01%]	±0.00 [0.00%]
alpha_MUON_EFF_ISO_SYS	±0.00 [0.00%]	±0.01 [0.01%]	±0.00 [0.00%]
alpha_JET_EffectiveNP_Detector2	±0.10 [0.05%]	±0.07 [0.12%]	±0.06 [0.01%]
alpha_MUON_EFF_ISO_STAT	±0.00 [0.00%]	±0.00 [0.01%]	±0.02 [0.00%]
alpha_JET_Comb_TotalStat_Kin	±0.00 [0.00%]	±0.00 [0.00%]	±0.00 [0.00%]
alpha_JET_Comb_Tracking_Kin	±0.00 [0.00%]	±0.00 [0.00%]	±0.00 [0.00%]
alpha_JET_Comb_Baseline_Kin	±0.00 [0.00%]	±0.00 [0.00%]	±0.00 [0.00%]
alpha_JET_SingleParticle_HighPt	±0.00 [0.00%]	±0.00 [0.00%]	±0.00 [0.00%]
alpha_JET_Comb_Modelling_Kin	±0.00 [0.00%]	±0.00 [0.00%]	±0.00 [0.00%]
alpha_JET_MassRes_Hbb	±0.00 [0.00%]	±0.00 [0.00%]	±0.00 [0.00%]
alpha_MUON_EFF_RECO_STAT	±0.00 [0.00%]	±0.00 [0.01%]	±0.01 [0.00%]
alpha_FT_EFF_extrapolation_from_charm	±0.00 [0.00%]	±0.00 [0.00%]	±0.02 [0.00%]
alpha_JET_EtaIntercalibration_NonClosure_highE	±0.00 [0.00%]	±0.00 [0.00%]	±0.00 [0.00%]
gamma_stat_VR-top-high_cuts_bin_0	±0.00 [0.00%]	±1.90 [3.6%]	±0.00 [0.00%]
gamma_stat_VR-top-WW_cuts_bin_0	±0.00 [0.00%]	±0.00 [0.00%]	±7.40 [0.87%]
gamma_stat_VR-top-low_cuts_bin_0	±3.55 [1.9%]	±0.00 [0.00%]	±0.00 [0.00%]

Table B.3: Breakdown of the dominant systematic uncertainties on background estimates in the top-quark VRs after the background-only fit. Note that the individual uncertainties can be correlated and do not necessarily add up quadratically to the total background uncertainty. The percentages show the size of the uncertainty relative to the total expected background.

Uncertainty of channel m_{T2} [GeV]	SRDF_0_inc100 > 100	SRDF_0_inc160 > 160	SRDF_0_A $\in [100, 120)$	SRDF_0_B $\in [120, 160)$
Total background expectation	96.37	18.77	45.37	32.52
Total statistical ($\sqrt{N_{exp}}$)	±9.82	±4.33	±6.74	±5.70
Total background systematic	±14.66 [15.21%]	±2.39 [12.71%]	±9.02 [19.87%]	±4.68 [14.40%]
mu_WW	±6.83 [7.1%]	±1.64 [8.7%]	±2.58 [5.7%]	±2.61 [8.0%]
alpha_syst_ttbar_gen	±6.68 [6.9%]	±0.00 [0.00%]	±5.63 [12.4%]	±1.05 [3.2%]
alpha_syst_VV_gen	±5.90 [6.1%]	±1.05 [5.6%]	±2.89 [6.4%]	±2.44 [7.5%]
alpha_syst_VV_PDF	±2.77 [2.9%]	±0.81 [4.3%]	±1.18 [2.6%]	±0.97 [3.0%]
gamma_stat_SRDF_0_inc100_cuts_bin_0	±2.63 [2.7%]	±0.00 [0.00%]	±0.00 [0.00%]	±0.00 [0.00%]
alpha_syst_wt_DS	±1.85 [1.9%]	±0.00 [0.00%]	±1.64 [3.6%]	±0.21 [0.65%]
alpha_JET_Flavor_Composition	±1.53 [1.6%]	±0.05 [0.26%]	±1.27 [2.8%]	±0.31 [0.96%]
mu_ttbar	±1.19 [1.2%]	±0.00 [0.00%]	±1.02 [2.2%]	±0.18 [0.54%]
alpha_JET_Pileup_RhoTopology	±1.13 [1.2%]	±0.04 [0.24%]	±0.91 [2.0%]	±0.26 [0.81%]
alpha_EL_EFF_ISO	±1.05 [1.1%]	±0.37 [2.0%]	±0.34 [0.74%]	±0.34 [1.1%]
alpha_JET_EffectiveNP_Modelling1	±1.03 [1.1%]	±0.01 [0.05%]	±0.87 [1.9%]	±0.17 [0.53%]
alpha_Factorization_VV	±0.97 [1.0%]	±0.30 [1.6%]	±0.26 [0.58%]	±0.33 [1.0%]
alpha_syst_ttbar_rad	±0.93 [0.96%]	±0.00 [0.00%]	±0.78 [1.7%]	±0.15 [0.45%]
alpha_syst_ttbar_show	±0.90 [0.93%]	±0.00 [0.00%]	±0.75 [1.7%]	±0.14 [0.43%]
alpha_MET_ScaleDown	±0.86 [0.90%]	±0.10 [0.53%]	±0.85 [1.9%]	±0.01 [0.04%]
alpha_JET_JER_EffectiveNP_2	±0.82 [0.85%]	±0.10 [0.53%]	±0.77 [1.7%]	±0.06 [0.17%]
alpha_JET_Flavor_Response	±0.62 [0.64%]	±0.03 [0.17%]	±0.51 [1.1%]	±0.14 [0.42%]
alpha_fakesSyst	±0.61 [0.64%]	±0.00 [0.00%]	±0.35 [0.77%]	±0.17 [0.52%]
alpha_JET_Pileup_OffsetNPV	±0.54 [0.56%]	±0.09 [0.45%]	±0.48 [1.1%]	±0.14 [0.44%]
alpha_EL_EFF_ID	±0.44 [0.46%]	±0.17 [0.89%]	±0.15 [0.34%]	±0.12 [0.37%]
alpha_JET_JER_EffectiveNP_11	±0.42 [0.44%]	±0.01 [0.04%]	±0.28 [0.63%]	±0.14 [0.44%]
alpha_JET_EtaIntercalibration_Modelling	±0.40 [0.42%]	±0.06 [0.31%]	±0.40 [0.89%]	±0.06 [0.17%]
alpha_Renormalization_VV	±0.39 [0.41%]	±0.11 [0.60%]	±0.14 [0.31%]	±0.13 [0.39%]
alpha_JET_JER_EffectiveNP_12restTerm	±0.39 [0.41%]	±0.02 [0.11%]	±0.38 [0.84%]	±0.03 [0.10%]
alpha_JET_JER_EffectiveNP_4	±0.37 [0.38%]	±0.10 [0.52%]	±0.22 [0.48%]	±0.05 [0.16%]
alpha_JET_JER_EffectiveNP_5	±0.36 [0.37%]	±0.05 [0.28%]	±0.27 [0.60%]	±0.03 [0.10%]
alpha_JET_JER_EffectiveNP_9	±0.34 [0.35%]	±0.03 [0.18%]	±0.12 [0.27%]	±0.25 [0.78%]
alpha_MET_ResoPerp	±0.33 [0.34%]	±0.10 [0.52%]	±0.20 [0.44%]	±0.07 [0.20%]
alpha_JET_JER_EffectiveNP_3	±0.31 [0.32%]	±0.06 [0.30%]	±0.25 [0.56%]	±0.00 [0.01%]
alpha_JET_JER_EffectiveNP_1	±0.30 [0.31%]	±0.12 [0.66%]	±0.07 [0.16%]	±0.10 [0.30%]
alpha_EG_SCALE	±0.27 [0.28%]	±0.03 [0.18%]	±0.06 [0.13%]	±0.29 [0.91%]
alpha_FT_EFF_B	±0.21 [0.22%]	±0.00 [0.01%]	±0.19 [0.42%]	±0.02 [0.07%]
alpha_MUON_EFF_RECO_SYS	±0.19 [0.19%]	±0.10 [0.54%]	±0.03 [0.07%]	±0.05 [0.16%]
alpha_MET_ResoPara	±0.18 [0.19%]	±0.08 [0.41%]	±0.42 [0.92%]	±0.06 [0.18%]
alpha_JET_Pileup_OffsetMu	±0.16 [0.16%]	±0.12 [0.62%]	±0.24 [0.54%]	±0.03 [0.09%]
alpha_JET_JvtEfficiency	±0.15 [0.16%]	±0.01 [0.06%]	±0.13 [0.28%]	±0.01 [0.04%]
alpha_JET_JER_EffectiveNP_10	±0.15 [0.15%]	±0.02 [0.11%]	±0.03 [0.07%]	±0.10 [0.30%]
alpha_JET_EtaIntercalibration_TotalStat	±0.13 [0.14%]	±0.00 [0.00%]	±0.16 [0.36%]	±0.03 [0.08%]
alpha_PRW_syst	±0.13 [0.14%]	±0.06 [0.34%]	±0.06 [0.13%]	±0.14 [0.43%]
alpha_MUONS_ID	±0.13 [0.13%]	±0.01 [0.04%]	±0.18 [0.40%]	±0.06 [0.19%]
alpha_MUONS_SagReb	±0.12 [0.12%]	±0.06 [0.31%]	±0.47 [1.0%]	±0.30 [0.92%]
alpha_MUONS_SagRho	±0.12 [0.12%]	±0.06 [0.32%]	±0.47 [1.0%]	±0.30 [0.92%]
alpha_JET_JER_EffectiveNP_7	±0.09 [0.09%]	±0.02 [0.10%]	±0.09 [0.20%]	±0.02 [0.05%]
alpha_JET_JER_DataVsMC	±0.09 [0.09%]	±0.18 [0.97%]	±0.16 [0.34%]	±0.06 [0.18%]
alpha_MET_ScaleUp	±0.08 [0.09%]	±0.05 [0.27%]	±0.14 [0.31%]	±0.09 [0.28%]
alpha_MUONS_SCALE	±0.08 [0.08%]	±0.02 [0.10%]	±0.06 [0.13%]	±0.04 [0.12%]
alpha_JET_Pileup_PtTerm	±0.08 [0.08%]	±0.01 [0.06%]	±0.11 [0.24%]	±0.02 [0.06%]
alpha_FT_EFF_Light	±0.06 [0.07%]	±0.01 [0.06%]	±0.04 [0.08%]	±0.02 [0.05%]
mu_VZ	±0.06 [0.06%]	±0.02 [0.12%]	±0.03 [0.06%]	±0.02 [0.06%]
alpha_JET_JER_EffectiveNP_8	±0.04 [0.04%]	±0.06 [0.30%]	±0.02 [0.04%]	±0.08 [0.24%]
alpha_MUONS_MS	±0.04 [0.04%]	±0.07 [0.37%]	±0.04 [0.09%]	±0.07 [0.22%]
alpha_JET_EtaIntercalibration_NonClosure_negEta	±0.04 [0.04%]	±0.00 [0.01%]	±0.02 [0.05%]	±0.01 [0.03%]
Lumi	±0.03 [0.04%]	±0.00 [0.01%]	±0.02 [0.05%]	±0.01 [0.03%]
alpha_JET_JER_EffectiveNP_6	±0.03 [0.03%]	±0.03 [0.15%]	±0.02 [0.04%]	±0.01 [0.04%]
alpha_JET_EffectiveNP_Statistical1	±0.02 [0.03%]	±0.01 [0.04%]	±0.02 [0.04%]	±0.01 [0.04%]
alpha_JET_EffectiveNP_Mixed2	±0.02 [0.03%]	±0.01 [0.03%]	±0.01 [0.03%]	±0.02 [0.05%]
alpha_JET_EffectiveNP_Modelling2	±0.02 [0.03%]	±0.01 [0.06%]	±0.01 [0.03%]	±0.02 [0.07%]
alpha_EG_RES	±0.02 [0.03%]	±0.01 [0.03%]	±0.04 [0.08%]	±0.07 [0.20%]
alpha_EL_EFF_RECO	±0.02 [0.02%]	±0.01 [0.03%]	±0.01 [0.02%]	±0.01 [0.02%]
alpha_JET_EffectiveNP_Statistical5	±0.02 [0.02%]	±0.00 [0.01%]	±0.01 [0.02%]	±0.01 [0.03%]
alpha_JET_EtaIntercalibration_NonClosure_posEta	±0.02 [0.02%]	±0.02 [0.08%]	±0.02 [0.05%]	±0.02 [0.06%]
alpha_JET_EffectiveNP_Statistical6	±0.02 [0.02%]	±0.00 [0.01%]	±0.02 [0.04%]	±0.00 [0.00%]
alpha_FT_EFF_C	±0.02 [0.02%]	±0.00 [0.02%]	±0.01 [0.02%]	±0.00 [0.02%]
alpha_JET_EffectiveNP_Statistical4	±0.02 [0.02%]	±0.01 [0.06%]	±0.01 [0.03%]	±0.01 [0.04%]
alpha_MUON_EFF_ISO_STAT	±0.01 [0.01%]	±0.01 [0.03%]	±0.00 [0.01%]	±0.00 [0.01%]
alpha_JET_EffectiveNP_Statistical3	±0.01 [0.01%]	±0.00 [0.00%]	±0.01 [0.02%]	±0.00 [0.01%]
alpha_JET_EffectiveNP_Modelling3	±0.01 [0.01%]	±0.02 [0.13%]	±0.01 [0.03%]	±0.02 [0.07%]
alpha_MUON_EFF_TrigStatUncertainty	±0.01 [0.01%]	±0.00 [0.02%]	±0.00 [0.01%]	±0.00 [0.01%]
alpha_JET_EffectiveNP_Statistical2	±0.01 [0.01%]	±0.01 [0.03%]	±0.03 [0.07%]	±0.03 [0.09%]
alpha_JET_EffectiveNP_Mixed1	±0.01 [0.01%]	±0.00 [0.01%]	±0.00 [0.01%]	±0.01 [0.02%]
alpha_JET_EffectiveNP_Modelling4	±0.00 [0.00%]	±0.00 [0.00%]	±0.00 [0.01%]	±0.01 [0.02%]
alpha_JET_EffectiveNP_Detector1	±0.00 [0.00%]	±0.01 [0.05%]	±0.01 [0.02%]	±0.00 [0.01%]
alpha_JET_EffectiveNP_Mixed3	±0.00 [0.00%]	±0.00 [0.00%]	±0.01 [0.02%]	±0.01 [0.02%]
alpha_JET_EffectiveNP_Detector2	±0.00 [0.00%]	±0.00 [0.00%]	±0.00 [0.01%]	±0.00 [0.00%]
gamma_stat_SRDF_0_inc160_cuts_bin_0	±0.00 [0.00%]	±0.82 [4.4%]	±0.00 [0.00%]	±0.00 [0.00%]
gamma_stat_SRDF_0_B_cuts_bin_0	±0.00 [0.00%]	±0.00 [0.00%]	±0.00 [0.00%]	±1.55 [4.8%]
gamma_stat_SRDF_0_A_cuts_bin_0	±0.00 [0.00%]	±0.00 [0.00%]	±1.89 [4.2%]	±0.00 [0.00%]

Table B.4: Breakdown of the dominant systematic uncertainties on background estimates in the inclusive SR-DF-0 after the background-only fit. Note that the individual uncertainties can be correlated and do not necessarily add up quadratically to the total background uncertainty. The percentages show the size of the uncertainty relative to the total expected background.

Uncertainty of channel m_{T2} [GeV]	SRDF_1_inc100 > 100	SRDF_1_inc160 > 160	SRDF_1_A $\in [100, 120)$	SRDF_1_B $\in [120, 160)$
Total background expectation	75.29	15.08	38.95	21.27
Total statistical ($\sqrt{N_{\mathrm{exp}}}$)	±8.68	±3.88	±6.24	±4.61
Total background systematic	±9.01 [11.97%]	±2.74 [18.16%]	±5.88 [15.10%]	±2.83 [13.31%]
alpha_syst_VV_gen	±4.78 [6.3%]	±1.78 [11.8%]	±0.68 [1.8%]	±1.51 [7.1%]
mu_WW	±4.35 [5.8%]	±1.21 [8.0%]	±1.60 [4.1%]	±1.54 [7.3%]
alpha_syst_ttbar_show	±3.97 [5.3%]	±0.02 [0.12%]	±3.46 [8.9%]	±0.49 [2.3%]
alpha_syst_ttbar_rad	±3.47 [4.6%]	±0.02 [0.10%]	±3.03 [7.8%]	±0.43 [2.0%]
alpha_syst_ttbar_gen	±2.98 [4.0%]	±0.01 [0.09%]	±2.60 [6.7%]	±0.37 [1.7%]
gamma_stat_SRDF_1_inc100_cuts_bin_0	±2.14 [2.8%]	±0.00 [0.00%]	±0.00 [0.00%]	±0.00 [0.00%]
alpha_syst_VV_PDF	±1.92 [2.5%]	±0.86 [5.7%]	±0.72 [1.9%]	±0.59 [2.8%]
alpha_JET_Flavor_Composition	±1.60 [2.1%]	±0.53 [3.5%]	±0.43 [1.1%]	±0.63 [3.0%]
mu_ttbar	±1.56 [2.1%]	±0.01 [0.04%]	±1.37 [3.5%]	±0.18 [0.87%]
alpha_FT_EFF_B	±1.31 [1.7%]	±0.02 [0.13%]	±1.12 [2.9%]	±0.17 [0.81%]
alpha_syst_wt_DS	±1.26 [1.7%]	±0.00 [0.00%]	±1.17 [3.0%]	±0.09 [0.45%]
alpha_JET_Pileup_RhoTopology	±1.18 [1.6%]	±0.29 [1.9%]	±0.34 [0.86%]	±0.56 [2.6%]
alpha_JET_EffectiveNP_Modelling1	±0.94 [1.3%]	±0.31 [2.1%]	±0.20 [0.52%]	±0.42 [2.0%]
alpha_Factorization_VV	±0.84 [1.1%]	±0.26 [1.7%]	±0.30 [0.76%]	±0.26 [1.2%]
alpha_JET_JER_EffectiveNP_9	±0.78 [1.0%]	±0.08 [0.51%]	±0.42 [1.1%]	±0.29 [1.4%]
alpha_JET_JER_EffectiveNP_2	±0.75 [0.99%]	±0.09 [0.57%]	±0.66 [1.7%]	±0.17 [0.82%]
alpha_fakesSyst	±0.59 [0.78%]	±0.15 [0.99%]	±0.29 [0.74%]	±0.15 [0.72%]
alpha_MET_ResoPara	±0.54 [0.71%]	±0.06 [0.38%]	±0.38 [0.99%]	±0.21 [0.98%]
alpha_JET_JER_EffectiveNP_3	±0.53 [0.70%]	±0.13 [0.87%]	±0.60 [1.5%]	±0.07 [0.31%]
alpha_PRW_syst	±0.50 [0.67%]	±0.12 [0.82%]	±0.34 [0.88%]	±0.04 [0.17%]
alpha_MET_ScaleUp	±0.50 [0.66%]	±0.02 [0.12%]	±0.35 [0.90%]	±0.13 [0.61%]
alpha_JET_JER_EffectiveNP_7	±0.49 [0.65%]	±0.06 [0.40%]	±0.34 [0.88%]	±0.09 [0.41%]
alpha_MET_ResoPerp	±0.47 [0.63%]	±0.03 [0.21%]	±0.59 [1.5%]	±0.09 [0.41%]
alpha_EL_EFF_ISO	±0.47 [0.62%]	±0.24 [1.6%]	±0.07 [0.18%]	±0.16 [0.77%]
alpha_EG_SCALE	±0.46 [0.60%]	±0.13 [0.87%]	±0.32 [0.83%]	±0.00 [0.01%]
alpha_FT_EFF_Light	±0.45 [0.59%]	±0.10 [0.67%]	±0.22 [0.56%]	±0.13 [0.59%]
alpha_JET_JER_EffectiveNP_1	±0.44 [0.58%]	±0.12 [0.77%]	±0.53 [1.4%]	±0.02 [0.10%]
alpha_JET_JER_EffectiveNP_11	±0.42 [0.55%]	±0.02 [0.13%]	±0.14 [0.35%]	±0.30 [1.4%]
alpha_JET_JER_EffectiveNP_5	±0.38 [0.51%]	±0.05 [0.34%]	±0.23 [0.59%]	±0.10 [0.49%]
alpha_JET_Pileup_OffsetNPV	±0.38 [0.51%]	±0.11 [0.75%]	±0.00 [0.00%]	±0.27 [1.2%]
alpha_EL_EFF_ID	±0.32 [0.43%]	±0.15 [0.96%]	±0.07 [0.19%]	±0.10 [0.48%]
alpha_MET_ScaleDown	±0.30 [0.40%]	±0.01 [0.07%]	±0.35 [0.89%]	±0.04 [0.18%]
alpha_JET_JER_DataVsMC	±0.29 [0.38%]	±0.12 [0.77%]	±0.41 [1.1%]	±0.01 [0.05%]
alpha_MUONS_MS	±0.29 [0.38%]	±0.04 [0.26%]	±0.12 [0.30%]	±0.13 [0.60%]
alpha_JET_JER_EffectiveNP_8	±0.28 [0.38%]	±0.02 [0.10%]	±0.27 [0.70%]	±0.03 [0.13%]
alpha_JET_JER_EffectiveNP_10	±0.27 [0.36%]	±0.03 [0.17%]	±0.13 [0.34%]	±0.17 [0.78%]
alpha_MUONS_ID	±0.26 [0.35%]	±0.07 [0.47%]	±0.25 [0.63%]	±0.05 [0.26%]
alpha_JET_Flavor_Response	±0.23 [0.31%]	±0.18 [1.2%]	±0.17 [0.44%]	±0.23 [1.1%]
alpha_JET_JER_EffectiveNP_6	±0.17 [0.23%]	±0.00 [0.02%]	±0.09 [0.24%]	±0.08 [0.39%]
alpha_JET_Pileup_OffsetMu	±0.16 [0.22%]	±0.09 [0.57%]	±0.36 [0.92%]	±0.11 [0.52%]
alpha_JET_Pileup_PtTerm	±0.13 [0.18%]	±0.03 [0.21%]	±0.12 [0.32%]	±0.02 [0.10%]
alpha_JET_JER_EffectiveNP_4	±0.13 [0.17%]	±0.14 [0.96%]	±0.16 [0.41%]	±0.18 [0.85%]
alpha_MUON_EFF_RECO_SYS	±0.12 [0.16%]	±0.07 [0.46%]	±0.02 [0.04%]	±0.03 [0.16%]
alpha_MUONS_SagRho	±0.11 [0.14%]	±0.06 [0.42%]	±0.11 [0.28%]	±0.15 [0.72%]
alpha_FT_EFF_C	±0.11 [0.14%]	±0.02 [0.10%]	±0.05 [0.13%]	±0.04 [0.19%]
alpha_JET_EffectiveNP_Statistical1	±0.11 [0.14%]	±0.02 [0.13%]	±0.12 [0.31%]	±0.00 [0.02%]
alpha_MUONS_SagReb	±0.10 [0.14%]	±0.07 [0.47%]	±0.11 [0.29%]	±0.15 [0.69%]
alpha_JET_EffectiveNP_Mixed2	±0.10 [0.14%]	±0.01 [0.07%]	±0.13 [0.34%]	±0.02 [0.10%]
alpha_JET_JER_EffectiveNP_12restTerm	±0.10 [0.13%]	±0.06 [0.39%]	±0.08 [0.20%]	±0.04 [0.18%]
alpha_JET_EffectiveNP_Mixed1	±0.09 [0.12%]	±0.01 [0.04%]	±0.07 [0.19%]	±0.01 [0.04%]
alpha_Renormalization_VV	±0.08 [0.11%]	±0.04 [0.30%]	±0.05 [0.12%]	±0.03 [0.16%]
alpha_JET_JvtEfficiency	±0.07 [0.10%]	±0.04 [0.25%]	±0.00 [0.01%]	±0.04 [0.18%]
mu_VZ	±0.07 [0.09%]	±0.02 [0.16%]	±0.02 [0.05%]	±0.02 [0.11%]
alpha_EG_RES	±0.06 [0.08%]	±0.11 [0.72%]	±0.03 [0.08%]	±0.14 [0.66%]
alpha_JET_EffectiveNP_Statistical4	±0.06 [0.08%]	±0.02 [0.11%]	±0.08 [0.21%]	±0.01 [0.02%]
alpha_JET_EffectiveNP_Statistical5	±0.05 [0.07%]	±0.00 [0.01%]	±0.06 [0.14%]	±0.00 [0.01%]
Lumi	±0.05 [0.07%]	±0.02 [0.11%]	±0.02 [0.05%]	±0.02 [0.08%]
alpha_JET_EffectiveNP_Detector1	±0.05 [0.07%]	±0.02 [0.12%]	±0.08 [0.20%]	±0.01 [0.04%]
alpha_JET_EffectiveNP_Statistical3	±0.04 [0.05%]	±0.00 [0.01%]	±0.04 [0.11%]	±0.00 [0.01%]
alpha_JET_EffectiveNP_Modelling2	±0.04 [0.05%]	±0.05 [0.32%]	±0.07 [0.17%]	±0.06 [0.27%]
alpha_JET_EffectiveNP_Statistical6	±0.04 [0.05%]	±0.00 [0.02%]	±0.04 [0.11%]	±0.00 [0.02%]
alpha_JET_EffectiveNP_Modelling3	±0.03 [0.04%]	±0.04 [0.25%]	±0.08 [0.21%]	±0.01 [0.06%]
alpha_JET_EtaIntercalibration_Modelling	±0.03 [0.03%]	±0.15 [0.99%]	±0.44 [1.1%]	±0.27 [1.3%]
alpha_JET_EtaIntercalibration_TotalStat	±0.02 [0.03%]	±0.03 [0.18%]	±0.07 [0.18%]	±0.07 [0.32%]
alpha_JET_EffectiveNP_Modelling4	±0.02 [0.03%]	±0.00 [0.00%]	±0.02 [0.06%]	±0.00 [0.00%]
alpha_JET_EffectiveNP_Statistical2	±0.02 [0.03%]	±0.03 [0.22%]	±0.06 [0.15%]	±0.05 [0.21%]
alpha_JET_EffectiveNP_Mixed3	±0.02 [0.03%]	±0.00 [0.00%]	±0.02 [0.05%]	±0.00 [0.01%]
alpha_MUONS_SCALE	±0.02 [0.02%]	±0.01 [0.09%]	±0.03 [0.09%]	±0.00 [0.01%]
alpha_EL_EFF_RECO	±0.02 [0.02%]	±0.01 [0.04%]	±0.00 [0.01%]	±0.01 [0.02%]
alpha_JET_EtaIntercalibration_NonClosure_posEta	±0.01 [0.02%]	±0.00 [0.01%]	±0.02 [0.04%]	±0.00 [0.00%]
alpha_MUON_EFF_ISO_STAT	±0.01 [0.01%]	±0.00 [0.03%]	±0.00 [0.01%]	±0.00 [0.01%]
alpha_MUON_EFF_TrigStatUncertainty	±0.01 [0.01%]	±0.00 [0.02%]	±0.00 [0.01%]	±0.00 [0.01%]
alpha_JET_EtaIntercalibration_NonClosure_negEta	±0.01 [0.01%]	±0.00 [0.01%]	±0.00 [0.00%]	±0.01 [0.03%]
alpha_JET_EffectiveNP_Detector2	±0.00 [0.01%]	±0.00 [0.00%]	±0.00 [0.01%]	±0.00 [0.00%]
alpha_FT_EFF_extrapolation	±0.00 [0.01%]	±0.00 [0.00%]	±0.00 [0.00%]	±0.00 [0.01%]
gamma_stat_SRDF_1_A_cuts_bin_0	±0.00 [0.00%]	±0.00 [0.00%]	±1.61 [4.1%]	±0.00 [0.00%]
gamma_stat_SRDF_1_inc160_cuts_bin_0	±0.00 [0.00%]	±0.87 [5.7%]	±0.00 [0.00%]	±0.00 [0.00%]
gamma_stat_SRDF_1_B_cuts_bin_0	±0.00 [0.00%]	±0.00 [0.00%]	±0.00 [0.00%]	±1.06 [5.0%]

Table B.5: Breakdown of the dominant systematic uncertainties on background estimates in the inclusive SR-DF-1 after the background-only fit. Note that the individual uncertainties can be correlated and do not necessarily add up quadratically to the total background uncertainty. The percentages show the size of the uncertainty relative to the total expected background.

Uncertainty of channel m_{T2} [GeV]	SRSF_0_inc100 > 100	SRSF_0_inc160 > 160	SRSF_0_A $\in [100, 120)$	SRSF_0_B $\in [120, 160)$
Total background expectation	144.47	37.30	56.39	50.78
Total statistical ($\sqrt{N_{\text{exp}}}$)	±12.02	±6.11	±7.51	±7.13
Total background systematic	±11.63 [8.05%]	±2.98 [7.98%]	±6.26 [11.10%]	±5.38 [10.60%]
mu_WW	±6.57 [4.5%]	±1.63 [4.4%]	±2.49 [4.4%]	±2.45 [4.8%]
alpha_syst_VV_gen	±5.04 [3.5%]	±0.52 [1.4%]	±1.03 [1.8%]	±3.71 [7.3%]
alpha_syst_ttbar_rad	±3.62 [2.5%]	±0.00 [0.00%]	±3.06 [5.4%]	±0.56 [1.1%]
gamma_stat_SRSF_0_inc100_cuts_bin_0	±3.47 [2.4%]	±0.00 [0.00%]	±0.00 [0.00%]	±0.00 [0.00%]
alpha_syst_VV_PDF	±3.34 [2.3%]	±1.02 [2.7%]	±1.40 [2.5%]	±1.07 [2.1%]
alpha_JET_Flavor_Composition	±2.12 [1.5%]	±0.01 [0.03%]	±1.95 [3.5%]	±0.18 [0.36%]
mu_VZ	±2.01 [1.4%]	±0.69 [1.8%]	±0.60 [1.1%]	±0.73 [1.4%]
alpha_fakesSyst	±1.40 [0.97%]	±0.34 [0.90%]	±0.55 [0.98%]	±0.51 [1.0%]
alpha_syst_wt_DS	±1.18 [0.82%]	±0.00 [0.00%]	±1.11 [2.0%]	±0.08 [0.15%]
mu_ttbar	±1.03 [0.72%]	±0.00 [0.00%]	±0.89 [1.6%]	±0.14 [0.29%]
alpha_JET_Flavor_Response	±1.01 [0.70%]	±0.00 [0.00%]	±0.86 [1.5%]	±0.15 [0.29%]
alpha_syst_ttbar_gen	±0.95 [0.66%]	±0.00 [0.00%]	±0.80 [1.4%]	±0.15 [0.29%]
alpha_EL_EFF_ISO	±0.94 [0.65%]	±0.60 [1.6%]	±0.08 [0.15%]	±0.26 [0.51%]
alpha_Factorization_VV	±0.92 [0.64%]	±0.34 [0.90%]	±0.21 [0.38%]	±0.27 [0.53%]
alpha_JET_Pileup_RhoTopology	±0.84 [0.58%]	±0.03 [0.09%]	±0.76 [1.4%]	±0.04 [0.08%]
alpha_JET_EffectiveNP_Modelling1	±0.81 [0.56%]	±0.05 [0.14%]	±0.89 [1.6%]	±0.03 [0.05%]
alpha_JET_JER_EffectiveNP_10	±0.77 [0.53%]	±0.03 [0.08%]	±0.65 [1.1%]	±0.08 [0.16%]
alpha_JET_JER_EffectiveNP_12restTerm	±0.69 [0.48%]	±0.01 [0.02%]	±0.79 [1.4%]	±0.10 [0.19%]
alpha_PRW_syst	±0.67 [0.46%]	±0.05 [0.13%]	±0.19 [0.33%]	±0.43 [0.85%]
alpha_JET_JER_EffectiveNP_3	±0.64 [0.44%]	±0.03 [0.09%]	±0.69 [1.2%]	±0.02 [0.05%]
alpha_JET_EtaIntercalibration_Modelling	±0.62 [0.43%]	±0.06 [0.16%]	±0.80 [1.4%]	±0.13 [0.26%]
alpha_EL_EFF_ID	±0.61 [0.42%]	±0.31 [0.82%]	±0.09 [0.16%]	±0.21 [0.42%]
alpha_MET_ScaleDown	±0.57 [0.39%]	±0.17 [0.45%]	±0.40 [0.71%]	±0.06 [0.13%]
alpha_Renormalization_VV	±0.51 [0.35%]	±0.15 [0.41%]	±0.18 [0.31%]	±0.17 [0.34%]
alpha_JET_JER_EffectiveNP_5	±0.48 [0.33%]	±0.03 [0.07%]	±0.36 [0.64%]	±0.14 [0.27%]
alpha_EG_SCALE	±0.42 [0.29%]	±0.18 [0.49%]	±0.20 [0.36%]	±0.03 [0.06%]
alpha_JET_JER_EffectiveNP_6	±0.34 [0.23%]	±0.04 [0.10%]	±0.17 [0.30%]	±0.12 [0.24%]
alpha_JET_Pileup_OffsetMu	±0.33 [0.23%]	±0.02 [0.05%]	±0.31 [0.55%]	±0.00 [0.01%]
alpha_MUON_EFF_RECO_SYS	±0.33 [0.23%]	±0.17 [0.45%]	±0.07 [0.12%]	±0.09 [0.18%]
alpha_syst_ttbar_show	±0.31 [0.21%]	±0.00 [0.00%]	±0.26 [0.47%]	±0.05 [0.09%]
alpha_JET_JER_EffectiveNP_7	±0.27 [0.19%]	±0.06 [0.17%]	±0.12 [0.22%]	±0.22 [0.43%]
alpha_MUONS_SagRho	±0.25 [0.18%]	±0.02 [0.05%]	±0.08 [0.13%]	±0.18 [0.36%]
alpha_MUONS_MS	±0.25 [0.18%]	±0.01 [0.03%]	±0.34 [0.60%]	±0.10 [0.19%]
alpha_MET_ScaleUp	±0.24 [0.16%]	±0.25 [0.67%]	±0.53 [0.94%]	±0.04 [0.08%]
alpha_MUONS_SagReb	±0.23 [0.16%]	±0.04 [0.12%]	±0.09 [0.16%]	±0.17 [0.34%]
alpha_JET_JER_EffectiveNP_1	±0.20 [0.14%]	±0.16 [0.43%]	±0.47 [0.83%]	±0.37 [0.72%]
alpha_EG_RES	±0.19 [0.13%]	±0.00 [0.00%]	±0.23 [0.41%]	±0.11 [0.22%]
alpha_JET_JER_EffectiveNP_8	±0.18 [0.12%]	±0.05 [0.14%]	±0.34 [0.60%]	±0.22 [0.43%]
alpha_FT_EFF_B	±0.17 [0.12%]	±0.00 [0.00%]	±0.15 [0.26%]	±0.03 [0.05%]
alpha_JET_JvtEfficiency	±0.16 [0.11%]	±0.01 [0.02%]	±0.12 [0.22%]	±0.03 [0.06%]
alpha_JET_Pileup_PtTerm	±0.16 [0.11%]	±0.04 [0.10%]	±0.12 [0.22%]	±0.07 [0.15%]
alpha_MUONS_ID	±0.16 [0.11%]	±0.05 [0.12%]	±0.16 [0.29%]	±0.05 [0.11%]
alpha_JET_JER_EffectiveNP_4	±0.14 [0.10%]	±0.03 [0.09%]	±0.03 [0.05%]	±0.15 [0.29%]
alpha_JET_JER_EffectiveNP_2	±0.14 [0.10%]	±0.08 [0.21%]	±0.16 [0.28%]	±0.26 [0.52%]
alpha_JET_JER_DataVsMC	±0.13 [0.09%]	±0.13 [0.36%]	±0.48 [0.86%]	±0.22 [0.44%]
Lumi	±0.13 [0.09%]	±0.04 [0.11%]	±0.02 [0.04%]	±0.06 [0.13%]
alpha_MET_ResoPerp	±0.12 [0.09%]	±0.26 [0.71%]	±0.39 [0.69%]	±0.25 [0.49%]
alpha_JET_Pileup_OffsetNPV	±0.11 [0.07%]	±0.04 [0.10%]	±0.07 [0.12%]	±0.08 [0.15%]
alpha_MET_ResoPara	±0.10 [0.07%]	±0.27 [0.72%]	±0.35 [0.62%]	±0.09 [0.18%]
alpha_FT_EFF_Light	±0.07 [0.05%]	±0.02 [0.05%]	±0.03 [0.06%]	±0.02 [0.04%]
alpha_MUONS_SCALE	±0.07 [0.05%]	±0.08 [0.21%]	±0.04 [0.08%]	±0.04 [0.07%]
alpha_JET_EffectiveNP_Statistical5	±0.05 [0.04%]	±0.00 [0.01%]	±0.04 [0.08%]	±0.01 [0.01%]
alpha_MUON_EFF_TrigStatUncertainty	±0.05 [0.03%]	±0.01 [0.02%]	±0.02 [0.04%]	±0.02 [0.03%]
alpha_JET_EffectiveNP_Statistical2	±0.05 [0.03%]	±0.02 [0.05%]	±0.01 [0.01%]	±0.03 [0.06%]
alpha_JET_JER_EffectiveNP_11	±0.04 [0.03%]	±0.06 [0.16%]	±0.14 [0.25%]	±0.12 [0.24%]
alpha_JET_EtaIntercalibration_NonClosure_posEta	±0.03 [0.02%]	±0.00 [0.00%]	±0.03 [0.06%]	±0.00 [0.00%]
alpha_JET_EffectiveNP_Modelling2	±0.03 [0.02%]	±0.01 [0.03%]	±0.01 [0.02%]	±0.04 [0.07%]
alpha_JET_EffectiveNP_Statistical1	±0.03 [0.02%]	±0.02 [0.05%]	±0.01 [0.01%]	±0.02 [0.04%]
alpha_JET_EffectiveNP_Mixed1	±0.03 [0.02%]	±0.00 [0.01%]	±0.04 [0.06%]	±0.00 [0.01%]
alpha_JET_EffectiveNP_Modelling3	±0.03 [0.02%]	±0.02 [0.05%]	±0.04 [0.08%]	±0.00 [0.00%]
alpha_EL_EFF_RECO	±0.03 [0.02%]	±0.01 [0.03%]	±0.00 [0.01%]	±0.01 [0.02%]
alpha_JET_EffectiveNP_Modelling4	±0.03 [0.02%]	±0.00 [0.00%]	±0.03 [0.05%]	±0.00 [0.00%]
alpha_JET_EffectiveNP_Mixed2	±0.02 [0.02%]	±0.02 [0.05%]	±0.01 [0.01%]	±0.01 [0.01%]
alpha_JET_EffectiveNP_Statistical4	±0.02 [0.02%]	±0.01 [0.02%]	±0.00 [0.01%]	±0.01 [0.02%]
alpha_MUON_EFF_ISO_STAT	±0.02 [0.01%]	±0.01 [0.03%]	±0.00 [0.01%]	±0.01 [0.01%]
alpha_JET_JER_EffectiveNP_9	±0.02 [0.01%]	±0.08 [0.20%]	±0.23 [0.40%]	±0.13 [0.26%]
alpha_JET_EffectiveNP_Mixed3	±0.02 [0.01%]	±0.00 [0.01%]	±0.02 [0.04%]	±0.00 [0.01%]
alpha_JET_EffectiveNP_Statistical3	±0.02 [0.01%]	±0.00 [0.01%]	±0.01 [0.02%]	±0.00 [0.01%]
alpha_FT_EFF_C	±0.01 [0.01%]	±0.00 [0.01%]	±0.01 [0.01%]	±0.00 [0.01%]
alpha_MUON_EFF_ISO_SYS	±0.01 [0.01%]	±0.00 [0.00%]	±0.01 [0.01%]	±0.01 [0.01%]
alpha_MUON_EFF_RECO_STAT	±0.01 [0.01%]	±0.00 [0.00%]	±0.00 [0.01%]	±0.01 [0.01%]
alpha_JET_EtaIntercalibration_NonClosure_negEta	±0.01 [0.01%]	±0.00 [0.01%]	±0.00 [0.00%]	±0.01 [0.01%]
alpha_JET_EtaIntercalibration_TotalStat	±0.01 [0.01%]	±0.02 [0.04%]	±0.03 [0.06%]	±0.03 [0.05%]
alpha_JET_MassRes_Hbb	±0.01 [0.00%]	±0.00 [0.00%]	±0.00 [0.00%]	±0.01 [0.01%]
alpha_JET_EffectiveNP_Detector2	±0.00 [0.00%]	±0.00 [0.00%]	±0.00 [0.01%]	±0.00 [0.00%]
alpha_JET_EffectiveNP_Statistical6	±0.00 [0.00%]	±0.01 [0.02%]	±0.02 [0.03%]	±0.01 [0.02%]
alpha_JET_EffectiveNP_Detector1	±0.00 [0.00%]	±0.01 [0.04%]	±0.02 [0.04%]	±0.01 [0.02%]
gamma_stat_SRSF_0_B_cuts_bin_0	±0.00 [0.00%]	±0.00 [0.00%]	±0.00 [0.00%]	±2.25 [4.4%]
gamma_stat_SRSF_0_A_cuts_bin_0	±0.00 [0.00%]	±0.00 [0.00%]	±1.90 [3.4%]	±0.00 [0.00%]
gamma_stat_SRSF_0_inc160_cuts_bin_0	±0.00 [0.00%]	±1.89 [5.1%]	±0.00 [0.00%]	±0.00 [0.00%]

Table B.6: Breakdown of the dominant systematic uncertainties on background estimates in the inclusive SR-SF-0 after the background-only fit. Note that the individual uncertainties can be correlated and do not necessarily add up quadratically to the total background uncertainty. The percentages show the size of the uncertainty relative to the total expected background.

Uncertainty of channel m_{T2} [GeV]	SRSF_1_inc100 > 100	SRSF_1_inc160 > 160	SRSF_1_A $\in [100, 120)$	SRSF_1_B $\in [120, 160)$
Total background expectation	124.25	35.87	48.09	40.28
Total statistical ($\sqrt{N_{\text{exp}}}$)	±11.15	±5.99	±6.93	±6.35
Total background systematic	±12.31 [9.91%]	±4.54 [12.65%]	±8.09 [16.82%]	±3.84 [9.53%]
alpha_syst_ttbar_show	±6.37 [5.1%]	±0.03 [0.08%]	±5.71 [11.9%]	±0.63 [1.6%]
mu_WW	±4.35 [3.5%]	±1.27 [3.6%]	±1.63 [3.4%]	±1.44 [3.6%]
gamma_stat_SRSF_1_inc100_cuts_bin_0	±4.21 [3.4%]	±0.00 [0.00%]	±0.00 [0.00%]	±0.00 [0.00%]
alpha_EL_EFF_ISO	±3.70 [3.0%]	±2.57 [7.2%]	±0.21 [0.43%]	±0.92 [2.3%]
alpha_syst_ttbar_gen	±3.67 [3.0%]	±0.02 [0.04%]	±3.29 [6.8%]	±0.36 [0.90%]
alpha_syst_VV_gen	±3.20 [2.6%]	±1.65 [4.6%]	±0.92 [1.9%]	±0.21 [0.53%]
alpha_syst_VV_PDF	±2.17 [1.7%]	±0.86 [2.4%]	±0.66 [1.4%]	±0.66 [1.6%]
alpha_MET_ScaleDown	±2.10 [1.7%]	±0.25 [0.69%]	±1.70 [3.5%]	±0.15 [0.37%]
alpha_syst_wt_DS	±1.64 [1.3%]	±0.00 [0.00%]	±1.29 [2.7%]	±0.35 [0.87%]
alpha_fakesSyst	±1.45 [1.2%]	±0.32 [0.90%]	±0.55 [1.2%]	±0.58 [1.4%]
mu_VZ	±1.45 [1.2%]	±0.58 [1.6%]	±0.34 [0.71%]	±0.52 [1.3%]
alpha_JET_JER_EffectiveNP_2	±1.42 [1.1%]	±0.14 [0.39%]	±0.99 [2.1%]	±0.29 [0.71%]
mu_ttbar	±1.33 [1.1%]	±0.00 [0.01%]	±1.17 [2.4%]	±0.16 [0.39%]
alpha_JET_Flavor_Composition	±1.22 [0.98%]	±0.59 [1.6%]	±0.12 [0.24%]	±0.52 [1.3%]
alpha_FT_EFF_B	±1.13 [0.91%]	±0.05 [0.14%]	±0.93 [1.9%]	±0.15 [0.37%]
alpha_JET_Pileup_RhoTopology	±1.08 [0.87%]	±0.30 [0.85%]	±0.46 [0.95%]	±0.32 [0.79%]
alpha_syst_ttbar_rad	±1.07 [0.86%]	±0.00 [0.01%]	±0.96 [2.0%]	±0.11 [0.26%]
alpha_Factorization_VV	±0.99 [0.80%]	±0.39 [1.1%]	±0.27 [0.57%]	±0.25 [0.63%]
alpha_EL_EFF_ID	±0.91 [0.73%]	±0.52 [1.5%]	±0.12 [0.24%]	±0.27 [0.66%]
alpha_JET_EffectiveNP_Modelling1	±0.85 [0.68%]	±0.39 [1.1%]	±0.30 [0.63%]	±0.16 [0.40%]
alpha_JET_JER_EffectiveNP_8	±0.77 [0.62%]	±0.08 [0.23%]	±0.71 [1.5%]	±0.15 [0.36%]
alpha_MET_ResoPerp	±0.76 [0.62%]	±0.35 [0.97%]	±0.02 [0.04%]	±0.40 [0.99%]
alpha_EG_SCALE	±0.71 [0.57%]	±0.22 [0.62%]	±0.36 [0.75%]	±0.13 [0.31%]
alpha_JET_JER_DataVsMC	±0.71 [0.57%]	±0.03 [0.09%]	±0.54 [1.1%]	±0.20 [0.50%]
alpha_MET_ResoPara	±0.68 [0.54%]	±0.35 [0.98%]	±0.37 [0.77%]	±0.69 [1.7%]
alpha_FT_EFF_Light	±0.67 [0.54%]	±0.22 [0.62%]	±0.23 [0.49%]	±0.21 [0.53%]
alpha_JET_JER_EffectiveNP_5	±0.65 [0.53%]	±0.16 [0.46%]	±0.48 [1.00%]	±0.34 [0.84%]
alpha_MUONS_ID	±0.64 [0.51%]	±0.21 [0.58%]	±0.66 [1.4%]	±0.18 [0.46%]
alpha_MUONS_MS	±0.62 [0.50%]	±0.07 [0.20%]	±0.67 [1.4%]	±0.02 [0.06%]
alpha_MET_ScaleUp	±0.61 [0.49%]	±0.33 [0.92%]	±0.05 [0.10%]	±0.23 [0.57%]
alpha_JET_JER_EffectiveNP_1	±0.59 [0.48%]	±0.31 [0.86%]	±0.21 [0.43%]	±0.08 [0.20%]
alpha_PRW_syst	±0.56 [0.45%]	±0.39 [1.1%]	±0.15 [0.30%]	±0.02 [0.06%]
alpha_JET_JER_EffectiveNP_10	±0.56 [0.45%]	±0.01 [0.04%]	±0.50 [1.0%]	±0.04 [0.10%]
alpha_MUONS_SagReb	±0.51 [0.41%]	±0.02 [0.05%]	±0.17 [0.36%]	±0.32 [0.79%]
alpha_JET_JER_EffectiveNP_3	±0.48 [0.39%]	±0.10 [0.28%]	±0.37 [0.77%]	±0.21 [0.53%]
alpha_JET_JER_EffectiveNP_7	±0.48 [0.38%]	±0.03 [0.10%]	±0.16 [0.33%]	±0.35 [0.88%]
alpha_MUON_EFF_RECO_SYS	±0.47 [0.38%]	±0.26 [0.72%]	±0.06 [0.13%]	±0.15 [0.36%]
alpha_JET_Pileup_OffsetNPV	±0.45 [0.36%]	±0.03 [0.09%]	±0.29 [0.61%]	±0.12 [0.30%]
alpha_FT_EFF_C	±0.40 [0.32%]	±0.15 [0.41%]	±0.14 [0.29%]	±0.11 [0.28%]
Lumi	±0.36 [0.29%]	±0.12 [0.35%]	±0.08 [0.17%]	±0.16 [0.39%]
alpha_MUONS_SagRho	±0.35 [0.28%]	±0.10 [0.27%]	±0.10 [0.21%]	±0.15 [0.38%]
alpha_JET_JER_EffectiveNP_6	±0.32 [0.25%]	±0.03 [0.08%]	±0.09 [0.20%]	±0.25 [0.62%]
alpha_JET_EtaIntercalibration_Modelling	±0.26 [0.21%]	±0.18 [0.50%]	±0.09 [0.19%]	±0.16 [0.41%]
alpha_EG_RES	±0.23 [0.18%]	±0.12 [0.33%]	±0.22 [0.45%]	±0.57 [1.4%]
alpha_JET_JER_EffectiveNP_11	±0.22 [0.17%]	±0.11 [0.30%]	±0.02 [0.04%]	±0.09 [0.22%]
alpha_JET_JER_EffectiveNP_9	±0.21 [0.17%]	±0.11 [0.29%]	±0.10 [0.20%]	±0.01 [0.03%]
alpha_JET_JvtEfficiency	±0.20 [0.16%]	±0.05 [0.14%]	±0.07 [0.14%]	±0.09 [0.21%]
alpha_JET_EffectiveNP_Detector1	±0.17 [0.13%]	±0.07 [0.19%]	±0.08 [0.16%]	±0.02 [0.05%]
alpha_JET_Flavor_Response	±0.15 [0.12%]	±0.36 [1.0%]	±0.61 [1.3%]	±0.10 [0.26%]
alpha_JET_EffectiveNP_Mixed2	±0.14 [0.12%]	±0.08 [0.22%]	±0.07 [0.14%]	±0.00 [0.00%]
alpha_JET_EffectiveNP_Mixed1	±0.11 [0.09%]	±0.03 [0.08%]	±0.08 [0.17%]	±0.00 [0.01%]
alpha_FT_EFF_extrapolation_from_charm	±0.10 [0.08%]	±0.05 [0.13%]	±0.02 [0.04%]	±0.04 [0.09%]
alpha_JET_EffectiveNP_Modelling3	±0.10 [0.08%]	±0.02 [0.06%]	±0.11 [0.24%]	±0.01 [0.02%]
alpha_JET_EffectiveNP_Statistical6	±0.10 [0.08%]	±0.06 [0.16%]	±0.05 [0.10%]	±0.01 [0.02%]
alpha_JET_Pileup_OffsetMu	±0.10 [0.08%]	±0.07 [0.19%]	±0.03 [0.07%]	±0.13 [0.32%]
alpha_JET_Pileup_PtTerm	±0.09 [0.07%]	±0.07 [0.20%]	±0.15 [0.32%]	±0.01 [0.04%]
alpha_JET_JER_EffectiveNP_4	±0.08 [0.07%]	±0.05 [0.15%]	±0.14 [0.30%]	±0.12 [0.29%]
alpha_JET_EffectiveNP_Statistical1	±0.08 [0.06%]	±0.07 [0.18%]	±0.00 [0.01%]	±0.02 [0.04%]
alpha_JET_EffectiveNP_Statistical3	±0.07 [0.06%]	±0.02 [0.05%]	±0.05 [0.10%]	±0.00 [0.01%]
alpha_JET_EffectiveNP_Modelling2	±0.06 [0.05%]	±0.00 [0.01%]	±0.04 [0.09%]	±0.01 [0.03%]
alpha_JET_JER_EffectiveNP_12restTerm	±0.06 [0.05%]	±0.10 [0.28%]	±0.27 [0.56%]	±0.11 [0.28%]
alpha_MUON_EFF_TrigStatUncertainty	±0.05 [0.04%]	±0.01 [0.04%]	±0.02 [0.04%]	±0.02 [0.05%]
alpha_EL_EFF_RECO	±0.04 [0.03%]	±0.03 [0.08%]	±0.00 [0.00%]	±0.01 [0.03%]
alpha_MUONS_SCALE	±0.04 [0.03%]	±0.02 [0.05%]	±0.07 [0.15%]	±0.01 [0.04%]
alpha_MUON_EFF_ISO_SYS	±0.03 [0.02%]	±0.01 [0.02%]	±0.01 [0.02%]	±0.01 [0.03%]
alpha_JET_EtaIntercalibration_TotalStat	±0.03 [0.02%]	±0.01 [0.03%]	±0.00 [0.01%]	±0.03 [0.08%]
alpha_MUON_EFF_ISO_STAT	±0.02 [0.02%]	±0.01 [0.03%]	±0.00 [0.01%]	±0.01 [0.02%]
alpha_JET_EffectiveNP_Statistical2	±0.02 [0.02%]	±0.00 [0.01%]	±0.01 [0.02%]	±0.03 [0.07%]
alpha_Renormalization_VV	±0.02 [0.02%]	±0.03 [0.07%]	±0.02 [0.05%]	±0.00 [0.01%]
alpha_JET_EtaIntercalibration_NonClosure_negEta	±0.02 [0.02%]	±0.00 [0.01%]	±0.03 [0.06%]	±0.00 [0.01%]
alpha_MUON_EFF_RECO_STAT	±0.01 [0.01%]	±0.01 [0.01%]	±0.00 [0.01%]	±0.01 [0.02%]
alpha_JET_EffectiveNP_Detector2	±0.01 [0.01%]	±0.02 [0.05%]	±0.00 [0.01%]	±0.00 [0.00%]
alpha_JET_EffectiveNP_Modelling4	±0.01 [0.01%]	±0.02 [0.05%]	±0.00 [0.01%]	±0.00 [0.00%]
alpha_JET_PunchThrough_MC16	±0.01 [0.01%]	±0.01 [0.03%]	±0.00 [0.00%]	±0.00 [0.00%]
alpha_FT_EFF_extrapolation	±0.01 [0.01%]	±0.00 [0.01%]	±0.01 [0.01%]	±0.00 [0.00%]
alpha_JET_EffectiveNP_Statistical5	±0.01 [0.01%]	±0.03 [0.07%]	±0.01 [0.02%]	±0.00 [0.01%]
alpha_JET_EffectiveNP_Statistical4	±0.01 [0.00%]	±0.04 [0.11%]	±0.08 [0.17%]	±0.04 [0.09%]
alpha_JET_EffectiveNP_Mixed3	±0.00 [0.00%]	±0.02 [0.04%]	±0.01 [0.02%]	±0.00 [0.01%]
gamma_stat_SRSF_1_A_cuts_bin_0	±0.00 [0.00%]	±0.00 [0.00%]	±2.20 [4.6%]	±0.00 [0.00%]
gamma_stat_SRSF_1_inc160_cuts_bin_0	±0.00 [0.00%]	±2.38 [6.6%]	±0.00 [0.00%]	±0.00 [0.00%]
gamma_stat_SRSF_1_B_cuts_bin_0	±0.00 [0.00%]	±0.00 [0.00%]	±0.00 [0.00%]	±2.76 [6.9%]

Table B.7: Breakdown of the dominant systematic uncertainties on background estimates in the inclusive SR-SF-1 after the background-only fit. Note that the individual uncertainties can be correlated and do not necessarily add up quadratically to the total background uncertainty. The percentages show the size of the uncertainty relative to the total expected background.

Bibliography

[1] ATLAS Collaboration, *Search for electroweak production of charginos and sleptons decaying into final states with two leptons and missing transverse momentum in $\sqrt{s} = 13$ TeV pp collisions using the ATLAS detector*, Eur. Phys. J. C **80** (2020) 123, arXiv: 1908.08215 [hep-ph].

[2] S. L. Glashow et al., *Weak Interactions with Lepton-Hadron Symmetry*, Phys. Rev. D **2** (7 1970) 1285.

[3] S. Weinberg, *A Model of Leptons*, Phys. Rev. Lett. **19** (21 1967) 1264.

[4] A. Salam and J. C. Ward, *Weak and electromagnetic interactions*, Il Nuovo Cimento (1955-1965) **11** (1959) 568, ISSN: 1827-6121.

[5] S. L. Glashow, *Partial-symmetries of weak interactions*, Nucl. Phys. **22** (1961) 579, ISSN: 0029-5582.

[6] G. Altarelli, *The physics of deep inelastic phenomena*, Il Nuovo Cimento (1971-1977) **4** (1974) 335, ISSN: 1826-9850.

[7] H. D. Politzer, *Asymptotic freedom: An approach to strong interactions*, Phys. Rep. **14** (1974) 129, ISSN: 0370-1573.

[8] A. Djouadi, *The anatomy of electroweak symmetry breaking Tome II: The Higgs bosons in the Minimal Supersymmetric Model*, Phys. Rep. **459** (2008) 1, ISSN: 0370-1573, arXiv: hep-ph/0503173 [hep-ph].

[9] G. Bertone et al., *Particle dark matter: evidence, candidates and constraints*, Phys. Rep. **405** (2005) 279, ISSN: 0370-1573, arXiv: hep-ph/0404175 [hep-ph].

[10] Yu. A. Golfand and E. P. Likhtman, *Extension of the Algebra of Poincaré Group Generators and Violation of p Invariance*, JETP Lett. **13** (1971) 323, [Pisma Zh. Eksp. Teor. Fiz. 13, 452 (1971)].

[11] D. V. Volkov and V. P. Akulov, *Is the neutrino a goldstone particle?*, Phys. Lett. B **46** (1973) 109, ISSN: 0370-2693.

[12] J. Wess and B. Zumino, *Supergauge transformations in four dimensions*, Nucl. Phys. B **70** (1974) 39, ISSN: 0550-3213.

[13] J. Wess and B. Zumino, *Supergauge invariant extension of quantum electrodynamics*, Nucl. Phys. B **78** (1974) 1, ISSN: 0550-3213.

[14] S. Ferrara and Zumino B., *Supergauge invariant Yang-Mills theories*, Nucl. Phys. B **79** (1974) 413, ISSN: 0550-3213.

[15] A. Salam and J. Strathdee, *Super-symmetry and non-Abelian gauges*, Phys. Lett. B **51** (1974) 353, ISSN: 0370-2693.

[16] S. P. Martin, *A Supersymmetry Primer*, Advanced Series on Directions in HEP (1998) 1, ISSN: 1793-1339, arXiv: hep-ph/9709356 [hep-ph].

[17] N. Cabibbo, *Unitary Symmetry and Leptonic Decays*, Phys. Rev. Lett. **10** (12 1963) 531.

[18] M. Kobayashi and T. Maskawa, *CP-Violation in the Renormalizable Theory of Weak Interaction*, Prog. Theor. Phys. **49** (1973) 652, ISSN: 0033-068X.

[19] M. Tanabashi et al., *Review of Particle Physics*, Phys. Rev. D **98** (3 2018) 030001.

[20] S. M. Bilenky and J. Hošek, *Glashow-Weinberg-Salam theory of electroweak interactions and the neutral currents*, Phys. Rep. **90** (1982) 73, ISSN: 0370-1573.

[21] P. W. Higgs, *Broken Symmetries and the Masses of Gauge Bosons*, Phys. Rev. Lett. **13** (1964) 508.

[22] F. Englert and R. Brout, *Broken Symmetry and the Mass of Gauge Vector Mesons*, Phys. Rev. Lett. **13** (1964) 321.

[23] J. Goldstone et al., *Broken Symmetries*, Phys. Rev. **127** (3 1962) 965.

[24] ATLAS Collaboration, *Measurement of the W-boson mass in pp collisions at* $\sqrt{s} = 7$ TeV *with the ATLAS detector*, Eur. Phys. J. C **78** (2018) 110, ISSN: 1434-6052, arXiv: `1701.07240 [hep-ex]`.

[25] ATLAS Collaboration, *The ATLAS Experiment at the CERN Large Hadron Collider*, JINST **3** (2008) S08003.

[26] M. Baak et al., *The global electroweak fit at NNLO and prospects for the LHC and ILC*, Eur. Phys. J. C **74** (2014) 3046, ISSN: 1434-6052, arXiv: `1407.3792 [hep-ph]`.

[27] ATLAS Collaboration, *Measurement of the top quark mass in the* $t\bar{t} \to$ *dilepton channel from* $\sqrt{s} = 8$ TeV *ATLAS data*, Phys. Lett. B **761** (2016) 350, ISSN: 0370-2693, arXiv: `1606.02179 [hep-ex]`.

[28] ATLAS and CMS Collaborations, *Combined Measurement of the Higgs Boson Mass in pp Collisions at* $\sqrt{s} = 7$ *and* 8 TeV *with the ATLAS and CMS Experiments*, Phys. Rev. Lett. **114** (2015) 191803, ISSN: 1079-7114, arXiv: `1503.07589 [hep-ex]`.

[29] *LEP design report*, Copies shelved as reports in LEP, PS and SPS libraries, CERN, 1984, URL: `https://cds.cern.ch/record/102083`.

[30] ALEPH Collaboration et al., *Electroweak Measurements in Electron-Positron Collisions at W-Boson-Pair Energies at LEP*, Phys. Rep. **532** (2013) 119, ISSN: 0370-1573, arXiv: `1302.3415 [hep-ex]`.

[31] CDF and D0 Collaborations, *Combination of CDF and D0 W-Boson mass measurements*, Phys. Rev. D **88** (2013) 052018, ISSN: 1550-2368, arXiv: `1307.7627 [hep-ex]`.

[32] ALEPH Collaboration et al., *Precision electroweak measurements on the Z resonance*, Phys. Rep. **427** (2006) 257, ISSN: 0370-1573, arXiv: `hep-ex/0509008 [hep-ex]`.

[33] ALEPH Collaboration, *ALEPH: A detector for electron-positron annihilations at LEP*, Nucl. Instrum. Meth. A **294** (1990) 121, ISSN: 0168-9002.

[34] ALEPH Collaboration, *Performance of the ALEPH detector at LEP*, Nucl. Instrum. Meth. A **360** (1995) 481, ISSN: 0168-9002.

[35] DELPHI Collaboration, *The DELPHI detector at LEP*, Nucl. Instrum. Meth. A **303** (1991) 233, ISSN: 0168-9002.

[36] DELPHI Collaboration, *Performance of the DELPHI detector*, Nucl. Instrum. Meth. A **378** (1996) 57, ISSN: 0168-9002.

[37] L3 Collaboration, *The construction of the L3 experiment*, Nucl. Instrum. Meth. A **289** (1990) 35, ISSN: 0168-9002.

[38] M. Chemarin et al., *Test beam results for an upgraded forward tagger of the L3 experiment at LEP II*, Nucl. Instrum. Meth. A **349** (1994) 345, ISSN: 0168-9002.

[39] M. Acciarri et al., *The L3 silicon microvertex detector*, Nucl. Instrum. Meth. A **351** (1994) 300, ISSN: 0168-9002.

[40] A. Adam et al., *The forward muon detector of L3*, Nucl. Instrum. Meth. A **383** (1996) 342, ISSN: 0168-9002.

[41] OPAL Collaboration, *The OPAL detector at LEP*, Nucl. Instrum. Meth. A **305** (1991) 275, ISSN: 0168-9002.

[42] OPAL Collaboration, *The OPAL silicon microvertex detector*, Nucl. Instrum. Meth. A **324** (1993) 34, ISSN: 0168-9002.

[43] OPAL Collaboration, *The OPAL silicon strip microvertex detector with two coordinate readout*, Nucl. Instrum. Meth. A **346** (1994) 476, ISSN: 0168-9002.

[44] OPAL Collaboration, *The OPAL silicon-tungsten calorimeter front end electronics*, IEEE Trans. Nucl. Sci. **41** (1994) 845, ISSN: 1558-1578.

[45] M. Gell-Mann, *A schematic model of baryons and mesons*, Phys. Lett. **8** (1964) 214, ISSN: 0031-9163.

[46] G. Zweig, *An SU_3 model for strong interaction symmetry and its breaking; Version 1*, tech. rep. CERN-TH-401, CERN, 1964, URL: `https://cds.cern.ch/record/352337`.

[47] J. Ellis, *Beyond the Standard Model for Hillwalkers*, 1998, arXiv: `hep-ph/9812235 [hep-ph]`.

[48] J. Ellis, *Limits of the Standard Model*, 2002, arXiv: `hep-ph/0211168 [hep-ph]`.

[49] D. I. Kazakov, *Beyond the Standard Model (In Search of Supersymmetry)*, 2000, arXiv: `hep-ph/0012288 [hep-ph]`.

[50] N. E. Pettersson, *R-Parity Violating SUSY Results from ATLAS and CMS*, tech. rep. ATL-PHYS-PROC-2015-198, CERN, 2015, URL: `https://cds.cern.ch/record/2117091`.

[51] L. Evans and P. Bryant, *LHC Machine*, JINST **3** (2008) S08001.

[52] C. Borschensky et al., *Squark and gluino production cross sections in pp collisions at $\sqrt{s} = 13, 14, 33$ and* 100 TeV, Eur. Phys. J. C **74** (2014) 3174, ISSN: 1434-6052, arXiv: `1407.5066 [hep-ph]`.

[53] CMS Collaboration, *The CMS experiment at the CERN LHC*, JINST **3** (2008) S08004.

[54] ATLAS Collaboration, *Search for squarks and gluinos in final states with hadronically decaying τ-leptons, jets, and missing transverse momentum using pp collisions at $\sqrt{s} = 13$ TeV with the ATLAS detector*, Phys. Rev. D **99** (2019) 012009, ISSN: 2470-0029, arXiv: `1808.06358 [hep-ex]`.

[55] ATLAS Collaboration, *Search for new phenomena using the invariant mass distribution of same-flavour opposite-sign dilepton pairs in events with missing transverse momentum in $\sqrt{s} = 13$ TeV pp collisions with the ATLAS detector*, Eur. Phys. J. C **78** (2018) 625, ISSN: 1434-6052, arXiv: `1805.11381 [hep-ex]`.

[56] ATLAS Collaboration, *Search for photonic signatures of gauge-mediated supersymmetry in 13 TeV pp collisions with the ATLAS detector*, Phys. Rev. D **97** (2018) 092006, ISSN: 2470-0029, arXiv: `1802.03158 [hep-ex]`.

[57] ATLAS Collaboration, *Search for squarks and gluinos in final states with jets and missing transverse momentum using* 36 *fb*$^{-1}$ *of* $\sqrt{s} = 13$ TeV *pp collision data with the ATLAS detector*, Phys. Rev. D **97** (2018) 112001, ISSN: 2470-0029, arXiv: `1712.02332 [hep-ex]`.

[58] ATLAS Collaboration, *Search for supersymmetry in final states with missing transverse momentum and multiple b-jets in proton–proton collisions at* $\sqrt{s} =$ 13 TeV *with the ATLAS detector*, JHEP **06** (2018) 107, arXiv: `1711.01901 [hep-ex]`.

[59] ATLAS Collaboration, *Search for new phenomena with large jet multiplicities and missing transverse momentum using large-radius jets and flavour-tagging at ATLAS in* 13 TeV *pp collisions*, JHEP **12** (2017) 034, arXiv: `1708.02794 [hep-ex]`.

[60] ATLAS Collaboration, *Search for supersymmetry in final states with two same-sign or three leptons and jets using* 36 *fb*$^{-1}$ *of* $\sqrt{s} = 13$ TeV *pp collision data with the ATLAS detector*, JHEP **09** (2017) 084, arXiv: `1706.03731 [hep-ex]`.

[61] CMS Collaboration, *Search for supersymmetry in multijet events with missing transverse momentum in proton–proton collisions at* 13 TeV, Phys. Rev. D **96** (2017) 032003, ISSN: 2470-0029, arXiv: `1704.07781 [hep-ex]`.

[62] CMS Collaboration, *Search for new phenomena with the* M_{T2} *variable in the all-hadronic final state produced in proton–proton collisions at* $\sqrt{s} = 13$ TeV, The Eur. Phys. J. C **77** (2017) 710, ISSN: 1434-6052, arXiv: `1705.04650 [hep-ex]`.

[63] CMS Collaboration, *Search for natural and split supersymmetry in proton–proton collisions at* $\sqrt{s} = 13$ TeV *in final states with jets and missing transverse momentum*, JHEP **05** (2018) 025, arXiv: `1802.02110 [hep-ex]`.

[64] CMS Collaboration, *Search for supersymmetry in proton–proton collisions at* 13 TeV *using identified top quarks*, Phys. Rev. D **97** (2018) 012007, arXiv: `1710.11188 [hep-ex]`.

[65] CMS Collaboration, *Search for physics beyond the standard Model in events with high-momentum Higgs bosons and missing transverse momentum in proton–proton collisions at* 13 TeV, Phys. Rev. Lett. **120** (2018) 241801, arXiv: `1712.08501 [hep-ex]`.

[66] CMS Collaboration, *Search for supersymmetry in events with a photon, a lepton, and missing transverse momentum in proton-proton collisions at* $\sqrt{s} = 13$ TeV, JHEP **2019** (2019) 154, ISSN: 1029-8479, arXiv: `1812.04066 [hep-ex]`.

[67] CMS Collaboration, *Inclusive search for supersymmetry in pp collisions at* $\sqrt{s} =$ 13 TeV *using razor variables and boosted object identification in zero and one lepton final states*, JHEP **2019** (2019) 31, ISSN: 1029-8479, arXiv: `1812.06302 [hep-ex]`.

[68] CMS Collaboration, *Search for supersymmetry in events with a photon, jets, b-jets, and missing transverse momentum in proton–proton collisions at 13 TeV*, Eur. Phys. J. C **79** (2019) 444, ISSN: 1434-6052, arXiv: `1901.06726 [hep-ex]`.

[69] CMS Collaboration, *Search for supersymmetry in final states with photons and missing transverse momentum in proton-proton collisions at 13 TeV*, JHEP **2019** (2019) 143, ISSN: 1029-8479, arXiv: 1903.07070 [hep-ex].

[70] CMS Collaboration, *Search for supersymmetry in proton-proton collisions at 13 TeV in final states with jets and missing transverse momentum*, JHEP **2019** (2019) 244, ISSN: 1029-8479, arXiv: 1908.04722 [hep-ex].

[71] J. Alwall et al., *Simplified models for a first characterization of new physics at the LHC*, Phys. Rev. D **79** (2009) 075020, ISSN: 1550-2368, arXiv: 0810.3921 [hep-ph].

[72] D. Alves et al., *Simplified models for LHC new physics searches*, J. Phys. G **39** (2012) 105005, arXiv: 1105.2838 [hep-ph].

[73] ATLAS Collaboration, *ATLAS Experiment - Public Results Supersymmetry Searches*, URL: https://twiki.cern.ch/twiki/bin/view/AtlasPublic/SupersymmetryPublicResults.

[74] ATLAS Collaboration, *Search for direct chargino pair production with W-boson mediated decays in events with two leptons and missing transverse momentum at $\sqrt{s} = 13$ TeV with the ATLAS detector*, tech. rep. ATLAS-CONF-2018-042, CERN, 2018, URL: https://cds.cern.ch/record/2632578.

[75] ATLAS Collaboration, *Search for direct production of charginos, neutralinos and sleptons in final states with two leptons and missing transverse momentum in pp collisions at* $\sqrt{s} = 8$ TeV *with the ATLAS detector*, JHEP **05** (2014) 71, arXiv: 1403.5294 [hep-ex].

[76] ATLAS Collaboration, *Search for electroweak production of supersymmetric particles in final states with two or three leptons at* $\sqrt{s} = 13$ TeV *with the ATLAS detector*, Eur. Phys. J. C **78** (2018) 995, arXiv: 1803.02762 [hep-ex].

[77] CMS Collaboration, *Searches for electroweak production of charginos, neutralinos, and sleptons decaying to leptons and W, Z, and Higgs bosons in pp collisions at* 8 TeV, Eur. Phys. J. C **74** (2014) 3036, arXiv: 1405.7570 [hep-ex].

[78] CMS Collaboration, *Searches for electroweak neutralino and chargino production in channels with Higgs, Z, and W bosons in pp collisions at* 8 TeV, Phys. Rev. D **90** (2014) 092007, arXiv: 1409.3168 [hep-ex].

[79] CMS Collaboration, *Search for electroweak production of charginos and neutralinos in multilepton final states in proton–proton collisions at* $\sqrt{s} = 13$ TeV, JHEP **03** (2018) 166, arXiv: 1709.05406 [hep-ex].

[80] CMS Collaboration, *Combined search for electroweak production of charginos and neutralinos in proton–proton collisions at* $\sqrt{s} = 13$ TeV, JHEP **03** (2018) 160, arXiv: 1801.03957 [hep-ex].

[81] CMS Collaboration, *Search for supersymmetric partners of electrons and muons in proton–proton collisions at* $\sqrt{s} = 13$ TeV, Phys. Lett. B **790** (2019) 140, arXiv: 1806.05264 [hep-ex].

[82] CMS Collaboration, *Searches for pair production of charginos and top squarks in final states with two oppositely charged leptons in proton–proton collisions at* $\sqrt{s} = 13$ TeV, JHEP **11** (2018) 079, arXiv: 1807.07799 [hep-ex].

[83] ATLAS Collaboration, *SUSY October 2019 Summary Plot Update*, tech. rep. ATL-PHYS-PUB-2019-044, CERN, 2019, URL: http://cds.cern.ch/record/2697155.

[84] ATLAS Collaboration, *Constraints on mediator-based dark matter and scalar dark energy models using* $\sqrt{s} = 13$ TeV *pp collision data collected by the ATLAS detector*, JHEP **2019** (2019) 142, ISSN: 1029-8479, arXiv: 1903.01400 [hep-ex].

[85] C. De Melis, *Timeline for the LHC and High-Luminosity LHC*, (2015), URL: https://cds.cern.ch/record/2063307.

[86] *CERN Accelerator Complex*, URL: https://te-epc-lpc.web.cern.ch/te-epc-lpc/machines/pagesources/Cern-Accelerator-Complex.jpg.

[87] D. Inaudi et al., *Displacement measurements in the cryogenically cooled dipoles of the new CERN-LHC particle accelerator*, Proceedings of SPIE - The International Society for Optical Engineering **4328** (2001).

[88] ALICE Collaboration, *The ALICE experiment at the CERN LHC*, JINST **3** (2008) S08002.

[89] LHCb Collaboration, *The LHCb Detector at the LHC*, JINST **3** (2008) S08005.

[90] *LHC Machine Layout*, URL: https://lhc-machine-outreach.web.cern.ch/lhc-machine-outreach/images/lhc-schematic.jpg.

[91] ATLAS Collaboration, *ATLAS Experiment - Public Results Luminosity Public Results Run 2*, URL: https://twiki.cern.ch/twiki/bin/view/AtlasPublic/LuminosityPublicResultsRun2.

[92] ATLAS Collaboration, *ATLAS inner detector: Technical Design Report, 2*, CERN-LHCC-97-017, CERN, 1997, URL: http://cds.cern.ch/record/331064.

[93] ATLAS Collaboration, *Combined performance tests before installation of the ATLAS Semiconductor and Transition Radiation Tracking Detectors*, JINST **3** (2008) P08003.

[94] ATLAS Collaboration, *ATLAS pixel detector: Technical Design Report*, CERN-LHCC-98-013, CERN, 1998, URL: http://cds.cern.ch/record/381263.

[95] ATLAS Collaboration, *ATLAS pixel detector electronics and sensors*, JINST **3** (2008) P07007.

[96] ATLAS Collaboration, *ATLAS Insertable B-Layer Technical Design Report*, tech. rep. CERN-LHCC-2010-013. ATLAS-TDR-19, 2010, URL: https://cds.cern.ch/record/1291633.

[97] ATLAS Collaboration, *IBL Efficiency and Single Point Resolution in Collision Events*, tech. rep. ATL-INDET-PUB-2016-001, CERN, 2016, URL: http://cds.cern.ch/record/2203893.

[98] ATLAS Collaboration, *Reconstruction of primary vertices at the ATLAS experiment in Run 1 proton–proton collisions at the LHC*, Eur. Phys. J. C **77** (2017) 332, ISSN: 1434-6052.

[99] J. R. Pater, *The ATLAS SemiConductor Tracker operation and performance*, JINST **7** (2012) C04001.

[100] ATLAS collaboration, *Operation and performance of the ATLAS semiconductor tracker*, JINST **9** (2014) P08009.

[101] A. Abdesselam et al., *The ATLAS semiconductor tracker end-cap module*, Nucl. Instrum. Meth. A **575** (2007) 353, ISSN: 0168-9002.

[102] ATLAS Collaboration, *The ATLAS Transition Radiation Tracker (TRT) proportional drift tube: design and performance*, JINST **3** (2008) P02013.

[103] ATLAS Collaboration, *Performance of the ATLAS Transition Radiation Tracker in Run 1 of the LHC: tracker properties*, JINST **12** (2017) P05002.

[104] ATLAS Collaboration, *ATLAS calorimeter performance: Technical Design Report*, CERN-LHCC-96-040, CERN, 1996, URL: http://cds.cern.ch/record/331059.

[105] B. Aubert et al., *Construction, assembly and tests of the ATLAS electromagnetic barrel calorimeter*, Nucl. Instrum. Meth. A **558** (2006) 388, ISSN: 0168-9002.

[106] ATLAS Electromagnetic Liquid Argon Group, *Construction, assembly and tests of the ATLAS electromagnetic end-cap calorimeters*, JINST **3** (2008) P06002.

[107] ATLAS Collaboration, *ATLAS tile calorimeter: Technical Design Report*, CERN-LHCC-96-042, CERN, 1996, URL: http://cds.cern.ch/record/331062.

[108] D. M. Gingrich, *Construction, assembly and testing of the ATLAS hadronic end-cap calorimeter*, JINST **2** (2007) P05005.

[109] A. Artamonov et al., *The ATLAS Forward Calorimeter*, JINST **3** (2008) P02010.

[110] ATLAS Collaboration, *ATLAS muon spectrometer: Technical Design Report*, CERN-LHCC-97-022, CERN, 1997, URL: http://cds.cern.ch/record/331068.

[111] J. Wotschack, *ATLAS Muon Chamber Construction Parameters for CSC, MDT and RPC chambers*, tech. rep. ATL-MUON-PUB-2008-006. ATL-COM-MUON-2008-008, CERN, 2008, URL: http://cds.cern.ch/record/1099400.

[112] ATLAS Collaboration, *ATLAS high-level trigger, data-acquisition and controls: Technical Design Report*, CERN-LHCC-2003-022, CERN, 2003, URL: https://cds.cern.ch/record/616089.

[113] ATLAS Collaboration, *2015 start-up trigger menu and initial performance assessment of the ATLAS trigger using Run-2 data*, tech. rep. ATL-DAQ-PUB-2016-001, CERN, 2016, URL: https://cds.cern.ch/record/2136007.

[114] R. Martínez, *The Run-2 ATLAS Trigger System*, J. Phys. Conf. Ser. **762** (2016) 012003.

[115] G. Avoni et al., *The new LUCID-2 detector for luminosity measurement and monitoring in ATLAS*, JINST **13** (2018) P07017.

[116] P. Jenni et al., *ATLAS Forward Detectors for Measurement of Elastic Scattering and Luminosity*, Technical Design Report ATLAS CERN-LHCC-2008-004, CERN, 2008, URL: http://cds.cern.ch/record/1095847.

[117] ATLAS Collaboration, *Zero Degree Calorimeters for ATLAS*, tech. rep. CERN-LHCC-2007-001. LHCC-I-016, CERN, 2007, URL: http://cds.cern.ch/record/1009649.

[118] M. Červ, *The ATLAS Diamond Beam Monitor*, JINST **9** (2014) C02026.

[119] V. Cindro et al., *The ATLAS Beam Conditions Monitor*, JINST **3** (2008) P02004.

[120] I. Dolenc, "The ATLAS Beam Condition and Beam Loss Monitors", *Astroparticle, Particle, Space Physics, Radiation Interaction, Detectors and Medical Physics Applications - Proceedings of the 11th Conference*, 2010 443, URL: https://www.worldscientific.com/doi/abs/10.1142/9789814307529_0073.

[121] T. Kawamoto et al., *New Small Wheel Technical Design Report*, tech. rep. CERN-LHCC-2013-006. ATLAS-TDR-020, 2013, URL: https://cds.cern.ch/record/1552862.

[122] S. Majewski et al., *A thin multiwire chamber operating in the high multiplication mode*, Nucl. Instrum. Meth. Phys. Res. **217** (1983) 265, ISSN: 0167-5087.

[123] V. Smakhtin et al., *Thin Gap Chamber upgrade for SLHC: Position resolution in a test beam*, Nucl. Instrum. Meth. A **598** (2009) 196, ISSN: 0168-9002.

[124] Y. Giomataris et al., *MICROMEGAS: a high-granularity position-sensitive gaseous detector for high particle-flux environments*, Nucl. Instrum. Meth. A **376** (1996) 29, ISSN: 0168-9002.

[125] ATLAS Collaboration, *ATLAS technical coordination: Technical Design Report*, CERN-LHCC-99-001, CERN, 1999, URL: https://cds.cern.ch/record/385482.

[126] T. Alexopoulos et al., *Construction techniques and performances of a full-size prototype Micromegas chamber for the ATLAS muon spectrometer upgrade*, Nucl. Instrum. Meth. A **955** (2020) 162086, ISSN: 0168-9002.

[127] T. Alexopoulos et al., *A spark-resistant bulk-micromegas chamber for high-rate applications*, Nucl. Instrum. Meth. A **640** (2011) 110, ISSN: 0168-9002.

[128] O. Atsuhiko, *Development of large area resistive electrodes for ATLAS NSW Micromegas*, EPJ Web Conf. **174** (2018) 03001, URL: https://doi.org/10.1051/epjconf/201817403001.

[129] J. Wotschack, *The development of large-area micromegas detectors for the ATLAS upgrade*, Mod. Phys. Lett. A **28** (2013) 1340020.

[130] M. Bianco et al., *Construction of two large-size four-plane micromegas detectors*, Nucl. Instrum. Meth. A **814** (2016) 117, ISSN: 0168-9002.

[131] G. De Geronimo et al., *VMM1 - An ASIC for Micropattern Detectors*, IEEE Trans. Nucl. Sci. **60** (2013) 2314, ISSN: 1558-1578.

[132] M. J. French et al., *Design and results from the APV25, a deep sub-micron CMOS front-end chip for the CMS tracker*, Nucl. Instrum. Meth. A **466** (2001) 359, ISSN: 0168-9002.

[133] S. Martoiu et al., "Front-end electronics for the Scalable Readout System of RD51", *2011 IEEE Nuclear Science Symposium Conference Record*, 2011 2036, URL: https://doi.org/10.1109/NSSMIC.2011.6154414.

[134] A. Gerbershagen and B. Rae, *The H8 Secondary Beam Line of EHN1/SPS*, URL: http://sba.web.cern.ch/sba/BeamsAndAreas/H8/H8_presentation.html.

[135] G. Iakovidis, *VMM3, an ASIC for Micropattern Detectors*, tech. rep. ATL-MUON-PROC-2018-003, CERN, 2018, URL: https://cds.cern.ch/record/2309951.

[136] G. De Geronimo and S. Li, *Shaper Design in CMOS for High Dynamic Range*, IEEE Trans. Nucl. Sci. **58** (2011) 2382, ISSN: 1558-1578.

[137] Gagnon L.-G., *Development and performance of track reconstruction algorithms at the energy frontier with the ATLAS detector*, J. Phys. Conf. Ser. **898** (2017) 042007.

[138] R. Frühwirth, *Application of Kalman filtering to track and vertex fitting*, Nucl. Instrum. Meth. A **262** (1987) 444, ISSN: 0168-9002.

[139] S. Boutle et al., *Primary vertex reconstruction at the ATLAS experiment*, J. Phys. Conf. Ser. **898** (2017) 042056.

[140] ATLAS Collaboration, *Electron and photon performance measurements with the ATLAS detector using the 2015-2017 LHC proton-proton collision data*, JINST **14** (2019) P12006, arXiv: 1908.00005 [hep-ex].

[141] ATLAS Collaboration, *Electron reconstruction and identification in the ATLAS experiment using the 2015 and 2016 LHC proton-proton collision data at* $\sqrt{s} =$ 13 TeV, Eur. Phys. J. C **79** (2019) 639, arXiv: 1902.04655 [physics.ins-det].

[142] ATLAS Collaboration, *Measurement of the photon identification efficiencies with the ATLAS detector using LHC Run 2 data collected in 2015 and 2016*, Eur. Phys. J. C **79** (2019) 205, ISSN: 1434-6052, arXiv: 1810.05087 [hep-ex].

[143] W. Lampl et al., *Calorimeter Clustering Algorithms: Description and Performance*, tech. rep. ATL-LARG-PUB-2008-002. ATL-COM-LARG-2008-003, CERN, 2008, URL: https://cds.cern.ch/record/1099735.

[144] ATLAS Collaboration, *Electron and photon energy calibration with the ATLAS detector using 2015-2016 LHC proton-proton collision data*, JINST **14** (2019) P03017, arXiv: 1812.03848 [hep-ex].

[145] ATLAS Collaboration, *Topological cell clustering in the ATLAS calorimeters and its performance in LHC Run 1*, Eur. Phys. J. C **77** (2017) 490, ISSN: 1434-6052, arXiv: 1603.02934 [hep-ex].

[146] T. Cornelissen et al., *Concepts, Design and Implementation of the ATLAS New Tracking (NEWT)*, tech. rep. ATL-SOFT-PUB-2007-007. ATL-COM-SOFT-2007-002, CERN, 2007, URL: http://cds.cern.ch/record/1020106.

[147] T. G. Cornelissen et al., *The global* χ^2 *track fitter in ATLAS*, J. Phys. Conf. Ser. **119** (2008) 032013.

[148] ATLAS Collaboration, *Improved electron reconstruction in ATLAS using the Gaussian Sum Filter-based model for bremsstrahlung*, tech. rep. ATLAS-CONF-2012-047, CERN, 2012, URL: http://cds.cern.ch/record/1449796.

[149] ATLAS Collaboration, *Measurement of the muon reconstruction performance of the ATLAS detector using 2011 and 2012 LHC proton–proton collision data*, Eur. Phys. J. C **74** (2014) 3130, ISSN: 1434-6052, arXiv: 1407.3935 [hep-ex].

[150] ATLAS Collaboration, *Muon reconstruction performance of the ATLAS detector in proton–proton collision data at* $\sqrt{s} = 13$ TeV, Eur. Phys. J. C **76** (2016) 292, ISSN: 1434-6052, arXiv: 1603.05598 [hep-ex].

[151] ATLAS Collaboration, *Muon identification and reconstruction efficiencies in full run-2 dataset*, URL: https://atlas.web.cern.ch/Atlas/GROUPS/PHYSICS/PLOTS/MUON-2019-03/index.html.

[152] ATLAS Collaboration, *Topological cell clustering in the ATLAS calorimeters and its performance in LHC Run 1*, Eur. Phys. J. C **77** (2016) 490, arXiv: 1603.02934 [hep-ex].

[153] M. Cacciari et al., *The anti-*k_t *jet clustering algorithm*, JHEP **04** (2008) 063, arXiv: 0802.1189 [hep-ph].

[154] ATLAS Collaboration, *Jet energy scale measurements and their systematic uncertainties in proton-proton collisions at* $\sqrt{s} = 13$ TeV *with the ATLAS detector*, Phys. Rev. D **96** (2017) 072002, arXiv: 1703.09665 [hep-ex].

[155] M. Cacciari and G. P. Salam, *Pileup subtraction using jet areas*, Phys. Lett. B **659** (2008) 119, ISSN: 0370-2693, arXiv: 0707.1378 [hep-ph].

[156] ATLAS Collaboration, *Tagging and suppression of pileup jets with the ATLAS detector*, tech. rep. ATLAS-CONF-2014-018, CERN, 2014, URL: http://cds.cern.ch/record/1700870.

[157] ATLAS Collaboration, *Identification and rejection of pile-up jets at high pseudorapidity with the ATLAS detector*, Eur. Phys. J. C **77** (2017) 580, ISSN: 1434-6052, arXiv: 1705.02211 [hep-ex].

[158] ATLAS Collaboration, *Optimisation of the ATLAS b-tagging performance for the 2016 LHC Run*, tech. rep. ATL-PHYS-PUB-2016-012, CERN, 2016, URL: https://cds.cern.ch/record/2160731.

[159] ATLAS Collaboration, *Performance of b-jet identification in the ATLAS experiment*, JINST **11** (2016) P04008, arXiv: 1512.01094 [hep-ex].

[160] A. Hoecker et al., *TMVA: Toolkit for Multivariate Data Analysis*, PoS **ACAT** (2007) 040, arXiv: physics/0703039 [physics.data-an].

[161] ATLAS Collaboration, *ATLAS b-jet identification performance and efficiency measurement with $t\bar{t}$ events in pp collisions at $\sqrt{s} = 13$ TeV*, Eur. Phys. J. C **79** (2019) 970, ISSN: 1434-6052, arXiv: 1907.05120 [hep-ex].

[162] ATLAS Collaboration, *Optimisation and performance studies of the ATLAS b-tagging algorithms for the 2017-18 LHC run*, tech. rep. ATL-PHYS-PUB-2017-013, CERN, 2017, URL: https://cds.cern.ch/record/2273281.

[163] ATLAS Collaboration, *Performance of missing transverse momentum reconstruction with the ATLAS detector using proton–proton collisions at $\sqrt{s} =$ 13 TeV*, Eur. Phys. J. C **78** (2018) 903, ISSN: 1434-6052, arXiv: 1802.08168 [hep-ex].

[164] ATLAS Collaboration, *Object-based missing transverse momentum significance in the ATLAS detector*, tech. rep. ATLAS-CONF-2018-038, CERN, 2018, URL: https://cds.cern.ch/record/2630948.

[165] ATLAS Collaboration, *Trigger Menu in 2017*, tech. rep. ATL-DAQ-PUB-2018-002, CERN, 2018, URL: http://cds.cern.ch/record/2625986.

[166] A. Roodman, "Blind Analysis in Particle Physics", *Proceedings of the Conference on Statistical Problems in Particle Physics, Astrophysics and Cosmology*, 2003 166, arXiv: physics/0312102 [physics.data-an], URL: http://www.slac.stanford.edu/econf/C030908.

[167] ATLAS Collaboration, *Selection of jets produced in 13 TeV proton-proton collisions with the ATLAS detector*, tech. rep. ATLAS-CONF-2015-029, CERN, 2015, URL: https://cds.cern.ch/record/2037702.

[168] J. C. Collins and D. E. Soper, *The Theorems of Perturbative QCD*, Annual Review of Nuclear and Particle Science **37** (1987) 383.

[169] P. Skands, *QCD for Collider Physics*, Lectures from the 2010 European School of High Energy Physics, Raseborg, Finland (2011), arXiv: 1104.2863 [hep-ph].

[170] S. Agostinelli et al., *GEANT4: A Simulation toolkit*, Nucl. Instrum. Meth. A **506** (2002) 250.

[171] ATLAS Collaboration, *The simulation principle and performance of the ATLAS fast calorimeter simulation FastCaloSim*, tech. rep. ATL-PHYS-PUB-2010-013, CERN, 2010, URL: https://cds.cern.ch/record/1300517.

[172] K. Edmonds et al., *The Fast ATLAS Track Simulation (FATRAS)*, tech. rep. ATL-SOFT-PUB-2008-001. ATL-COM-SOFT-2008-002, CERN, 2008, URL: http://cds.cern.ch/record/1091969.

[173] J. Alwall et al., *The automated computation of tree-level and next-to-leading order differential cross sections, and their matching to parton shower simulations*, JHEP **07** (2014) 079, arXiv: 1405.0301 [hep-ph].

[174] T. Sjöstrand et al., *A brief introduction to PYTHIA 8.1*, Comp. Phys. Comm. **178** (2008) 852, arXiv: 0710.3820 [hep-ph].

[175] ATLAS Collaboration, *ATLAS Run 1 Pythia8 tunes*, tech. rep. ATL-PHYS-PUB-2014-021, CERN, 2014, URL: https://cds.cern.ch/record/1966419.

[176] Z. Nagy and D. E. Soper, *What is a parton shower?*, Phys. Rev. D **98** (2018) 014034, ISSN: 2470-0029, arXiv: 1705.08093 [hep-ph].

[177] R. D. Ball et al., *Parton distributions with LHC data*, Nucl. Phys. B **867** (2013) 244, arXiv: 1207.1303 [hep-ph].

[178] L. Lönnblad and S. Prestel, *Merging multi-leg NLO matrix elements with parton showers*, JHEP **03** (2013) 166, arXiv: 1211.7278 [hep-ph].

[179] J. Debove et al., *Threshold resummation for gaugino pair production at hadron colliders*, Nucl. Phys. B **842** (2011) 51, arXiv: 1005.2909 [hep-ph].

[180] B. Fuks et al., *Gaugino production in proton-proton collisions at a center-of-mass energy of 8 TeV*, JHEP **10** (2012) 081, arXiv: 1207.2159 [hep-ph].

[181] B. Fuks et al., *Precision predictions for electroweak superpartner production at hadron colliders with RESUMMINO*, Eur. Phys. J. C **73** (2013) 2480, arXiv: 1304.0790 [hep-ph].

[182] J. Fiaschi and M. Klasen, *Neutralino-chargino pair production at NLO+NLL with resummation-improved parton density functions for LHC Run II*, Phys. Rev. D **98** (2018) 055014, arXiv: 1805.11322 [hep-ph].

[183] G. Bozzi et al., *Threshold resummation for slepton-pair production at hadron colliders*, Nucl. Phys. B **777** (2007) 157, arXiv: hep-ph/0701202 [hep-ph].

[184] B. Fuks et al., *Revisiting slepton pair production at the Large Hadron Collider*, JHEP **01** (2014) 168, arXiv: 1310.2621 [hep-ph].

[185] J. Fiaschi and M. Klasen, *Slepton pair production at the LHC in NLO+NLL with resummation-improved parton densities*, JHEP **03** (2018) 094, arXiv: 1801.10357 [hep-ph].

[186] C. Borschensky et al., *Squark and gluino production cross sections in pp collisions at* $\sqrt{s} = 13, 14, 33$ *and* 100 TeV, Eur. Phys. J. C **74** (2014) 3174, arXiv: 1407.5066 [hep-ph].

[187] R. Gavin et al., *FEWZ 2.0: A code for hadronic Z production at next-to-next-to-leading order*, Comp. Phys. Comm. **182** (2011) 2388, arXiv: 1011.3540 [hep-ph].

[188] S. Frixione et al., *A positive-weight next-to-leading-order Monte Carlo for heavy flavour hadroproduction*, JHEP **09** (2007) 126, arXiv: 0707.3088 [hep-ph].

[189] S. Frixione et al., *Matching NLO QCD computations with Parton Shower simulations: the POWHEG method*, JHEP **11** (2007) 070, arXiv: 0709.2092 [hep-ph].

[190] S. Alioli et al., *A general framework for implementing NLO calculations in shower Monte Carlo programs: the POWHEG BOX*, JHEP **06** (2010) 043, arXiv: 1002.2581 [hep-ph].

[191] J. M. Campbell et al., *Top-pair production and decay at NLO matched with parton showers*, JHEP **04** (2015) 114, arXiv: 1412.1828 [hep-ph].

[192] T. Sjöstrand et al., *An Introduction to PYTHIA 8.2*, Comp. Phys. Comm. **191** (2015) 159, arXiv: 1410.3012 [hep-ph].

[193] M. Czakon and A. Mitov, *Top++: A program for the calculation of the top-pair cross-section at hadron colliders*, Comp. Phys. Comm. **185** (2014) 2930, arXiv: 1112.5675 [hep-ph].

[194] R. D. Ball et al., *Parton distributions for the LHC Run II*, JHEP **04** (2015) 040, arXiv: 1410.8849 [hep-ph].

[195] ATLAS Collaboration, *Modelling of the $t\bar{t}H$ and $t\bar{t}V$ $(V = W, Z)$ processes for $\sqrt{s} = 13$ TeV ATLAS analyses*, tech. rep. ATL-PHYS-PUB-2016-005, CERN, 2016, URL: https://cds.cern.ch/record/2120826.

[196] E. Re, *Single-top Wt-channel production matched with parton showers using the POWHEG method*, Eur. Phys. J. C **71** (2011) 1547, arXiv: 1009.2450 [hep-ph].

[197] M. Aliev et al., *HATHOR - HAdronic Top and Heavy quarks crOss section calculatoR*, Comp. Phys. Comm. **182** (2011) 1034, arXiv: 1007.1327 [hep-ph].

[198] P. Kant et al., *HATHOR for single top-quark production: Updated predictions and uncertainty estimates for single top-quark production in hadronic collisions*, Comp. Phys. Comm. **191** (2015) 74, arXiv: 1406.4403 [hep-ph].

[199] T. Gleisberg et al., *Event generation with SHERPA 1.1*, JHEP **02** (2009) 007, arXiv: 0811.4622 [hep-ph].

[200] E. Bothmann et al., *Event Generation with Sherpa 2.2*, SciPost Phys. **7** (3 2019) 34, arXiv: 1905.09127 [hep-ph].

[201] ATLAS Collaboration, *Monte Carlo Generators for the Production of a W or Z/γ^* Boson in Association with Jets at ATLAS in Run 2*, tech. rep. ATL-PHYS-PUB-2016-003, CERN, 2016, URL: https://cds.cern.ch/record/2120133.

[202] T. Melia et al., *W^+W^-, WZ and ZZ production in the POWHEG BOX*, JHEP **11** (2011) 078, arXiv: 1107.5051 [hep-ph].

[203] P. Nason and G. Zanderighi, *W^+W^- , WZ and ZZ production in the POWHEG-BOX-V2*, Eur. Phys. J. C **74** (2014) 2702, arXiv: 1311.1365 [hep-ph].

[204] ATLAS Collaboration, *Multi-Boson Simulation for 13 TeV ATLAS Analyses*, tech. rep. ATL-PHYS-PUB-2017-005, CERN, 2017, URL: https://cds.cern.ch/record/2261933.

[205] ATLAS Collaboration, *Measurement of the Z/γ^* boson transverse momentum distribution in pp collisions at $\sqrt{s} = 7$ TeV with the ATLAS detector*, JHEP **09** (2014) 145, arXiv: 1406.3660 [hep-ex].

[206] H.-L. Lai et al., *New parton distributions for collider physics*, Phys. Rev. D **82** (2010) 074024, arXiv: 1007.2241 [hep-ph].

[207] J. Pumplin et al., *New generation of parton distributions with uncertainties from global QCD analysis*, JHEP **07** (2002) 012, arXiv: hep-ph/0201195 [hep-ph].

[208] S. Alioli et al., *NLO Higgs boson production via gluon fusion matched with shower in POWHEG*, JHEP **04** (2009) 002, arXiv: 0812.0578 [hep-ph].

[209] P. Nason and Oleari C., *NLO Higgs boson production via vector-boson fusion matched with shower in POWHEG*, JHEP **1002** (2010) 037, arXiv: 0911.5299 [hep-ph].

[210] K. Hamilton et al., *NNLOPS simulation of Higgs boson production*, JHEP **1310** (2013) 222, arXiv: 1309.0017 [hep-ph].

[211] K. Hamilton et al., *Finite quark-mass effects in the NNLOPS POWHEG+MiNLO Higgs generator*, JHEP **1505** (2015) 140, arXiv: 1501.04637 [hep-ph].

[212] D. de Florian et al., *Handbook of LHC Higgs Cross Sections: 4. Deciphering the nature of the Higgs sector*, CERN-2017-002-M (2017), arXiv: 1610.07922 [hep-ph].

[213] ATLAS Collaboration, *Summary plots from the ATLAS Standard Model physics group*, URL: https://atlas.web.cern.ch/Atlas/GROUPS/PHYSICS/CombinedSummaryPlots/SM/index.html.

[214] ATLAS Collaboration, *E_T^{miss} performance in the ATLAS detector using 2015-2016 LHC p-p collisions*, tech. rep. ATLAS-CONF-2018-023, CERN, 2018, URL: https://cds.cern.ch/record/2625233.

[215] G. Cowan, *Statistical Data Analysis*, Oxford University Press, 1998, ISBN: 0198501552.

[216] R. D. Cousins et al., *Evaluation of three methods for calculating statistical significance when incorporating a systematic uncertainty into a test of the background-only hypothesis for a Poisson process*, Nucl. Instrum. Meth. A **595** (2008) 480, arXiv: physics/0702156 [physics.data-an].

[217] C. Tao, *The UA1 Experiment*, Int. J. Mod. Phys. A **01** (1986) 749.

[218] UA1 Collaboration, *Experimental observation of isolated large transverse energy electrons with associated missing energy at s=540 GeV*, Phys. Lett. B **122** (1983) 103, ISSN: 0370-2693.

[219] C. G. Lester and D. J. Summers, *Measuring masses of semi-invisibly decaying particles pair produced at hadron colliders*, Phys. Lett. B **463** (1999) 99, arXiv: hep-ph/9906349 [hep-ph].

[220] A. Barr et al., *A variable for measuring masses at hadron colliders when missing energy is expected; m_{T2}: the truth behind the glamour*, J. Phys. G **29** (2003) 2343, arXiv: hep-ph/0304226 [hep-ph].

[221] D. Kim and K. Kong, *Kinematic discrimination of tW and $t\bar{t}$ productions using initial state radiation*, Phys. Lett. B **751** (2015) 512, arXiv: 1503.03872 [hep-ph].

[222] A. L. Read, *Presentation of search results: the CL_S technique*, J. Phys. G **28** (2002) 2693.

[223] ATLAS Collaboration, *Measurement of the top quark-pair production cross section with ATLAS in pp collisions at $\sqrt{s}$ = 7 TeV*, Eur. Phys. J. C **71** (2011) 1577, arXiv: 1012.1792 [hep-ex].

[224] M. Baak et al., *HistFitter software framework for statistical data analysis*, Eur. Phys. J. C **75** (2015) 153, ISSN: 1434-6052, arXiv: 1410.1280 [hep-ex].

[225] K. Cranmer et al., *HistFactory: A tool for creating statistical models for use with RooFit and RooStats*, tech. rep. CERN-OPEN-2012-016, 2012, URL: `https://cds.cern.ch/record/1456844`.

[226] L. Moneta et al., "The RooStats Project", *Proceedings of the 13th International Workshop of Advanced Computing and Analysis Techniques in Physics Research*, 2010 57, arXiv: `1009.1003 [physics.data-an]`.

[227] W. Verkerke and D. Kirkby, "The RooFit toolkit for data modelling", *Proceedings of the 13th International Conderence for Computing in High-Energy and Nuclear Physics*, 2003, arXiv: `physics/0306116 [physics.data-an]`, URL: `http://www.slac.stanford.edu/econf/C0303241`.

[228] R. Brun and F. Rademakers, *ROOT – An object oriented data analysis framework*, Nucl. Instrum. Meth. A **389** (1997) 81, ISSN: 0168-9002.

[229] I. Antcheva et al., *ROOT – A C++ framework for petabyte data storage, statistical analysis and visualization*, Comp. Phys. Comm. **182** (2011) 1384, ISSN: 0010-4655.

[230] G. Cowan et al., *Asymptotic formulae for likelihood-based tests of new physics*, Eur. Phys. J. C **71** (2011) 1554, ISSN: 1434-6052, arXiv: `1007.1727 [physics.data-an]`.

[231] ATLAS Collaboration, *Luminosity determination in pp collisions at $\sqrt{s} = 13$ TeV using the ATLAS detector at the LHC*, tech. rep. ATLAS-CONF-2019-021, CERN, 2019, URL: `https://cds.cern.ch/record/2677054`.

[232] ATLAS Collaboration, *Studies on top-quark Monte Carlo modelling for Top2016*, tech. rep. ATL-PHYS-PUB-2016-020, CERN, 2016, URL: `https://cds.cern.ch/record/2216168`.

[233] P. Artoisenet et al., *Automatic spin-entangled decays of heavy resonances in Monte Carlo simulations*, JHEP **03** (2013) 015, arXiv: `1212.3460 [hep-ph]`.

[234] S. Širca and M. Horvat, *Computational methods in physics: compendium for students; 2nd ed.* Springer, 2018, URL: `https://cds.cern.ch/record/2628681`.

[235] F. Chollet et al., *Keras*, 2015, URL: `https://keras.io`.

[236] Theano Development Team, *Theano: A Python framework for fast computation of mathematical expressions*, 2016, arXiv: `1605.02688 [cs.SC]`.

[237] D. P. Kingma and J. Ba, *Adam: A Method for Stochastic Optimization*, 2014, arXiv: `1412.6980 [cs.LG]`.

[238] Y. Freund and R. E. Schapire, *A Decision-Theoretic Generalization of On-Line Learning and an Application to Boosting*, J. Comp. Syst. Sc. **55** (1997) 119, ISSN: 0022-0000.

[239] T. Gleisberg and S. Höche, *Comix, a new matrix element generator*, JHEP **12** (2008) 039, arXiv: `0808.3674 [hep-ph]`.

[240] S. Schumann and F. Krauss, *A Parton shower algorithm based on Catani-Seymour dipole factorisation*, JHEP **03** (2008) 038, arXiv: `0709.1027 [hep-ph]`.

[241] S. Höche et al., *A critical appraisal of NLO+PS matching methods*, JHEP **09** (2012) 049, arXiv: `1111.1220 [hep-ph]`.

[242] S. Höche et al., *QCD matrix elements + parton showers. The NLO case*, JHEP **04** (2013) 027, arXiv: `1207.5030 [hep-ph]`.

[243] S. Catani et al., *QCD Matrix Elements + Parton Showers*, JHEP **11** (2001) 063, arXiv: hep-ph/0109231 [hep-ph].

[244] S. Höche et al., *QCD matrix elements and truncated showers*, JHEP **05** (2009) 053, arXiv: 0903.1219 [hep-ph].

[245] F. Cascioli et al., *Scattering Amplitudes with Open Loops*, Phys. Rev. Lett. **108** (2012) 111601, arXiv: 1111.5206 [hep-ph].

[246] A. Denner et al., *Collier: A fortran-based complex one-loop library in extended regularizations*, Comp. Phys. Comm. **212** (2017) 220, arXiv: 1604.06792 [hep-ph].

[247] A. J. Barr, *Measuring slepton spin at the LHC*, JHEP **2006** (2006) 042, arXiv: hep-ph/0511115 [hep-ph].

[248] V. Nair and G. E. Hinton, "Rectified Linear Units improve Restricted Boltzmann Machines", *Proceedings of the 27th International Conference on Machine Learning*, Omnipress, 2010 807, ISBN: 9781605589077, URL: https://dl.acm.org/doi/10.5555/3104322.3104425.

[249] X. Glorot and J. Bengio, "Understanding the difficulty of training deep feedforward neural networks", *Proceedings of the 13th International Conference on Artificial Intelligence and Statistics*, vol. 9, 2010 249, URL: http://proceedings.mlr.press/v9/glorot10a.html.

[250] I. Goodfellow et al., *Deep Learning*, MIT Press, 2016, URL: http://www.deeplearningbook.org.

[251] S. Ioffe and C. Szegedy, *Batch Normalization: Accelerating Deep Network Training by Reducing Internal Covariate Shift*, 2015, arXiv: 1502.03167 [cs.LG].

[252] K. Cranmer, "Statistical challenges for searches for new physics at the LHC", *Statistical Problems in Particle Physics, Astrophysics and Cosmology* 112, arXiv: physics/0511028 [physics.data-an], URL: https://www.worldscientific.com/doi/abs/10.1142/9781860948985_0026.

[253] J. T. Linnemann, "Measures of Significance in HEP and Astrophysics", *Proceedings of the Conference on Statistical Problems in Particle Physics, Astrophysics and Cosmology*, 2003 166, arXiv: physics/0312059 [physics.data-an], URL: http://www.slac.stanford.edu/econf/C030908.

Acknowledgements

First and foremost, I would like to express my sincere gratitude to Dr. Margherita Primavera for the continuous support (and patience) during these three years, for her knowledge, motivation and enthusiasm in physics analyses and SUSY searches.

My sincere thanks also go to Prof. Edoardo Gorini for his guidance in the MicroMegas sector and in other exciting side projects, always adopting tools and techniques which may have some interesting implications in daily life.

My fellow mates Luigi, Marilea and Alessandro (the only Doc) deserve a particular mention: their experience and helpfulness were crucial, besides always relying on them.

I would like to thank all the members of the 2L0J team: the 2019 ATLAS SUSY Workshop, which took place in Lecce, was an invaluable occasion to make their acquaintance, although the time spent in the dark cave. The social dinner we had all together was the perfect gift to celebrate my birthday, with excellent food, drinks, discussions, laughs and prickly pears.

Still concerning university, special thanks go to all my colleagues, PhD ones and not, with whom I shared unforgettable moments, not only during the last three years! You are all awesome: Alessandro, Antonio, Antonio fortunello, Chiara (x3), Elena, Enrico, Erika, Fabio, Federica, Francesca, Francesco, Irene, Isabella, Laura (x2), Lollo, Mara, Marco, Margherita, Matteo, Mosè, Pierpaolo, Sasà, Shuby, Ziggy. In addition to all of them, it is impossible to forget Alessandro and Salvatore: our discussions, the best ones about football when I am regarded as the jinx of the situation, our 21 matches on a beach still crowded are epic moments, just to cite a few. Finally, despite not being physicists, the engineering crew was an always welcomed, although unauthorized, presence; thanks to Enzo, Gigi, Mario and Stefano.

To make the list even longer, there are all my friends not involved in physics; all of you made a mark on me. A big thanks to Adalgisa, Agnese, Alessandra, Alex, Andrea & Marco, Annalisa, Antonio, Biondo, Camilla, Cannone, Carmen, Chiara, Claretta, Cocco, Cristian, Cristiano, Daniela & Giulia, Danilo, Elena, Elisabetta, Francesca (x2), Francesco, Francesco (the judge), Giacomo, Gianmarco, Gianni, Giorgio, Giorgio (the mayor), Giuseppe, Luca, Lucia, Luisa, Manuel, Marco, Mario (x2), Marta (x2), Mattia, Michele, Piero, Sabrina, Silvia, Simona, Sparrow, Stefania, Stefano, Straffo, Vanessa, Vincenzo. Finally, thanks to Mattia, Steven and Daniele, who recently joined the team, for our epic round trips by bus and ~ 4 km walks in August, under the harsh sun.

Another special thanks go to two very different women, Miriana and Vittoria; the former is exuberant and we shared lots of moments, while the latter has a unique, fascinating perspective and her attitude testified to what I pursue is real.

Last but not the least, I would like to thank my family, my uncle Vanni and my aunt Annarita for the encouragement they gave me throughout my life.

And if you, dear reader, know me and you are a friend of mine, but I missed your name when writing this last page...well, it was not done on purpose. I owe you a drink!